IMPEDANCE-BASED ANALYSIS OF 3D TISSUE MODELS: A NOVEL MEASUREMENT SETUP FOR NOVEL MEASUREMENT MODES

DISSERTATION ZUR ERLANGUNG DES DOKTORGRADES DER NATURWISSENSCHAFTEN (DR. RER. NAT.) DER FAKULTÄT CHEMIE UND PHARMAZIE

DER UNIVERSITÄT REGENSBURG

vorgelegt von

Christina Hupf

aus Lam

im Jahr 2017

Diese Doktorarbeit entstand in der Zeit von März 2012 bis Januar 2017 am Institut für Analytische Chemie, Chemo- und Biosensorik der Fakultät Chemie und Pharmazie der Universität Regensburg.

Die Arbeit wurde angeleitet von Prof. Dr. J. Wegener.

Promotionsgesuch eingereicht am:	05.01.2017
Kolloquiumstermin:	17.03.2017

Prüfungsausschuss:

Vorsitzender:	Prof. Dr. Müller
Erstgutachter:	Prof. Dr. Wegener
Zweitgutachter:	Prof. Dr. Bäumner
Drittprüfer:	PD Dr. Breunig

Table of Contents

1 Introduction

The understanding of the development, function and pathology of tissues and organs is a fundamental human effort. Initially, there have been two model systems mimicking *in vivo* human tissues - the *in vivo* animal model system and the *in vitro* two-dimensional cell culture. While cell monolayers exhibit a comparatively low complexity and less similarity with real tissue, animal models are highly complex. To date animal testing is extensively applied in biomedical research (e.g. stem cell research, genome research, preclinical drug testing). Statistics of the German Federal Ministry of Food and Agriculture show that the total number of animals used for scientific purposes was constantly increasing with ~ 1.8 Mio in the year 2000 to ~ 3.1 Mio in 2012. Only since 2013 the number is slightly decreasing (appendix A2, Fig. S1). In this context, it seems mandatory to pursue the reduction, refinement and replacement of animal testings (the so called “3R”). Reduction and replacement can be achieved with cell culture based testings. Beside 2D cell culture another more recent approach is the application of *in vitro* 3D tissue models. With their intermediate complexity they bridge the gap between traditional cell culture and animal models. In this chapter 3D tissue models are introduced, giving first a brief overview of the different types of 3D models. As this thesis is focused on multicellular spheroids, their structure, formation and application in research are highlighted in subsequent paragraphs. Then, 3D culture is compared to 2D cell culture with regard to their application in biomedical research. Finally, common analytical techniques are presented that are used to monitor the response of cells within multicellular spheroids. In this context, special emphasis is placed on devices based on electrochemical impedance spectroscopy (EIS) that have been developed in the last years.

1.1 Multicellular Spheroids as 3D Tissue Models

1.1.1 Three-Dimensional Cell Culture Models

Three-dimensional cell culture models with their intermediate complexity became an emerging cell-based model system in recent years. For this reason, 3D models using different structural concepts have been developed over time. There are for example microcarrier cultures, spherical monolayered cysts, artificial skin, organotypic explant cultures or multicellular spheroids (Pampaloni et al., 2007). These models are introduced in brief below.

The microcarrier culture is a technique where anchorage-dependent cells adhere and grow upon the surface of small spherical particles in suspension (Van Wezel, 1967). The microcarriers can be porous or non-porous in nature, made from biocompatible materials like cross-linked dextran, collagen, gelatin, polystyrene, cellulose or glass (Kadouri, 1994). Different cell lines are described to grow on microcarriers for different applications. For example epithelial cells were cultured this way to study epithelial functions (Jakob et al., 2016) or infection (Carterson et al., 2005). Also human mesenchymal stem cells with the ability to differentiate into osteoblasts, adipocytes and chondrocytes have been cultured on microcarriers (Petry et al., 2016). Due to their multipotency they are considered as an important tool in regenerative medicine. Since high amounts of these cells are needed for clinical use the microcarrier-based stirred tank bioreactor process turned out to be an appropriate propagation technique.

The so-called cysts are spherical monolayers of polarized cells enclosing a central lumen. In organisms they are present in different kinds of tissue. In the mammary gland they are found as acini, in the lung as alveoli or in the thyroid as follicles (O'Brien et al., 2002). Epithelial cells that can form a self-enclosed monolayer are Madin-Darby Canine Kidney (MDCK) cells when embedded in a collagen matrix. The cells in the monolayer show three types of membrane surfaces. These are the apical surface next to the lumen, the lateral surface between neighboring cells and the basal membrane that adheres to the extracellular matrix (Rehder et al., 2006). Cysts are appropriate models to study the factors leading to cyst formation and expansion (Buchholz et al., 2011; Buchholz et al., 2013; Yuajit et al., 2013) and the establishment of apico-basal

polarity in epithelial cells as well as the tight junction integrity (Rehder et al., 2006).

A more complex epithelial structure is the artificial skin used for example as graft especially for burn treatments. Here, primary fibroblasts are cultured in a petri-dish before they are seeded onto a biodegradable fibre mesh. After a few weeks in culture, keratinocytes are seeded above the new dermal tissue in order to form an epidermal layer (Horch et al., 2005). The approach to generate a skin substitute by combining these two cell types and extracellular matrix components is very promising and might become a good alternative to autografts (Chua et al., 2016). Furthermore, artificial skin is used as alternative to animal testings for the assessment of skin irritations, corrosiveness, phototoxicity and genotoxicity of a variety of reagents e.g. in the cosmetic industry (Brohem et al., 2011). Other applications are the use as photoaging model, in drug penetration studies or for the skin cancer and skin disorder research (Brohem et al., 2011)

Organotypic explant cultures offer the highest complexity among the examples in this chapter. They use dissected organ slices which are typically cultured on porous membranes at the liquid-air interface (Stoppini et al., 1991), on multielectrode array structures (Berdichevsky et al., 2009), or as minced tissue embedded in 3D collagen gels (Toda et al., 2002). Since they preserve the tissue architecture of the original organ they are valuable 3D models for pharmacodynamic profiling of human tumors (Vaira et al., 2010), for the investigation of fetal testis development (Livera et al., 2006) or the study of brain physiology and neuronal activity (Holopainen, 2005; Berdichevsky et al., 2009).

Another 3D model with intermediate complexity is represented by multicellular spheroids. These are spherical cell aggregates formed by a few hundred to several thousand cells resulting in spheroid diameters of a few hundred micrometers. The intercellular spaces are filled with extracellular matrix. Spheroids can be prepared from many different types of cell lines using a variety of formation techniques (for detailed information see chapter 1.1.2). It is also possible to generate co-culture spheroids from two different cell lines that model the cellular heterogeneity of tumors very well. The most important application of spheroids is their use in therapeutically oriented biomedical studies and (high-throughput) drug screening (for detailed information see chapter 1.1.4). Since this

thesis is focusing on the work with multicellular spheroids they are introduced in detail in the following chapters.

There is a variety of scientific problems and questions in the biomedical field that promoted the development of different three-dimensional cell cultures with different levels of complexity. Following the special demands in the respective research fields they were created as cellular aggregates, cellular multilayers or spherical monolayers and have proven to be valuable tools. Especially multicellular spheroids show a high diversity regarding the high number of cell lines that can be used and the formation techniques that have emerged for numerous applications.

1.1.2 Spheroid Formation Process and Techniques

The first researchers who reported about the formation of cellular aggregates in suspension were Holtfreter (1944) and Moscona (1952). Since then multicellular spheroids have been generated from several cell lines using different techniques. All of them are based on the common principle to prevent cell attachment to the culture substrate. In this way, the cell-cell interaction is promoted and three-dimensional aggregates are formed.

The mechanism of spheroid formation can be regarded as a three-step process (Lin et al., 2006). In the first phase suspended cells, typically several hundred / thousand cells form a loose aggregate. This process is promoted by the secretion of long-chain extracellular matrix (ECM) fibers like collagen or fibronectin and a high expression of integrins leading to subsequent integrin-ECM adhesion and consequently to the attachment of neighboring dispersed single cells (Robinson et al., 2004). This phase is followed by a delay period where no morphological changes are observed (Lin et al., 2006). During this delay period the cells express and accumulate E-cadherin. Finally, the compaction of the cell aggregate to a spheroid with strong cell-cell adhesions is proceeded by homophilic interaction of the previously produced E-cadherins between adjacent cells (Ivascu and Kubbies, 2007). In this process the cells on the surface of the aggregate undergo a specific differentiation to smooth, tightly packed polarized

cells that act like a physical barrier very similar to epithelial cells (O'Brien et al., 2002).

In order to generate spheroids several techniques have been developed. In the following, a brief overview of the most common formation techniques is given.
In the liquid overlay culture spheroids are formed by seeding cells on a non-adhesive surface. This can be prepared by coating petri dishes or 96-well plates with agarose or hydrophobic polymers like poly(2-hydroxyethyl methacrylate) (poly-HEMA) (Lin and Chang, 2008). Meanwhile, petri dishes and microplates with non-adhesive coating are also commercially available (ultra-low attachment plates). While spheroid formation on non-adhesive petri dishes produces generally spheroids with a broad size distribution and irregular shape, the formation in coated 96-well plates yields spheroids with a defined cell number in a reproducible size with the formation of one spheroid per well. In order to enhance cell aggregation, centrifugation (Ivascu and Kubbies, 2006; Laurent et al., 2013) or orbital shaking (Frankel et al., 2000; Ong et al., 2010) after cell seeding can be applied. The liquid overlay technique is often used by researchers because it is cheap, simple to perform without the requirement of sophisticated equipment and with the option for scale up (Lin and Chang, 2008; Nguyen et al., 2016).
The hanging drop technique generates spheroids in a microgravity environment. For this purpose, the cell suspension is seeded in drops of 15 – 40 µL upon the inner side of the lid of a petri dish. Then, the lid is inverted and placed back on the petri dish that is generally filled with buffer to prevent evaporation of water from the hanging drops. The surface tension holds the hanging drops in place and the microgravity causes concentration and aggregation of the cells at the liquid-air interface. This technique provides a cost-efficient, simple and reproducible generation of spheroids. The medium exchange however, is complicated (Nguyen et al., 2016) and microscopic observation is difficult using inverted microscopes. Nevertheless, this technique has been improved over the last years in order to overcome some of the above mentioned drawbacks. To be applicable to high-throughput screening hanging drop arrays were developed where up to 384 uniform spheroids can be formed in parallel, cultured for long time and applied to drug testing using liquid handling robots and plate readers

(Tung et al., 2011). Multi-well arrays suitable for the hanging drop approach are also commercially available (InSphero AG, 3D Biomatrix). Furthermore, the hanging drop formation has been combined with fluorescence-activated cell sorting and microfluidic devices enabling perfused culture and easy drug application providing a promising technology for body-on-a-chip research (Frey et al., 2014; Birchler et al., 2016).

Spheroid formation can be performed also in 3D microwells with a defined size. These are fabricated from non-adhesive inert materials like agarose, polyacrylamide gels (Achilli et al., 2012) or poly(dimethylsiloxane) (PDMS) (No et al., 2012), which are polymerized in a mold. A more complex preparation is the fabrication of micromolds in combination with microchannels prepared from poly(methyl methacrylate) (PMMA) using a programmable micromilling system and bonding by press heating (Fukuda and Nakazawa, 2011). After cell seeding spheroids are formed with a diameter that depends on the dimensions of the microwell, thereby guaranteeing defined spheroid size and geometry (Karp et al., 2007). The fabrication of the micromolds however, requires specialized facilities (Lin and Chang, 2008).

Porous scaffolds provide a three-dimensional ECM-mimicking environment and structural support for tissue engineering especially with achorage-dependent cells that require attachment for optimal viability and function (Athanasiou et al., 2013). The fabrication of such scaffolds can be realized with a variety of possible materials. In order to resemble the natural ECM as much as possible, one should choose biocompatible and biodegradable naturally derived matrix materials like collagen, fibronectin, Matrigel (extract from Engelbreth-Holm-Swarm mouse sarcoma, rich in ECM proteins), gelatin, alginate or chitosan (Rijal and Li, 2016). There are also synthetic materials like polycaprolactone (PCL), poly(lactic-co-glycolic acid (PLGA), poly(ethylene glycol) (PEG) and others that have proven to be applicable (Rijal and Li, 2016). Scaffolds can be adapted to the needs of different cell lines by regulating solubility, stiffness, porosity and size during chemical and physical processing (Athanasiou et al., 2013). However, scaffolds from some materials are reported to alter the phenotype of cells (Levy-Mishali et al., 2009) and to produce toxic degradation byproducts with the potential for scaffold-based immunogenicity (Anderson, 2001).

Rotary bioreactors are the method of choice to prepare spheroids in large

quantities (Lin and Chang, 2008). Typically, spinners flasks (Korniski et al., 1999; Wartenberg et al., 2001) or roller bottles (Song et al., 2004) with surface treatment are used for spheroid production (Bilodeau and Mantovani, 2006). This way, spheroids can be formed easily by continuous moving fluid with dynamic control of culture conditions and the option for long-term cultivation. The spheroid size can be influenced by the cell seeding density, the medium composition and the spinning rate as well as the culture time. On the other hand expensive specialized equipment is needed, the generated spheroids show a heterogeneous size distribution (Lin and Chang, 2008) and the technique is very labor-intensive (Nguyen et al., 2016).

All in all, many spheroid formation techniques have been developed to date. The selection of a method is dependent on different criteria that determine the applicability for a certain field of research. For some applications it is important to generate a high number of spheroids, others prefer a uniform size. Other factors are the production efficiency and convenience as well as the possible damage or influence on the spheroid physiology. Of course also the laboratories' conditions and available financial resources have to be considered for the choice of a spheroid formation technique (Lin and Chang, 2008).

1.1.3 Microenvironment of Spheroids and Multicellular Resistance

Multicellular spheroids are avascular tissue models. For large spheroids with diameters above a certain threshold microenvironmental changes occur due to inexistant vascularity (Sutherland, 1988). As a result, gradients of important metabolites like oxygen (Mueller-Klieser, 1984), glucose, lactate (Curcio et al., 2007) and other nutrients, hormones and growth factors are observed. While the spheroid lacks these substances due to their insufficient penetration, toxic metabolic wastes accumulate inside the spheroid ultimately leading to the formation of a concentric heterogeneous microenvironment in the spheroid. At the periphery of the spheroid proliferating viable cells are present while in an intermediate zone viable but quiescent cells can be found. The core of such spheroids is composed of necrotic cells (Mueller-Klieser, 1997; Nguyen et al., 2016). The distance from the spheroid surface at which necrosis arises can vary

for different cell lines, seeding densities and growth conditions. It is also assumed that the development of necrosis is related to a combination of several factors like hypoxia, low pH, lack of nutrients and waste accumulation. Some cells, however, are able to adapt to the insufficient supply (O_2, nutrients) and reduce their metabolic turnover rates, consequently decreasing the steepness of the gradients (Mueller-Klieser et al., 1986; Sutherland et al., 1986). Very similar microenvironmental characteristics can be found also in *in vivo* tumors, making the spheroids an appropriate model system to investigate cancer therapy.

A phenomenon, which is also often observed in tumors and spheroids likewise is the multicellular resistance (MCR). It was first described by Durand and Sutherland (1972) who observed that cells in a multicellular spheroid were more resistant to radiation damage than single cells. They linked this to an enhanced repair capability of cells cultured with a high number of intercellular contacts. Several years of experiments confirm these assumptions. MCR is observed for cancer as well as some normal cells cultured as spheroids with a high degree of cell-cell and cell-extracellular matrix contacts and the typical microenvironment with quiescent and necrotic cells (Desoize and Jardillier, 2000). It has been shown that the resistance to anticancer drugs is induced within 24 h after cell seeding and increased for spheroids with progressive establishment of the typical microenvironment (Olive et al., 1991). However, MCR is reversible when the spheroid is disaggregated. There are two supposed types of MCR mechanisms, the contact resistance due to cell-cell contacts (like in confluent monolayer culture) and the resistance based on the heterogeneous three-dimensional structure. Both are partly related to an altered gene expression that can lead to the inhibition of apoptosis, the efflux of drugs or to a cell cycle arrest.

For instance, $\alpha 5\beta 1$ integrin is a membrane protein that mediates cell adhesion to the ECM. Integrin-mediated cell-attachment is important for cell survival since loss of attachment provokes apoptosis, a process named anoikis. $\alpha 5\beta 1$ integrin is reported to suppress apoptotic cell death by activating downstream survival pathways like the Bcl-2 pathway and thereby inhibiting drug-induced apoptosis in confluent cells and spheroids (Zhang et al., 1995; Nista et al., 1997; Aoudjit and Vuori, 2001; Casey et al., 2001; Weaver et al., 2002).

The multidrug resistance protein 1 (MDR1) protects organs from toxic substances

by an energy-dependent efflux. This protein is over-expressed in many types of cancer cells leading to the efflux of chemotherapeutic agents, whereas knockdown of MDR1 in 3D cell cultures increased chemosensitivity (Liang et al., 2016). It is assumed that E-cadherin also contributes to MDR1 related MCR. As a member of the cadherin family it plays an important role in mediating cell-cell anchoring junctions. A study revealed that the knockdown of E-cadherin led to a decrease in the MDR1 protein, suggesting an E-cadherin dependent regulation of MDR1.

Several antitumor agents are targeted on the inhibition of cell growth and division. The effectiveness of these therapeutic agents is dependent on the rate of cell proliferation. It was found out that cancer cells in tumors show low proliferation rates and thus the effectiveness of cell-cycle dependent antitumor agents was reduced (Croix et al., 1996). This effect was investigated by studying the expression of the protein p27Kip1, which is a known inhibitor of the cyclin-dependent kinases (Cdks). By inhibition of Cdks p27Kip1 regulates the progression from G1 to S phase. Compared with monolayer cells, spheroids showed an upregulated expression of p27Kip1 and an increased number of cells in the G0-G1 phase, whereas the number of cells in S and G2-M phase was decreased. When spheroids and monolayer cells were treated with chemotherapeutic agents the spheroids showed a higher resistance to the drugs than the monolayer cells. However, a down regulation of p27Kip1 in spheroids reduced the intercellular adhesion, increased the cell proliferation and restored the drug-induced cell cycle perturbations (Croix et al., 1996; Xing et al., 2005).

Besides alterations of gene expression another factor that is linked to MCR is the cell kinetic phenomenon of regrowth resistance, as found in cancer patients and spheroids. When spheroids are treated by radio- or chemotherapy the viable proliferating cells on the surface are dying. Subsequently, this damage is compensated by recruiting quiescent cells to return to cell cycle and resume growth (Olive and Durand, 1994; Sham and Durand, 1998; Tan et al., 2015).

Furthermore, the limited drug distribution in *in vitro* cancer spheroids and *in vivo* solid tumors plays a role in MCR. These tissues are mostly avascular or distant from blood vessels (in the case of *in vivo* tumors) and therefore not each cancer cell in the tumor is evenly exposed to the drug (Tannock et al., 2002). Also the

composition and structure of the ECM as well as the microenvironment in the tissue can slow down the diffusion of drugs and lead to gradients. The penetration efficiency is also dependent on the drug itself. Physico-chemical properties like the molecular weight, shape, charge and the drug's solubility influence the penetration as well as its availability and flux inside the tissue. Cellular metabolism, binding and enclosure in endosomes can increase the drug concentration in the outer layers of the tissue and prevent further drug penetration (Minchinton and Tannock, 2006). Limited penetration is for example reported for doxorubicin and mitoxantrone due to their sequestration in acidic endosomes and their binding to DNA (Lankelma et al., 1999; Desoize and Jardillier, 2000; Cowan and Tannock, 2001; Tannock et al., 2002).

A number of mechanisms and structural characteristics in tissue models can lead to multicellular resistance and only a few have been introduced in brief in this section. However, it can be stated that MCR is a serious problem in cancer therapy which needs more investigations and the development of techniques to overcome MCR. The fact that multicellular spheroids exhibit a high resemblance to *in vivo* solid tumors including MCR makes them an appropriate 3D model for their investigation.

1.1.4 Applications

Multicellular spheroids are versatile models for different fields of research for example in medicine, basic research and application-oriented approaches.

Tumor spheroids, an often used type of spheroids, are generally applied as tumor tissue models in drug screening, pharmaco-dynamics and related topics like the investigation of multidrug resistance or multicellular resistance which is further specified with examples from literature in the next passages.
Especially the combination of spheroid formation, culture and subsequent drug testing on specialized platforms / devices is very popular among researchers. A current report describes the testing of eight clinically used antitumor agents (capecitabine, 5-fluorouracil, irinotecan, oxaliplatin, cetuximab, panitumumab, bevacizumab, regorafenib) for colon cancer using colon cancer spheroids in comparison to a mouse model (Yoshii et al., 2016). The spheroids were prepared

on a nanoimprinted microplate from red fluorescent HCT116 cells. The drug 5-fluorouracil (5-FU), which is commonly used for chemotherapy with only limited efficiency (de Vos tot Nederveen Cappel et al., 2004), was used as a reference. The study revealed that regorafenib was the most efficient drug against the tumors *in vitro*. This observation was also confirmed by the *in vivo* model treatment. The drug inhibited the tumor growth significantly compared to the untreated control and the 5-FU reference and is therefore recommended for further preclinical and clinical studies.

Another group developed a 384 hanging drop array which is used to form and culture spheroids from different cell lines (kidney fibroblasts, embryonic stem cells and epithelial carcinoma cells) (Tung et al., 2011). After formation, the epithelial carcinoma spheroids were used for drug sensitivity testing in the array applying different concentrations of tirapazamine (TPZ) or 5-FU. This 3D model system was able to show that 5-FU, which inhibits proliferation, was not efficient in reducing the viability of the cancer spheroids. TPZ, on the other hand, is a hypoxia-triggered cytotoxin that causes DNA damage and led to increased reduction of viability in the same kind of spheroids. A combined treatment though, showed an additive effect since the mechanisms of action complemented each other. While 5-FU acted on the proliferating cells in the spheroid periphery, TPZ killed the cells in the hypoxic core of the spheroid.

The work of Zhang et al. (2005) describes the formation of microencapsulated spheroids from MCF-7 breast cancer cells for screening of the anticancer effect of mitomycin C (MC), adriamycin (ADM) and 5-FU with monolayer cultures as control. The results show that MC induces the highest cytotoxicity in spheroids and monolayers, followed by 5-FU and ADM. The authors were also able to demonstrate that all drugs which were applied to monolayer cells and spheroids (using the same concentration and incubation time) induced a higher cytotoxicity in the 2D cell culture. This result is consistent with several other studies where multicellular resistance was observed for spheroids (Desoize and Jardillier, 2000).

Lee et al. (2010) for example, investigated the chemoresistance of MCF-7 spheroids to 5-FU. While MCF-7 monolayer cultures and 6 d old spheroids without necrotic core showed drug induced apoptosis, 9 d old spheroids with a necrotic core exhibited a significantly reduced level of apoptosis. Furthermore,

the protein p53 which acts as tumor suppressor was found in an aggregated, inactivated form in spheroids with a necrotic core. Therefore, the results indicate that chemoresistance can be provoked by the necrosis-linked aggregation of p53.

Beside the assessment of drug efficiency, spheroids can be used also for cytotoxicity testing after treatment with radiation and / or hyperthermia (Asayesh et al., 2016; Mahdavi et al., 2016) as well as potential toxins like chemical compounds (Lee et al., 2016) or nanoparticles (Lee et al., 2009; Senyavina et al., 2016).

More frequently however, spheroids are used to investigate differentiation as well as cell-cell and cell-ECM interactions in a three-dimensional architecture.
Differentiation was for example studied by Hildebrandt et al. (2010) who monitored the osteogenic differentiation of spheroids from human mesenchymal stem cells. Another cell line, which is very popular among researchers in this field are P19 embryonic carcinoma stem cells which are able to undergo neuronal or cardiac differentiation in the form of embryonic bodies. Several groups were investigating the influence of different induction reagents and experimental parameters on differentiation (Yang et al., 2009; Jasmin et al., 2010) as well as the mechanisms behind this process (Gao et al., 2001; van der Heyden and Defize, 2003).
A prerequisite for differentiation as well as maintenance of tissue architecture and function are cell-cell interactions. Co-culture spheroids from two or more cell lines represent a model system with high complexity which can be used to study heterotypic intercellular cross-talk and its consequences. Using co-cultures, Achilli et al. (2012) investigated the kinetics and extent of self-sorting of a mixture of different cell types. This is a natural process that is known for example during embryogenesis, morphogenesis or cancer metastasis (Duguay et al., 2003). The differential adhesion hypothesis (DAH) tried to explain this phenomenon by assuming that different cell types express different surface adhesion molecules with cohesive or adhesive forces. These lead to the sorting of cells with high cohesion in the core and of cells with low cohesion on the outside (Foty and Steinberg, 2005). The group around Achilli seeded a mixture of human fibroblasts (NHF) and hepatocyte cells (H35) and observed the formation of spheroids with NHF cells in the core and H35 in the shell. They were also able to determine

parameters like the rate and extent of self-sorting as well as the time to reach 50 % sorting.

Furthermore, co-cultures have been used extensively to study the enhancement of liver-specific functions of hepatocyte spheroids (Lin and Chang, 2008). Tissue-specific functional maintenance was increased in co-cultures of hepatocytes in combination with either fibroblasts (Lu et al., 2005), or pancreatic islet cells (Lee et al., 2004), or bone marrow cells (Murakami et al., 2004) or adipose-derived stem cells (No et al., 2012). Spheroids with hepatic function are valuable models for investigations on liver physiology and may serve as sources for human liver transplantation or cell therapy in the future. They have been also incorporated successfully in bioartificial liver devices (Figaro et al., 2015). This is basically a bioreactor containing a high number of functional hepatocyte spheroids providing an extracorporeal liver support device.

In further medical approaches, spheroids can serve as building blocks for organ reconstruction in tissue engineering. Spheroids have been already used for the replication of several complex tissues like liver, cartilage, pancreas, cardiac muscle, pituitary gland, the optic cup or bone tissue (Lin and Chang, 2008; Fennema et al., 2013). Another approach is the vascularization of tissue (Kelm and Fussenegger, 2004) or bone models (Rouwkema et al., 2006). In this process prevascular structures develop within another tissue (*in situ)* or together with a tissue model (*in vitro)*. This can be achieved in different ways, for example by the generation of spheroids from a mixture of endothelial cells and tissue-specific cells. Over time a dense network of vessel-like structures develops within the spheroid. This prevascularization enables a better integration in the host by improving oxygen and nutrient distribution and consequently the survival of the implant (Fennema et al., 2013; Laschke and Menger, 2016).

As could be demonstrated, multicellular spheroids have numerous applications in fundamental application-oriented biomedical research. The great suitability of spheroids as *in vitro* models is based on their three-dimensional architecture with cell-cell and cell-ECM interactions as well as their microenvironment. Furthermore, the formation of spheroids is, in most cases, easy and inexpensive using standardized formation protocols and commercially available growth substrates.

1.2 2D Versus 3D Models

In the preceding chapters characteristics and applications of three-dimensional models, in particular multicellular spheroids were presented. An alternative to 3D *in vitro* models is the use of two-dimensional cell cultures. A huge number of studies using standard 2D cell culture have produced important conceptual advances. In 2D the cells of interest are simply cultured on flat polystyrene substrates to generate a well-controllable and homogeneous cell environment. Medium changes and microscopic analysis can be performed easily and the cell proliferation can be sustained for most cell lines by regular subculturing (Fennema et al., 2013). Cell-based assays using 2D models belong to the key tools in basic research and drug discovery. Although, 2D cell culture was helpful to get an impression of tissue function and mechanistic processes, the 2D approach is not able to reflect *in vivo* tissue characteristics and substitute 3D cultures (Hirschhaeuser et al., 2010). Cells grown on 2D substrates differ from 3D cultures in morphology, cell-cell and cell-matrix interactions and differentiation (Yamada and Cukierman, 2007). Due to the unnatural microenvironment of 2D cultures phenomena like multicellular resistance is not typical for these cells (Desoize and Jardillier, 2000). This can lead, especially in drug discovery, to wrong test outcomes. In the following, the differences between 2D and 3D cell cultures are illustrated in more detail by giving some examples from literature.

When fibroblasts are cultured in 2D or 3D they differ in morphology and cytoskeletal organization. It is reported that when fibroblasts grow on a flat substrate the cells flatten, form stress fibres and become immotile. In contrast to fibroblasts in 3D culture that elongate, are mobile and show an actin cortex and extended filopodia similar to the *in vivo* situation (Walpita and Hay, 2002; Grinnell, 2003). This effect is also observed for primary articular chondrocytes or hepatocytes. When these cells are taken out of the body and cultured on flat substrates they tend to lose their normal phenotype. This effect is, however, reversible by culturing these cells in 3D (von der Mark et al., 1977; Bierwolf et al., 2011).

As an alternative to a whole liver transplantation single hepatocytes can be transplanted. The 2D mature cells, however, lose their differentiation and proliferation capabilities after transplantation. Li et al. (2010) showed that

multipotent mesenchymal stem cells grown in 3D were able to differentiate into hepatocytes which exhibit and maintain more liver-specific functions, like albumin and urea synthesis or the clearance of ammonia and drugs, in comparison to 2D cultured hepatocytes.

Li et al. (2008) characterized the human hepatoma cell line HepG2 in 2D and 3D cell cultures.They reported that spheroids in comparison to monolayer cells showed a higher level of cell-cell adhesion and a greater fraction of cells in G1 phase cell cycle arrest. Spheroids were less apoptotic under regular culture conditions and more resistant to drug-induced apoptosis. Furthermore, protein levels of E-cadherin, cytochrome-c, endostatin and others were increased in spheroids. Their conclusion was that 3D cultures should be preferred over 2D cultures in cancer biology investigations.

Desoize and Jardillier (2000) investigated multicellular resistance (chapter 1.1.2). The group determined the EC_{50} values of five anticancer drugs on human lung cells (A549) cultured as monolayer and as spheroid. The EC_{50} values of spheroids were throughout higher than those of monolayer cells. For spheroid treatment the drug concentration had to be increased, dependent on the drug, by a factor of ~ 10 to ~ 1000. They state that for anticancer drug screening spheroids rather than monolayer cells should be used.

Several studies followed in which the drug response of spheroids and cell monolayers from different cell lines was compared. Horning et al. (2008) reported that MCF-7 cells in 3D culture were more resistant to typical anticancer drugs (doxorubicin, paclitaxel, tamoxifen) than in 2D culture, with a 12- to 23-fold difference in the EC_{50} values. The group showed that spheroids express two times more collagen than monolayer cells pointing to the ECM as a barrier to drug diffusion. The expression of many genes differed significantly for both model systems. Similar results for MCF-7 cells have been reported by Zhang et al. (2005) and Lee et al. (2010).

Summed up, when 2D and 3D cell cultures are compared they differ significantly in biological functions like the cell shape, gene expression, growth behavior, morphogenesis and differentiation (Yamada and Cukierman, 2007). As literature demonstrates, 3D cell cultures are the model system which resembles *in vivo* tissue much better than monolayer cells. Therefore, researchers in the field of

biomedical science prefer 3D tissue models with their intermediate complexity over 2D cell monolayers.

1.3 Analytical Techniques to Study 3D Tissue Models

For 2D cell cultures many well-established analytical techniques are available, ranging from methods for cell staining over cell viability assays to biophysical detection methods such as flow cytometry. These methods have proven also applicability for 3D cell cultures (Tab. 1). Sometimes the protocols have been modified to comply with the requirements of 3D models using increased dye / reagent concentrations or longer incubation times. In some cases the spheroids needed to be dissociated or mechanical sections had to be prepared. Meanwhile, there is an increasing awareness in life science companies to offer optimized protocols and reagents for spheroids in the field of cell viability assays (e.g. the ATP assay CellTiter-Glo® 3D by Promega).

Tab. 1: Overview of techniques for 3D cell culture analysis. Different methods are shown together with their information content and some remarks on preparational steps and references.

Method	***Specification****	***Information Content***	***Remarks on Sample Preparation***	***References***
Microscopy	SEM TEM	Visualization of morphology, internal cellular structure	Cross-linking, dehydration, freezing or embedding, mechanical sectioning	Li et al. (2008); No et al. (2012)
	CLSM 2P Mic. SPIM	Visualization and localization of internal structures	Optical sections, labeling	Wartenberg and Acker (1995); Thurber and Wittrup (2008); Lorenzo et al. (2011)
Cell Staining	Live/Dead Lucifer Yellow Ho/Pi H&E Immunostaining	Visualization of cell viability and morphology; localization of proteins	Labeling, Cross-linking, mechanical sectioning	Wartenberg et al. (2001); Lee et al. (2010); No et al. (2012); Laurent et al. (2013)

DNA-Analog Labeling	BrdU Assay EdU Assay TUNEL Assay	Cell proliferation, Cell cycle kinetics Detection of DNA fragmentation – a hallmark of late apoptosis	Cryosectioning, cross-linking, permeabilization, labeling	Zhang et al. (2005); Laurent et al. (2013) Kotov et al. (2004); Bartholomä et al. (2005)
(Colorimetric) Cell Viability Assays	MTT LDH Presto ATP Assay	Quantification of cell viability, cell proliferation, cytotoxicity	Labeling Cell lysis	Lee et al. (2009); Lee et al. (2013); Frey et al. (2014)
Flow Cytometry		Cell counting, sorting and biomarker detection	Labeling, spheroid dissociation	Khaitan et al. (2006); Li et al. (2008); Weiswald et al. (2010)

* Abbreviations used in the column ***Specification*** are given in the appendix A1.

Although, these methods feature a high information content and good results they are either invasive, need labels or continuous observation, which is very time consuming or not intended (endpoint assays). An alternative to these techniques represents EIS that is non-invasive, label-free and enables continuous monitoring (details about the theoretical background of EIS are given in chapter 3.1). In this context, electric cell-substrate impedance sensing (ECIS) is an established technique for 2D cell culture analysis (chapter 3.3). For 3D cell culture, however, there are only a few devices which were developed for this purpose over the last years.

Most reports on the development and usage of devices for EIS measurements of spheroids have been published by the group around Andrea Robitzki. Their objective was to develop an efficient biomedical screening method based on EIS and 3D cell cultures. In 2001 they published reports on two devices for 3D analysis based on different concepts. One device was constituted by a glass capillary system with four platinum wire electrodes (Thielecke et al., 2001). The capillary (inner diameter: 400 µm) had funnel shaped ends that were bonded to glass tubes. On both sides of these tubes two holes were drilled respectively for the insertion of the electrodes. The capillary was filled with culture medium and

the spheroid was positioned in the center of the capillary using a pump. A sinusoidal current was applied via the two outer electrodes and adjusted to measure a voltage drop of 10 mV across the inner electrodes. Using this setup, they were able to distinguish impedimetrically between control tumor spheroids and spheroids with manipulated genes resulting in decreased growth and increased necrosis. In subsequent reports the same setup was successfully applied for the impedimetric measurement of physiological alterations in spheroids after gene modification and drug application (Bartholomä et al., 2005). Furthermore, this setup was used for the EIS-based detection of osteogenic differentiation of mesenchymal stem cells (Hildebrandt et al., 2010).

The other device comprised an array with planar circular gold electrodes and iridium microring electrodes (Thielecke et al., 2001). The positioning of spheroids on the planar electrodes was performed using a micromanipulator and a microscope. They also developed a simplified equivalent circuit model and an appropriate transfer function for data fitting. Using a three-electrode arrangement they conducted proof-of-concept experiments investigating the effects of Triton X-100 and DMSO on tumor spheroids (T47D clone 11 human breast carcinoma cells) covering the electrodes. The results show that in the frequency range between 50 kHz and 500 kHz they were able to measure a spheroid-related decrease in impedance originating from morphology changes after treatment with the reagents. In the conclusion they already describe how an optimized array with cavities around the electrodes and micro-holes for suction-controlled spheroid positioning should be constructed.

This vision was in fact realized a few years later with the development of their microcavity array (MCA) for drug testing (Kloss et al., 2008). This setup includes 15 square microcavities with different widths (200, 300 and 400 µm) for spheroids with different diameters and a depth of 100 µm. Each of the four sides of a cavity holds a rectangular gold electrode. Positioning of spheroids into the cavities was performed using a micropipette or a micromanipulator and was controlled via light microscopy. For all cavity sizes a difference in impedance magnitude was observed for electrodes with or without spheroids. Using this impedance-based setup the group published two reports in 2008. In one report they compared impedance spectra of spheroids from five different cell types as well as zeolith

and glass beads as inorganic spherical models. Furthermore, they determined the effect of various anti-tumor drugs on spheroids (Kloss et al., 2008). In another report they investigated the effect of the apoptosis inducing agent camptothecin (CTT) on human melanoma spheroids and monitored the contractions of cardiomyocyte spheroids by recording of extracellular potentials with the setup (Kloss et al., 2008). Although the MCA chip was in principle applicable to measure impedimetric changes resulting from morphology alterations in spheroids, they had to cope with high signal to noise ratios and a high impedance variance for spheroids of the same size. For this purpose, the MCA chip was optimized by broadened circuit paths, an increased electrode size, a thicker passivation layer and advanced automatic data processing resulting in an increase in chip sensitivity (Krinke et al., 2010). Further optimization was realized by incorporation of a suction hole in the cavity bottom for automated positioning (Jahnke et al., 2013). Applying this improved MCA chip impedance measurements were performed on brain tumor cultures for drug efficacy testing (Eichler et al., 2015).

The group around Olivier Frey is also working on the development of smart impedance-based devices for spheroid analysis. His team presented different concepts for devices in the last years. One design comprises a microfluidic chip that enables retention, cultivation and continuous analysis of spheroids (Schumacher et al., 2011). As can be seen in Fig. 1 A the spheroid is loaded from the side and is trapped in the main channel at a PDMS retention block. Two planar platinum electrodes are located close to the trap and two other electrodes are further upstream. For increased EIS resolution hydrodynamic focusing can be applied using three independent inlets upstream in the main channel. A conductive liquid in the middle and two non-conductive liquids on the sides generate a liquid sheet in the form of a vertical plane, which can be scanned precisely across the spheroid. This way, impedance spectra of defined cross-sectional areas of the spheroid can be recorded. They were able to demonstrate that spheroid trapping is reproducibly possible and a significant increase of impedance is measured after spheroid insertion. Results also prove that the sheath flow is adjustable, however, there is still a fraction of conductive liquid going also around the spheroid indicating that the system needs optimizations.

Another concept describes a microchannel prepared from SU-8 sealed with glass at the top and bottom (Bürgel, 2013) (Fig. 1 B). A spheroid is dragged by gravity through the channel with a cross-section of 500 x 500 µm^2 and passes an electric field applied by a set of opposing platinum electrodes fixed on the top and bottom. It is stated that the flow-through approach leads to more consistent impedance signals when compared to systems with immobilized spheroids. This device was used to monitor the growth of spheroids and to demonstrate the effect of growth-inhibiting drugs like NaN_3 on HCT-116 spheroids and Diclofenac on Hep G2 spheroids.

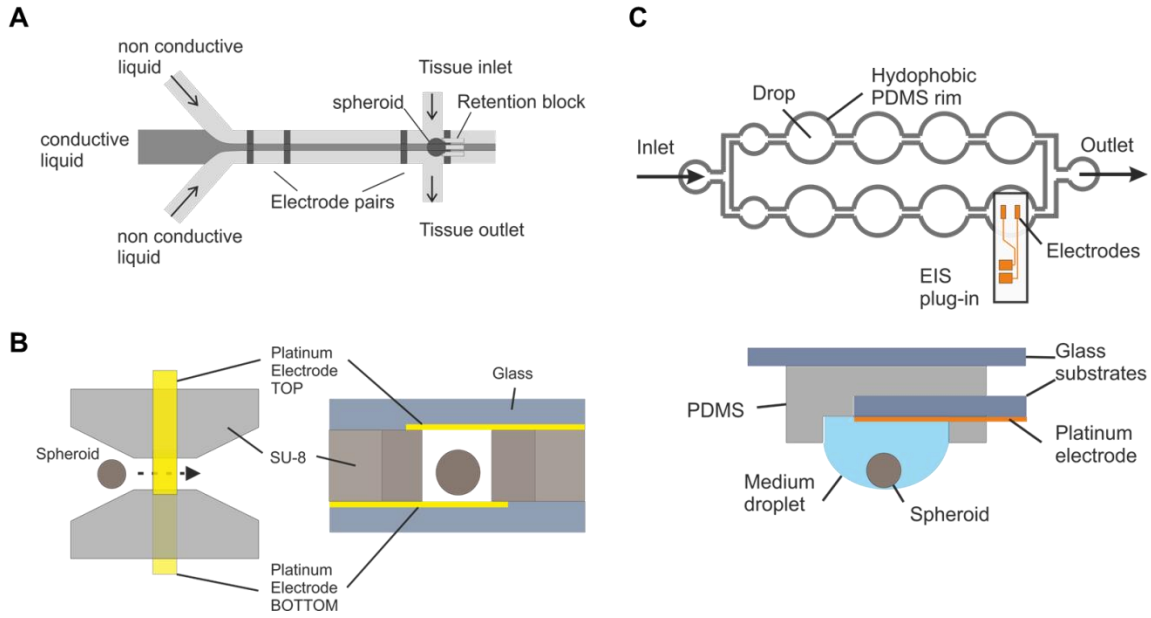

Fig. 1: Illustration of the impedance-based devices presented in the reports of Schumacher et al. (2011) (**A**), Bürgel et al. (2013) (**B**) and Bürgel et al. (2015) (**C**). In **A** a microfluidic chip with a hydrodynamically focussed vertical sheet of conductive liquid is shown. In **B** the spheroid passes the electric field of two opposing platinum electrodes within a microchannel (left side: top view, right side: side view). The EIS measurement in **C** is performed with a removable EIS unit comprising a set of coplanar electrodes that is used as plug-in for a hanging drop network enabling spheroid formation and growth (top: top view, bottom: side view of drop nr. Eight with the EIS plug-in).

A third approach uses a hanging drop device with an exchangeable EIS plug-in (Bürgel et al., 2015). As shown in Fig. 1 C the hanging drop network contains eight spheroids in separate drops that are interconnected by microchannels. It is used to combine spheroid formation and microfluidic culturing in one platform. The EIS plug-in consists of a glass substrate with a set of integrated coplanar

platinum microelectrodes. The plug-in is inserted in a recess between the drop and its PDMS substrate. Using this integrated device the group was able to characterize the beating of human cardiospheres optically and by EIS simultaneously. Furthermore, they observed an amplitude / frequency modulation upon a varied electrical stimulation of the cardiospheres.

Overall, there are few groups working on the development of devices for an impedance-based analysis of multicellular spheroids. The devices which were discussed above are promising, especially the MCA chip seems to be applicable for drug screening after years of device optimization. However, the presented devices show different disadvantages like high parasitic capacitances (Thielecke et al, 2001), high self-impedance of the device and high impedance variances for control spheroids (MCA device). Positioning of spheroids inside the device is sometimes impractical and requires microscopic monitoring (MCA). Most of the devices show a low impedance change upon spheroid addition into the measurement setup leading to a low sensitivity and require an optimization of the device.

2 Objectives

The motivation of this thesis was to develop an impedance-based device to quantify the dielectric properties of multicellular spheroids online in a non-invasive and label-free manner. Handling of the device and positioning of the spheroids should be straightforward. Ideally, the device enables simultaneous microscopic and impedimetric analysis of spheroids.

For this purpose, it was the aim to design and optimize a flow channel including an appropriate electrode layout using transparent electrode and channel material. Three types of 3D tissue models - tumor spheroids, embryonic bodies and cardiospheres - should be cultured and characterized prior to their application in proof-of-concept studies using the novel flow channel for impedance measurements.

The impedimetric characterization of the flow channel with and without spheroid had to be demonstrated first, in order to optimize handling, experimental procedure and measurement parameters. Subsequently, basic correlations between spheroid size and resulting impedance values as well as reproducibility of impedance values upon measurement of one and the same spheroid should be established.

These preliminary experiments should be followed by model studies addressing the individual nature of the three different tissue models: (i) Investigation of tumor spheroid injury and death upon exposure to different invasive chemicals, hyperthermia and photosensitizers, (ii) changes in beating rate of cardiospheres upon exposure to pharmaceutical model substances, (iii) embryonic body differentiation into neurons or cardiomyocytes.

Finally, these results will provide a comprehensive overview of the performance and applicability of the novel impedimetric channel device in the study of 3D spheroid models.

3 Theoretical Background

3.1 Electrochemical Impedance Spectroscopy (EIS)

Impedance spectroscopy is a useful tool for the investigation of the electric properties of biological systems like cells. An alternating voltage of low amplitude is applied to the system at a given frequency. The resulting current is measured and converted to impedance according to Ohm's law. Another approach, which is in use likewise is to apply an alternating current and measure the resulting voltage from which the impedance is calculated. EIS uses low amplitude signals, which makes the technique non-invasive to the cells under study. The data acquisition can be performed in real time with high temporal resolution, which makes EIS highly informative for dynamic systems (Lvovich, 2012). Besides bioanalytical applications EIS is also used for the investigation of interfaces, solid materials or electrochemical kinetics (Lasia, 2002). This thesis makes use of EIS to study cells in the form of two-dimensional monolayer cultures and three-dimensional multicellular spheroids.

3.1.1 Physical Background of EIS

Impedance is the complex resistance to alternating current reflecting the ability of an electric system to resist current flow and to store electrical energy. This is the case when an alternating current is applied to a circuit that is composed of resistors, capacitors and inductors.

The electrical impedance *Z* of a system can be expressed based on Ohm's law as the ratio of sinusoidal voltage *U(t)* and current *I(t)* at time *t*:

$$Z = \frac{U(t)}{I(t)} = \frac{U_0 \cdot \sin(\omega t)}{I_0 \cdot \sin(\omega t - \varphi)} = |Z| \frac{\sin(\omega t)}{\sin(\omega t - \varphi)} \qquad \textbf{Eq. 3.1}$$

with U_0: amplitude of voltage, I_0: amplitude of current, |*Z*|: magnitude of impedance, φ: phase shift between voltage and current and ω: angular frequency ($\omega = 2\pi f$).

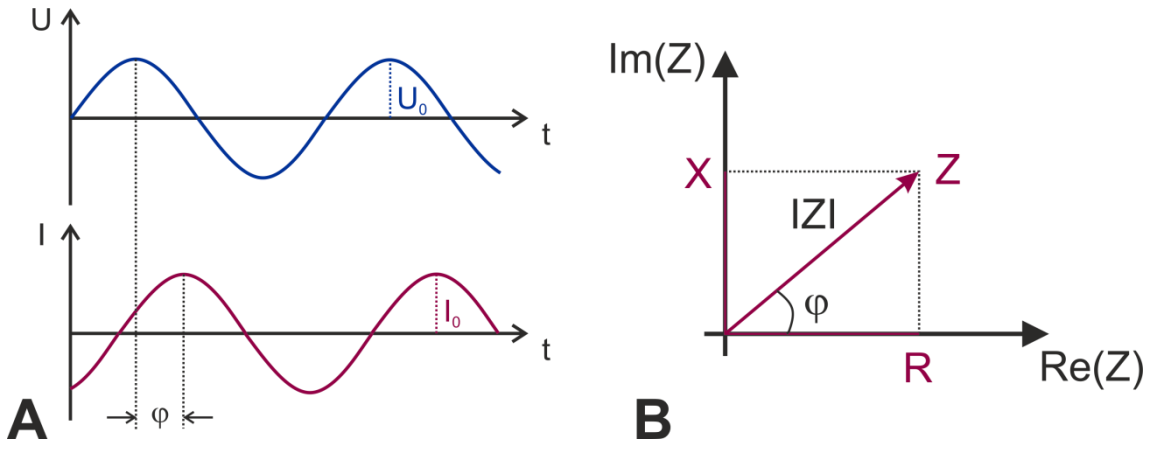

Fig. 2: **A**: Relationship between voltage, current and impedance. A sinusoidal voltage with amplitude U_0 induces a sinusoidal current with amplitude I_0 and a shift in phase by φ. **B**: Illustration of the complex impedance *Z* as a vector in the Gaussian plane. *Z* is composed of a real and imaginary part (*R*, *X*) reflected in the x- and y-axis. The length of the vector *Z* represents the magnitude of impedance I*Z*I and the angle between the vector and the real axis reflects the phase angle φ.

As depicted in Fig. 2 A voltage and current are both sine waves with the same frequency, but the current may be shifted with respect to the voltage by the phase angle φ.

Alternatively, the impedance can also be expressed as a complex function. Using the complex notations for voltage and current:

$$U(t) = U_0 \cdot e^{i\omega t} \qquad \textbf{Eq. 3.2}$$

$$I(t) = I_0 \cdot e^{i(\omega t - \varphi)} \qquad \textbf{Eq. 3.3}$$

with *i*: imaginary unit ($i = \sqrt{-1}$), and Euler's relationship:

$$e^{i\varphi} = cos\varphi + i\, sin\varphi \qquad \textbf{Eq. 3.4}$$

the complex electrical impedance in Eq. 3.1 translates into:

$$Z = \frac{U_0 \cdot e^{i\omega t}}{I_0 \cdot e^{i(\omega t - \varphi)}} = |Z| \cdot e^{i\varphi} = |Z| \cdot (cos\varphi + i\, sin\varphi) \qquad \textbf{Eq. 3.5}$$

So the complex impedance is a combination of the real part, also called *resistance R* arising from current in-phase with the voltage, and the imaginary part, also termed *reactance X* arising from 90 ° out-of-phase current:

$$Z = R + iX \quad \textbf{Eq. 3.6}$$

$$R = Re(Z) = |Z| \cdot \cos\varphi \quad \textbf{Eq. 3.7}$$

$$X = Im(Z) = |Z| \cdot \sin\varphi \quad \textbf{Eq. 3.8}$$

An illustration of the complex impedance *Z* with its real (*R*) and imaginary (*X)* part in the Gaussian plane is given in Fig. 2 B.
Using the following expressions the Cartesian coordinates *R* and *X* can be converted into the polar coordinates I*Z*I and φ and vice versa:

$$|Z| = \sqrt{R^2 + X^2} \quad \textbf{Eq. 3.9}$$

$$\varphi = \arctan\left(\frac{X}{R}\right) \quad \textbf{Eq. 3.10}$$

3.1.2 Data Representation

The two types of data presentation that are typically used in literature are the Bode diagram and the complex plane plot. In the Bode diagram the magnitude of impedance I*Z*I and the phase angle φ are plotted as a function of frequency on double- or semi-logarithmic scales, respectively. Using a logarithmic scale is beneficial when plotting a broad range of frequencies or impedances.
A complex plane plot displays the negative imaginary part (- Im(Z)) of the impedance on the y-axis versus the real part (Re(Z)) on the x-axis. For a system containing resistive and capacitive contributions the complex plane plot typically shows a semicircle providing information on the electrical structure of the system. A drawback of this presentation is that there is no direct information on the frequency dependence. Often, only an arrow pointing to the direction of increasing sampling frequency is included in the plot.

In this thesis the data is presented using the Bode diagram without the phase angle data.

3.1.3 Data Analysis

In impedance spectroscopy an alternating current is applied to a system under investigation and the resulting voltage is measured over a range of frequencies. In order to evaluate the obtained data the electrical structure of the system can be described by an equivalent circuit which is composed of serial or parallel connections of ideal (resistor, capacitor, inductor) and non-ideal (Warburg impedance, constant phase element) equivalent circuit elements. Then, the transfer function of the equivalent circuit is determined considering Ohm's law and Kirchhoff's circuit laws. Finally, the transfer function is fitted to the recorded data to provide quantitative information about the parameters of the circuit elements and how they change during an experiment.

3.1.4 Equivalent Circuit Modeling

In order to build an equivalent circuit that fits to the electrical behavior of the system under study there are five elements that can be used (Tab.2).

Tab. 2: Overview of the ideal and empirical circuit elements, their respective impedance contribution and phase shift. The symbol of each element is given in brackets after the full term.

Equivalent Circuit Element	*Impedance Z*	*Phase Shift φ*
Resistor (R)	R	0
Capacitor (C)	$\frac{1}{i\omega C}$	$-\frac{\pi}{2}$
Inductor (L)	$i\omega L$	$+\frac{\pi}{2}$
Constant Phase Element (CPE) A, n (0 < n < 1)	$\frac{1}{(i\omega)^n \cdot A}$	$-n \cdot \frac{\pi}{2}$
Warburg Impedance (σ)	$\frac{\sigma\,(1-i)}{\sqrt{\omega}}$	$-\frac{\pi}{4}$

The network can hold ideal elements like resistance, capacitance and inductance. An ideal resistor is frequency-independent but influences the amplitude of the current without causing a phase shift. Capacitor and inductor, on

the other hand, are frequency-dependent. While the impedance of a capacitor is decreasing for increasing frequency with a phase shift of -90 °, the impedance of an inductor behaves in the opposite way with a phase shift of +90 °.

The constant phase element (*CPE*) and the Warburg impedance are non-ideal elements since they are themselves frequency-dependent. The Warburg impedance is used to describe a system with diffusion limitations of electrochemical reactions. The *CPE* as a non-ideal capacitor is used to model the impedance of an electrode-electrolyte interface using the parameters *A* and *n*. For $n = 0$ the *CPE* acts as a frequency-independent ideal resistor with $|Z|_{CPE} = A^{-1}$. For $n = 1$ the *CPE* acts as an ideal capacitor with $|Z|_{CPE} = (i\omega A)^{-1}$. For values between 0 and 1 the *CPE* shows both, resistive and capacitive behavior. The *CPE* is an important element in EIS of biological systems since it describes the non-ideal capacitance of membranes as well as the interface of metal electrodes and the overlying electrolyte solutions like physiological buffers or cell culture medium.

3.2 Electric Properties of Tissue Models

The electrical properties of tissues have been investigated and described extensively by researchers (McAdams and Jossinet, 1995). Based on the assumption that these fundamental properties are also valid for 3D tissue models this chapter describes the electric characterization of spheroids. The scientific findings on this topic were used to derive an equivalent circuit and the corresponding transfer function.

Equivalent Circuit Model

The general internal structure of a spheroid is illustrated by the schematic cross section in Fig. 3. A spheroid is made up of several hundred to thousand individual cells connected via cell-cell junctions. The intercellular space can vary depending on whether neighboring cells are in close contact or with a certain distance between them. This “free” space contains extracellular matrix that provides structural and biochemical support. The ECM is composed of fibrous proteins (e.g. Collagen, Elastin) and glycosaminoglycans (carbohydrate polymers forming

negatively charged proteoglycans after attachment to ECM proteins) as well as ions and water. The ECM and the interior of the cells is separated by the hydrophobic bi-layer membrane. It encloses the aqueous cell cytoplasm that is composed of several organelles and ions.

Generally speaking, spheroids are composed of intra- and extracellular electrolytes that are separated by the insulating cell membranes (Martinsen and Grimnes, 2011). Translated in an electrical point of view a spheroid can be described by three parameters. The first is the intracellular resistance R_{int}, which is related to the resistivity of the cytoplasm. The second parameter is the extracellular resistance R_{ext}, which reflects the resistivity caused by the current flow through narrow intercellular spaces and the ECM. And the last one is the non-ideal spheroid capacitance A_{sph}, which comprises the total capacitance of the cell membranes (Fig. 3 A). The spheroid capacitance was modeled by a constant phase element rather than a capacitance as it describes the biological sample better. Typical n-values for tissues were found to be between 0.5 – 0.8 (Kyle et al., 1999), which are significantly different from 1.0 for ideal capacitors.

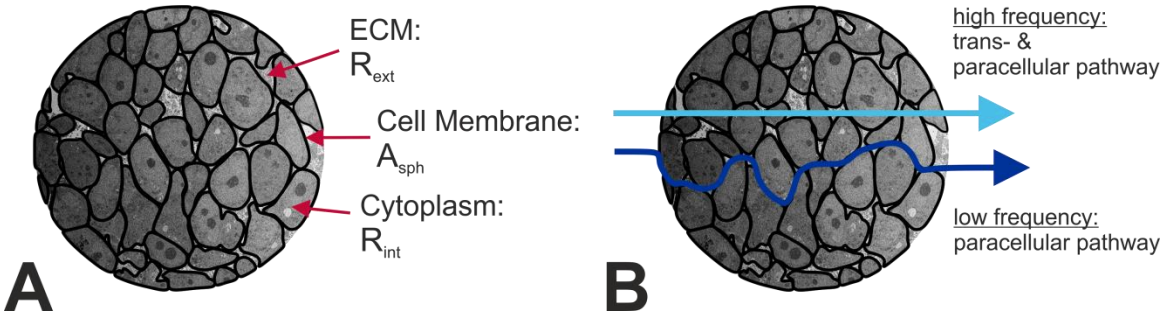

Fig. 3: Schematic of a spheroidal cross section showing the internal structure with neighboring cells and intercellular spaces filled with ECM. When current flows through the spheroid it has to overcome the resistive (R_{ext}, R_{int}) and capacitive (A_{sph}) components of the ECM, the cell cytoplasm and the cell membranes of several cells (**A**). Thereby, the current prefers the paracellular pathway at low frequencies and the trans- and paracellular pathway at high frequencies (**B**).

Upon application of an external electric field the current flow through the spheroid is dependent on the applied frequency (Fig. 3 B). At low frequencies the current flows mainly around the cells and through the extracellular matrix (Gerth and Watke, 1993). With increasing frequency the current is able to couple capacitively

across the cell membranes and flows through the intracellular fluid (Martinsen and Grimnes, 2011).

In order to describe the electric structure of a spheroid with an equivalent circuit the parameters R_{int} and A_{sph} are arranged in series and R_{ext} is connected in parallel to both. This is a commonly used circuit to represent the electrical behavior of 3D tissues (Kyle et al., 1999; Thielecke et al., 2001; Kyle et al., 2004). It is an adaption of the circuit model by Fricke and Morse (1925) that represented the electrical properties of cell suspensions. As a two electrode arrangement was used for the measurement, the electrodes have to be included in the model. Components like the resistance of the spheroid-surrounding bulk medium R_{bulk} and the electrode capacitance described by a constant phase element (A_{el}) have to be connected in series. Additionally, it has to be considered that for electronic readout systems and cables a parasitic contribution can arise, which is also modeled by a *CPE* (A_{para}) parallel to the other elements in the equivalent circuit. The final equivalent circuit (Fig. 4) was used for fitting of the impedance data measured in the novel setup.

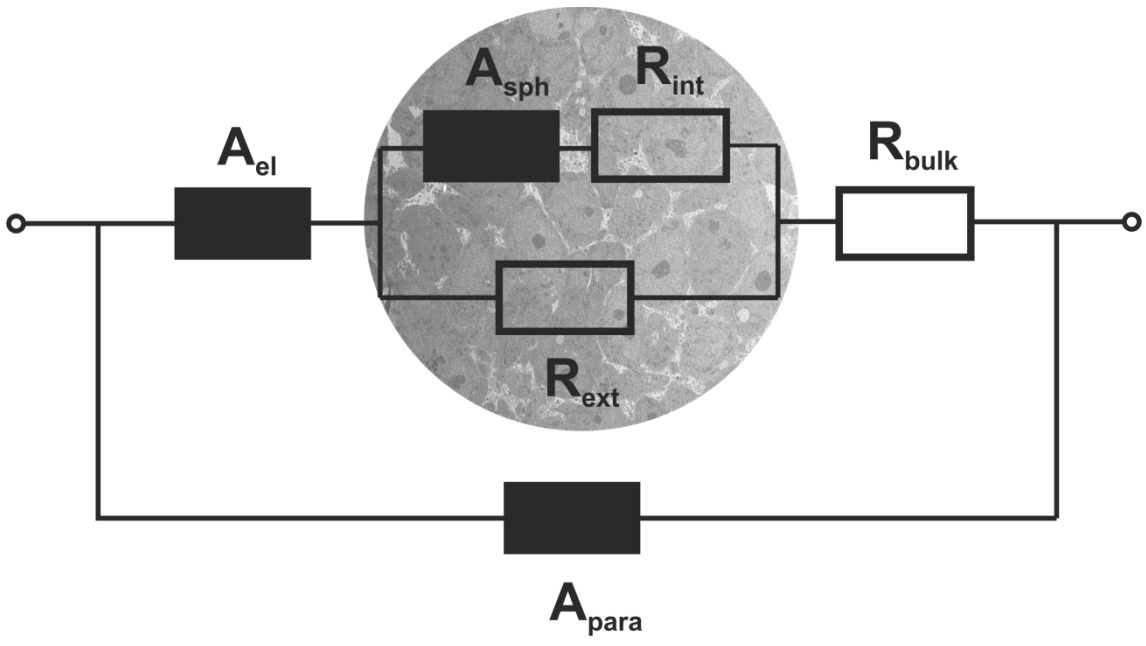

Fig. 4: Equivalent circuit model representing the spheroid as tissue model in an electric device for EIS analysis. The impedance contribution from the spheroid is represented by the spheroid capacitance A_{sph} and n_{sph}, the intracellular resistance R_{int} and the extracellular resistance R_{ext}. Additional circuit elements represent the resistance of the bulk medium R_{bulk}, the capacitive contribution from the electrode-electrolyte interface, A_{el} and n_{el} and the parasitic contribution A_{para} and n_{para}.

Derivation of the Transfer Function

The transfer function for the equivalent circuit in Fig. 4 can be derived stepwise from the impedance of a single cell to the impedance of the spheroid within the EIS measurement setup using Kirchhoff's laws.

The impedance of a single cell Z_{cell} is the sum of its intracellular resistance and membrane capacitance represented as constant phase element:

$$Z_{cell} = R_{int} + \frac{1}{(i\omega)^{n_{mem}} A_{mem}} \qquad \textbf{Eq. 3.11}$$

where A_{mem} and n_{mem} are the *CPE* terms reflecting the cell membrane.

The impedance of a spheroid Z_{sph} is composed of the extracellular resistance R_{ext} and the total impedance of the cells in the spheroid Z_{cell} along the current pathway:

$$Z_{sph} = \left(\frac{1}{Z_{cell}} + \frac{1}{R_{ext}}\right)^{-1} \qquad \textbf{Eq. 3.12}$$

When Eq. 3.11 is applied to Eq. 3.12 and subsequently converted, the following expression for the spheroid impedance is obtained:

$$Z_{sph} = \frac{R_{ext}\,(R_{int}(i\omega)^{n_{sph}} A_{sph} + 1)}{(R_{ext} + R_{int})(i\omega)^{n_{sph}} A_{sph} + 1} \qquad \textbf{Eq. 3.13}$$

where A_{mem} and n_{mem} were replaced by the terms A_{sph} and n_{sph} that should express the total capacitance contribution of the spheroid and not just of one cell membrane (Eq. 3.11). Finally, the total impedance considering the spheroid, the electrode, the bulk medium and the parasitic contribution is given in Eq. 3.14. For the representation of the parasitic stray capacitance as well as the electrode capacitance a constant phase element was chosen with A_{para}, n_{para} and A_{el}, n_{el} as the corresponding terms.

$$Z_{total} = \left[\frac{1}{Z_{sph} + R_{bulk} + \frac{1}{(i\omega)^{n_{el}} A_{el}}} + (i\omega)^{n_{para}} A_{para}\right]^{-1} \qquad \textbf{Eq. 3.14}$$

The three spheroid parameters R_{ext}, R_{int} and A_{sph} which are of interest can now be determined by fitting the transfer function (Eq. 3.14) to the experimental data.

3.3 Electric Cell-Substrate Impedance Sensing (ECIS)

Electric cell-substrate impedance sensing is one of the standardized bioanalytical applications of impedance spectroscopy taking advantage from all its technical benefits (see chapter 3.1). The technique, which was introduced by Giaever and Keese (1984), is used to monitor changes in cell morphology of adherently growing cells.

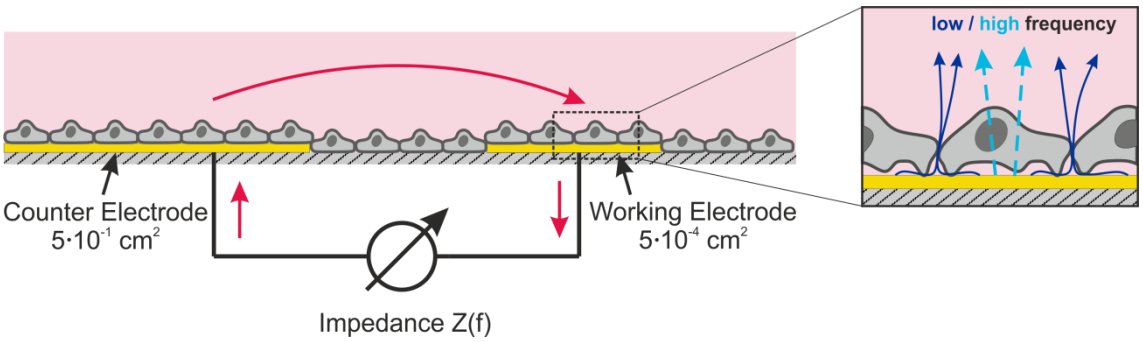

Fig. 5: Schematic showing the principle of ECIS. The setup comprises a large counter electrode and a small working electrode. The conductive supernatant enables the flow of alternating current (red arrows; drawn unidirectional for clarity) between the two cell-covered gold-film electrodes. The zoom-in (right) shows the frequency-dependent current pathways. At low frequencies the current flows along the subcellular and paracellular spaces (dark blue arrows). At high frequencies the current takes the transcellular pathway (light blue dashed arrows).

As can be seen in the scheme above (Fig. 5) the technique uses a two-electrode setup. The cells are growing on coplanar gold-film electrodes and the conductive culture medium above enables the electric connection between the electrodes. A low sinusoidal ac voltage is applied to the electrodes at varying frequencies and the resulting current is measured providing the frequency-dependent impedance.

Using a very small working electrode ($5 \cdot 10^{-4}$ cm^2) compared to the much bigger counter electrode ($5 \cdot 10^{-1}$ cm^2) ensures that the measured total impedance is dominated by the small working electrode while the impedance contribution from the counter electrode can be neglected (Lukic and Wegener, 2015).
When cells are seeded onto this electrode setup, they are adhering and growing to confluence in close proximity to the electrode surface. By applying an AC voltage, the impedance of the cells on the working electrode is measured with high sensitivity. There are two possible current pathways into the conductive

culture medium to overcome the cell layer with the capacitive, non-conductive membranes. Using low frequencies, the current can flow around and between adjacent cells. At high frequencies the current can also couple capacitively through the cell membranes. When frequency spectra of electrodes with and without cells are compared a significant increase in impedance is measured for cell-covered electrodes in a middle frequency range between 10^2 and 10^5 Hz, dependent on the cell line. When the cells respond to a certain stimuli the cell shape change can be observed as the change in impedance.

Typical applications of ECIS are the measurement of cell adhesion and spreading (Wegener et al., 2000), proliferation of cells (Stolwijk et al., 2012), cytotoxicity screenings (Arndt et al., 2004) or the investigation of the wound healing efficiency (Keese et al., 2004). By using a measurement mode with a higher time resolution it is also possible to measure the so-called micromotion of cells (Giaever and Keese, 1991).

3.4 Confocal Laser Scanning Microscopy and its Limitations for Spheroid Imaging

The confocal laser scanning microscope (CLSM) is basically a fluorescence microscope with some innovative improvements. The first optimization was the application of confocal optics (Minsky, 1988) using a source and a detector aperture to suppress out-of-focus fluorescence and to enable the optical sectioning of samples. Further improvements like the application of lasers as light source and the scanning of the fine laser beam over the sample (Amos and White, 2003) make the CLSM an imaging technique of good lateral and axial resolution with the potential to generate three-dimensional images using computerized reconstruction algorithms (Brakenhoff et al., 1986; Chen et al., 2011). Therefore, the CLSM is often used to visualize structural properties of tissues and cells (Wartenberg et al., 1998; Patel and McGhee, 2007; Ramu et al., 2015).

Principle

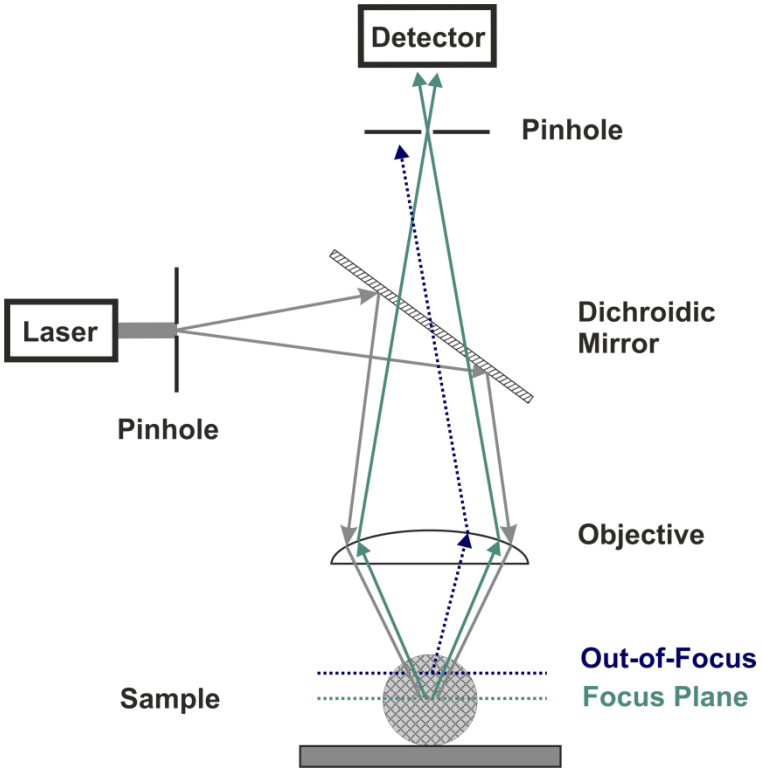

Fig. 6: Schematic illustration of the light path through the CLSM. A point source (grey arrows) is reflected at the dichroidic mirror and focused onto the sample, e.g. a spheroid. Emitted fluorescence from the focus plane (green arrows) and from out-of-focus (blue dotted arrows) is able to pass through the dichroidic mirror and is led to the detector pinhole where only the light coming from the focal plane can pass.

The sample is positioned on the motorized microscope stage, which is used to adjust the focal plane in the z direction. The monochromatic laser beam is focused on the sample, using the dichroidic mirror and the objective, where it excites the fluorophors in the sample to emit light. The emitted light is led back to the dichroidic mirror where it passes through and reaches the detector pinhole and the light sensitive detector, a photomultiplier tube. Reflected light or fluorescence from above or below the focal plane is excluded at the detector pinhole. By choosing a very small pinhole diameter the axial resolution can be improved because more out-of-focus light is suppressed. This way, the laser beam is scanned across the sample in the horizontal direction using oscillating mirrors and thus the whole image is created on the computer screen pixel-by-pixel. In order to achieve three-dimensional information on the sample a series of

optical sections from different planes within the specimen can be aquired and processed on the computer.

Limitations and Alternatives

The CLSM with its potential to generate optical sections of a sample seems to be an attractive technique to gain insight in tissues. There are, however, some limitations that have to be considered. Spheroids are thick biological specimens with diameters of up to 500 µm and bigger. When such a specimen is imaged with the CLSM the excitation light is partly absorbed or scattered in deeper tissue layers causing an attenuated fluorescence intensity with increasing sample depth. High-resolution imaging is therefore limited to the cell layers at the tissue surface in 100 – 200 µm depth (Tadrous, 2000; Helmchen and Denk, 2005). Beside the limited imaging depth there is also the limited penetration of fluorophores (and other substances) into multicellular spheroids, often referred to as multicellular resistance (Desoize and Jardillier, 2000; Lin and Chang, 2008).
A study of Wartenberg and Acker (1995) is dealing with this exact topic. They were investigating the vitality status of living brain cancer spheroids and thereby also determined the imaging depth of the confocal microscope they used. As vital cell stains they used fluorescein diacetate or calcein AM which are converted to polar fluorescent molecules by intracellular esterases. In order to overcome the dye accumulation in the peripheral cell layers (at 24 °C: 60 µm of outermost spheroid rim was stained) they performed the staining procedure at low temperatures (8 °C) and were able to achieve a homogeneous staining in spheroids with diameters of up to 250 µm. For spheroids with increased diameters they observed attenuation of the fluorescence intensity in deeper layers of homogeneously stained spheroids. This was corrected by a monoexponential decay law and an attenuation coefficient was determined that was used to correct the raw data for light absorption and scattering with increasing depth of the laser beam. After mathematical correction they were able to prove the three-dimensional vitality pattern of spheroids. This pattern includes viable stained cells in the outer spheroid shell whose extension was decreased for an increasing spheroid diameter and reached 64 ± 7 µm in spheroids with a diameter of 500 µm. The pattern contains also a middle shell of unstained quiescent cells with a thickness of 50 – 150 µm and a central core region with

lucifer yellow/VS stained dead cells. As this example shows the limitations pointed out above can be overcome by a smart experiment design and mathematical correction procedures. Another way to avoid the limitations of the CLSM is to use alternative microscopy techniques.

In order to visualize the internal structure of tissues or spheroids it is possible to prepare ultrathin sections and perform subsequent imaging by transmission electron microscopy. Also, cryosections can be prepared and imaged with the light or fluorescence microscope after histological preparations. Although, these techniques achieve good results, they are invasive.

For imaging of intact viable tissues or even animals the two photon-excited fluorescence laser scanning microscopy can be applied. A pulsed laser is used to excite a fluorophor with two photons that have to be absorbed almost simultaneously. Therefore, excitation light with wavelengths in the near-infrared range can be used, which is able to penetrate deeper into scattering tissue with reported depths of up to 1 mm (Theer et al., 2003). Furthermore, less bleaching and phototoxic effects are observed due to the lower energy of the irradiated light. Only in the focal point the photon density is high enough for a simultaneous two-photon absorption, whereas beyond this point the light intensity is too weak for fluorescence excitation. In addition, this kind of microscopy is far less sensitive to light scattering in thick tissues because the density of scattered excitation photons is generally too low to generate a significant signal (Helmchen and Denk, 2005).

Another alternative is the selective plane illumination microscopy (SPIM) that combines widefield microscopy with optical sectioning. It allows for imaging of large living samples with high resolution and a minimum of photodamage and scattering artifacts (Verveer et al., 2007). In SPIM the optical fluorescence excitation and detection paths are distinct and perpendicular to each other. The sample, which is placed at the intersection of the illumination and detection axes, is irradiated with a sheet of light and the emitted fluorescence is collected by a charge coupled device (CCD) camera. For optical sectioning of a whole sample, the latter is moved stepwise along the detection axes or rotated around the vertical axis to aquire a stack of images (Huisken and Stainier, 2009). This

technique is very well suited to perform extended time-lapse imaging of viable specimen (Huisken et al., 2004; Lorenzo et al., 2011).

4 Materials and Methods

4.1 Cell Culture Techniques

4.1.1 Cell Lines

In order to analyze three different types of tissue models the cell lines MCF-7 (*Michigan Cancer Foundation-7*), P19 and Cor.At® were chosen.

MCF-7 is a commonly used human breast adenocarcinoma cell line. The acronym refers to the institute in Detroit where the cell line was established in 1973 by Herbert Soule and co-workers. The group isolated the cells from the pleural effusion of a 69 year old Caucasian woman (Frances Mallon, † 1970) with metastatic mammary carcinoma and succeeded as first in obtaining a stable mammary cell line. MCF-7 cells show an epithelial-like morphology and are adherently growing. Characteristics like for example the expression of estrogen receptors make MCF-7 cells a very popular mammary cell line for investigations of estrogen response (Levenson and Jordan, 1997) and in breast cancer therapy (Lee et al., 2010). MCF-7 cells that were used in this thesis were kindly provided by the research group of Prof. Göpferich (University of Regensburg).

P19 is an embryonic carcinoma cell line derived from a murine teratocarcinoma. McBurney and Rogers (1982) were the first who transplanted an early embryo into the testis of a mouse and thereby formed P19 carcinoma cells. When P19 cells are seeded on a non-adhesive surface at high density they spontaneously form so-called embryoid bodies. A further characteristic of P19 cells is the pluripotency. When induced by certain chemical agents they can differentiate into cell types that are representative for the three different germ layers (McBurney, 1993). This makes the cells a popular model system to study the differentiation into neuronal and cardiac cells. P19 cells used in this thesis were purchased from the *Deutsche Sammlung von Mikroorganismen und Zellkulturen GmbH* (Leibniz-Institut DSMZ, Braunschweig).

Cor.At® cells, which were purchased from Axiogenesis AG, are cardiomyocytes derived from transgenic mouse embryonic stem cells. According to the supplier

these cells are highly standardized and 99.9 % pure with a full functional cardiac phenotype. Similarly to primary cells they exhibit limited proliferative capacity and therefore, they should not be subcultured. The cells are generally used for *in vitro* assays in pharmacology and toxicology.

4.1.2 General Culture Conditions

The cell culture work was done in a laminar flow hood under sterile conditions. All consumables were purchased sterile or got autoclaved (20 min at 120 °C). Sterile culture medium and solutions were used. Solutions that were not purchased in sterile form were passed through a sterile filter (pore diameter: 0.2 µm). MCF-7 and P19 cells were grown in polystyrene culture flasks with a growth area of 25 cm^2 and 4 mL of culture medium. They were kept in an incubator at 37 °C and 5 % CO_2 in a humidified atmosphere. All culture media, physiological buffers and solutions were warmed to 37 °C in the water bath before they were added to the cells.

4.1.3 Subculturing

When MCF-7 or P19 cells reached ~ 90 % confluence, they were transferred to fresh culture flasks following individual subculturing protocols. Cor.At® cells, however, show limited proliferative capacity and it is recommended by the supplier not to passage them. Therefore, the cells were thawed (see chapter 4.1.4) and directly seeded to form cardiospheres (chapter 4.1.5).

MCF-7

First, the cell monolayer was washed twice with phosphate buffered saline (PBS^{--} without Ca^{2+} and Mg^{2+}). Then, the cells were incubated with 0.25 % (w/v) Trypsin supplemented with 1 mM EDTA (ethylenediamine-tetraacetic acid) for 3 min in the incubator in order to detach the cells from the culture substrate. The chelating agent EDTA is supporting this process by binding the adhesion co-factors Ca^{2+} and Mg^{2+}. The trypsin digestion process was terminated by adding an excess of the culture medium (10 mL) to the cell suspension. The cells were spun down using centrifugation with 200 x g for 5 min at room temperature (RT). Afterwards,

the supernatant was aspirated and the cell pellet was resuspended in fresh culture medium. The cell suspension was transferred to fresh culture flasks with a ratio of 1:4 or 1:10 relative to the original cell density per cm^2. Following this protocol, the MCF-7 cells were subcultured twice a week.

P19

The cell monolayer was washed twice with PBS^{--} before 1 mM EDTA in PBS^{--} was added to the cells for 5 min at RT. Afterwards, the cell detachment was induced by incubating the cells in 0.05 % Trypsin-EDTA solution for 2 min at 37 °C. Culture medium (10 mL) was added to inactivate trypsin and the cell suspension was centrifuged with 110 x g for 10 min at RT. The supernatant was discarded and the remaining cell pellet was resuspended in fresh culture medium. Aliquots of the cell suspension were transferred to new culture flasks with a ratio of 1:10 or 1:20 relative to the original cell density per cm^2. Following this protocol, the P19 cells were subcultured twice a week.

Tab. 3: Composition of MCF-7 or P19 cell culture medium. Cor.At® culture medium was purchased ready to use together with a Puromycin stock solution (10 mg/mL).

MCF-7	***P19***
Minimum Essential Medium Eagle	Minimum Essential Medium Eagle (Alpha Modification)
2.2 g/L $NaHCO_3$	2.2 g/L $NaHCO_3$
1 g/L D-glucose	1 g/L D-glucose
10 % (v/v) FCS	10 % (v/v) FCS
2 mM L-glutamine	4 mM L-glutamine
100 µg/mL penicillin	100 µg/mL penicillin
100 µg/mL streptomycin	100 µg/mL streptomycin
1 mM pyruvate	

4.1.4 Cryopreservation

MCF-7 and P19

For routine cryopreservation cells were detached from the bottom of the culture flask following the respective subculture protocol (chapter 4.1.3). After centrifugation the cells were resuspended in a cryoprotective solution consisting of 90 % (v/v) FCS (fetal calf serum) and 10 % (v/v) DMSO (dimethylsulfoxide). Aliquots of about 1.5 – 2 mL cell suspension were frozen in cryovials using a two-step process. In the first phase the vials with cell suspension were kept in an isopropanol bath at - 70 °C that enables slow cooling with a rate of 1 °C/min. Afterwards, the cells were transferred to liquid nitrogen for longtime storage.
The frozen cells were reactivated by keeping the cryovial first at – 20 °C for 1 – 2 h and subsequent rapid thawing in the waterbath at 37 °C. Then, the cell suspension was transferred to a sterile centrifugation tube (50 mL) and fresh culture medium (10-fold amount of cell suspension) was added dropwise. The cells were spun down and the supernatant was removed. The cells were resuspended in fresh culture medium and seeded in culture flasks in the ratios 1:2, 1:4 and 1:8 with respect to their growth area prior to freezing. Exchange of the culture medium was done 24 h post-thawing. Afterwards, cell cultivation was performed following the standard protocol.

Cor.At®

These cells were purchased frozen in cryovials containing 1 million cells and kept in the gas phase of the liquid nitrogen tank until use. For recultivation the cells were thawed in the waterbath at 37 °C within 2 min and transferred into a centrifugation tube (50 mL) containing 8 mL of Cor.At® culture medium. The remaining cells in the vial were rinsed with 1 mL culture medium and added to the tube. After centrifugation at 200 x g for 5 min at RT the supernatant was aspirated and the cell pellet was resuspended in 4 mL culture medium supplemented with the selecting antibiotic (10 mg/L puromycin). The cells were cultured in puromycin-containing culture medium for 48 h. Afterwards, the cells were cultured in medium without puromycin and it was exchanged every other day. The cells were kept in a standard cell culture incubator at 34 °C. Due to their

restricted proliferative capacity they were in culture only for the duration of experiments (7 – 14 d).

4.1.5 Formation of 3D Tissue Models

In this thesis spheroids were formed using two commonly used techniques. First, the formation on a non-adhesive surface is described, which was used for all three cell lines (MCF-7, P19 and Cor.At®) and second the hanging drop technique, which was applied for P19 and Cor.At® cells.

Spheroid Formation on a Non-Adhesive Surface

Non-adhesive plates were generated by coating standard 96-well plates with 1.5 % agarose in the respective serum-free culture medium at least one day prior to cell seeding. The plate for Cor.At® cells was prepared using Dulbecco's Modified Eagle's Medium (DMEM) without any further additives as the commercially available Cor.At® medium is already supplemented with serum.
MCF-7 and P19 cells were subcultured following the respective protocol in chapter 4.1.3. After resuspension of the cell pellet, the cells were counted using a Bürker hemacytometer. Cor.At® cells were prepared as described in chapter 4.1.4, without cell counting. Then, the cells were diluted in fresh culture medium (Cor.At®: puromycin-containing medium) supplemented with 20 mM HEPES (4-(2-hydroxyethyl)-1-piperazineethane-sulfonic acid) buffer. The use of the latter was necessary because the cells were kept in an incubator without CO_2 for the first hours of the formation process. The cell suspension was pipetted in the wells of the non-adhesive 96-well plate (200 µL/well). After cell seeding the plate was sealed with parafilm and kept in an incubator at 37 °C (Cor.At®: 34 °C) without CO_2 on an orbital shaker. The plate with MCF-7 cells was rotated for 4 h at 120 rpm and afterwards over night at 50 rpm. P19 cells were rotated for 3 – 4 h at 75 rpm, and Cor.At® cells were rotated at 75 rpm over night. The aggregation of cells was enhanced by orbital shaking of the plate in the first hours after cell seeding. Afterwards, the plate was transferred to a standard cell culture incubator with 37 °C (Cor.At®: 34 °C) and 5 % CO_2.

Hanging Drop Technique

P19 and Cor.At® cells were prepared (see chapter 4.1.3 and 4.1.4) and diluted in the respective fresh culture medium. The respective seeding densities are specified in the following chapters or in the respective results chapters. Then, the cells were seeded as 35 µL drops in the lid of a standard petri dish (Ø = 10 cm). In order to prevent the drops from drying the bottom of the petri dish was filled with PBS^{--} before it was transferred to a standard cell culture incubator.

4.1.6 Growth Studies

Growth studies were performed for MCF-7 spheroids and P19 embryonic bodies, which were generated in the agarose coated 96-well plate (formation on a non-adhesive surface technique). For this purpose, the protocol in chapter 4.1.5 was followed and the cells were seeded in appropriate densities. Using MCF-7 cells, spheroids with a seeding density of 1000 / 2000 / 3000 / 4000 / 5000 / 6000 cells/well were prepared. Using P19 cells, embryonic bodies with a seeding density of 200 / 400 / 600 / 800 / 1000 cells/well were formed in the 96-well plate. The growth of the 3D tissue models of both cell lines was documented for seven days by taking phase contrast photographs. The spheroid diameters were evaluated using imageJ software.

4.1.7 Induction of Cardiac or Neuronal Differentiation in P19 Cells

P19 embryonic bodies (EB) were formed on non-adhesive petri dishes or 96-well plates as well as by the hanging drop approach. For the formation in the petri dish the seeding density for cardio-differentiation was 10^6 cells (Jasmin et al., 2010) and for neuro-differentiation 10^5 cells (Bain et al., 1993; Gao et al., 2001). The seeding densities for hanging drops and in 96-well plates varied and were specified in the respective results chapters. In order to induce cardiac differentiation 1 % (v/v) DMSO was added to the cell suspension. For neuronal differentiation 1 µM retinoic acid (RA) was added as inducing agent to the cell suspension immediately before seeding. The concentrations for both inducers apply for each method of EB formation. After 3 – 4 d the culture medium was exchanged by fresh medium without inducers.

4.1.8 Cell Viability Assay for Spheroids

The viability of spheroids was determined using the PrestoBlue® cell viability assay which contains the redox indicator resazurin. This cell membrane permeable compound is blue and non-flourescent. When it is added to viable cells resazurin is reduced within the cytoplasm to pink resorufin that shows strong fluorescence (λ_{exc} = ~ 535 nm, λ_{em} = ~ 615 nm). The higher the number of viable and metabolically active cells the more intense is the fluorescence.

Effect of Saponin on Spheroid Viability

MCF-7 cells were seeded in a density of 3000 cells/well in the columns 1 – 11 of an agarose coated 96-well plate following the standard protocol for MCF-7 cells in chapter 4.1.5. Seven days after cell seeding the supernatant in each well was removed carefully and the spheroids were incubated for 4 h at 37 °C with 150 µL/well of different saponin concentrations in PBS^{++} with 1 g/L glucose (PBS^{++}/glc) in the columns 1 – 9. The wells in columns 10 and 12 were filled with 150 µL/well PBS^{++}/glc and in column 11 they were filled with 100 µL/well PBS^{++}/glc. After 3 h of incubation 50 µL/well of 1.5 % Triton® X-100 in PBS^{++} were added to the wells of column 11. These spheroids served as positive control.

Tab. 4: Pipetting scheme for columns with (w) and without (wo) MCF-7 spheroids incubated with saponin (Sap), Triton® X-100 or PBS^{++}/glc.

Column nr.	***Well Content***	***Column nr.***	***Well Content***
1	1.00 ‰ Sap. (w)	7	0.05 ‰ Sap. (w)
2	0.75 ‰ Sap. (w)	8	0.025 ‰ Sap. (w)
3	0.50 ‰ Sap. (w)	9	0.01 ‰ Sap. (w)
4	0.25 ‰ Sap. (w)	10	0 ‰ Sap. (w)
5	0.10 ‰ Sap. (w)	11	0.5 % Triton (w)
6	0.075 ‰ Sap. (w)	12	PBS^{++}/glc (wo)

After completed saponin or Triton® X-100 incubation the supernatant in each well was removed carefully and the wells containing spheroids were washed with

PBS^{++}/glc. Then, 150 µL/well PrestoBlue® reagent (diluted 1:10 in PBS^{++}/glc) were added in each well and the spheroids were incubated for 17 – 18 h in a CO_2-free incubator on an orbital shaker at 50 rpm before the fluorescence (λ_{exc} = ~ 532 nm, λ_{em} = ~ 600 nm) was measured at the Tecan Genios reader (top read mode).

For data analysis the measured fluorescence intensities were corrected by the value of the positive control and then the cytotoxicity index (*CI*) was calculated using Eq. 4.1 with I_{sample} as the corrected average intensity in saponin treated wells and $I_{control}$ as corrected average intensity of negative control wells.

The *CI* values were then plotted against the log of saponin concentrations to determine the concentration of half-maximum MCF-7 spheroid response, EC_{50}. This was done by fitting the dose response sigmoidal transfer function of OriginPro 8 (Eq. 4.2) to the plotted data points. The parameters reflect the signal response *y* at a given concentration *x* with a maximal response *A2*, a minimal response *A1*, the point of inflection x_0 and the Hill slope *p*.

$$CI\ [\%] = \left(1 - \frac{I_{sample}}{I_{control}}\right) \cdot 100 \qquad \textbf{Eq. 4.1}$$

$$y = A1 + \frac{A2 - A1}{1 + 10^{(logx0 - x)p}} \qquad \textbf{Eq. 4.2}$$

Effect of Hyperthermia on Spheroid Viability

For this assay, two 96-well plates of seven day old spheroids (3000 cells/well) were prepared following the standard protocol for MCF-7 cells in chapter 4.1.5. The spheroids were transferred within culture medium to 1.5 mL eppendorf cups and were incubated for 1 h or 3 h at 41 / 43 / 45 °C in the Thermomixer. Afterwards, the spheroids were transferred in a fresh agarose 96-well plate (one plate per temperature; two spheroids/well). For a negative control untreated spheroids from the incubator were used. For a positive control untreated spheroids were transferred on the respective 96-well plates and incubated for 1 h in 150 µL of 0.5 % Triton® X-100 in medium. Subsequently, the supernatant in each well was removed and 150 µL/well PrestoBlue® reagent (diluted 1:10 in medium) were added. The spheroids were incubated for 3 h in a CO_2-free

incubator on an orbital shaker at 50 rpm before the fluorescence (λ_{exc} = ~ 532 nm, λ_{em} = ~ 600 nm) was measured at the Tecan Genios reader (top read mode). For data analysis the measured fluorescence intensities were corrected by the value of the positive control and then the cytotoxicity index was calculated using Eq. 4.1.

4.1.9 Preparation of Hypo- and Hyper-Osmotic Buffers

For the model studies on the effect of osmotic stress in MCF-7 spheroids buffers with varying osmolarity but equal conductivity were prepared following the protocol of O'Connor and co-workers (1993). First, a standard buffer was prepared (Tab. 5) and adjusted to pH 7.4 by adding 1 M NaOH. In order to prepare an isoosmotic (~ 300 mOsmol/kg), two hyperosmotic (~ 400 / ~ 500 mOsmol/kg) and a hypoosmotic buffer different amounts of NaCl and sucrose were added to the standard buffer (Tab. 6). Then, the conductivity of each buffer was adjusted to the same value (9.1 mS/cm) by addition of 2 mM NaCl. This was done to ensure that the buffers show the same baseline impedance in EIS measurements. The final osmolarities were determined and the buffers were passed through a sterile filter.

Tab. 5: Composition of the standard buffer.

3.3 mM KCl
1.2 mM KH_2PO_4
1.3 mM $CaCl_2$
0.4 mM $MgSO_4$
10 mM D-(+)-Glucose
25 mM HEPES

Tab. 6: Overview of the NaCl and sucrose additions to the standard buffer and the measured osmolarity and conductivity of the resulting buffers.

	Hypo-osmotic	***Iso-osmotic***	***Hyper-osmotic I***	***Hyper-osmotic II***
Standard buffer + NaCl / mM	73	75	84	90
+ Sucrose / mM	-	94	194	264
Osmolarity / mOsmol/kg	191	309	433	532
Conductivity / mS/cm	9.1	9.1	9.1	9.1

4.2 Microscopy

Microscopy was applied in this thesis for different purposes using different microscope types. Phase contrast microscopy was used in laboratory routine to check confluence of cell cultures and to confirm the formation of spheroids. It was also used to observe spheroids over time to investigate their growth or to monitor the swelling and shrinking of spheroids in solutions with varying osmolarity. Fluorescence microscopy with epi-illumination was applied in the phototoxicity studies. Confocal laser scanning microscopy was used for visualizing fluorescently labeled spheroids inside the flow channel. In order to monitor the spheroids in the channel also during an impedance measurement a digital USB microscope was used.

4.2.1 Microscopes

The microscopes which were applied in this work are listed Tab. 7.

The Nikon Diaphot is equipped with a super high pressure mercury lamp (Nikon) and two filter blocks for the excitation of blue, green and red emitting fluorophors (Nikon, UV-2A and B/G). Further information about the filter block specifications can be found in the appendix A2 (Tab. S1). The microscope was connected to a Nikon digital camera for image acquisition using a memory card for data storage.

Tab. 7: List of microscopes and their specifications (including mode of microscopy, objective setup, type, magnification and aperture).

Microscope	*Modes of Microscopy*	*Setup*	*Objectives (type, magnification / aperture)*
Nikon Diaphot	Phase contrast Epifluorescence	inverted	Plan, 4× / 0.13 Plan, 10× / 0.25 Plan, 20× / 0.4
Nikon Eclipse 90i	Phase contrast CLSM	upright	Plan, 10× / 0.25
Zeiss Axiovert 200M	Phase contrast CLSM	inverted	Plan-Neofluar, 10× / 0.3
Supereyes Digital Microscope		optional	10× - 500×

The Nikon Eclipse 90 i is equipped with three lasers for sample excitation with monochromatic light (408, 488 and 543 nm) and three detectors (450/35, 515/30 and 650 nm LP). The microscope is connected to an ordinary computer for image acquisition and for data storage. The scanning head C1 on top of the microscope is controlled by the EZ-C1 software.

The digital USB microscope (Supereyes, Shenzhen D&F Co.) (Fig. 7) was used in order to monitor a spheroid during an impedimetric measurement. This is a variation of the traditional optical microscope but instead of the optics for illumination it uses a macro lens and a CCD camera. Due to its small size and its portability it is possible to install it inside the incubator on a simple stand. A ring of LED lights around the camera illuminates the sample in the dark incubator. When the camera is connected via USB to a computer with the supereyes software (supereyes 3.54) a live image of the sample can be seen on the monitor. With the software it is possible to take photos or to record a video and the obtained data is stored directly on the computer.

Fig. 7: Digital microscope with USB cable on the stand. The position can be adjusted in z-direction.

4.2.2 Live/Dead Staining with CalceinAM and Ethidium Homodimer

For simultaneous staining of live and dead cells in 2D and 3D cell culture the two probes calcein acetoxymethylester (CaAM) and ethidium homodimer-1 (EthD-1) were used (LIVE/DEAD® viability/cytotoxicity kit; Molecular Probes, Invitrogen). CaAM is a non-fluorescent probe that can permeate the intact cell membrane of viable cells. In the cytoplasm the ester groups are hydrolyzed by intracellular esterases generating the green fluorescent calcein (λ_{exc} = ~ 495 nm, λ_{em} = ~ 515 nm), which is no longer membrane permeable. This way, only live cells with intact cell membranes and active esterases are stained with CaAM. EthD-1 is not membrane permeable and can only enter cells with damaged membranes. Upon intercalation with nucleic acids EthD-1 shows a 40-fold enhanced red fluorescence (λ_{exc} = ~ 495 nm, λ_{em} = ~ 635 nm). Thus, cell nuclei of dead cells appear red and the cytosol of viable cells appears green.

Staining of Monolayer Cells

The cells were washed two times with $EBSS^{++}$ before they were incubated with the staining solution (2 µM CaAM and 4 µM EthD-1 in $EBSS^{++}$) for 45 min in the incubator. Fluorescence imaging was done using the Nikon Diaphot.

Staining of Spheroids

First, the staining solution was prepared in $EBSS^{++}$ containing 2 µM CaAM and 4 µM EthD-1. Then, spheroids were transferred to a 1.5 mL reaction tube and washed with $EBSS^{++}$ before they were incubated with the staining mix for 3 h in the dark at RT under gentle shaking. Afterwards, the staining solution was removed and the spheroids were washed with $EBSS^{++}$ and imaged using the Nikon Eclipse 90i or the Zeiss Axiovert 200M.

4.2.3 DAPI Staining of Spheroids

In order to stain the cell nuclei of spheroids the blue fluorescent stain 4',6-diamidino-2-phenylindole (DAPI) was used. When it is bound to AT-rich regions of the DNA the absorption maximum is 358 nm and the emission maximum is at 461 nm.

Spheroids were cross-linked with 4 % (w/v) paraformaldehyde (PFA) in PBS^{++} for 1 h at RT. Then, the spheroids were permeabilized with 0.5 % Triton X-100 in PBS^{++} for 30 min at RT and 75 rpm. Finally, the spheroids were stained with 10 ng/mL DAPI in PBS^{++} for 90 min at 75 rpm and under light protection. In between the single steps the spheroids were washed with PBS^{++}.

4.2.4 Microscopic Investigation of the Spheroid Response to Hypo- and Hyper-Osmotic Buffers

The shrinking and swelling of MCF-7 spheroids was evaluated using the Nikon Eclipse 90 i when they were challenged with the osmotic buffers, which were introduced in chapter 4.1.9. For imaging, one spheroid at a time was transferred to a 35 mm petri dish with a PDMS ring insert which was used to reduce the buffer volume.

The ring was prepared by mixing ~ 25 mL PDMS base polymer and curing agent in a ratio of 10:1 in a 100 mm petri dish. After complete polymerization at RT a ring was cut out of the polymer with an inner diameter of ~ 1.5 cm (Fig. 8 A) and a variable outer diameter fitting into the 35 mm petri dish.

In order to keep the spheroids warm during the time lapse studies the dish was placed in a brazen holder that was connected via flexible tubes to a temperature controlled water bath. This way, the warm water circulated through the holder and generated a holder temperature of 35.1 °C – 35.8 °C as measured by an external thermometer. The petri dish holder featured a hole underneath the dish to enable microscopy when the holder was placed on the microscope stage (Fig. 8 B / C).

First, the area inside the PDMS ring in the petri dish was filled with isotonic buffer and placed in the temperature-controlled holder. Then, a spheroid was pipetted into the dish and phase contrast pictures of the spheroid were taken at defined time points over 35 min. For the hypotonic and the two hypertonic solutions the respective spheroids were first incubated in the isotonic solution and documented every minute for 4 min. Afterwards, they were transferred in a second petri dish with the respective hypo- or hypertonic buffer and changes in size were documented over 31 min. From each of the obtained phase contrast pictures the spheroid perimeter was determined using imageJ software. The spheroid perimeter was converted into the spheroid diameter, which was plotted as a function of time.

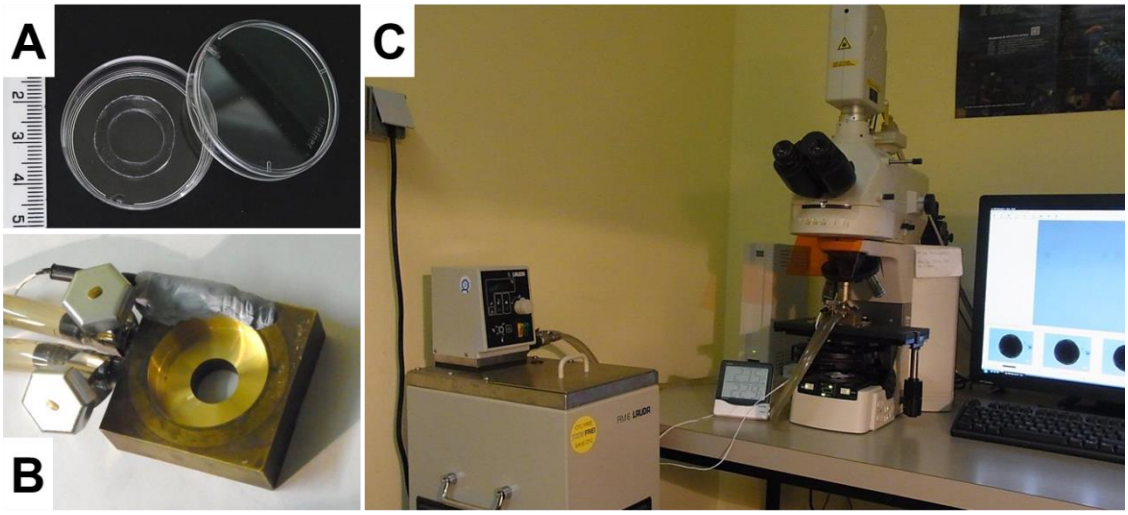

Fig. 8: Overview of the microscopic setup for swelling and shrinking experiments. The petri dish with the PDMS ring inside (**A**) is positioned in the brazen holder (**B**) that is warmed to ~ 35 °C by the circulating water of the temperature controlled water bath. The actual temperature of the holder is determined by an ordinary digital thermometer whose sensing element is fixed on the holder with Blu-Tack. For spheroid observation the holder is placed on the microscope stage of the Nikon Eclipse 90i microscope (**C**).

4.3 Impedance Analysis

Impedance spectroscopy was the method of choice to conduct non-invasive and label-free investigations of monolayer cells and tissue models. A novel measurement setup for impedimetric analysis of 3D tissue models was tested and compared with the standard technique for 2D cell culture (ECIS). Using tumor spheroids, embryonic bodies and cardiospheres a variety of model studies was performed. Chemical stimuli with well-known impact on cells like the cross-linker paraformaldehyde (PFA), the detergent saponin, buffers with different osmolarities or the actin polymerization inhibitor cytochalasin D were chosen to investigate their influence on MCF-7 spheroids impedimetrically. Furthermore, the phototoxicity of the live stain calceinAM or N-doped carbon dots was studied and the response of MCF-7 spheroids to hyperthermia was investigated. Cardiospheres were exposed to calcium-free buffer, the gap-junction blocker 1-heptanol or the β-adrenergic agonist isoprenaline and the differences in the impedance signal were monitored with high time resolution. P19 embryonic bodies were treated with inducing agents for cardiac or neuronal differentiation and monitored in the flow channel to investigate if phenotypic differences can be detected impedimetrically.

4.3.1 Experimental Setup and Instrumentation

Most experiments with 3D tissue models were performed using the measurement setup shown in illustration Fig. 9. The centerpiece of the whole setup is the prototype 2 flow channel on the planar indium tin oxide (ITO) electrode layout (Fig. 12 B). Since the experiments were performed in duplicates or with at least one control condition, two flow channels were used. The electrodes were connected to an impedance analyzer via a relay using simple metal clamps that were screwed on a self-made measurement table. The relay enabled switching between the electrodes of the two flow channels. The relay and the impedance analyzer were both connected to an ordinary PC. The flow channels were placed inside an incubator with 37 °C and 5 % CO_2 to provide physiological conditions throughout the measurement. A portable digital microscope (chapter 4.2.1, Fig. 7)

was also placed in the incubator to enable microscopic observation of the spheroid(s) during the impedimetric analysis.

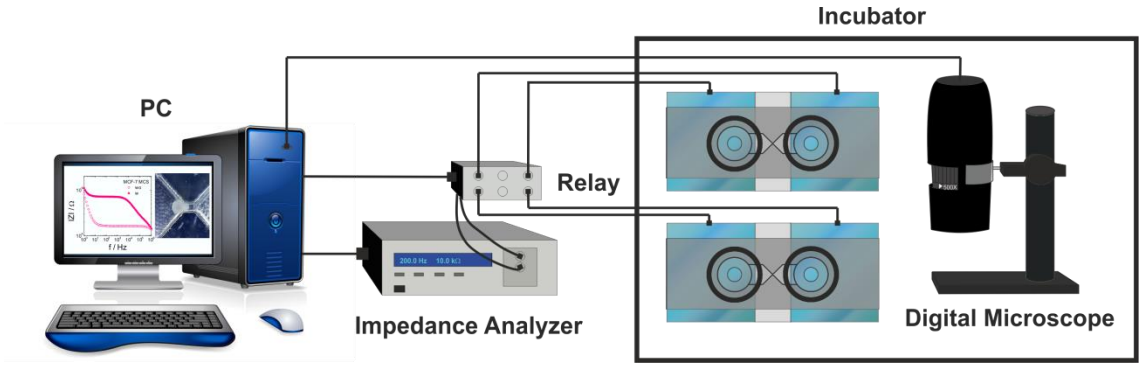

Fig. 9: Illustration of the impedance measurement setup for 3D tissue models. A relay, which is connected to a computer and an impedance analyzer enables switching between the electrodes of two prototype 2 flow channels on planar ITO electrode layouts. Spheroids can be monitored during the measurement with a digital microscope, which is adapted via USB to the computer.

Measurements were performed using an alternating voltage with an amplitude of 50 mV and 61 different frequencies in the range of $10^0 – 10^6$ Hz. The measurement was controlled using a *LabView* based software written by J. Wegener.

For the measurement of very small sized cardiospheres it was necessary to use the prototype 1 flow channel with the reduced aperture height and the ITO electrode layout on the glass substrate (chapter 4.3.2).

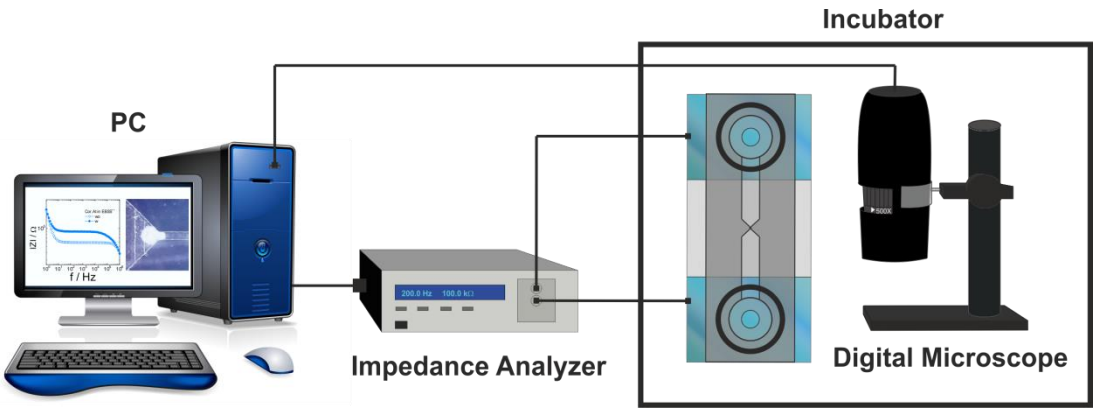

Fig. 10: Illustration of the measurement setup for cardiospheres. The prototype 1 flow channel on a planar ITO electrode layout is directly connected to the impedance analyzer.

Measurements with this prototype were not performed as duplicates and therefore, the flow channel was directly connected to the impedance analyzer. An illustration of the setup is shown in Fig. 10 and a photograph of the prototype 1 flow channel on the ITO electrode layout is shown in Fig. 12 A.

The experiments with monolayer cells were performed by Romy Freund (R.F.) or Pierre Pütz (P.P.) using another impedance setup shown in Fig. 11. For these measurements self-made ITO electrode arrays (R.F.) were used. They were connected to a relay that is able to address 2 x 8 electrodes using a commercial array holder. The measurement parameters were the same as for the spheroid measurements stated above.

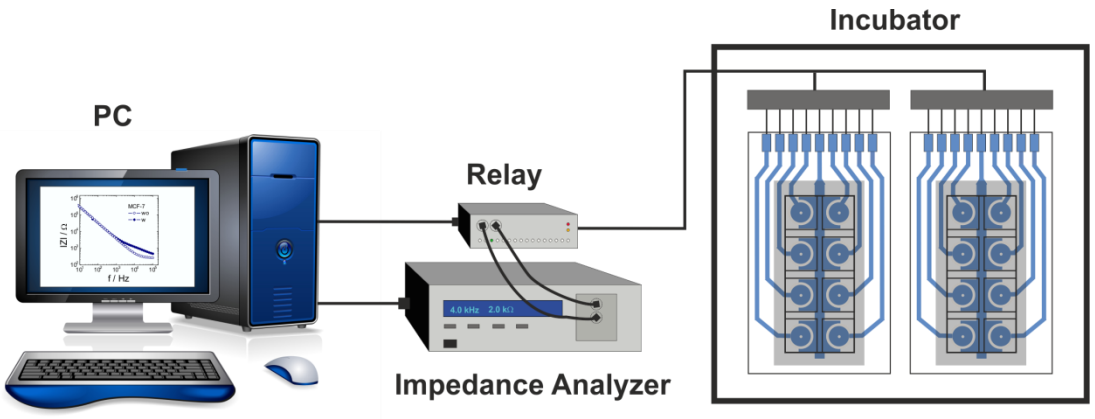

Fig. 11: Illustration of the impedance measurement setup for monolayer cells. Up to two self-made ITO 8-well arrays can be connected to a relay via a commercial array holder.

The electrode array was inspired by the design of the commercially available *8W1E* array from Applied BioPhysics (Troy / NY, USA), but the electrode layout was made of indium tin oxide instead of gold. This way, transparent electrodes were generated, which offer microscopic advantages. On top of the electrode layout an 8-well *LabTek*®-chamber was sealed using silicone glue. Thus, eight individual measurement chambers per array were available (Fig. 12 C).

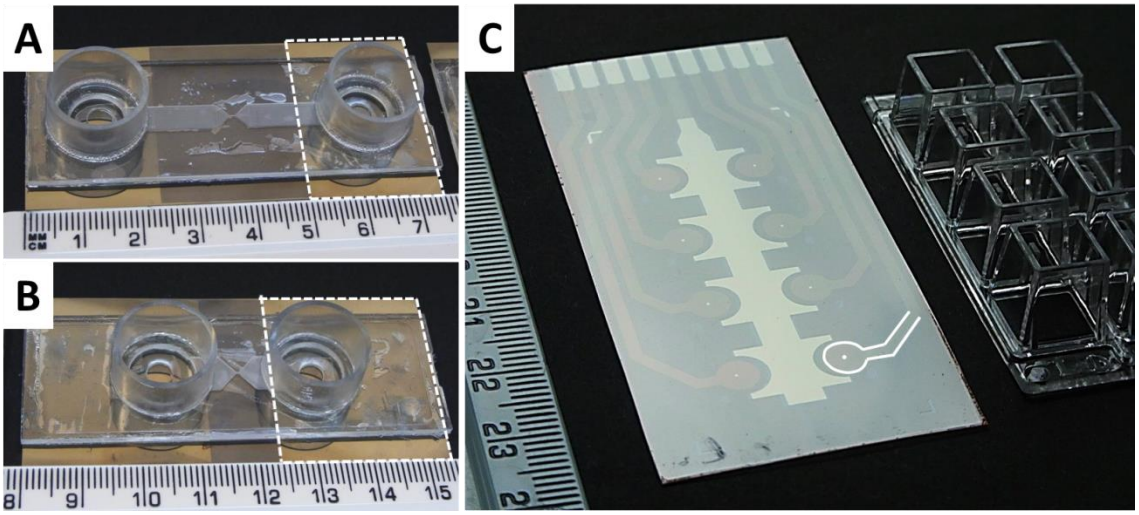

Fig. 12: Photographs of the prototype 1 (**A**) and 2 (**B**) flow channels on ITO electrode layouts for the measurement of 3D tissue models. Monolayer cells were measured using self-made *8W1E* ITO electrode arrays (**C**). For a better recognition of the dimensions of the electrode structures they were reconstructed in white dashed or solid lines exemplarily.

4.3.2 Generation of the Flow Channel Electrode Layout Using Photolithography

The electrode layout for the flow channel was prepared from indium tin oxide coated polyethylene terephthalate (PET) foils (Sigma-Aldrich Co.). The foil (0.3 x 0.3 m) has a surface resistivity of 60 Ω/sq and the ITO coating has a thickness of 130 nm. For the electrode layout a piece of foil was cut off with a length of 7.5 cm and a width of 3.5 cm. Via spin coating (1 min at 2000 rpm) a thin layer of photopolymer (AZ ECI3027, MicroChemicals) was deposited on the ITO foil that was baked subsequently for 30 min at 100 °C. Afterwards, the photoresist was exposed to UV light for 2 min through a mask. This mask showed the electrode layout that consists of two electrodes in the same size (PT1: 2.3 x 3.5 cm ; PT2: 3.1 x 3.5 cm). It was simply prepared by printing the design on a transparency film. In the UV exposed area the photoresist was then removed by incubation with NaOH solution (7 g/L) for 20 s. The substrate was rinsed with destilled water before the ITO was etched away at exposed areas with a mixture of destilled water, concentrated hydrochloric acid (37 %) and nitric acid (65 %) (mixing ratio of 47:47:6) within 30 s. The substrate was rinsed again and the remaining photopolymer was removed with acetone.

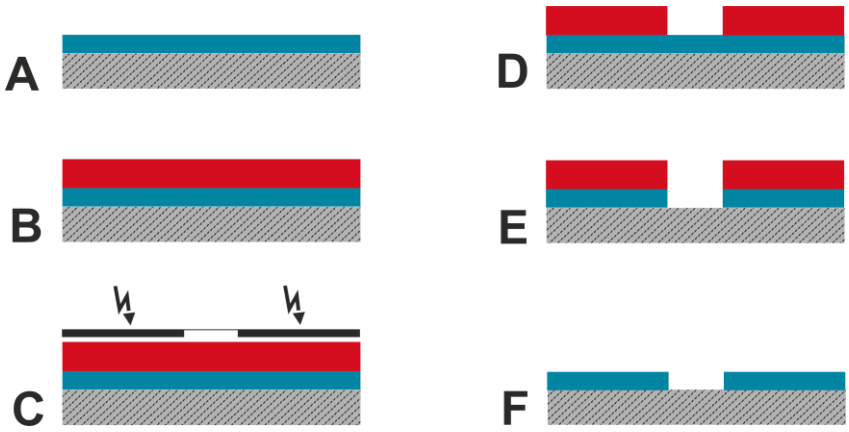

Fig. 13: Photolithographic process starting with the ITO coated PET foil (**A**) that was spin coated with photoresist (**B**). A mask was placed on top and the uncovered photoresist was exposed to UV light (**C**). In the UV exposed area the photoresist was removed with a solution of basic pH (**D**). Etching with an acidic solution removed the underlying ITO (**E**) and the residual photoresist was removed with acetone (**F**).

An alternative to the ITO PET foil are ITO coated glass substrates. These were purchased from pgo (Präzisions Glas & Optik GmbH, Iserlohn, Germany) featuring a substrate thickness of 1.1 mm, an ITO thickness of 180 nm and a SiO_2 passivation layer between the glass substrate and the ITO layer. The surface resistivity is determined to be ≤ 10 Ω/sq. For the ITO glass substrates the photolithography protocol was applied as described above with the exception that the etching time was extended to 20 min. The dimensions of the ITO electrodes were prepared to fit the prototype 1 flow channel.

4.3.3 Different Modes of Impedance Measurements

Multi-Frequency/Time (MFT)

In the MFT mode the impedance is measured at 61 pre-determined frequencies in a frequency range from 1 Hz – 10^6 Hz as a function of time. The resulting impedance spectra were used to determine the spheroid parameters R_{ext}, R_{int} and A_{sph}, which describe the electrical properties of the spheroid. For this purpose, the elements of an equivalent circuit (chapter 3.2) are fitted to the recorded impedance spectra. An automated data fitting was performed with a *LabView*-based software (Nr. 1) written by J. Wegener using a numerical non-linear least-square approach. For the automated data fitting starting values of the

parameters R_{ext}, R_{int} and A_{sph} had to be specified and the values of R_{bulk}, A_{el}, n_{el}, A_{para} and n_{para} had to be known. The latter parameters were determined by analyzing the impedance spectra of a spheroid-free flow channel. Factors like the slightly varying flow channel geometries (FC-1 – FC-4), temperature fluctuations and minor changes in medium conductivity can cause a slight variation of the parameters R_{bulk}, A_{el}, n_{el}, A_{para} and n_{para}. Therefore, sometimes more than one value for each of these parameters is given in the heading of the results tables for the spheroid parameters. The value for the electrode area was always set to 1.0 cm^2, except for the simulations in chapter 5.2.3. Analysis of repeatedly recorded impedance spectra was performed using dynamic start values. Thereby, the best fit results for spectrum *i* were used as start values for spectrum (*i* + 1).

Rapid Time Collect (RTC)

In the RTC mode time series measured at a single frequency with high time resolution were performed to monitor cellular micromotion within spheroids. These small cell shape fluctuations were recorded electrically already in the early 90's by Giaever and Keese (1991) and Lo (1993) using adherently growing monolayer cells. With the ECIS technique they observed cellular movements in the nanometer range that were detected as fast impedance fluctuations. The authors correlated the micromotion with dynamic cellular processes like metabolic activity and cytoskeleton integrity. Hence, impedance fluctuations can be an indicator for the vitality of cells. In the impedimetric model studies of different types of spheroids the high time resolution measurement mode at a single frequency was applied at strategic time points during the multiple frequency scans in order to gain additional information about the viability of the spheroids. However, in the beginning of these experiments it was not clear if the small fluctuations of cells within a spheroid could be measured with this setup.

Micromotion data was aquired at 200 Hz and 50 mV for 5 min and a time resolution of 0.5 s. For numeric analysis the variance of increments was determined for 32 s data packages after segmented detrending. This was performed using a *LabView*-based software (Nr. 2) written by J. Wegener. A detailed description of the evaluation process is given in chapter 6.2.

Determination of beats per minute (BPM) and mean amplitude of fluctuations from beating cardiospheres was performed with another *LabView* based software (Nr. 3) (written by J. Wegener) using 300 data points for evaluation. All cardiosphere experiments are three-step measurements. First, a beating cardiosphere is measured, then stimuli are added that induce a beating arrest or an enhanced beating (second step), followed by the return to culture medium or buffer without stimuli, measuring a possible recovery to the initial beating pattern (third step). The BPM of beating cardiospheres (first step) were determined by counting all peaks in the (5 min-) time course exceeding a manually defined threshold value and dividing this value by 5 min. The BPM of cardiospheres in the second and third step of the measurement were determined similarly using the pre-defined threshold value from step one.

4.3.4 Flow Channel Handling and Experimental Procedure of an EIS Measurement with Spheroids

The flow channel is mounted onto the electrode layout using silicone glue and should be dried at least over night before use. The electrode layout can be re-used several times and can be replaced easily with a new one. For this purpose, the flexible ITO foil is pulled off the channel. The flow channel without electrode layout was then cleaned by incubation in a 5 % solution of elma clean 10. In the beginning, the channel was sonicated in this solution for 5 min until it turned out that the ultrasound led to tiny cracks in the thin structure of the channels. After this observation the channels were instead incubated for several hours in the elma clean solution without sonication. Afterwards, they were washed several times with destilled water and dried before a fresh electrode layout was glued onto it.

The flow channels were washed with 2 mL of 70 % ethanol and 2 mL of ultrapure water prior to and subsequent to each measurement. Then, the channels were connected to the electronics and put inside the incubator together with the culture medium or buffer to let them warm up before measurement. The channels were once washed and then filled with pre-warmed medium/buffer.

Each measurement started with a baseline of the medium-/buffer-filled channel before a spheroid was inserted in the channel. The spheroid was placed at the entrance of the flow channel with a pipette and it was positioned at the central restriction by tilting and hydrodynamic pressure. In order to remove the spheroid, the reservoir volume was transferred from the reservoir on the spheroid side to the opposite side reservoir. In the case that the generated hydrodynamic pressure was insufficient to move the spheroid, medium was gently pipetted into the flow channel entrance at the spheroid-free side of the channel.

These basic procedures were applied in each measurement using the flow channel and are not mentioned anymore in the following chapters.

For monolayer experiments, the self-made 8-well ITO array was sterilized in an argon plasma for one minute. Then, MCF-7 cells were seeded in a density of 80.000 cells/cm^2 four days prior to the measurement. One day before measurement, the cell culture medium was exchanged. In the end of a measurement the cells were detached with EDTA (~ 25 min) and Trypsin (~ 20 min), washed with sterilized destilled water and let dry in order to re-use the array.

4.3.5 Model Studies with MCF-7 Spheroids

All the measurements were performed with the PT-2 flow channel and the measurement setup for 3D tissue models shown in chapter 4.3.1 Fig. 9, unless stated otherwise. Data evaluation was done using individual *LabView*-based software programs for MFT and RTC mode (written by J. Wegener).

4.3.5.1 Spheroid Size and Repositioning

The measurements described in this subchapter were all performed using a single flow channel directly connected to the impedance analyzer. The spheroids were all measured in culture medium.

Spheroids of the Same Seeding Density and Growth Duration

Spheroids with a seeding density of 3000 cells/well were prepared following the standard protocol (chapter 4.1.5). For impedance measurements seven or eight

day old spheroids were used. First, the empty, medium-filled flow channel was measured to record baseline impedance. Then, a spheroid was transferred from the 96-well plate into the flow channel (without pausing the measurement) and measured for ~ 40 min. Afterwards, the spheroid was removed and at least three baseline spectra were recorded before the next spheroid was inserted. This procedure was applied for a total of five spheroids.

Spheroids of Different Seeding Densities and the Same Growth Duration

MCF-7 spheroids with three seeding densities (1000, 3000 and 6000 cells/well) were prepared following the standard protocol (chapter 4.1.5). Eight days after seeding the impedance analysis was performed measuring two spheroids of each seeding density successively with at least three baseline spectra in between.

Spheroid Repositioning

This experiment was performed using spheroids with a seeding density of 3000 cells/well nine days after seeding. A spheroid was inserted in the flow channel and measured for ~ 40 min. Then, the spheroid was repositioned by carefully removing it from the central restriction and remaining it on the reservoir bottom for a few baseline spectra before it was positioned again at the restriction. This procedure was repeated in total three times per spheroid without stopping the measurement in between.

4.3.5.2 Cross-Linked Spheroids

The measurement was performed using 7 d old spheroids (3000 cells/well) that were pre-incubated for 1 h in different concentrations of PFA in PBS^{++} (0.01 / 0.1 / 0.5 %). In order to perform duplicate data sets per PFA concentration two flow channels were used simultaneously. The whole measurement was performed in culture medium. When the medium was equilibrated during baseline recording (without spheroid), the measurement mode was switched from MFT to RTC (5 min/channel, 200 Hz, 50 mV). Afterwards, the mode was switched back to MFT and two control spheroids (no PFA incubation) were inserted and measured for ~ 1 h before RTC time series were recorded. Thereafter, the spheroids were removed from the channels and a few baseline spectra were recorded. The spheroids that were pre-incubated in the three PFA concentrations were washed

with PBS^{++} and culture medium before they were measured successively in the same way than the control spheroids. The spheroids were also monitored with the digital microscope and photographs were taken in the beginning and in the end of each measurement.

4.3.5.3 Permeabilized Spheroids

Spheroids (7 / 8 d; 3000 cells/well) were pre-incubated for 4 h in different concentrations of saponin in $EBSS^{++}$ (0 / 0.01 / 0.05 / 0.1 / 0.25 ‰). The measurement was performed in duplicate and baseline as well as spheroids were measured in $EBSS^{++}$. The spheroids were washed with $EBSS^{++}$, measured for 30 – 40 min in MFT mode and then RTC time series data was recorded. The digital microscope was used to monitor the spheroids at the central restriction.

4.3.5.4 Spheroids Under Osmotic Pressure

The iso-, hypo- and the two hyperosmotic buffers were prepared as outlined in chapter 4.1.9. Spheroids were generated (8 d; 3000 cells/well) and measured in duplicate without pre-incubation in isoosmotic buffer. The measurement procedure was the same for each buffer, starting with the baseline MFT in the respective buffer without spheroid. The measurement was switched to RTC as soon as the signal remained constant. Then, the measurement mode was switched back to MFT, spheroids were inserted into the channels and measured for ~ 1 h until the measurement in RTC mode. Afterwards, the spheroid and the buffer were removed from the flow channel. The channel was first washed and then filled with the next buffer. The spheroids were monitored during the measurement and photographs were taken using the digital microscope.

4.3.5.5 Spheroid Response to Cytochalasin D

In order to test the impact of actin disruption by cytochalasin D (cytD) on 7 d old spheroids (3000 cells/well) they were pre-incubated for 0 / 2 / 4 / 6 / 8 h in 5 µM cytochalasin D in culture medium at 37 °C. The baseline of the medium-filled channel without cytD and without spheroid was recorded in MFT and RTC mode. Then the control spheroids were analyzed in medium as described previously (MFT for ~ 1 h, RTC) followed by the spheroids, which were incubated in cytD.

Those were washed once with culture medium before they were inserted in the channel. The microscopic observation of the spheroids during the measurement was done using the digital microscope.

4.3.5.6 Spheroid Response to Hyperthermia

In order to investigate the spheroid response to hyperthermia, 7 d old spheroids (3000 cells/well) were used. They were exposed to 41 / 43 / 45 °C in culture medium filled 1.5 mL tubes for 1 h or 3 h using the Thermomixer compact. The control spheroids (37 °C) were taken directly from the 96-well plate in the cell culture incubator. The measurement was performed in culture medium in duplicate and the spheroids were monitored using the digital microscope. The time course of impedance spectra was followed for ~ 50 min and RTC time series were taken from the medium-filled channel with and without (baseline) spheroids.

4.3.5.7 Phototoxicity of CaAM on Monolayer Cells and Spheroids

The experiments with monolayer cells were performed by Romy Freund and Pierre Pütz using the self-made 8-well ITO arrays and the measurement setup shown in chapter 4.3.1, Fig. 11. The cells were prepared as explained in chapter 4.3.4. The confluent cell layers were washed with $EBSS^{++}$ and incubated with 2 µM CaAM in $EBSS^{++}$ for 90 min in a standard cell culture incubator. With the staining solution in the supernatant the cells were taken to the Nikon Diaphot for irradiation with three different excitation wavelengths (~ 355 / 483 / 553 nm) for 3 min using the 10× objective focused on the working electrodes. In the controll well(s) the cells were not irradiated. Then, the array was connected to the measurement setup and the time course of impedance was followed for 12 – 24 h by repeated frequency scans (MFT). When the impedance measurement was finished the cells were washed carefully with $EBSS^{++}$ and a live/dead staining was performed following the protocol for monolayer cells in chapter 4.2.2. The measured impedance magnitude was corrected for the lead resistances and then normalized to the time point right after irradiation.

For the experiments with 3D tissue models spheroids were prepared (3000 cells/well) and measured on day seven or eight after seeding. For this purpose, spheroids were incubated in 2 µM CaAM in $EBSS^{++}$ or in $EBSS^{++}$ only

(control spheroids) for 3 h in the dark at RT and 75 rpm. Meanwhile, the baseline of the $EBSS^{++}$ filled channel was measured and RTC data was recorded. Then, the CaAM-loaded and the control spheroids were washed and inserted in the flow channel. They were measured for ~ 30 min in MFT mode. The channels were disconnected and brought to the Nikon Diaphot microscope where the spheroids were photographed (phase contrast) and exposed to epi illumination at 420 – 490 nm for 10 min using the 10× objective. The channels were re-connected to the impedance analyzer and the MFT measurement continued. At the end of the measurement the spheroids in the channels were photographed again at the Nikon Diaphot.

4.3.5.8 Phototoxicity of Carbon Dots on Monolayer Cells and Spheroids

N-doped carbon dots (C-dots) from starch and L-tryptophan with an average diameter of (1.6 ± 0.8) nm were produced and characterized by Michael Lemberger. The particles show a good water dispersibility and the uptake into cells is in the time range of a few minutes. For low concentrated particle suspensions the excitation / emission maximum is ~ 370 / 450 nm. From cytotoxicity investigations on NRK (normal rat kidney) monolayer cells it is known that C-dot concentrations up to 1.1 mg/mL are uncritical in the dark. Furthermore, it is known that the particles are generating reactive oxygen species (ROS) upon photo-excitation and thus fulfill essential prerequisites of a potential photodynamic therapy agent.

The phototoxicity studies with monolayer cells were performed by Pierre Pütz using the self-made 8-well ITO array (R.F.) and the measurement setup for monolayer cells (chapter 4.3.1, Fig. 11). The array with the confluent cell monolayer (for preparation details see chapter 4.3.4) was measured in MFT mode. The initial baseline was recorded in medium. Then, the cells were washed twice with $EBSS^{++}$ and in some wells the cells were incubated with 1 mg/mL C-dots in $EBSS^{++}$ for 1 h while other wells served as controls. The C-dot solution was removed and the cells were washed twice with $EBSS^{++}$. Afterwards, the measurement was interrupted to take the array to the Nikon Diaphot where the C-dot stained cells were exposed to epi illumination at 330 – 380 nm (UV-2A filter)

for 3 min using the 10× objective. The measurement was continued for ~ 20 h. Controls with or without C-dots were not irradiated.

For the phototoxicity studies with 3D tissue models, spheroids (3000 cells/well) were prepared and used on day seven after seeding. They were incubated in 1.5 mg/mL C-dots in $EBSS^{++}$ for 2 h in a standard cell culture incubator. In the meantime, the baseline of the $EBSS^{++}$ filled channels was measured in MFT mode. Then, the spheroids were washed, inserted in the channels and measured for ~ 30 min. Afterwards, both channels were brought to the Nikon Diaphot microscope to take phase contrast photographs and to expose one of the C-dot spheroids to epi illumination at 330 – 380 nm (UV-2A filter) for 15 min using the 10× objective. The other C-dot spheroid served as control and was not exposed to illumination. The channels were re-connected to the measurement setup and spheroids were followed in MFT mode. At the end of the measurement the spheroids in the channels were documented by phase contrast micrographs.

4.3.5.9 Testing of Carbon Dot Cytotoxicity on Spheroids

MCF-7 spheroids (3000 cells/well) were used for the cytotoxicity experiments 7 d after seeding. They were incubated in either 1.5 mg/mL C-dots in $EBSS^{++}$ or in pure $EBSS^{++}$ (control spheroid) for 2 h in a standard cell culture incubator. The baseline of the $EBSS^{++}$ filled channel was measured before the spheroids were washed and inserted in the channels. The spheroids were monitored during the measurement using the digital microscope.

4.3.6 Measurement Protocol for P19 Embryonic Bodies

Embryonic bodies (EBs) were prepared with and without inducing agents for cardiac or neuronal differentiation (chapter 4.1.5 and 4.1.7) from 1000 cells/well and were measured 3 d or 4 d after seeding. The measurement was performed using the setup with two PT-2 flow channels on the ITO PET electrode layout (chapter 4.3.1, Fig. 9) and the digital microscope for the observation of EBs. MFT (~ 45 min) and RTC (5 min/channel) measurements were performed for the flow channel filled with P19 culture medium without EBs, with undifferentiated EBs or

EBs that were prepared in presence of inducing agents for cardiac or neuronal differentiation.

4.3.7 Model Studies with Cor.At® Cardiospheres

In the first set of model studies cardiospheres were prepared using the hanging drop technique. One cardiosphere formed from 3000 cells/drop was chosen for measurement 3 d after seeding. For subsequent measurements cardiospheres were generated by inoculation on a non-adhesive surface. Cardiospheres formed from 10.000 cells/well and 6000 cells/well were chosen for the measurements 3 / 4 / 5 d after seeding. In both cases the prepared cardiospheres were usually too small for a measurement in the PT-2 flow channel. Since the height and width of the central restriction of the PT-1 flow channel was smaller, it was better suited for the studies on cardiospheres. The PT-1 flow channel on the ITO glass electrode layout as well as the measurement setup are further described in chapter 4.3.1 and 4.3.2. All impedance measurements were performed in an incubator at 34 °C.

In one measurement one single cardiosphere was used to investigate its response to isoprenaline, 1-heptanol and withdrawal of extracellular calcium. Therefore, it was necessary to perform medium or buffer exchanges in the channel. This was realized by carefully removing the cardiosphere from the restriction and temporarily keeping it on the reservoire bottom while extensively washing the channel with the next buffer, medium or reagent. Afterwards, the cardiosphere was brought back to the restriction site. During the experiments the cardiospheres were monitored and photographs as well as videos were recorded using the digital microscope.

4.3.7.1 Cardiospheres Under Calcium-Free Conditions

The flow channel was filled with $EBSS^{++}$ and the cardiosphere was brought in front of the central restriction. It was monitored in MFT mode for ~ 30 min and in RTC mode for 5 min. Then, the mode was switched back to MFT and the buffer was replaced by $EBSS^{--}$ supplemented with 0.5 mM $MgCl_2$, in the following referred to as $EBSS^{-+}$. The cardiosphere was measured again for ~ 30 min in

MFT mode and RTC data was recorded at the beginning and end of the incubation in calcium-free buffer. Finally, the procedure was repeated after re-setting to EBSS^{++} buffer.

4.3.7.2 Cardiosphere Response to 1-Heptanol

The cardiosphere was measured successively (1) in medium, (2) in Cor.At® medium supplemented with 1 mM 1-heptanol and (3) again in medium. In each solution the spheroid was monitored for ~ 30 min in MFT mode and one or two RTC time series were recorded.

4.3.7.3 Cardiosphere Response to Isoprenaline

The cardiosphere was measured successively (1) in medium, (2) in Cor.At® medium supplemented with 100 nM isoprenaline and (3) again in medium. In each solution the cardiosphere was measured in MFT mode for ~ 30 min and in RTC mode for 5 min.

5 Setup Development and Characterization of MCS in Flow Channels

This chapter provides fundamental considerations concerning channel design (chapter 5.1), measurement principle (chapter 5.2.1) and impedimetric characterization of the flow channel (chapter 5.2.2). By recording impedance spectra of the channel with and without spheroid the most sensitive frequency for time-dependent monitoring was determined. To assess the influence of the spheroid parameters R_{int}, R_{ext} and A_{sph} on the shape of the spectral curve impedance spectra were simulated (chapter 5.2.3). Furthermore, the influence of possible parasitic impedance contributions was investigated (chapter 5.2.4). The impact of spheroid size and the repositioning process on the impedimetric signal was determined using MCF-7 spheroids (chapter 5.3). In the realization process of the flow channel the transparency of the base and channel material was an important feature to enable microscopic monitoring of spheroids inside the device. In order to verify this, spheroids were visualized in the flow channel via confocal microscopy, phase contrast microscopy and the digital microscope that was mainly used during impedance measurements (chapter 5.4).

5.1 Flow Channel-Based Measurement Setup

5.1.1 Evolution of the Flow Channel Design

The flow channel prototypes were fabricated by ibidi® following our custom design wishes. The first prototype can be seen in Fig. 14 A and the exact channel dimensions are listed in Tab. 8. The design features a long channel (~ 2.5 cm) with a width of 0.5 cm, a height of 0.05 cm and a central aperture of 150 µm height and width. The central opening is created by stepwise lowering of the upper channel material as visualized by confocal fluorescence microscopy (Fig. 14 B, C) and a digital microscope with large depth-of-field (Keyence VHX; D). These channel dimensions lead to a rather high channel resistance of ~ 40 kΩ (Tab. 8) and the gradual decline of the channel top towards the aperture

prevents spheroids with diameters above ~ 180 – 200 µm to reach the central aperture as can be seen in Fig. 14 C. Dependent on the spheroid size they are held back in different distances to the aperture. Thereby, the applied current flows around and not through the spheroid making it impossible to detect its impedance contribution. In order to overcome this problem and the high resistance of the setup making it less sensitive for spheroid-related impedance changes the design was optimized.

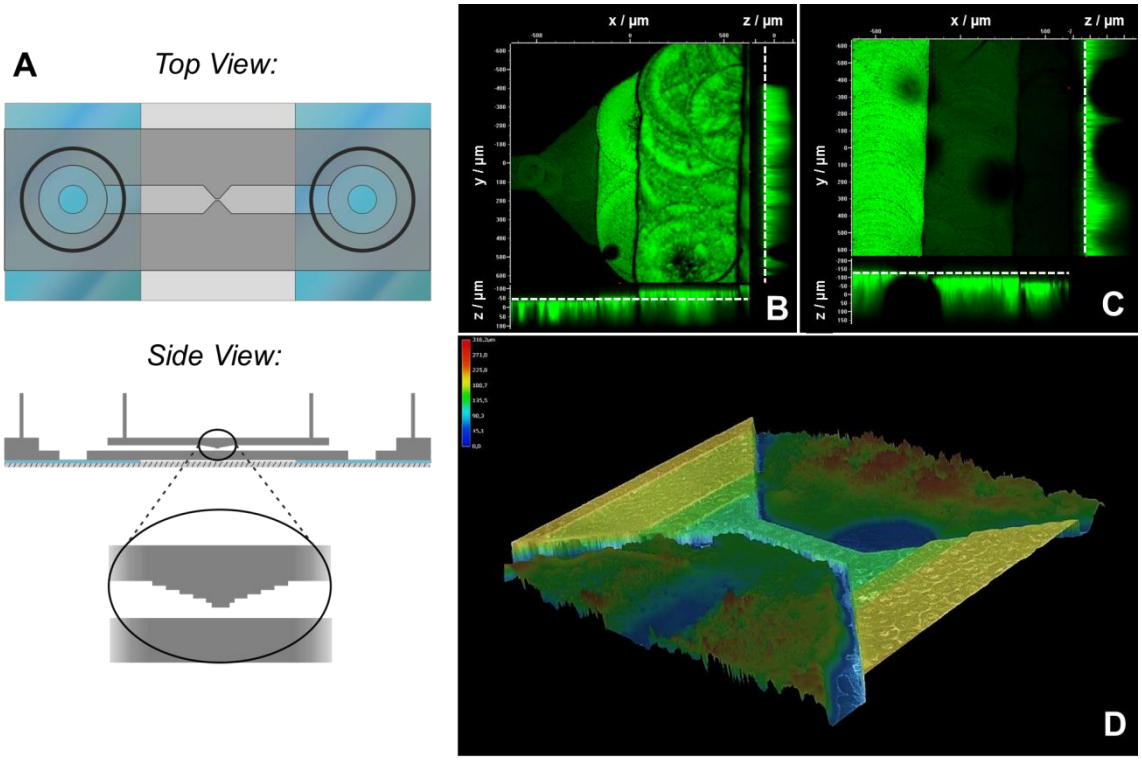

Fig. 14: Schematic illustration of the prototype 1 flow channel (PT-1) in top view and side view as well as an enlarged view on the gradual decline towards the channel aperture (**A**). The latter was visualized by confocal fluorescence micrographs of the FITC-filled channel at aperture-near regions (**B**) and further away where three spheroids were held back in different distances to the central aperture (**C**). White dashed lines in the xz and yz images (B and C) mark the z-position, which is shown in the xy images. Additionally, a 3D surface profile of the narrowing and the aperture was performed with the digital microscope Keyence VHX (**D**).

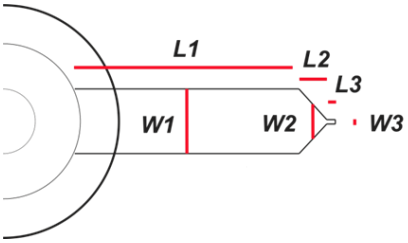

Fig. 15: Schematic of one half of a flow channel where the length (**L**) and width (**W**) of the three channel parts (1 – 3) are marked.

Tab. 8: Dimensions and channel resistances of prototype 1 channel (**PT-1**). Given are the length (**L**), width (**W**) and height (**H**) for one half of a channel (except **L3**: complete length of the aperture) as shown in the Fig. 15. From this data the channel resistance R_{ch} was calculated using Eq. 5.1 – 5.3 with ρ = 60 Ω·cm.

	L1 / cm	L2 / cm	L3 / cm	W1 / cm	W2 / cm	W3 / cm	H1 / cm	H2 / cm	H3 / cm	R_{ch} / kΩ
PT-1	2.000	0.250	0.100	0.500	0.260	0.015	0.050	0.030	0.015	39.85

$$R_i = \frac{\rho \cdot L_i}{A_i} \qquad \textbf{Eq 5.1}$$

$$A_i = W_i \cdot H_i \qquad \textbf{Eq 5.2}$$

$$R_{ch} = 2\ R_1 + 2\ R_2 + R_3 \qquad \textbf{Eq 5.3}$$

For this purpose, in the prototype 2 design the channel length was shortened (L1), the channel width (W1) and the height in the aperture (H3) was increased and the gradual decrease of the channel height towards the aperture was removed (Fig. 16 A, Tab. 9). Four channels of this prototype (FC-1 – FC-4) were fabricated and used in this thesis. Their dimensions and channel resistances are listed in Tab. 9. The new aperture was again visualized by confocal fluorescence micrographs. Two different xy-sections show the upside of the channel (B) and the upside of the central aperture (C) visualizing the different heights. The xz- and yz-planes in both images are identical and show the side view of the channel along the longitudinal axis and the transverse axis of the narrowed channel section. The design optimizations resulted in a 4 – 5-fold decrease of the channel resistance and without the steps in front of the narrowed section also spheroids

with a bigger diameter were able to reach the aperture without any difficulty (Fig. 16 D).

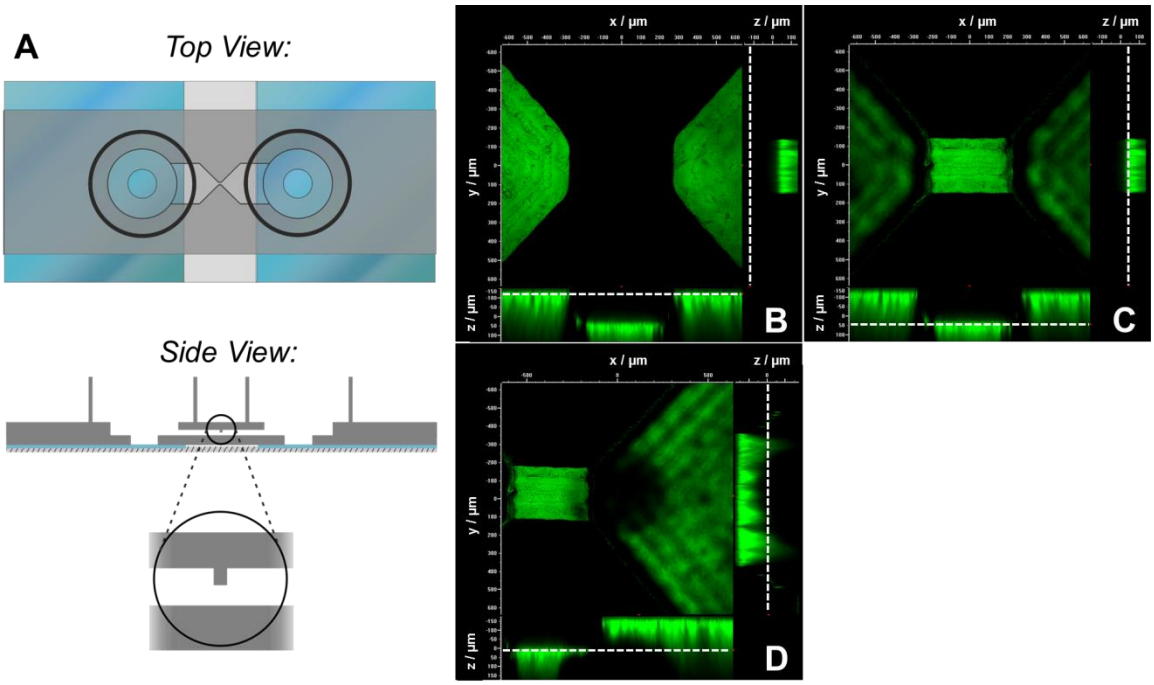

Fig. 16: Schematic illustration of the prototype 2 flow channel (PT-2) in top view and side view as well as an enlarged view on the narrowed channel section (**A**). Confocal fluorescence micrographs visualize the difference in height between the channel and the central aperture (**B**,**C**) in the xy-plane and the respective side views in the xz- and yz-plane. When a spheroid is introduced into the channel it is held back at the central aperture where it partly moves into the narrowed channel section (**D**). White dashed lines in the xz and yz images (B, C and D) mark the z-position, which is shown in the xy images.

Tab. 9: Dimensions and channel resistances of the four PT-2 flow channels. Given are the length (**L**), width (**W**) and height (**H**) for one half of the channel (except **L3**: complete length of the aperture) as shown in Fig. 15. From this data the channel resistance R_{ch} was calculated using Eq. 5.1 – 5.3 with ρ = 60 Ω·cm.

	L1 / cm	***L2 / cm***	***L3 / cm***	***W1 / cm***	***W2 / cm***	***W3 / cm***	***H1 / cm***	***H2 / cm***	***H3 / cm***	R_{ch} / *kΩ*
FC-1	0.420	0.280	0.042	0.700	0.365	0.032	0.050	0.035	0.020	8.11
FC-2	0.420	0.280	0.043	0.700	0.365	0.028	0.050	0.037	0.018	9.05
FC-3	0.420	0.280	0.041	0.700	0.365	0.030	0.050	0.036	0.017	8.97
FC-4	0.420	0.280	0.045	0.700	0.365	0.026	0.050	0.035	0.017	10.36

The improved PT-2 flow channels featured optimal dimensions for the spheroids used in this thesis and was thus used as standard setup. For measurements on cardiomyocyte spheroids however, the PT-1 flow channel was applied since the cardiosphere diameter was too small for the PT-2 aperture.

5.1.2 Materials for the Electrode Layout

Beside the flow channel, the electrode layout is an important part of the setup. Based on the prerequisite that it should be transparent, ITO-PET foil and ITO-coated glass substrates were tested. Using photolithography, a strip of ITO was removed in the middle of the respective substrates to generate two planar electrode areas (chapter 4.3.2). Although, both substrates are applicable for EIS measurements and the ITO-glass substrates are available with a smaller surface resistivity, the use of ITO-PET has some advantages: (i) ITO-PET is cheaper than the ITO-coated glass substrates. (ii) The ITO foil is available as one or five sheets in a size of 0.3 m × 0.3 m and can be easily cut in the size and shape which is needed. The ITO-glass slides are commercially available in custom defined dimensions and shapes. (iii) The flexible ITO-PET foil including the silicon glue residues can be pulled off the flow channel easily so that the channel can be re-used. This is not the case for the ITO-glass substrates. Here, the removal is time-consuming and difficult. Summed up, theoretically both ITO substrates can be used for impedance measurements but ITO-PET is more convenient in handling and was therefore used as standard material. ITO-glass was used only in combination with the PT-1 flow channel for the cardiomyocyte measurements.

5.1.3 Determination of the Flow Behavior

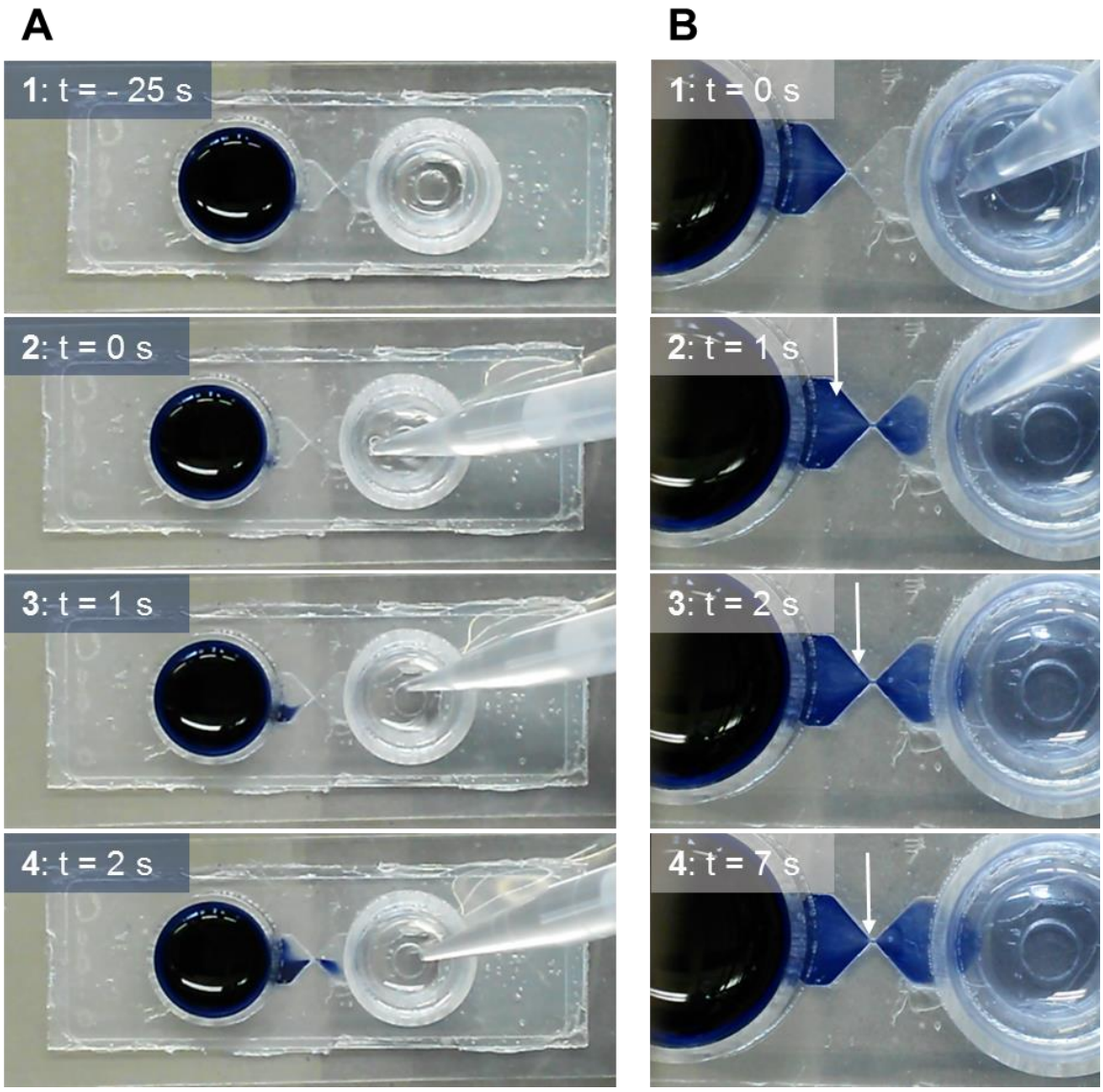

Fig. 17: Pictures extracted from a video of the flow behavior in the PT-2 flow channel using Trypan Blue (TB) solution. As long as the spheroid is positioned at the aperture TB migration through the channel is inhibited (**A1/2**). But when the spheroid is removed (**A2**, **B1**) TB migrates very fast through the channel (**A3**, **B2/3**) until the spheroid is back at the aperture (**A4**, **B4**). The white arrows mark the position of the spheroid that is approaching the aperture.

In order to investigate the flow behavior in the channel when a spheroid is at/in the aperture the channel was prepared as follows: The channel was filled with PBS^{++} and a spheroid was introduced in the channel at the aperture. To make sure that the spheroid stayed at the aperture the reservoir on the spheroid side was filled completely, whereas the spheroid opposing reservoir was almost empty. Then, a very concentrated Trypan Blue (TB) solution was added to the

reservoir on the spheroid side. During the TB addition as well as during the thorough mixing in the reservoir or several seconds afterwards no migration of TB into the channel was observable (Fig. 17 A 1/2). Subsequently, the spheroid was shortly removed from the aperture by softly pipetting PBS^{++} (without TB) into the channel from the other side (Fig. 17 A 2, B 1). As soon as the spheroid was away from the aperture TB migrated through the channel (Fig. 17 A 3, B 2/3). With the fluid flow the spheroid was brought back to the aperture and sealed it again. Immediately afterwards the migration stopped and further increase in TB intensity in the acceptor compartment was inhibited (Fig. 17 A 4, B 4).

This experiment clearly showed that when a spheroid is positioned at the aperture to the narrowed section it seals the channel and inhibits solute flow through the channel, which is an important prerequisite for measuring the spheroid impedance. On the other hand the sealing is also a challenge as it means that spheroid manipulating substances can not reach the spheroid when added to the reservoir. This challenge was circumvented by either pre-incubating the spheroids with the respective substances or by repositioning (see more details in chapter 5.3.3).

5.2 Impedimetric Characterization of the Flow Channel

5.2.1 Measurement Principle

Via the reservoires the channel is filled with a conductive solution, like physiological buffer or cell culture medium. Between the two electrodes the applied alternating current can flow freely through the channel.The impedance of this system arises from the bulk resistance of the conductive solution R_{bulk} and the non-ideal electrode capacitance *CPE* (chapter 3.2). A spheroid is positioned in the central opening of the channel by tilting and hydrodynamic pressure. The spheroid is held back at the aperture and due to the hydrodynamic pressure it is also forced to move partly inside the narrowed channel section (Fig. 18).

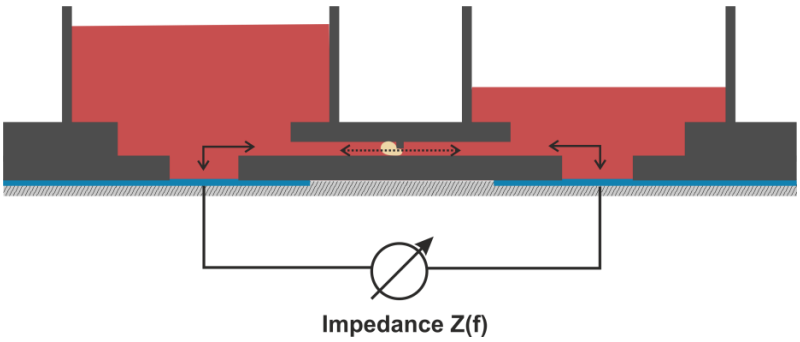

Fig. 18: Illustration of the measurement principle. A spheroid is trapped at the central aperture of the flow channel and forces the alternating current to flow through the spheroid.

This significantly inhibits medium flow between the reservoires (chapter 5.1.3) and consequently also current flow through the channel. This way, the measured impedance is dominated by the contribution of the spheroid body resulting in a significant increase in impedance (chapter 5.2.2). The impedance contribution of the spheroid is composed of the intra- and extracellular resistance R_{int} and R_{ext} as well as the non-ideal spheroid capacitance A_{sph} (chapter 3.2).

5.2.2 Frequency-Dependent Impedance of the Flow Channel

In Fig. 19 A a typical impedance spectrum of the medium-filled flow channel with and without spheroid is shown. Using this data, the relative impedance was calculated ($|Z|_{rel} = 100 \cdot (|Z|_{w} - |Z|_{wo})/|Z|_{wo}$) and plotted in order to determine the frequency where spheroid associated impedance changes can be recorded with highest sensitivity (Fig. 19 B). For the flow channel without spheroid the spectrum shows a linear decrease for frequencies between 1 Hz and 10 Hz due to the non-ideal electrode capacitance. At higher frequencies the impedance stays constant reflecting the electrolyte resistance R_{bulk}. Upon insertion of a spheroid into the flow channel and the sealing of the central aperture, the spectrum is shifted to higher impedance values. The linear decrease from the electrode capacitance is now only visible at very low frequencies (1 – 3 Hz).

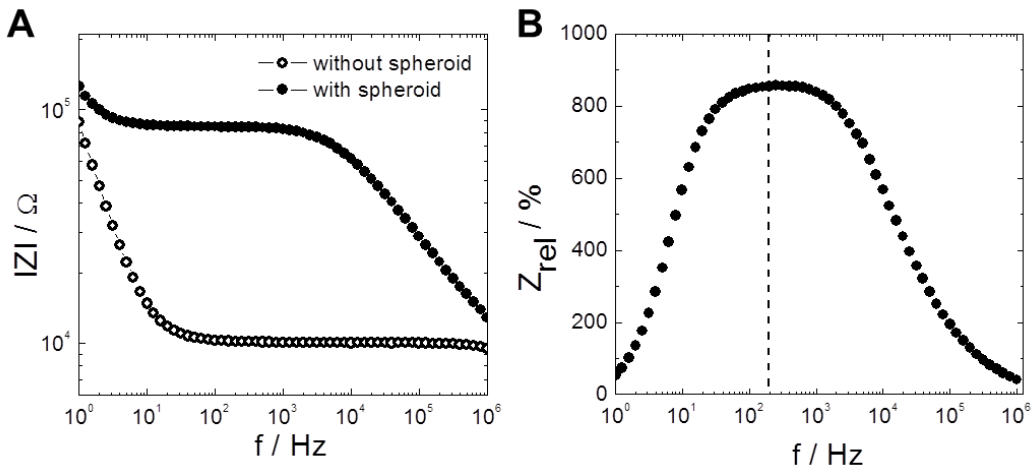

Fig. 19: Exemplary impedance spectrum with and without spheroid at the aperture of the PT-2 channel (**A**) and the according relative impedance plot with a dashed line at 200 Hz to indicate the sampling frequency in time-resolved experiments (**B**).

It is followed by a plateau phase (3 Hz – $2 \cdot 10^3$ Hz) and a further linear decrease of impedance in the frequency range $2 \cdot 10^3$ Hz – 10^6 Hz. The plateau reflects a frequency-independent phase resulting from ohmic resistance contributions originating from the spheroid. The second decline in impedance is related to capacitive contributions of the spheroid.

The normalized impedance plot reveals that the newly designed flow channel has a high sensitivity showing an increase of relative impedance of generally (300 – 1000) % (in B: ~ 800 %) for a channel sealed by a spheroid compared to an empty channel. The normalized impedance plot also shows a broad peak maximum in the frequency range of ~ $5 \cdot 10^1$ – 10^3 Hz. Out of these plateau frequencies 200 Hz was chosen for the presentation of all time courses of impedance. A typical time course of impedance at 200 Hz can be seen in Fig. 20 A. For the initially spheroid-free channel the impedance stays constant at ~ 10 kΩ, which is similar to the channel resistance R_{ch} of a medium-filled channel. As listed in Tab. 9 the channel resistances vary within 8 and 10 kΩ for different PT-2 flow channels (FC-1 – FC-4). When a spheroid is introduced in the channel an immediate and strong increase in impedance is measured which reaches a constant impedance value (here: 93 kΩ) within ~ 15 min. Fig. 20 B provides the time- and frequency-dependent changes of the channel impedance when a spheroid is inserted as a 3D surface plot.

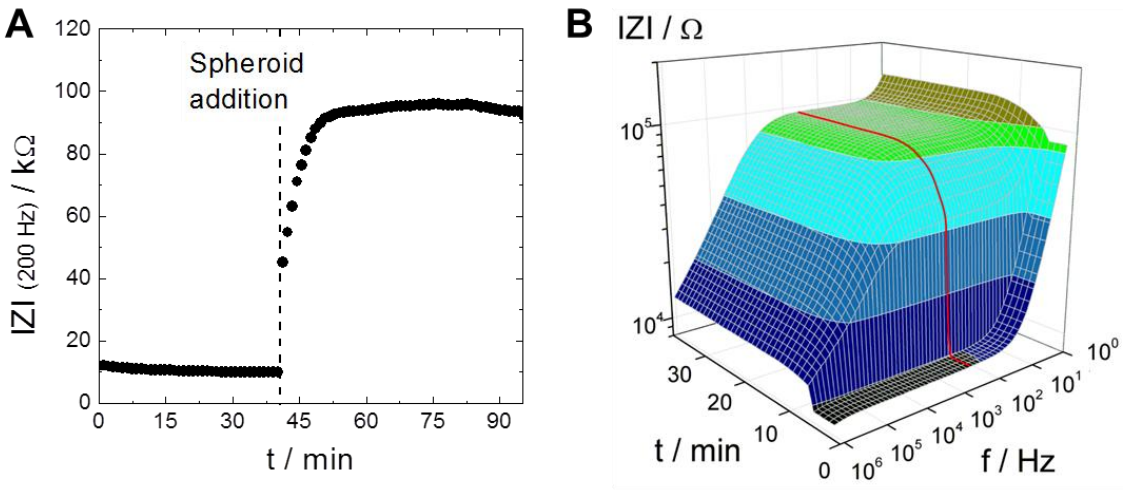

Fig. 20: Typical time course of the impedance magnitude at 200 Hz (**A**) and 3D surface plot showing the time and frequency dependence of the impedance magnitude of a channel with and without spheroid (**B**).

5.2.3 Simulated Spectra

Simulations based on the equivalent circuit shown in Fig. 4 were performed to illustrate the influence of the spheroid parameters R_{ext}, R_{int} and A_{sph} introduced in chapter 3.2 on the shape of an impedance spectrum. Using a *LabView*-based software (Nr. 1) (J. Wegener) the changes in impedance upon variation of the respective spheroid parameters are visualized in Fig. 21. As introduced in Eq. 3.6 (chapter 3.1.1) the impedance can be split up in its real and imaginary part. Therefore, the dependence of resistance R and reactance X on the spheroid parameters are included.

For increasing values of R_{ext} the level of the first plateau of impedance (IZI) and resistance (R) is increased. The reactance (X) of the channel without spheroid is represented as a linear declining slope. For the channel with spheroid the reactance is no longer monotonic but biphasic with local extrema. At low frequencies the reactance is linearly decreasing until a minimum value. Then it is linearly increasing until a maximum value followed by a second linear decrease. For increasing values of R_{ext} the curve minimum and maximum are shifted to higher reactance values and slightly lower frequencies.

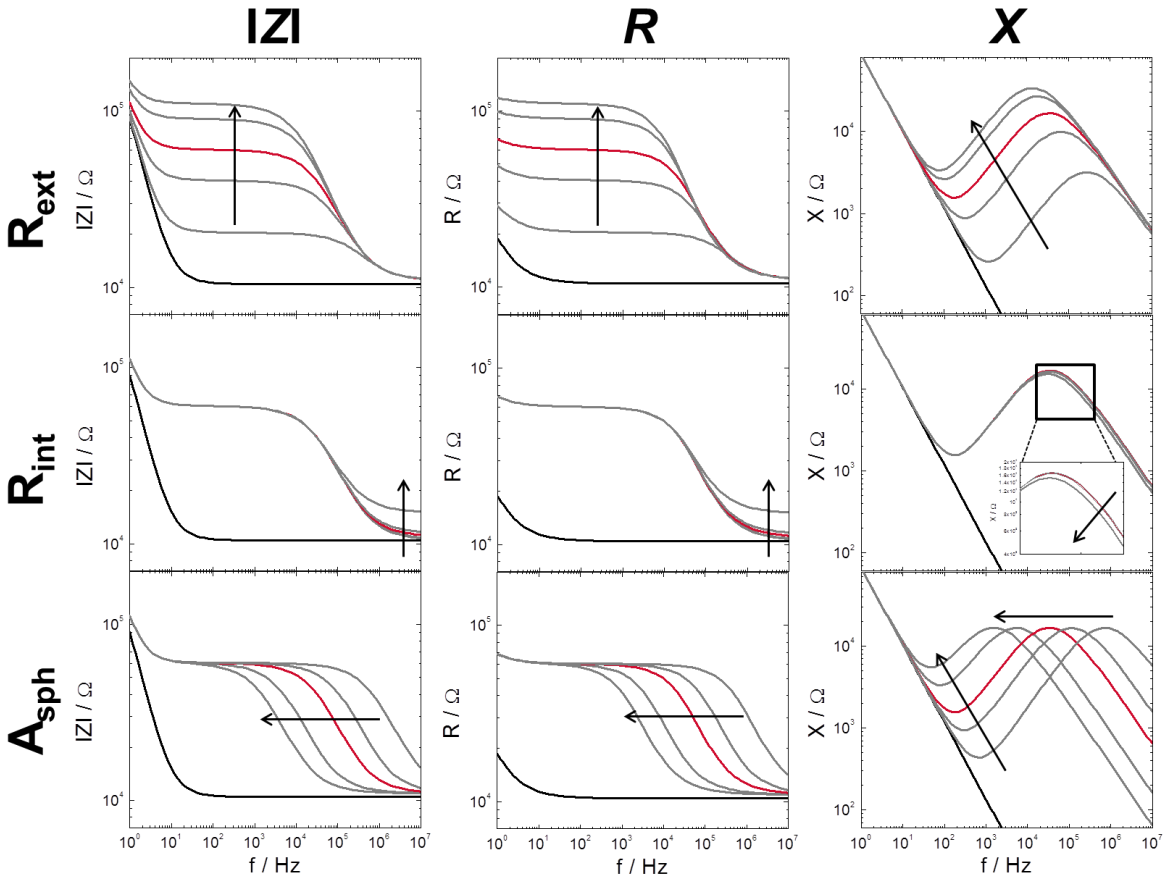

Fig. 21: Simulated spectra of the frequency dependent impedance **IZI**, resistance ***R*** and reactance ***X*** for a flow channel with (grey) and without (black) a spheroid. One of the parameters $\boldsymbol{R_{ext}}$, $\boldsymbol{R_{int}}$ and $\boldsymbol{A_{sph}}$ was varied while the other two parameters were kept constant. The standard values for the parameters (red line) were chosen to be: R_{ext} = 50 kΩ, R_{int} = 500 Ω, A_{sph} = $2 \cdot 10^{-9}$ $Fs^{n-1}cm^{-2}$ and n_{sph} = 0.75. The bulk resistance was set to 10.45 kΩ, the CPE parameters of the electrodes were A_{el} = $1 \cdot 10^{-5}$ $Fs^{n-1}cm^{-2}$, n_{el} = 0.94 and the electrode area was set to 0.2 cm^2. The values of the parameters were varied to: R_{ext} = 10, 30, 50, 80, 100 kΩ; R_{int} = 10, 100, 500, 1000, 5000 Ω; A_{sph} = $2 \cdot 10^{-8}$, $8 \cdot 10^{-9}$, $2 \cdot 10^{-9}$, $8 \cdot 10^{-10}$, $2 \cdot 10^{-10}$ $Fs^{n-1}cm^{-2}$. The arrows indicate the direction of increasing parameter values.

Upon variation of R_{int} impedance and resistance are slightly increased in the second plateau at very high frequencies (> 10^6 Hz). This change is only marginal for the R_{int} values between 10 – 1000 Ω, whereas a clear increase at 5 kΩ can be observed. The changes in reactance are marginal for all but the highest R_{int} value where the curve in the range between 10^4 Hz and 10^7 Hz is shifted to smaller reactances and frequencies.

An increase in the non-ideal spheroid capacitance A_{sph} at a constant n_{sph} value results in a reduced width of the first plateau for impedance and resistance resulting from the shift of the second linear decrease to lower frequencies. For

the reactance it can be observed that with increased A_{sph} values the curve minimum is shifted to higher values of reactance and to slightly lower frequencies. The maximum stays at the same reactance level but is shifted to significantly lower frequencies.

5.2.4 Parasitic Impedance Contribution

Beside the capacitive and resistive impedance contributions arising from the electrolyte, the electrodes and the spheroid in the flow channel there are also contributions arising from the electronic system and cables. These are the so-called parasitic contributions that can consist of capacitive, resistive and inductive parts. In the equivalent circuit introduced in chapter 3.2 the parasitic contribution is modeled by a constant phase element (A_{para}, n_{para}) in parallel to the rest of the circuit assuming that this contribution is mainly of non-ideal capacitive nature. In this chapter the influence of the parasitic contribution, arising from the electronic equipment, on the shape of an impedance spectrum is illustrated and the amount of A_{para} is quantitatively evaluated for the given experimental setup.

In order to determine the parasitic contribution of the electronic equipment that was used for all impedance measurements with the flow channel, four simple serial combinations of a capacitor (9.4 µF) and a resistor (10 / 27 / 47 / 100 kΩ) were prepared (Fig. 22, A) and connected to the electronic equipment. The impedance magnitude was measured for the different R-C combinations at frequencies between 10^{-1} and 10^{6} Hz (Fig. 22 B).
If there would be no parasitic contribution the spectra would show only a decline in impedance at low frequencies and a horizontal, frequency-independent part at high frequencies. However, there is a second decline at very high frequencies highlighted in the plot by the dashed box reflecting the impedance contribution from the electronic equipment. In order to determine A_{para} and n_{para} for each spectrum, all spectra were fitted using a *LabView*-based software (Nr.1) (J. Wegener). The results are listed in Tab. 10 showing a parasitic capacitance A_{para} of $2 \cdot 10^{-12}$ $Fs^{n-1}cm^{-2}$ and n_{para} values between 0.97 and 0.98 for R > 10 kΩ. For R = 10 kΩ A_{para} is $3 \cdot 10^{-12}$ $Fs^{n-1}cm^{-2}$ and n_{para} is 0.95.

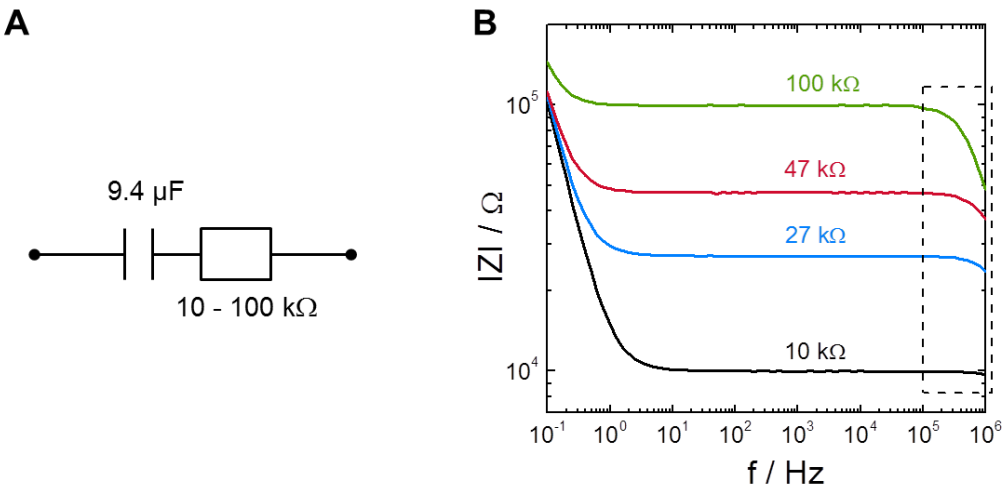

Fig. 22: The serial combination of a 9.4 µF capacitor and resistors of 10 / 27 / 47 / 100 kΩ (**A**) were measured and the resulting impedance spectra were plotted (**B**). The impact of parasitic contributions of the setup are highlighted by the dashed box.

Tab. 10: Overview of the parasitic contribution given as A_{para} and n_{para} for the four resistances R under test.

***R* / kΩ**	***10***	***27***	***47***	***100***
A_{para} / $Fs^{n-1}cm^{-2}$	$3 \cdot 10^{-12}$	$2 \cdot 10^{-12}$	$2 \cdot 10^{-12}$	$2 \cdot 10^{-12}$
n_{para}	0.95	0.98	0.97	0.98

For comparison, the impedance spectra of the medium-filled PT-2 flow channel without spheroid ($R_{bulk} \approx 10$ kΩ) were also used to determine their parasitic impedance contribution. The obtained value for A_{para} is in the range of $(3 - 4) \cdot 10^{-12}$ $Fs^{n-1}cm^{-2}$ with $n_{para} = 0.98$ for a single channel, which was directly connected to the impedance analyzer. This value is in good agreement with that for the test circuit with $R = 10$ kΩ. When two flow channels were measured at a time and connected to the impedance analyzer via the relais, A_{para} is slightly higher due to additional cables with values in the range of $4.1 \cdot 10^{-12}$ – $4.8 \cdot 10^{-12}$ $Fs^{n-1}cm^{-2}$ ($n_{para} = 0.98$). Summed up, there is a measureable parasitic impedance contribution in the experimental setup, which can be seen in impedance spectra at frequencies above 10^5 Hz. Unfortunately, changes in R_{int} are only observed in the same frequency range (see previous chapter). For this purpose, impedance spectra were corrected by A_{para} (quantified by pre-analysis

of the spectra) before they were fitted to determine the spheroid parameters R_{ext}, R_{int} and A_{sph} (automated fit).

5.3 Influence of Spheroid Size and Repositioning on the Impedance

The first impedimetric measurements using the novel device were performed to learn about general correlations between spheroid size/handling and the corresponding impedance signal. These experiments were all performed using MCF-7 spheroids and the PT-2 flow channel (chapter 4.3.5.1).

5.3.1 Impedance Variations for Spheroids of the Same Batch

This measurement was performed three times using 7 or 8 d old spheroids and FC-2 following the established protocol (chapter 4.3.5.1). Five spheroids of the same age and prepared from the same initial cell number were measured sequentially with at least three baseline spectra in between (Fig. 23 A) (appendix A2, Fig. S2). The typical time course of impedance shows a fast increase in impedance followed by a slower increasing or a plateau phase, which only slightly differs in kinetics and height for the individual spheroids. As soon as the spheroid is removed from the channel the impedance drops down to baseline level (~ 10 kΩ).

The corresponding average impedance spectra of the flow channel loaded sequentially with five individual spheroids and without spheroid are shown in Fig. 23 B. They were determined by averaging five impedance spectra 30 min after spheroid introduction (impedance values were generally stable at this time point) and by averaging five spectra directly before the spheroids were introduced. The averaged impedance spectra show the typical curve characteristics of a flow channel with and without spheroid (chapter 5.2.2) and a small standard error. For a quantitative comparison of all measurements the relative impedance ($|Z|_{rel} = (|Z|_{w}-|Z|_{wo})/|Z|_{wo}$) of the spheroids was determined 30 min after spheroid addition ($t_{a.a.}$ = 30 min) (Tab. 11).

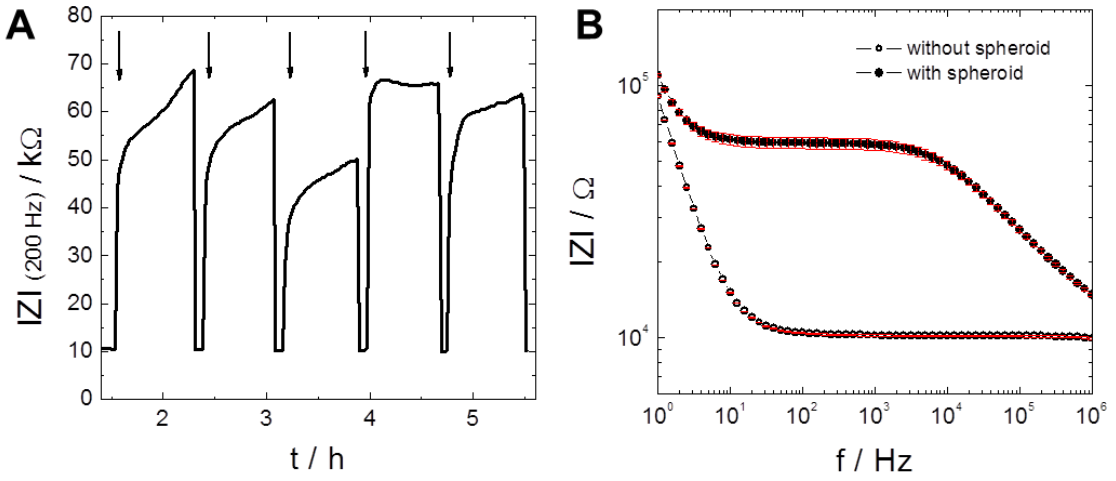

Fig. 23: Typical time course of the impedance magnitude at 200 Hz for five spheroids of the same batch (#3) (**A**). The arrows mark the time points when the spheroids were introduced in the channel. Corresponding averaged impedance spectra for a PT-2 channel with and without spheroid recorded immediately before and 30 min after spheroid introduction (**B**; mean ± SE; n = 5). T = 37 °C.

Tab. 11: Overview of individual (values extracted at $t_{a.a.}$ = 30 min) and averaged relative spheroid impedances ($|Z|_{rel} = (|Z|_w - |Z|_{wo})/|Z|_{wo}$) from three batches (**#1** - **#3**) with five spheroids per batch (**S-1** - **S-5**) each. T = 37 °C.

	$\|Z\|_{rel}$					
Batch	***S-1***	***S-2***	***S-3***	***S-4***	***S-5***	***Mean ± SD***
# 1	4.9	5.4	4.1	4.2	3.6	4.4 ± 0.7
# 2	5.8	5.1	4.5	5.0	4.2	4.9 ± 0.6
# 3	4.8	4.7	3.6	5.2	5.1	4.7 ± 0.6

The evaluated data shows that $|Z|_{rel}$ values vary within one batch and also for different batches. A calculation of the relative errors of $|Z|_{rel}$ for the three batches results in 16 % for batch # 1, 12 % for batch # 2 and 14 % for batch # 3. A two-sample t-test with a level of significance of 0.01 proves that the mean values of the three batches are not significantly different.

Although, small variations in the $|Z|_{rel}$ values of spheroids of the same and different batches are observed it can be concluded that spheroids of the same age and size show impedance values in a reproducible range.

5.3.2 Impedance Variations for Different Spheroid Sizes

The size of a spheroid can be controlled by the cell seeding density and the growth time before an experiment. In order to evaluate if the spheroid size has an influence on the impedance, spheroids originating from three seeding densities (1000 / 3000 / 6000 cells/well) were prepared (average MCF-7 spheroid diameters on day 7: ~ 390 / 470 / 560 µm; for more information see chapter 6.1) and measured 8 d after seeding using FC-2 following the protocol in chapter 4.3.5.1.

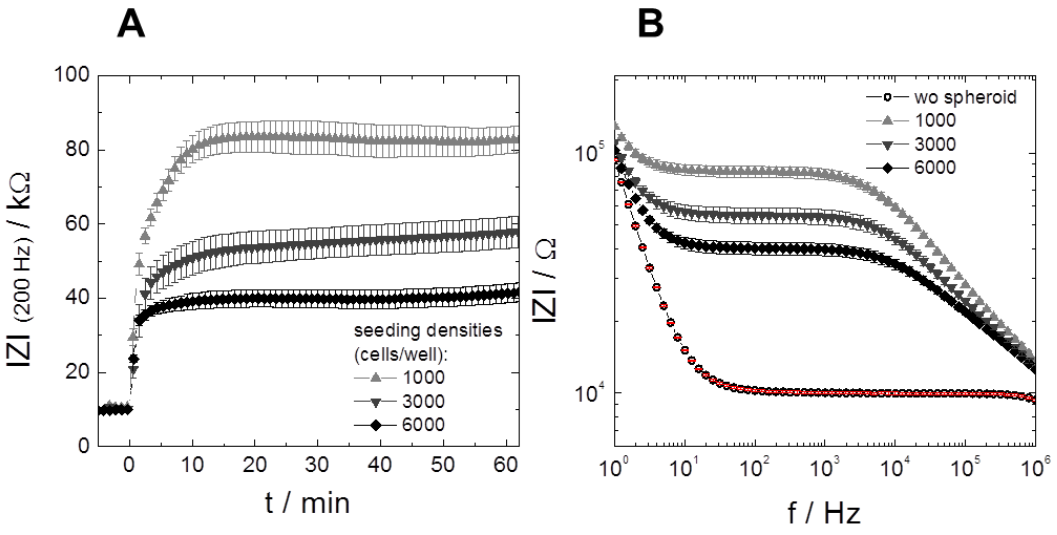

Fig. 24: Impact of different spheroid sizes on impedance. Time course of impedance magnitude at 200 Hz for 8 d old spheroids originating from seeding densities of 1000/3000/6000 cells/well that were introduced at t = 0 min into the channel (mean ± SE, n = 6) (**A**). Impedance spectra extracted at t = 30 min after spheroid insertion (mean ± SE, wo: n = 18, w: n = 6) (**B**).

As can be seen in Fig. 24 the impedance for differently sized spheroids is size dependent. Small-sized spheroids with the lowest seeding density (1000 cells/well) show the highest impedance with (83 ± 4) kΩ (200 Hz, 30 min). Medium-sized spheroids (3000 cells/well) show an impedance value of (55 ± 4) kΩ and big spheroids (6000 cells/well) show the lowest impedance of (40 ± 2) kΩ (both: 200 Hz, 30 min).

Using a *LabView*-based software (Nr. 1) (written by J. Wegener) the spectra for each seeding density at $t_{a.a.}$ = 30 min were fitted and the spheroid parameters R_{ext}, R_{int} and A_{sph} were determined (Tab. 12).

Tab. 12: Overview of the parameters R_{ext}, R_{int} and A_{sph} for spheroids with seeding densities of 1000/3000/6000 cells/well. Spectra recorded 30 min after spheroid introduction were fitted as described in chapter 4.3.3 using the following parameter values: A_{el} = 1.8·10^{-6} Fs^{n-1}cm^{-2}, n_{el} = 0.95 (electrode area = 1.0 cm^2), R_{bulk} = 9.9 kΩ, A_{para} =3·10^{-12} Fs^{n-1}cm^{-2}, n_{para} = 0.98, n_{sph} = 0.75 (mean ± SE, n = 6).

Seeding density / cells/well	***1000***	***3000***	***6000***
R_{ext} / kΩ	73 ± 5	45 ± 4	30 ± 2
R_{int} / kΩ	5.2 ± 0.7	4.2 ± 0.4	4.0 ± 0.1
A_{sph} / ·10^{-9} Fs^{n-1}cm^{-2}	2.15 ± 0.07	2.49 ± 0.09	2.77 ± 0.07

The extracellular resistance of the spheroids decreases for increasing seeding density or spheroid size, respectively. The same trend but less pronounced is seen for the intracellular resistance. The values of A_{sph} are slightly increasing for increasing spheroid size.

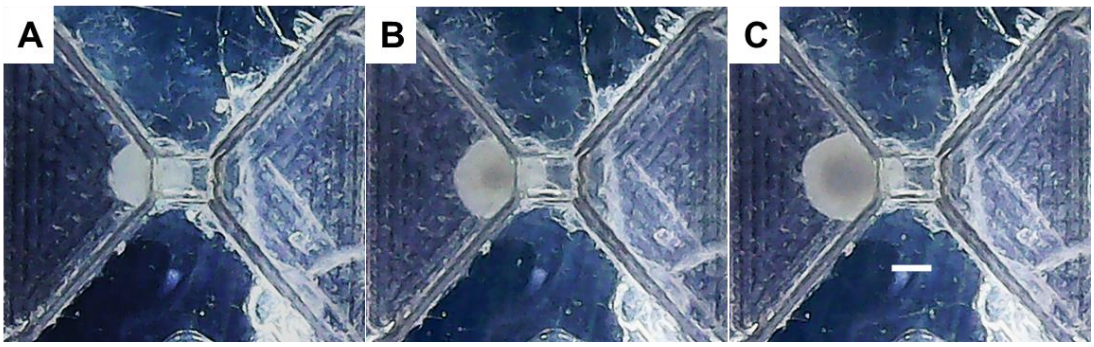

Fig. 25: Typical micrographs of a 1000 cells/well spheroid (**A**), a 3000 cells/well spheroid (**B**) and a 6000 cells/well spheroid (**C**) 20 min after introduction into the FC-2 (scale bar: 250 µm).

In a microscopic study the translocation of spheroids originated from the three seeding densities into the aperture of FC-2 was investigated (Fig. 25). For this purpose, micrographs of the spheroids at the aperture were taken 20 min after introduction into the channel using the digital microscope. The photographs were evaluated using imageJ to determine the area of the narrowed channel that is occupied by the spheroid. The study shows that small spheroids (1000 cells/well) are occupying 56 ± 6 % of the whole volume in the central restriction, while middle spheroids are only occupying 44 ± 1 % and big spheroids occupy only 38 ± 4 % of the total aperture inner volume (mean ± SE, n = 3).

The results of the impedimetric and microscopic study clearly show that the spheroid impedance and the spheroid's tendency to migrate into the aperture are dependent on the spheroid size. In conclusion, replicates of impedimetric experiments using the new flow channel should be conducted with spheroids of the same size. In the following, impedance measurements with MCF-7 spheroids from a seeding densitiy of 3000 cells/well was usually used.

5.3.3 Influence of Repositioning on Spheroid Impedance

As explained before (chapter 5.1.3) liquid and current flow through the channel are inhibited as long as a spheroid seals the aperture. Therefore, it is not possible to measure the cellular response of a spheroid to chemical stimuli online when the substance is added during the measurement as there will be no mixing. A possible way to bypass this problem is by removing the spheroid from the aperture, add the stimuli and bring the same spheroid back to the aperture. This process was called 'repositioning'. In this subchapter it was investigated if the spheroid impedance is influenced by this process. For this purpose, 9 d old spheroids (3000 cells/well) were introduced in FC-2 or FC-3 and repositioned three times (chapter 4.3.5.1).

As can be seen in the typical time course of impedance for one of the tested spheroids (S-2) and the corresponding impedance spectra (Fig. 26 A, B) (appendix A2, Fig. S3) the impedance values before and after repositioning are very similar. The average relative spheroid impedances $|Z|_{rel}$ for the five tested spheroids (S-1– S-5), which were repositioned three times are shown in Fig. 27. A table with the exact values can be found in the appendix A2 (Tab. S2). A look at the mean values shows smaller relative impedances for S-1/-2/-5 (~ 3.3 – 3.9) measured in FC-2 and higher values for S-3/-4 (6.7 / 10.3) measured in FC-3. A calculation of the relative errors of $|Z|_{rel}$ for S-1/-2/-5 results in 26 / 5 / 21 % and for S-3/-4 the values are 11 / 20 %. A two-sample t-test with a level of significance of 0.01 shows that the spheroid impedances of S-1/-2/-5 are not significantly different and the same is true for the spheroid impedances of S-3 and S-4

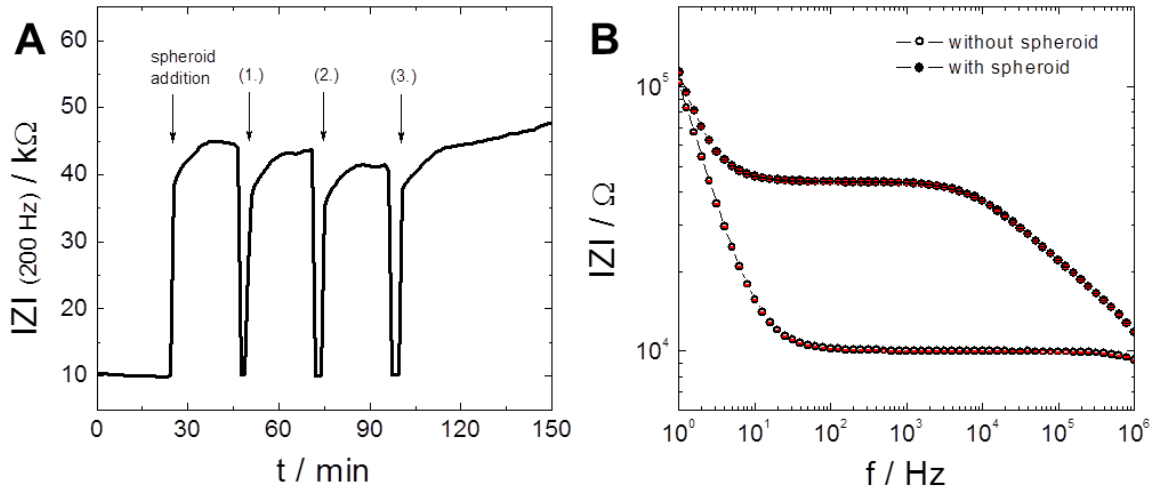

Fig. 26: Influence of repositioning of spheroids (3000 cells/well) on the impedance. Typical time course of impedance magnitude at 200 Hz for a 9 d old spheroid (S-2) that was repositioned three times (1. – 3.) after first addition (arrows) (**A**). Corresponding impedance spectra with and without spheroid (mean ± SE, n = 4) (**B**). T = 37°C.

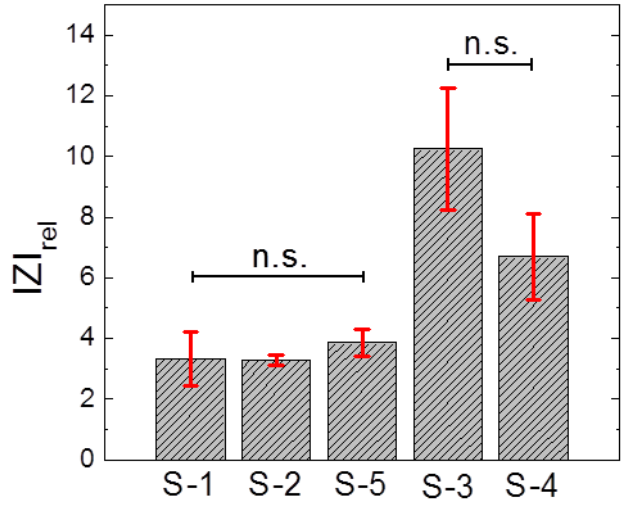

Fig. 27: Overview of the relative spheroid impedances $|Z|_{rel}$ of five spheroids (S-1 – S-5) determined from impedance values extracted 22 min after initial addition and after three subsequent repositionings (mean ± SE, n = 4). Significance was determined by a two-sample t-test using a significance level of 0.01. T = 37°C.

The study shows that the repositioning process influences the spheroid impedance to a certain degree, which should be kept in mind when impedance experiments including repositioning are planned and analyzed.

5.4 Visualization of Spheroids in the Channel Using Microscopy

Transparent materials for the channel and the electrode layout were chosen to enable the microscopic visualization of a spheroid in the channel. Accordingly, spheroids were documented at the central channel aperture using different microscopes.

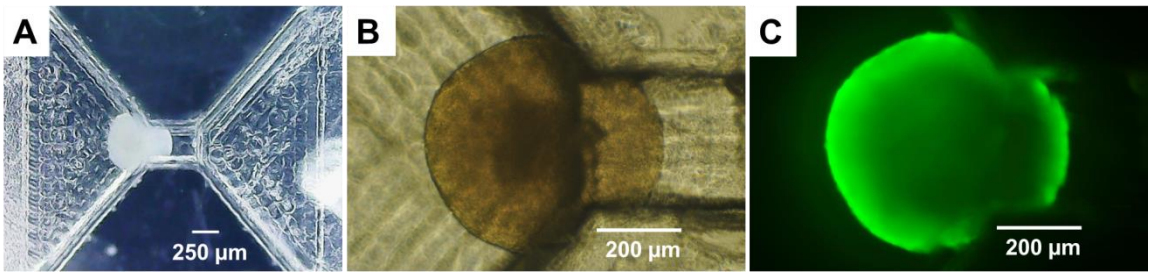

Fig. 28: Microscopic visualization of spheroids in the central aperture using the digital microscope (**A**) and the phase contrast (**B**) or epifluorescence (**C**) mode of the Nikon Diaphot.

Fig. 28 A was obtained with the digital microscope in the incubator during an impedance measurement. This device sends live pictures to the monitor and pictures or videos can be taken manually at designated time points. With this technique the spheroid is well visible throughout an impedimetric measurement, it is possible to sort out spheroids that are injured by the manual transfer and to observe the migration of the spheroid into the central channel. For pictures with a higher magnification and an increased contrast the phase contrast microscope Nikon Diaphot was used (Fig. 28 B). This microscope was also equipped with a mercury lamp and filter blocks for epifluorescence microscopy. Fig. 28 C shows a green fluorescent CaAM stained spheroid. Since spheroids in the transparent channel are visible in phase contrast and epifluorescence this microscope is most suitable for the documentation of spheroids before, after and during irradiation in phototoxicity studies (chapter 6.7).

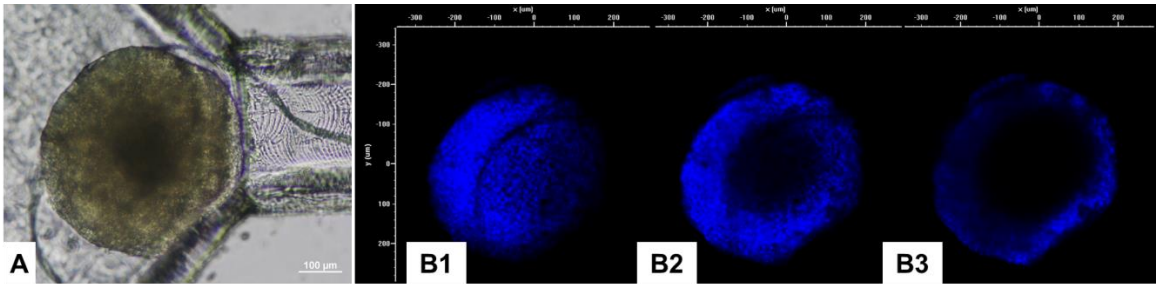

Fig. 29: Microscopic visualization of a DAPI stained spheroid in the flow channel using the upright CLSM. The phase contrast photograph shows that the spheroid is lying loosely in front of the aperture (**A**) (scale bar: 100 µm). Optical sections from the top of the spheroid to its center (**B1** – **B3**) visualize the cell nuclei in blue.

The upright CLSM was used to image the spheroid interior. For this purpose, a spheroid was stained with DAPI after cross-linking and permeabilization (protocol in chapter 4.2.3). As can be seen in the phase contrast image in Fig. 29 A the stained spheroid is lying loosely in front of the aperture. Apparently, the fixation enhanced the stiffness and decreased the deformability of the spheroid and therefore prevented the migration of the spheroid into the aperture, which is otherwise generally seen for viable spheroids. Fluorescent micrographs of different sections from the top to the center of a spheroid are shown in Fig. 29 B1 – B3. Single blue spots indicating the cell nuclei of the spheroid can be seen. The outer spheroid surface (B1) is completely covered with blue nuclei. However, optical sections from deeper planes (B2, B3) of the spheroid show blue nuclei only at rim regions, whereas the interior is black. This is a well-known phenomenon in confocal microscopy already dicussed in chapter 3.4. In short, limited penetration of fluorophores into spheroids and a limited imaging depth of the CLSM lead to a strongly attenuated fluorescence intensity in central spheroid regions.

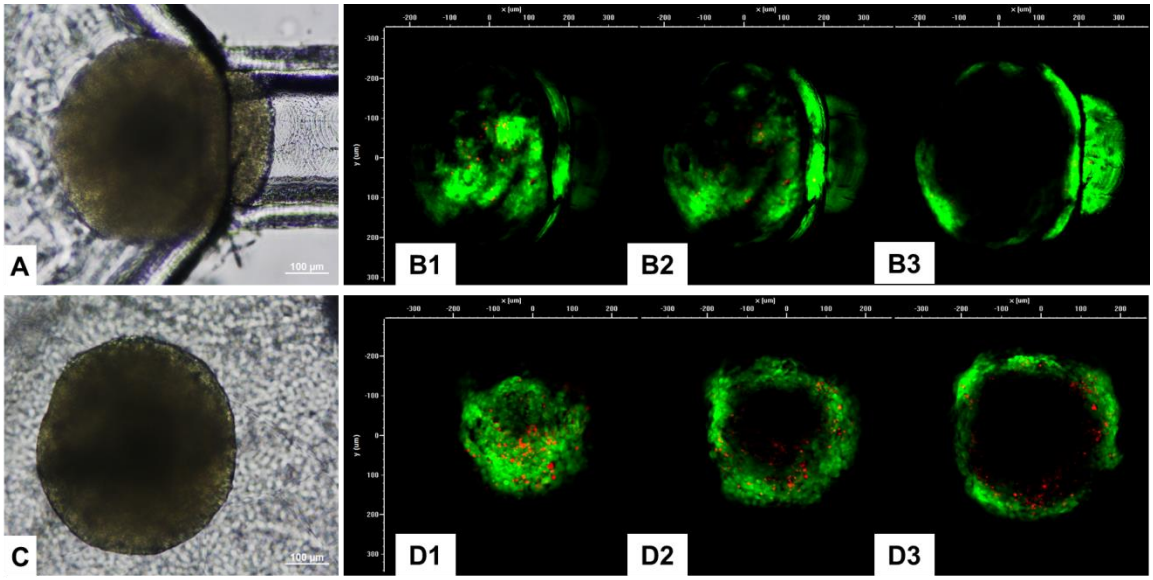

Fig. 30: Microscopic visualization of a Live/Dead stained spheroid using the upright CLSM. Phase contrast images (**A**, **C**) as well as optical sections (**B**, **D**) from the top to the center (**1** – **3**) have been taken for the spheroid when the objective approached the top side of the channel (**A**, **B**) or the under side of the channel (**C**, **D**).

Spheroids with Live/Dead staining (protocol in chapter 4.2.2) were also visualized in the channel using the upright CLSM (Fig. 30). Again, the spheroid is shown in a phase contrast image (A) and in fluorescence micrographs from different planes from spheroid top to center (B1 – B3). Here, the step from normal channel height to aperture height produces a shadow on the fluorescent spheroid image. Furthermore, the staining seems to be imcomplete and optical sections appear blurry making it hard to identify individual cells. The flow channel inner surface was prepared by milling that left a microstructure, which can influence the quality of the fluorescent micrograph (see the microstructures in chapter 5.1.1 Fig. 14 B, C xy-planes). Since the flow channel is bonded onto a base plate with smooth surface the same spheroid was inspected after the flow channel was flipped over with the channel underside now facing the objective (C, D1 – D3). Without the disturbing milling structures sharp fluorescence images without any shadows were taken and single cells could be identified. Microscopy from the bottom side of the channel allowed to distinguish between live and dead cells. The latter could be located mostly in the rim regions of the spheroid.

The flipping of the channel however, is not a final technical solution since it is inefficient and the spheroid can not be examined at the aperture. Because the hydrostatic pressure ratio changes upon flipping the channel upside down the spheroid leaves the aperture. The easiest way to prevent these challenges is by using an inverted CLSM.

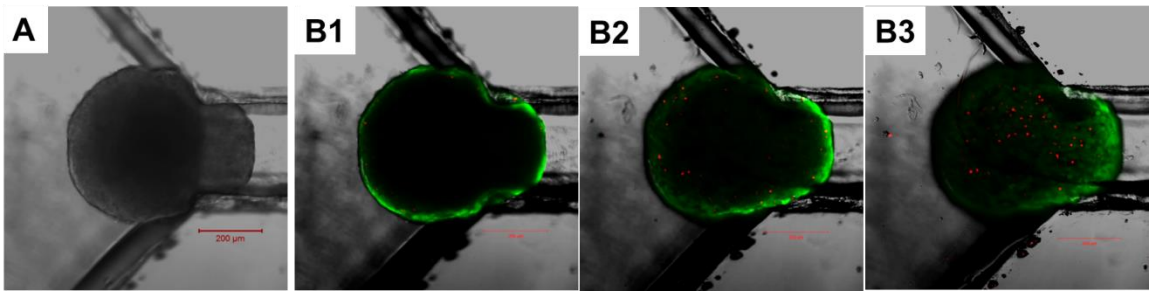

Fig. 31: Microscopic visualization of a Live/Dead stained spheroid using an inverted CLSM. A phase contrast image (**A**) as well as optical sections from top to bottom (**B1** – **B3**) as overlays of phase contrast and fluorescence images were taken. (scale bars: 200 µm).

As can be seen in Fig. 31 the inverted CLSM produced optical sections of the Live/Dead stained spheroid (B1- B3) in a good quality similar to the images in Fig. 30 D1 – D3. Viable cells and a few dead cells can be identified and the overlay with the phase contrast image clearly depicts the position of the spheroid in the channel.

5.5 Discussion

5.5.1 Characterization of the New EIS-Based Device

The novel impedimetric device is a flow channel with a central aperture and a planar ITO-PET electrode layout beneath. Two prototypes of this channel with different channel geometries were developed. A characterization of both prototypes shows that PT-1 is less applicable than PT-2 due to a higher channel resistance and a gradual decrease of the channel height towards the aperture (chapter 5.1.1). When a spheroid is introduced into the flow channel via one of the two reservoires at both ends of the channel it is held back at the central aperture and due to the hydrodynamic pressure from the medium-filled reservoir

on the spheroid side the spheroid is partly pressed into the narrowed channel in the center leading to the sealing of the channel by the spheroid, which enables its impedimetric analysis (chapter 5.1.3, 5.2.1). The relative impedance determined from the spectra of a spheroid-free and spheroid-loaded flow channel shows generally values up to 1000 % (in the presented example in Fig. 19 ~ 800 %) proving that the signal change due to the sealing of the channel by a spheroid can be detected with high sensitivity. Time courses of impedance are shown at 200 Hz, which was chosen as monitoring frequency (chapter 5.2.2). Simulated spectra illustrate the influence of the three spheroid parameters on the spectral curve (chapter 5.2.3). Increasing R_{ext} and R_{int} values are reflected by an increase in the first and second plateau phase of the impedance spectrum, respectively. An increase in A_{sph} is reflected by a shift of the second decline to lower frequencies. In the high frequency range of the spectral curve the influence of the parasitic impedance contribution from the electronic equipment can be detected, which was determined to range between $(3 – 5)\cdot10^{-12}$ $Fs^{n-1}cm^{-2}$ (with $n_{para} = 0.98$) (chapter 5.2.4).

The new device comprising the transparent flow channel and the transparent planar ITO-PET electrode layout can be prepared in a cost-efficient way and the ITO-PET foil can be structured easily by photolithography technique. For the re-use of the device the channel is simply cleaned by rinsing with ultrapure water and 70 % ethanol. When the electrode layout shows extensive signs of use it can be exchanged easily by a new one. The EIS-based setup can measure the impedance contribution of a spheroid in a highly sensitive way and has a low parasitic impedance contribution.

In chapter 1.3 different impedance-based setups for analysis of spheroids were already presented. The most characterized systems are presented for the microcavity array (Krinke et al., 2010) and for the capillary setup described in the report of Thielecke et al. (2001). For spheroid positioning in the capillary setup a pump system is needed. Upon the applied hydrodynamic force the spheroid is completely pressed into the glass capillary with a diameter of 300 µm. They declare that a possible influence of the capillary on spheroids, due to their compression, will be investigated in future work. The corresponding equivalent circuit model comprised also the parameters R_{ext}, R_{int} and C_{mem}. However, they

state that the parasitic capacitance (C_s) of their setup was too high (without declaration of the value) so that C_{mem} and R_{int}, which are also impedance contributions reflected at higher frequencies in the impedance spectrum, could not be specified in a reliable way. Nevertheless, they were able to determine the R_{ext} values of healthy and gene-manipulated T47D human breast carcinoma spheroids (decreased proliferation and tumor growth) via data fitting using a nonlinear least square fitting technique. For control and gene-manipulated spheroids with diameters of 400 – 500 µm the resulting R_{ext} values were distinguishable with 18 kΩ and 4 kΩ.

When the capillary system is compared to the new EIS device in this thesis it can be stated that the new device does not need pump systems and has a low parasitic contribution enabling also the determination of the parameters R_{int} and A_{sph} (equals C_{mem} in the capillary system). The determined R_{ext} values from the capillary system are, however, in a comparable range than those determined from the new EIS device (see e.g. chapter 5.3.2).

Krinke et al. (2010) described the microcavity array chip, where 15 spheroids can be measured simultaneously in cavities with an edge length between 200 and 400 µm. Positioning of spheroids can be performed using a pipette and a light microscope. They had to cope with a high self-impedance of the 200 µm cavities, high parasitic capacitance and inter-cavity variance. After some optimization they achieved a mean relative spheroid impedance of (49 ± 1) % for SH-SY5Y spheroids (in comparison to formerly (21.8 ± 0.5) %). With this setup the group was able to determine the relative spheroid impedance and distinguish healthy and mutant spheroids.

Compared to the new EIS device the positioning in the cavities is more laborious. Although, optimizations were performed the relative spheroid impedance measured in the MCA chip is lower than in the new EIS device. A detailed comparison is provided in chapter 5.5.2.

5.5.2 Influence of Spheroid Size and Repositioning on Impedance

Impedance Variations of Spheroids Prepared by the Same Initial Cell Number and Growth Duration

It is possible to generate spheroids of a defined size using a defined cell seeding density and growth duration (chapter 6.1). Five MCF-7 spheroids of a batch, which were prepared in the same way (same seeding density / age) were measured sequentially and the impedance variation between these spheroids was estimated. Three batches were measured this way obtaining the results below:

- Within the respective spheroid batches the $|Z|_{rel}$ values have a relative error of 12 – 16 %.
- Comparison of the results of three batches show no significant differences in impedance.

Variability in spheroid impedance likely comes from minor differences in the spheroid structure. Even though, spheroids originate from the same initial cell density and are measured at the same age they differ slightly in size, shape and internal composition (ratio of cells to extracellular matrix; amount of dead cells). No two spheroids are completely alike and consequently, also their measured impedance is fluctuating to a certain degree.

Impedance Variations of Spheroids Prepared by Different Initial Cell Numbers and the Same Growth Duration

In this experiment an impedimetric and microscopic analysis of MCF-7 spheroids from three different seeding densities (1000 / 3000 / 6000 cells/well) and consequently, different sizes was performed using the new device.

- With increasing spheroid size the impedance is decreased.
- With increasing spheroid size R_{ext} and R_{int} are decreasing and A_{sph} is increasing.
- With increasing spheroid size the penetration into the narrowed channel is reduced.

The impedimetric results were counter intuitive since it was expected that spheroids with the highest seeding density tested would show the highest impedance as well as extra- / intracellular resistance values. This was for example reported in the work of Thielecke et al. (2001) who performed EIS measurements in a capillary system with T47D human breast carcinoma spheroids. Via subsequent data fitting using a nonlinear least square fitting technique they determined the R_{ext} value of bigger spheroids with diameters of 600 – 700 µm to be 92 kΩ, whereas smaller spheroids with diameters of 400 – 500 µm had a R_{ext} value of only 18 kΩ. The path of current flow is longer through the bigger spheroid and it has to cross more cell layers and consequently, it provides also a higher resistance than the smaller spheroid.

But obviously, there are other parameters that influence the impedance of the spheroid-loaded flow channel in this thesis. The microscopic study of the translocation of differently sized spheroids (Fig. 25) indicates that the small spheroids are able to adapt their shape to the dimensions of the narrow channel more easily than larger spheroids. A huge part of the small spheroids was inside the narrowed channel leading to smaller extracellular spaces (and higher R_{ext}) and an increased effective length of the spheroid that had to be crossed by the current. Bigger spheroids showed less tendency for deformation and consequently, the spheroid part inside the narrow channel was significantly smaller (with lower R_{ext}) offering more extracellular space where the current could pass the spheroid.

Another aspect which would explain the lower R_{ext} value of the bigger spheroids could be that they possibly contain more dead cells than the small spheroids due to the nutrition and waste gradients in big spheroids (chapter 1.1.3). Therefore, the ratio of the volume of viable cells to the volume of the whole spheroid is decreasing, which is generally linked to a decrease in R_{ext} (Thielecke et al., 2001).

Nevertheless, the results of the microscopic study clearly indicate that the position of the spheroid in the aperture has an influence on the spheroid impedance. A spheroid that is completely inside the central aperture thus, should lead to a higher impedance than a spheroid that is partly inside the aperture. In all impedance experiments using the flow channel the spheroid sizes are

selected in the way that they are only partly inside the aperture to ensure reproducible experiment conditions. Only in experiments where substances lead to the disintegration of the spheroid and consequently to a reduced spheroid diameter it is possible that the spheroid enters the aperture completely. In this case it might be possible that the high impedance signal, due to the maximal deformation of the spheroid, is overlapping the actually low impedance of the disrupted spheroid.

Impedance Variations Upon Spheroid Repositioning

Repositioning is performed when the solution in the flow channel has to be exchanged during an impedimetric analysis of a spheroid (chapter 5.1.3, 5.3.3). For this purpose, the influence of the repositioning process on the spheroid impedance was investigated. Five spheroids were analyzed performing three repositionings after the initial introduction into the channel.

- The relative error of $|Z|_{rel}$ for the five spheroids ranges between 5 – 26 %.
- The mean relative impedance values of three spheroids measured in FC-2 are not significantly different. The mean relative impedance values of two spheroids measured in FC-3 are also not significantly different.

It is possible to reposition a spheroid for solution exchange without creating too strong deviations in impedance. If extraordinary deviations in impedance occur after repositioning however, this might hint to an irregular spheroid shape. These could lead to differences in spheroid impedance due to a different effective spheroid size that has to be overcome by the current. A strong decrease in impedance after spheroid repositioning could indicate a damage of the spheroid during its removal before repositioning. To avoid such incidents the repositioning has to be performed very cautiously.

Another group also reported of a variance in impedance for identical spheroids. Krinke et al. (2010) performed a similar experiment using their impedance-based microcavity array (chapter 1.3). They measured the same spheroid 15 times and evaluated the corresponding average relative impedance (~ 50 %) observing a standard deviation of ~ 20 %. This would result in a relative error of ~ 40 %.

In the study of this thesis typical relative impedance values were higher ranging

between ~ 300 % and ~ 1000 % and the corresponding standard deviations were ranging between ~ 20 % and ~ 200 %. The relative errors of $|Z|_{rel}$ range between 5 – 26 % and are, thus, smaller than those reported of Krinke et al. (2010).

A general phenomenon in the experiments of this thesis (as well as for the repositioning experiment) is that the impedance values after spheroid introduction are clearly different for different PT-2 flow channels. For this purpose, the results from different channels were evaluated separately in this thesis. The reason for the distinct differences in impedance values could not be resolved. It is assumed that due to hair cracks in the channel bottom, which were seen in all four flow channels (Fig. 32, upper row), the bottom-surface around the aperture was roughened and thereby influenced the deformation of the spheroid into the aperture. Especially FC-2 shows a lot of cracks in comparison to FC-3 and might have resulted in the decreased impedance values. However, in the penetration of the spheroids into the central channel of FC-2, -3 and -4 no distinct differences could be observed (Fig. 32, lower row). The spheroid in FC-1 is the only one that shows a reduced penetration of the narrow channel.

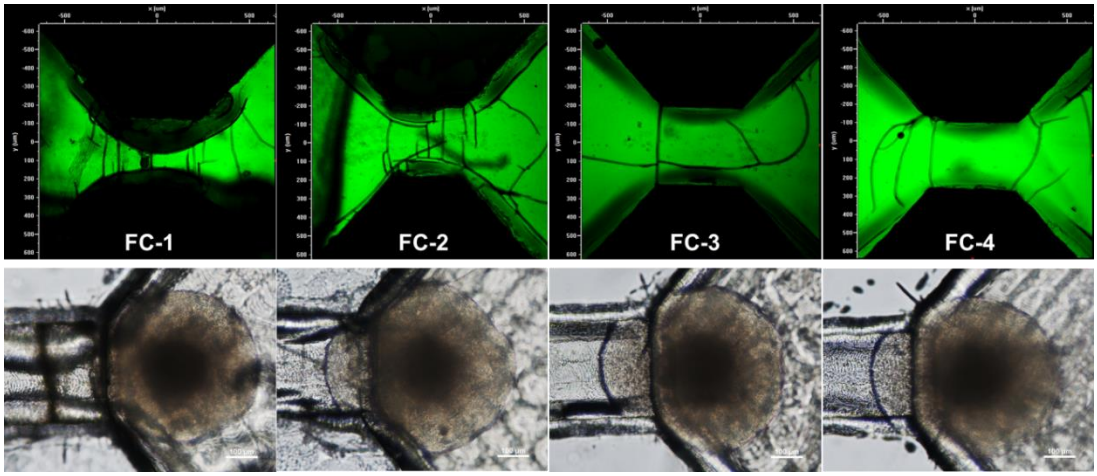

Fig. 32: Confocal fluorescence micrographs of FITC-filled FC-1 – FC-4 showing hair cracks in the base material of the channel. These appear black in front of the green background from the FITC solution. Beneath the respective flow channel images corresponding phase contrast micrographs of 3000 cells/well spheroids are shown that are positioned at the aperture and partly inside the narrowed space.

5.5.3 Visualization of Spheroids in the Flow Channel

A spheroid positioned in the novel channel setup can be imaged with most conventional microscope types used for visualization of spheroids and cell monolayers. The use of transparent electrode and channel materials enables:

- Spheroid observation during an impedance measurement.
- Documentation of spheroid characteristics such as shape and position by phase contrast and epifluorescence micrographs.
- Visualization of internal structures of the spheroid by CLSM, which is however limited (microscopic limitations and channel related challenges).
- Spheroid exposure to excitation light for phototoxicity studies.

Overall, the novel EIS-based flow channel has a lot of advantages discussed in the previous chapters, enabling the sensitive impedimetric readout of 3D multicellular spheroids and the microscopic visualization at the same time.

6 Impedimetric Model Studies with Tumor Spheroids

Morphological alterations of cells upon exposure to external stimuli can be detected sensitively using impedance spectroscopy. This was proven especially for 2D monolayer cells investigated by ECIS technology (Wegener et al., 2000; Stolwijk et al., 2011; Lieb et al., 2016). For 3D multicellular spheroids, however, appropriate EIS measurement devices are still in development (chapter 1.3). In this thesis a novel impedance-based device is introduced (chapter 5) and tested on spheroids.

Distinct morphological alterations are often observed in conjunction with cellular stress, injuries or cell death. In tumor therapy for example, these alterations are induced by potential therapeutic drugs, heat or irradiation. In this thesis the tumor spheroids formed from MCF-7 breast cancer cells (chapter 4.1.1) were used as 3D tissue models to study the morphological alterations upon different invasive external stimuli. First, their morphology and growth behavior is described (chapter 6.1). These characteristics are important information to generate spheroids with reproducible size being conform to the PT-2 flow channel geometries (chapter 5.1.1). In the following, proof-of-concept studies were performed using the new EIS-device investigating the response of MCF-7 spheroids to different stimuli with well-known effect. Upon exposure of spheroids to a chemical cross-linker (chapter 6.2), a detergent (chapter 6.3), buffers with different osmolarities (chapter 6.4) or an actin filament polymerization inhibitor (chapter 6.5) the spheroid morphology and structure is significantly altered. This way, dead spheroids with intact structure, spheroids with damaged membranes, swollen/shrinked spheroids and spheroids with disrupted actin filaments could be studied. Furthermore, the tumor spheroids were subjected to two cancer treatment therapies investigating the effect of hyperthermia (chapter 6.6) and photodynamic therapy (chapter 6.7).

The spheroidal response to the different stimuli was analyzed using impedance measurements as well as supplementary microscopic images, impedance measurements on cell monolayers or biochemical endpoint assays like the Presto

Blue® assay. Comparing the results of these additional methods the sensitivity and applicability of the newly designed device was evaluated.

6.1 Growth Behavior of Breast Cancer Spheroids

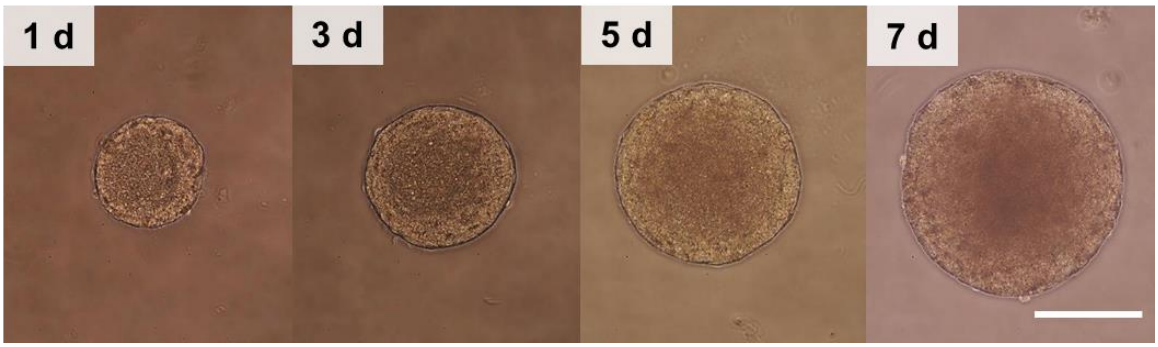

Fig. 33: Phase contrast photographs of a MCF-7 spheroid (1000 cells/well) shown at 1 / 3 / 5 / 7 d after seeding (scale bar: 200 µm).

MCF-7 spheroids can be prepared easily in different defined sizes following the protocol in chapter 4.1.5. In order to be applicable for the novel setup, it is important to prepare spheroids small enough to fit into the flow channel and big enough to be held back at the central aperture. The size of the spheroid can be controlled by the seeding density and the growth time before the experiment. To determine the optimum seeding density and growth duration, MCF-7 spheroids were prepared with seeding densities between 1000 – 6000 cells/well and their growth was documented by phase contrast images over seven days. As can be seen in Fig. 33 the MCF-7 spheroids exhibit already on the first day after seeding a round smooth shape and they increase in diameter over time.

The diameter of eight spheroids per seeding density and day was determined as described in chapter 4.1.6 and shown in Fig. 34 A. For each seeding density and growth duration spheroids with characteristic diameters formed. MCF-7 spheroids show a linear growth behavior over seven days. A linear fit was applied to the growth curves of each seeding density and the respective slopes, reflecting the change in diameter per day, were plotted against the seeding densities (Fig. 34 B).

The change in diameter per day is linearly decreasing for seeding densities between 1000 cells/well (daily growth of 33.3 ± 0.5 µm/d) and 4000 cells/well (27.0 ± 0.9 µm/d) but levels off for higher seeding densities (5000 and 6000 cells/well: 26 ± 1 µm/d), showing that smaller spheroids grow faster than bigger spheroids.

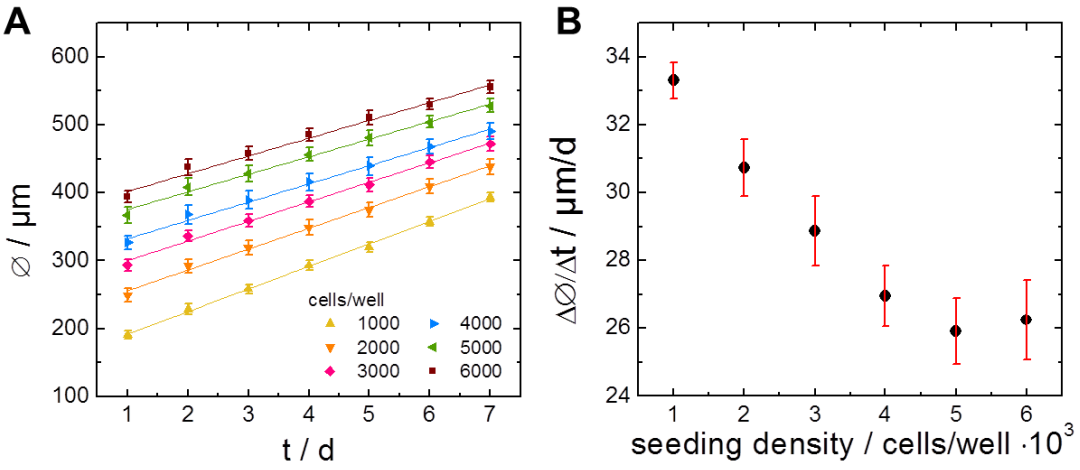

Fig. 34: Growth study of MCF-7 spheroids from different seeding densities (1000 – 6000 cells/well) documented over seven days (mean ± SD, n = 8) (**A**). From this data the spheroid growth per day was determined for all six seeding densities (mean ± SE, n = 7) (**B**).

6.2 Impedimetric Analysis of Cross-Linked Spheroids

Apoptosis and necrosis are the types of cell death most researchers are familiar with. Another not so well-known type of cell death is the cornification in mammalian skin. The epidermis as uppermost compartment of the skin providing a barrier against the environment is formed by multiple layers of terminally differentiated, dead keratinocytes. The process of epidermal differentiation begins with the migration of viable, proliferating keratinocytes from the basal layer of epidermis through a granular layer where the plasma membrane is replaced by a cornified cell envelope. This envelope is formed by a mixture of proteins on the cell surface that are cross-linked by transglutaminases and surrounded by a lipid envelope. The endpoint of differentiation is achieved in the cornified uppermost layer of the skin containing dead keratinocytes with widely intact cell structure (Candi et al., 2005). In order to model such a cell state artificially, cells can be chemically cross-linked. Cross-linking or fixation of cells and tissues is a standard

cytochemical method performed to preserve the cellular morphology for subsequent fluorescence stainings or histochemical preparations. Aldehydes like glutaraldehyde or paraformaldehyde are often used fixation chemicals, which lead to a cross-linking of the proteins within the biological sample. During this process the structures within the sample are stabilized and ongoing biochemical reactions are terminated (Ganjali and Ganjali, 2013). This way, the cells in the sample are mortified but their internal structure is preserved and reflects a snap-shot of the cell status at the moment of fixation.

In this thesis the concentration-dependent fixation of a spheroid was performed to study the impedimetric signal change upon different stages of spheroidal fixation with the novel setup. For these experiments paraformaldehyde was used as chemical cross-linker. In standard protocols a 4 % (w/v) solution of PFA is used to perform a complete fixation of tissue/cells within hours/minutes. Moreover, dilutions of PFA were prepared (0.01 – 0.5 %) to generate spheroids in different stages of incomplete fixation. Subsequently, the prepared spheroids were analyzed by impedance spectroscopy in culture medium (chapter 4.3.5.2). Impedance measurements at multiple frequencies (MFT) over ~ 45 min as well as high time resolution measurements (RTC) at 200 Hz for 5 min were performed and supported by microscopic images taken during the measurements.

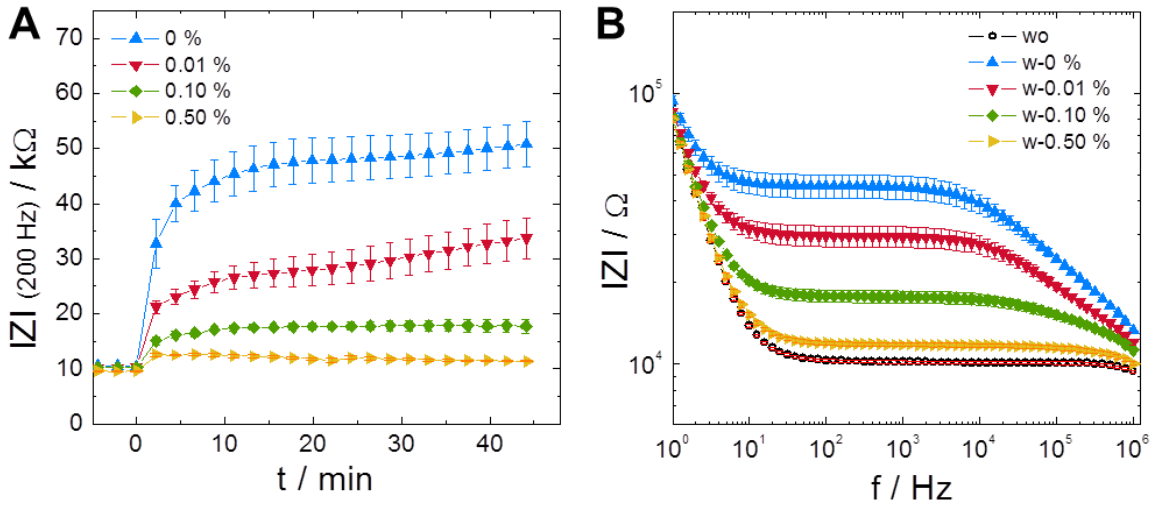

Fig. 35: MFT results for cross-linked spheroids. Time course of impedance magnitude at 200 Hz for spheroids that were pre-incubated with different PFA concentrations (0 / 0.01 / 0.1 / 0.5 %) for 1 h (mean ± SE, n ≥ 4) (**A**). Impedance spectra of individually cross-linked spheroids at t = 30 min after insertion into the flow channel (mean ± SE, wo: n = 24, w: n = 6) (**B**). T = 37 °C.

In Fig. 35 the resulting time course (A) at a sampling frequency of 200 Hz and the respective impedance spectra (B) recorded by MFT measurements are shown. Both plots clearly demonstrate that the spheroid impedance is decreasing for increasing concentrations of PFA and consequently, increasing percentage of fixation. While the control spheroid reaches an average impedance value of 49 ± 4 kΩ, the spheroids which were pre-incubated with increasing concentrations of PFA (0.01 / 0.1 / 0.5 %) only reach 30 ± 3 kΩ, 17.8 ± 0.9 kΩ and 11.7 ± 0.2 kΩ, respectively (average impedance values at t = 30 min and 200 Hz).

For a better understanding of the impedance decrease upon fixation, the equivalent circuit derived for spheroids in the flow channel containing the spheroid parameters R_{ext}, R_{int} and A_{sph} (chapter 3.2) was fitted to the experimental data for the control condition and the spheroids with increasing levels of cross-linking (Tab. 13). The values for R_{ext} and R_{int} are strongly decreasing for increasing cross-linking from 36 ± 5 kΩ to 2.2 ± 0.2 kΩ and 4.7 ± 0.8 kΩ to 0.6 ± 0.2 kΩ, respectively. The spheroid capacitance A_{sph} is slightly increasing for increasing cross-linking.

Tab. 13: Overview of the spheroid parameters R_{ext}, R_{int} and A_{sph} for spheroids incubated with 0 / 0.01 / 0.1 / 0.5 % PFA. Spectra, 30 min after spheroid introduction into the flow channel were fitted as described in chapter 4.3.3 using the following parameter values: A_{el} = 2.1/2.3/ 2.0·10^{-6} Fs^{n-1}cm^{-2}, n_{el} = 0.96, R_{bulk} = 9.7/10/9 kΩ, A_{para} = 4·10^{-12} Fs^{n-1}cm^{-2}, n_{para} = 0.98, n_{sph} = 0.75 (mean ± SE, n = 6).

c(PFA) / %	***0***	***0.01***	***0.1***	***0.5***
R_{ext} / kΩ	36 ± 5	20 ± 3	8.1 ± 0.8	2.2 ± 0.2
R_{int} / kΩ	4.7 ± 0.8	3.3 ± 0.5	2.0 ± 0.3	0.6 ± 0.2
A_{sph} / ·10^{-9} Fs^{n-1}cm^{-2}	2.0 ± 0.2	2.7 ± 0.1	2.9 ± 0.2	4.6 ± 0.6

RTC measurements were performed to investigate the influence of cross-linking on cell shape dynamics (micromotion) within spheroids. Typical results for two spheroids for each PFA concentration are shown in Fig. 36. The viable control spheroids show distinct super- and subordinate fluctuations (A). For the time course of detrended impedance, shown in dark blue, the superordinate

fluctuations are in the range of -50 to 50 Ω, whereas the subordinate fluctuations are below 25 Ω. The spheroids which were exposed to 0.01 % PFA (B) still show both types of fluctuations but with a significantly lower amplitude of the superordinate fluctuations compared to the control.

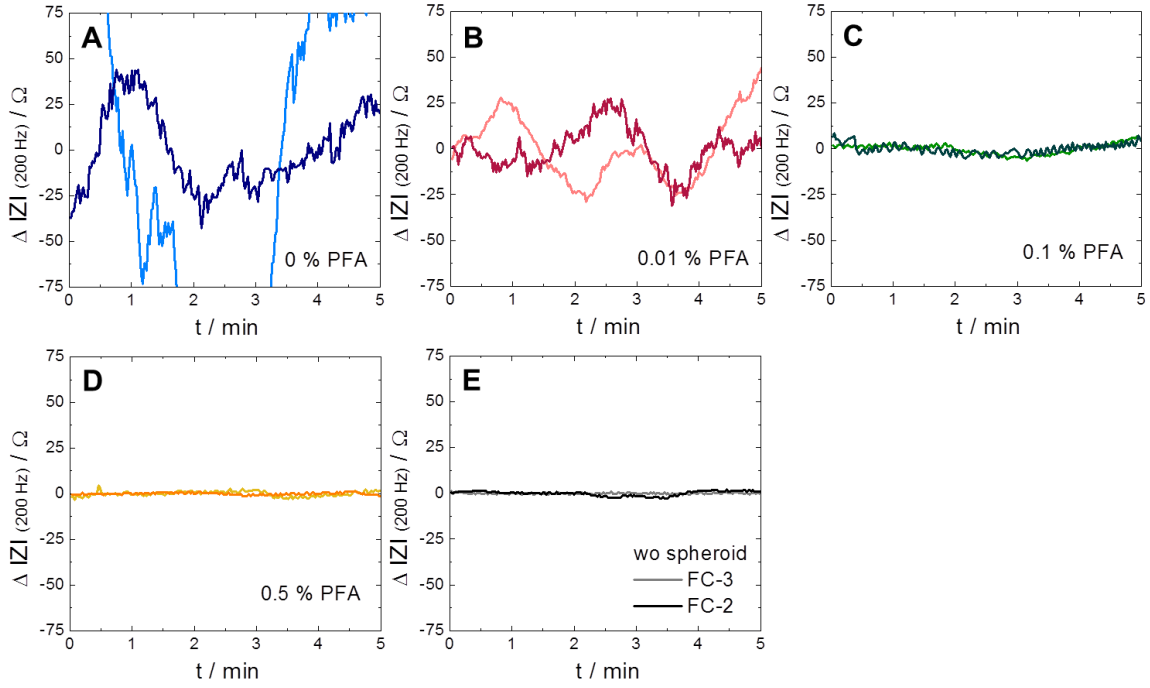

Fig. 36: Typical detrended RTC data at 200 Hz for two spheroids respectively that were pre-incubated with 0 % (**A**), 0.01 % (**B**), 0.1 % (**C**) and 0.5 % PFA (**D**) for 1 h and the medium-filled FC-2/-3 without spheroid (**E**). T = 37 °C.

Spheroids pre-incubated with 0.1 % PFA show no distinct superordinate fluctuations and subordinate fluctuations similar to spheroids treated with 0.01 % PFA (C). Spheroids that were almost completely cross-linked with 0.5 % PFA show no superordinate and very weak subordinate fluctuations (D) similar to the time course of the medium-filled channels without spheroids (E). The numerical analysis of the level of fluctuations is typically performed by evaluation of the power spectrum (fast Fourier transform), the variance or the variance of increments (Lo et al., 1993; Opp et al., 2009). Typical power spectra for a flow channel without spheroid and loaded with an untreated, viable spheroid are shown in Fig. 37. Upon linear fitting the slope of the power spectrum can be determined which is reported to provide information on the viability of the cells. Opp et al. (2009) observed a change in the power slope from -2.9 for untreated

monolayer cells to -2.0 for cells exposed to the toxin cytochalasin B (10 µM). An evaluation of the power spectra presented below results in a slope of -1.7 for a spheroid-free channel and -2.1 for the control spheroid confirming the reported trend for 3D tissue models as well. However, evaluation of power spectra of partly cross-linked spheroids did not show any characteristic changes. Therefore, analysis of power spectra was not pursued in this thesis any further.

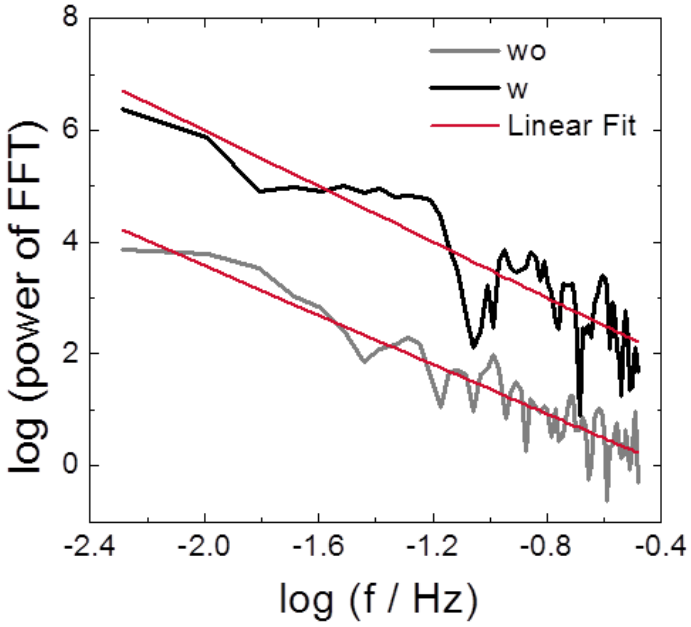

Fig. 37: Typical power spectra determined by fast Fourier transformation of the time courses of impedance (RTC data) for the flow channel without a spheroid (wo) and a viable spheroid (0 % PFA). The red lines represent the respective linear fits with a slope of -1.7 for the spheroid-free flow channel and a slope of -2.1 for a spheroid-loaded flow channel.

As an alternative evaluation method the *analysis of variance after segmented detrending of normalized data* was performed. The raw data was first normalized by subtracting the time average impedance from every data point. The normalized data was then split in data sets of 16 s time intervals. The data within these sets was then linearly detrended. The detrending process was essential to eliminate the strong drifting of the impedance, which was observed in the majority of the RTC experiments. By performing the detrending for segmented data sets (Fig. 38 A) and not for the whole data set the superordinate fluctuations were eliminated as well (B). From the resulting time course the variance of impedance was determined and averaged over all data subsets. The whole process of

evaluation was repeated with time intervals of 32 s and 64 s in order to obtain an impression of the fluctuations on different time scales. This way, the variances V_{16}, V_{32} and V_{64} were determined for the RTC data of all cross-linking experiments (C). The results for the three different time intervals all show a decrease in variance for increasing levels of spheroid cross-linking. But they differ with respect to the absolute variances. The bigger the time interval the higher are the variances.

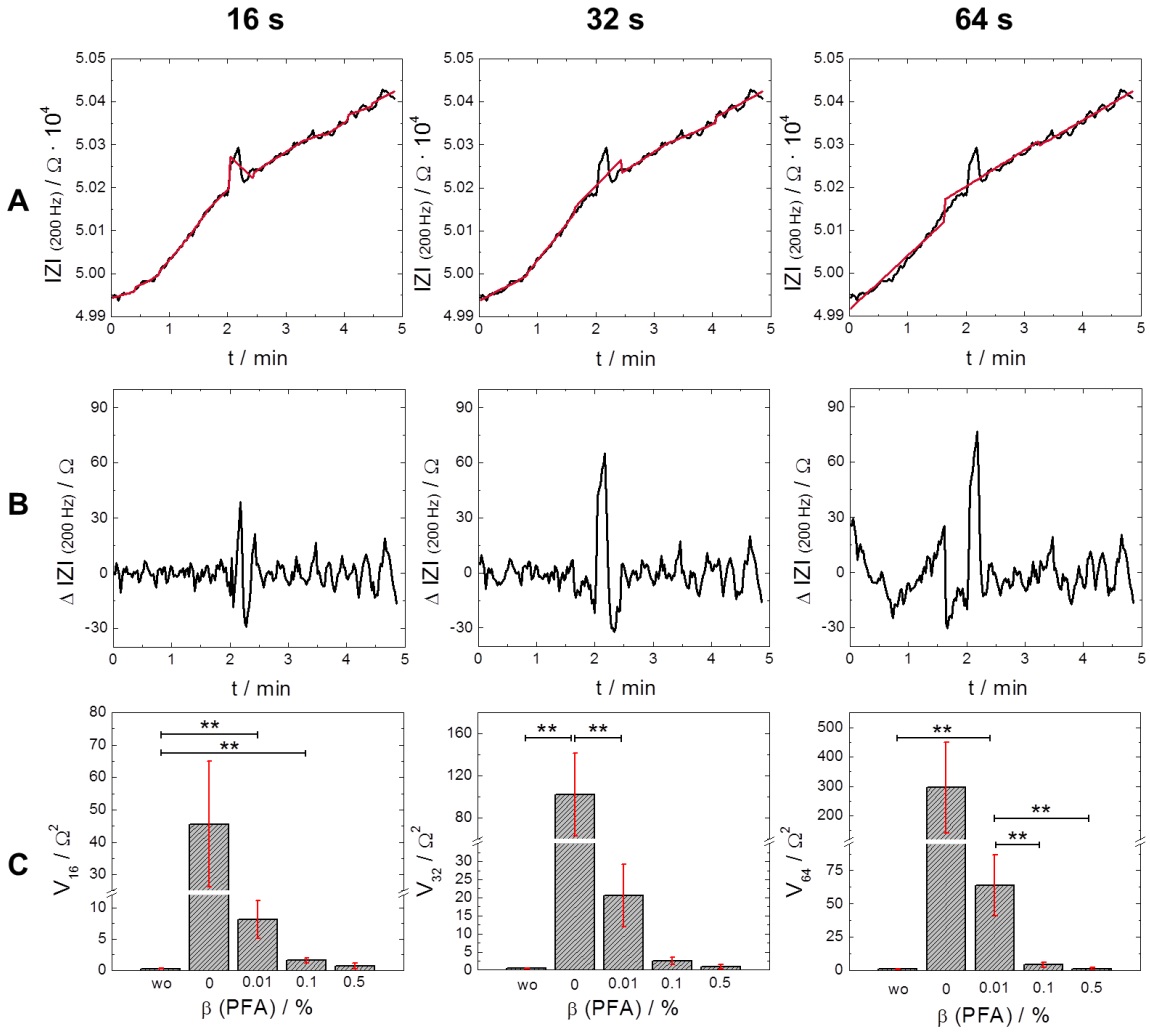

Fig. 38: Overview of data processing from raw data via detrended datasets to a quantification of impedance fluctuations. The strongly drifting raw data is split in different time intervals (16 s, 32 s or 64 s) (**A**) and data within these sets is linearly detrended (**B**). Subsequent calculation of the resulting variance was performed. The variance of each experimental condition was determined for the three time intervals (V_{16}, V_{32} and V_{64}) (mean ± SE, n ≥ 5) (**C**). Significance was determined by a two-sample t-test using a significance level of 0.05 (**).

Using a time interval of 32 s resulted in variances showing a significant difference between the control spheroid (0 % PFA) and the spheroid-free channel (wo) as well as between the control and these spheroids that were exposed to different concentrations of PFA. Thus, in future evaluations of RTC data results are shown and described only by the parameter V_{32} with the intermediate time interval of 32 s.

The flow channel without spheroid shows only electrical noise and has therefore a very small variance of (0.4 ± 0.1) Ω^2 (Fig. 38 C V_{32}). The flow channel with an intact viable spheroid at the aperture shows distinct fluctuations with a variance of (122 ± 38) Ω^2. For spheroids with increasing level of cross-linking the variance decreases to (21 ± 9) Ω^2 (0.01 % PFA), (3 ± 1) Ω^2 (0.1 % PFA) and (0.9 ± 0.6) Ω^2 (0.5 % PFA), respectively. These results indicate a dose-dependent influence of PFA on the micromotion of spheroids.

The spheroids in this study were observed throughout the impedance measurement using the digital microscope. Fig. 39 shows typical images of spheroids that were pre-incubated with 0 / 0.01 / 0.1 / 0.5 % PFA and photographed directly after the introduction into the flow channel (A) and at the end of the measurement (B).

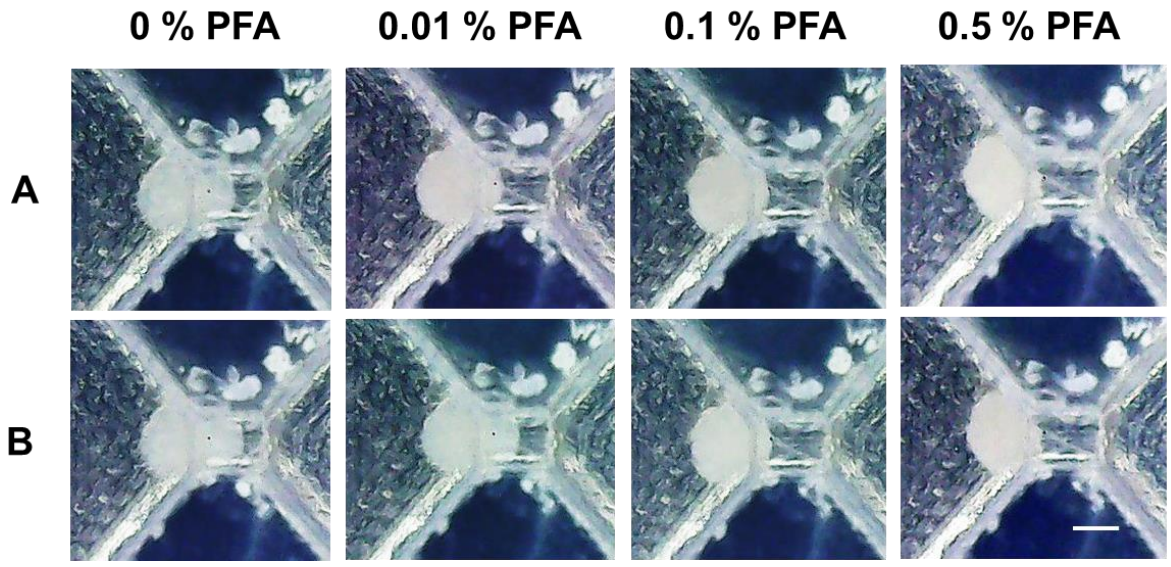

Fig. 39: Images of four representative spheroids at the aperture of the channel after pre-incubation with 0 / 0.01 / 0.1 / 0.5 % PFA for 1 h. The images were taken right after spheroid introduction in the channel (**A**) and at the end of the measurement (~ 45 min after introduction) (**B**) using the digital microscope (scale bar: 250 µm). T = 37 °C.

The pre-incubated spheroids penetrate into the central opening to different degrees after introduction into the channel (A). The control spheroid occupies almost half of the entire channel. The spheroid with the lowest level of fixation (0.01 % PFA) still fills approximately a fourth of the channel volume and with increasing level of fixation (0.1 and 0.5 % PFA) the portion of the spheroid penetrating the channel decreases. Within ~ 45 min (B) the control spheroid and the 0.01 % PFA spheroid move deeper into the channel (approx. to the center), whereas for the highest level of fixation no migration is observable.

6.3 Impedimetric Analysis of Permeabilized Spheroids

One of the hallmarks of necrotic cell death is the loss of cell membrane integrity (Edinger and Thompson, 2004; Ouyang et al., 2012). This drastic dysfunction of a structural key element of every cell should be emulated using spheroids and measure these with the novel EIS channel. In order to mimic different stages of membrane permeabilization, spheroids were exposed to different concentrations of the detergent saponin. Saponins are a group of amphipathic glycosides which is widely distributed in higher plants. A characteristic of different saponins is the soap-like foam production (Sparg, 2004) and the ability to form a complex with cholesterol in the cell membrane resulting in pore formation and consequently in cell permeabilization (Podolak, 2010).

The effect of saponin on spheroids was first analyzed via PrestoBlue® assays to determine the invasiveness of different saponin concentrations. Then, impedimetric measurements were performed on spheroids with different degrees of permeabilization.

PrestoBlue® Assay Results

A cell viability assay was performed and evaluated as described in chapter 4.1.8 to investigate the effect of nine different saponin concentrations (0.01 – 1 ‰ (w/v), 4 h, at 37 °C) on spheroid viability (Fig. 40). An EC_{50} value of **(0.17 ± 0.01) ‰** (mean ± SE, n = 3) was determined.

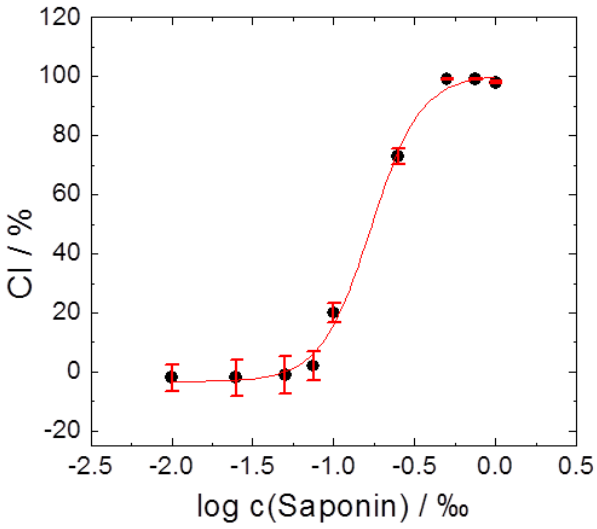

Fig. 40: Typical dose response curve showing the cytotoxicity index (CI) in dependence of the mass concentration β of saponin for one out of three independent experiments (n ≥ 5). The total EC_{50} was determined to (0.17 ± 0.01) ‰. T = 37 °C.

Impedimetric Analysis

The spheroids were pre-incubated for 4 h with different concentrations of saponin (0 – 0.25 ‰) and measured as described in chapter 4.3.5.3. Five individual measurements were performed using the channels FC-1, -3 and -4. The results of one typical measurement series for the five different concentrations are shown in Fig. 41 (appendix A2, Fig. S4).

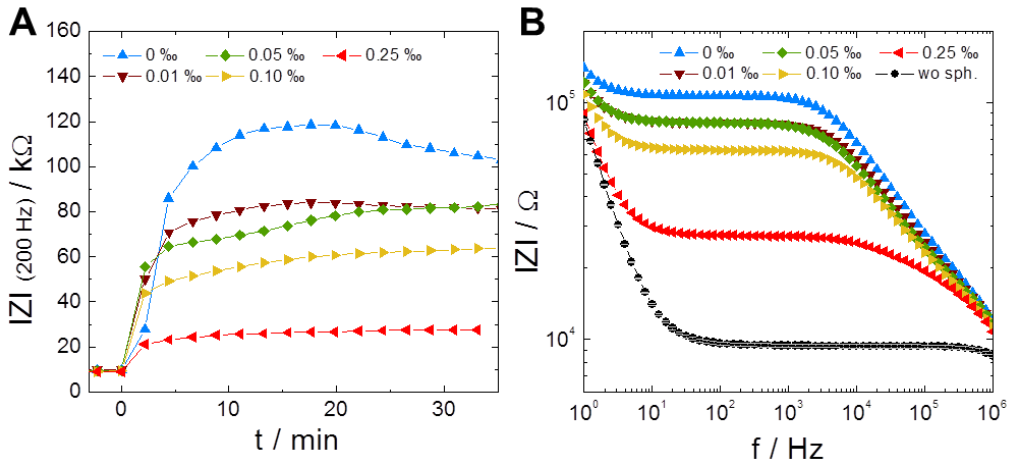

Fig. 41: Typical results for gradually permeabilized spheroids measured in FC-3. Time course of impedance magnitude at 200 Hz (**A**) and corresponding impedance spectra at t = 30 min (**B**) for spheroids after pre-incubation with different saponin concentrations (0 ‰ – 0.25 ‰) for 4 h. Spectra of the spheroid-free channels (wo) immediately before spheroid introduction at t = 0 min were also averaged (mean ± SE, n = 5). T = 37 °C.

As can be seen in the time course (A) as well as in the impedance spectra (B) the control spheroid shows the highest impedance change upon insertion into the channel, followed by the spheroid pre-incubated with the lowest saponin concentration (0.01 ‰). This is observed in all five measurements. In the example presented in Fig. 41 the spheroid exposed to 0.05 ‰ saponin shows a slightly lower impedance change upon introduction into the channel than the 0.01 ‰ spheroid in the first 10 min, followed by an increase in impedance until both impedance signals reach the similar level of ~ 80 kΩ. This behavior is not consistent across all measurements. In three cases the impedance increase after exposure to 0.05 ‰ levels off between values of the 0.01 ‰ spheroid and the 0.1 ‰ spheroid and in one case the impedance change measured for the 0.05 ‰ spheroid is slightly lower than compared to the 0.1 ‰ spheroid. The spheroid that was incubated with the highest saponin concentration (0.25 ‰) shows the lowest impedance change in the measurement presented here. In two other measurement series the spheroids pass almost immediately the narrowed aperture of the channel, and this leads to impedance values of a spheroid-free channel. In two further cases the impedance first increases to impedance values higher than that of the 0.1 ‰ spheroid and slowly decreases afterwards.

Tab. 14: Overview of spheroid parameters R_{ext}, R_{int} and A_{sph} determined from spheroids pre-incubated with saponin concentrations of 0 / 0.01 / 0.05 / 0.1 / 0.25 ‰ (w/v). Spectra, recorded 30 min after spheroid introduction in FC-3/-4 were fitted as described in chapter 4.3.3 using the following parameter values: A_{el} = 2.3/2.2/2.15·10^{-6} $Fs^{n-1}cm^{-2}$, n_{el} = 0.95/0.94/0.95, R_{bulk} = 9.7/9.7/10.6 kΩ, A_{para} =4.9/4.0/4.0·10^{-12} $Fs^{n-1}cm^{-2}$, n_{para} = 0.98, n_{sph} =0.75 (mean ± SE, n ≥ 2).

β (saponin) / ‰	***0***	***0.01***	***0.05***	***0.10***	***0.25***
R_{ext} / kΩ	98 ± 3	70 ± 3	51 ± 10	39 ± 8	21 ± 3
R_{int} / kΩ	5.4 ± 0.5	4.5 ± 0.4	4.3 ± 0.2	3.1 ± 0.3	4 ± 2
A_{sph} / ·10^{-9} $Fs^{n-1}cm^{-2}$	2.4 ± 0.1	2.6 ± 0.1	2.6 ± 0.1	2.6 ± 0.1	1.9 ± 0.5

An evaluation of the three spheroid parameters shows a constant decrease of R_{ext} for increasing concentrations of saponin (Tab. 14). The decrease of R_{int} is, however, less distinct and shows similar values for spheroids that were treated

with 0.01 ‰ and 0.05 ‰. For the 0.25 ‰ spheroids the value is even higher than that of 0.10 ‰ spheroids. The non-ideal spheroid capacitance A_{sph} is approximately constant for spheroids treated with 0.01 – 0.10 ‰ saponin and slightly increases compared to the control spheroid. The highest saponin concentration shows a lower capacitance than the control spheroid.

The images taken from spheroids during the impedimetric measurements do not show reproducible differences with respect to penetration depth or spheroid size for saponin concentrations between 0.01 ‰ and 0.1 ‰. However, spheroids incubated for 4 h in 0.25 ‰ saponin show a reduced diameter (Fig. 42; B1, B2.1) in comparison to control spheroids (Fig. 42; A1, A2) in all replicates. This size reduction leads in some cases to the complete migration of the spheroid into the narrowed space of the aperture (B2.2).

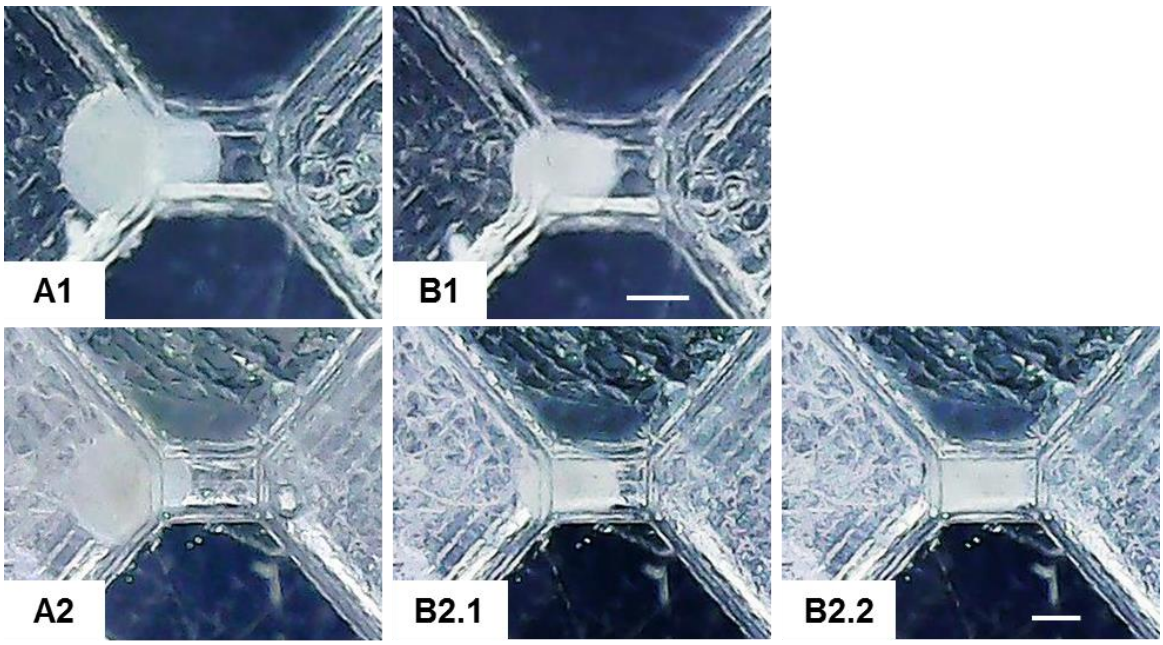

Fig. 42: Typical micrographs of two control spheroids (**A1**, **A2**) and two spheroids which were pre-incubated with 0.25 ‰ saponin for 4 h and photographed directly after introduction in the flow channel (**B1**, **B2.1**) and at the end of the experiment (**B2.2**) (scale bars: 250 µm). T = 37 °C.

In order to enable a comparison with the results of the PrestoBlue® assay, an EC_{50} value was determined from the impedance measurements of spheroids exposed to saponin. For this purpose, the impedance values for each condition were extracted at t = 30 min and $\Delta|Z|_{norm}$ values were calculated from these

impedances using the equation: $\Delta|Z|_{norm} = 1 - (|Z|_{x‰} / |Z|_{0‰})$. The $\Delta|Z|_{norm}$ values were plotted against the log of the saponin mass concentrations (Fig. 43) and the dose response fit (chapter 4.1.8, Eq. 4.2) was used to evaluate the EC_{50} values of the five measurements. The average EC_{50} value was determined to be **(0.10 ± 0.02) ‰** (mean ± SE, n = 5).

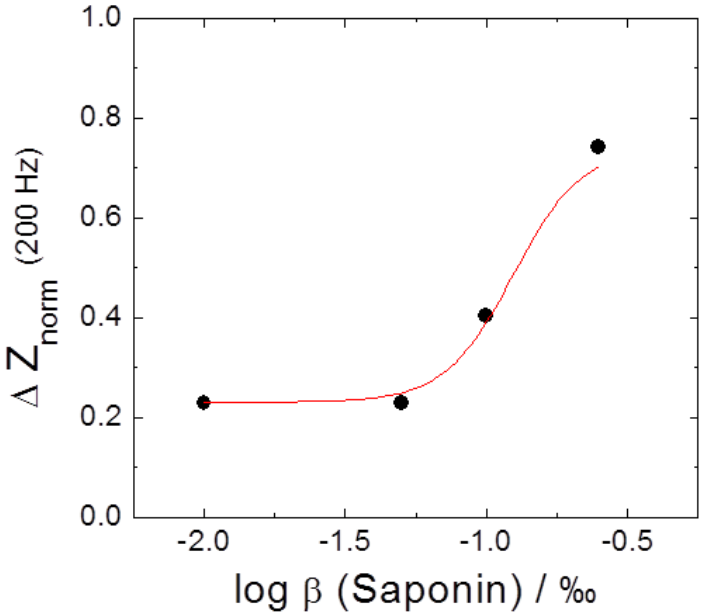

Fig. 43: Typical dose response curve according to the impedance data shown in Fig 41. The average EC_{50} of five individual experiments was determined to be (0.10 ± 0.02) ‰. T = 37 °C.

As can be seen in the exemplary dose response curve (Fig. 43) the fit was applied to only four data points. Generally, it would be better to have more data points to get a more reliable fit. In this case however, it was temporally not possible to test more saponin concentrations within one measurement series as the incubation and sequential measurement of each condition was very time consuming.

Additionally, high time resolution measurements were analyzed to investigate if different levels of spheroid permeabilization have an effect on the spheroid's internal dynamics and micromotion. Typical data for each condition is shown in Fig. 44 revealing no clear dependency of micromotion activity on the level of permeabilization.

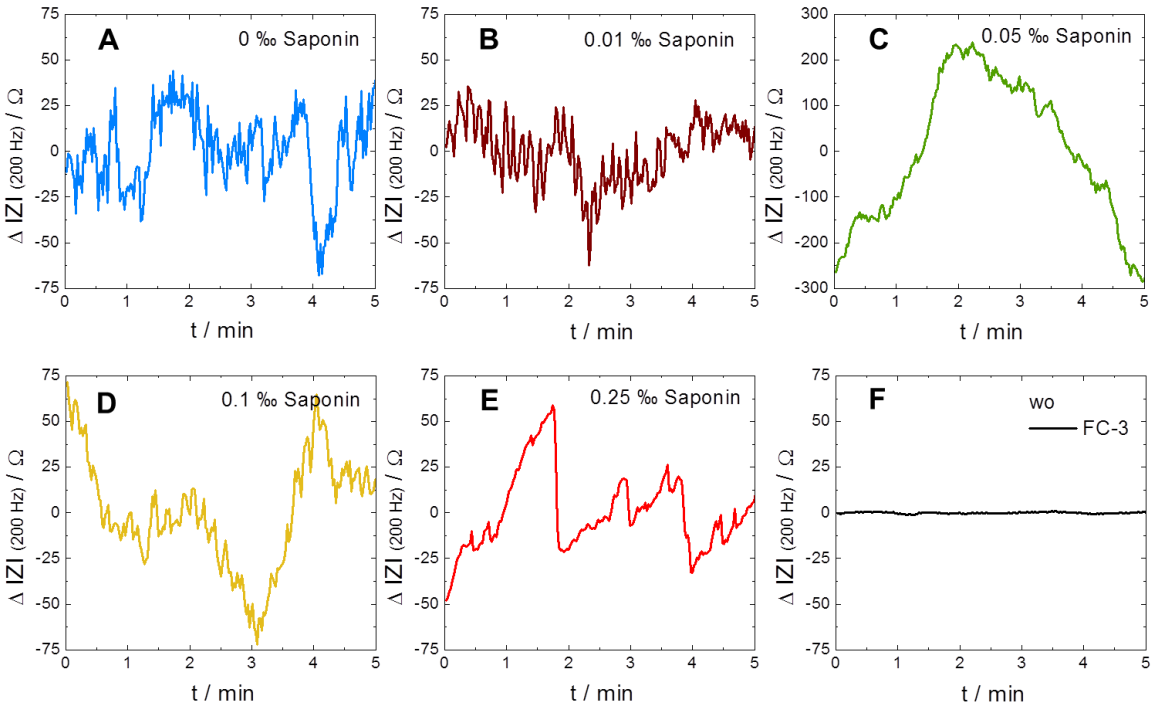

Fig. 44: Typical detrended RTC data at 200 Hz for spheroids that were pre-incubated with 0 ‰ (**A**), 0.01 ‰ (**B**), 0.05 ‰ (**C**), 0.1 ‰ (**D**) and 0.25 ‰ saponin (**E**) for 4 h and the medium-filled FC-3 without spheroid (**F**). T = 37 °C.

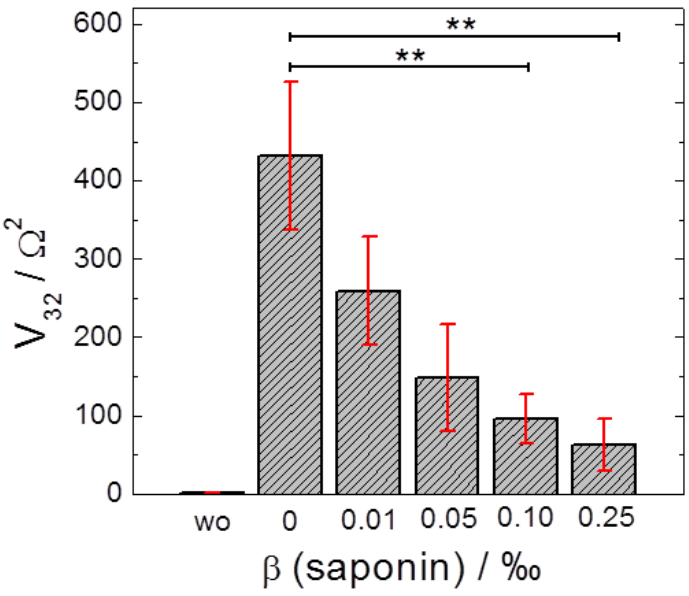

Fig. 45: Variance of the impedance fluctuations after segmented detrending of spheroids treated with four different saponin concentrations (0.01 – 0.25 ‰) for 4 h, a control spheroid (0 ‰) and the channel without spheroids (wo) (mean ± SE; n = 4). Significance was determined by a two-sample t-test using a significance level of 0.05 (**).T = 37 °C.

However, a variance analysis (Fig. 45) shows a decreasing variance for spheroids with increasing levels of permeabilization, approaching the variance of a spheroid-free channel (wo). A two-sample t-test shows that there is only a significant difference between the variances of control spheroids and spheroids exposed to 0.10 and 0.25 ‰ saponin.

In summary, it can be stated that MCF-7 spheroids in different stages of permeabilization can be distinguished by impedance analysis using the new EIS device. This type of analysis furthermore produces results comparable to those of a standard cell viability assay but without the use of labels.

6.4 Study of Spheroids Under Osmotic Pressure

Necrosis and apoptosis are two mechanisms of cell death that differ in characteristic morphological hallmarks (Fig. 46). Necrosis induces cell swelling, organelle dysfunction and cell lysis, whereas apoptosis is characterized by cell shrinkage, nuclear condensation and fragmentation as well as the formation of apoptotic bodies (Ouyang et al., 2012).

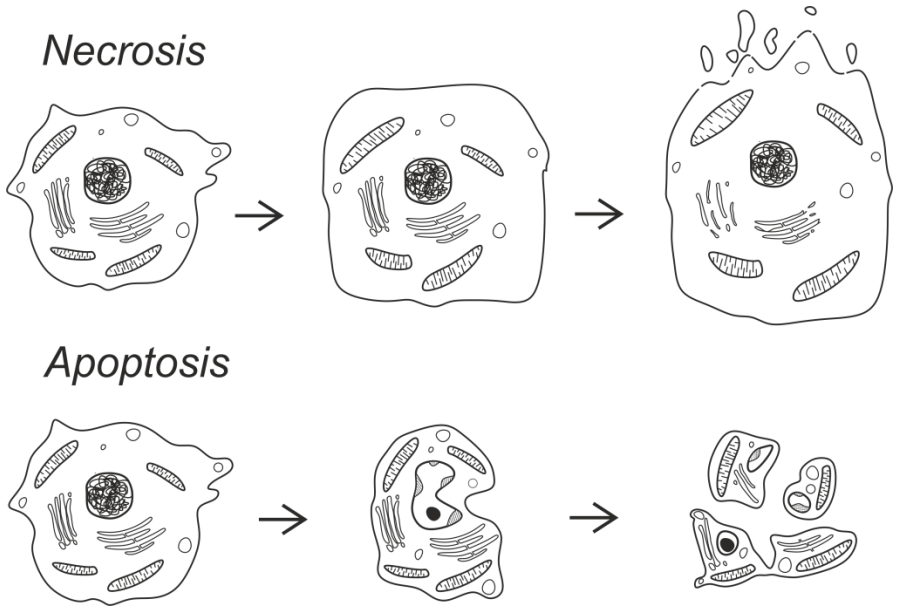

Fig. 46: Schematic of general morphological alterations of a cell going through necrosis or apoptosis. Necrotic cells undergo swelling, organelle dysfunction and breakdown of the plasma membrane. Apoptotic cells go through cell shrinkage, nuclear condensation and fragmentation as well as the formation of apoptotic bodies.

In order to mimic necrotic or apoptotic cell death in a spheroid, the shrinking and swelling as early characteristics of cell death were induced by bringing the spheroid into a hyper- or hypotonic environment. The spheroidal response to changing osmotic pressure was first observed microscopically and then measured with the novel impedimetric channel setup.

Microscopic Analysis of Spheroid Shrinking and Swelling

The extent of shrinking and swelling of spheroids was investigated microscopically as explained in chapter 4.2.4. The change in spheroid diameter was plotted against the observation time (Fig. 47). First, the spheroid was brought in isoosmotic buffer for a few minutes. At t = 0 min the buffer was exchanged by a hypoosmotic (~ 190 mOsmol/kg) or hyperosmotic buffer, I (~ 430 mOsmol/kg) or II (~ 530 mOsmol/kg). Control spheroids were observed in isoosmotic buffer (~ 310 mOsmol/kg) showing a slow and weak decrease in spheroid diameter over 30 min by (17 ±3) µm. This shrinkage may be attributed to the slow cooling of the spheroid in the experimental setup. Spheroids were placed on a heated holder with an average temperature of ~ 35 – 36 °C but the petri dish with buffer and spheroid was not closed by a lid.

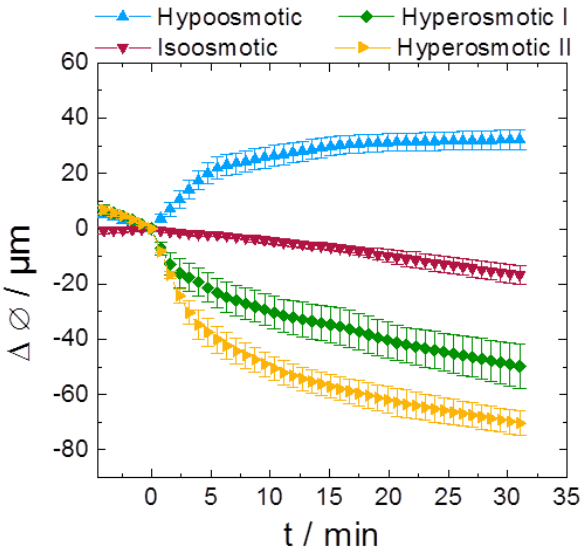

Fig. 47: Change in spheroid diameter Δ Ø over time when exposed to buffers with different osmolarity. The spheroid diameter was first determined in isoosmotic buffer. At t = 0 min the buffer was exchanged by hypo-/hyper- I/hyperosmotic II buffer and the swelling or shrinking of the spheroids was documented with phase contrast photographs over ~ 30 min (mean ± SE, n = 4). Spheroids were also observed in isoosmotic buffer over time as control (mean ± SE, n = 3).

Incubation of spheroids in the hypoosmotic buffer led to an immediate swelling, reflected by a fast increase in diameter by (22 ± 4) µm in the first 5 min followed by a continued slow increase. After 30 min the spheroid diameter is (32 ± 4) µm bigger than the initial value. The low osmolarity leads to the influx of water into the cells of the spheroid, which causes the swelling.

When the spheroids were incubated with the two hyperosmotic buffers, an immediate shrinking was observed, which is reflected by the decrease in spheroid diameter. Furthermore, the degree of shrinking is dependent on the osmolarity of the hyperosmotic buffers. After 30 min of incubation spheroids in hyperosmotic buffer I (~ 430 mOsmol/kg) show a decrease in diameter by (50 ± 8) µm, whereas spheroids in buffer II (~ 530 mOsmol/kg) show a stronger decrease by (70 ± 4) µM. With increasing extracellular osmolarity the efflux of water from the cells of the spheroid into the buffer was increased leading to the shrinking of the whole spheroid.

Impedimetric Analysis

The swelling and shrinking of spheroids in the extracellular buffers with different osmolarities was then analyzed using the novel impedimetric setup following the descriptions in chapter 4.3.5.4. For these experiments the spheroids were not pre-incubated in isoosmotic buffer but introduced into the flow channel filled with the respective buffer. The conductivity of each buffer was adjusted to the value of the control and caused a baseline impedance (wo spheroid, at 200 Hz) of ~ 17 kΩ. The measurements were performed using FC-1/-2/-3 and time courses are shown separately for results obtained in FC-3 (Fig. 48 A) and FC-1/-2 (Fig. 48 B). Spheroids in the hypoosmotic buffer show the highest impedance (t = 30 min; A: (340 ± 60) kΩ, B: (74 ± 3) kΩ), spheroids in isoosmotic buffer an intermediate impedance (t = 30 min; A: (128 ± 5) kΩ, B: (59.5 ± 0.5) kΩ) and spheroids in hyperosmotic buffer I and II the lowest impedance (t = 30 min; A: (85 ± 5) kΩ, (61 ± 2) kΩ, B: (47.4 ± 0.8) kΩ, (39 ± 2) kΩ). In short, the spheroid impedance decreased for increasing osmolarity. In Fig. 48 B the trend is the same but all spheroid impedances are shifted to lower values. This phenomenon was already discussed (chapter 5.5.2) and is assumed to be based on the individual surface morphology of the flow channels.

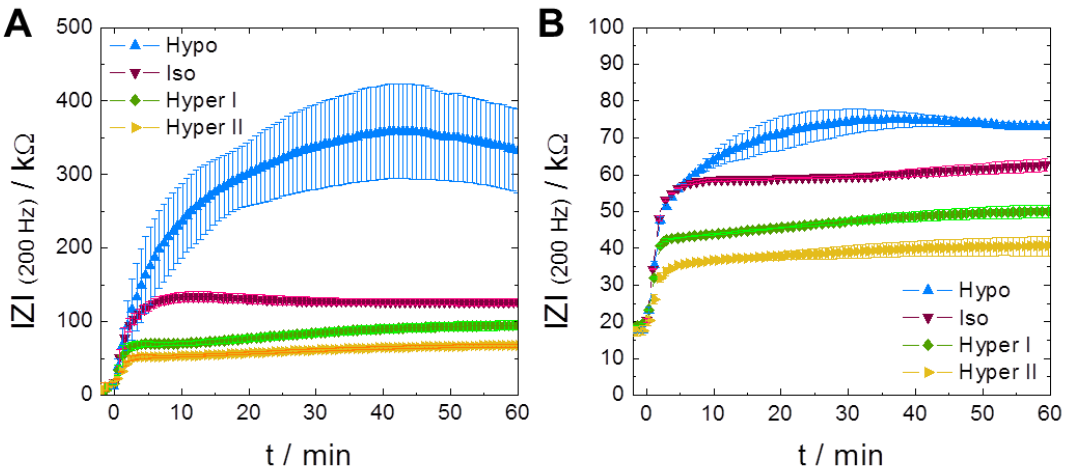

Fig. 48: Time courses of the impedance magnitude IZI at 200 Hz for spheroids measured in hypo- / iso- / hyper-I / hyper-II osmotic buffer in FC-3 (mean ± SE, n = 3) (**A**) and in FC-1/-2 (mean ± SE, n = 2) (**B**). At t = 0 min the spheroids without pre-incubation were introduced into the flow channels filled with the respective buffers. T = 37 °C.

An evaluation of the spheroid parameters based on the measured data in FC-3 resulted in the values listed in Tab. 15. It shows that the extracellular resistance R_{ext} decreases with increasing osmolarity of the external buffer. For the intracellular resistance R_{int} the Hypo value is slightly lower than that of the Iso value. And the values for Hyper I and II are even lower. The non-ideal membrane capacitance of the spheroid A_{sph} is increasing for increasing osmolarity.

Tab. 15: Overview of the spheroid parameters R_{ext}, R_{int} and A_{sph} for spheroids measured in hypoosmotic, isoosmotic, and two hyperosmotic buffers with the same conductivity. Spectra, recorded 45 min after spheroid introduction in FC-3 were fitted as described in chapter 4.3.3 using the following parameter values: A_{el} = 2.3/2.3/2.2·10^{-6} Fs^{n-1}cm^{-2}, n_{el} = 0.95/0.96/0.95, R_{bulk} = 16.4/15.9/16.1 kΩ, A_{para} = 3.5/4.6/3.8·10^{-12} Fs^{n-1}cm^{-2}, n_{para} = 0.98, n_{sph} = 0.75 (mean ± SE, n = 3).

Osmolarity	***Hypo***	***Iso***	***Hyper I***	***Hyper II***
R_{ext} / kΩ	347 ± 64	112 ± 5	77 ± 6	50 ± 2
R_{int} / kΩ	2.7 ± 0.8	3.1 ± 0.2	1.9 ± 0.2	1.2 ± 0.1
A_{sph} / ·10^{-9} Fs^{n-1}cm^{-2}	1.86 ± 0.06	2.42 ± 0.05	2.8 ± 0.1	3.1 ± 0.3

Furthermore, high resolution impedance time courses at 200 Hz were measured for each condition with and without spheroid (Fig. 49) to investigate the influence of swelling and shrinking on the micromotion in spheroids.

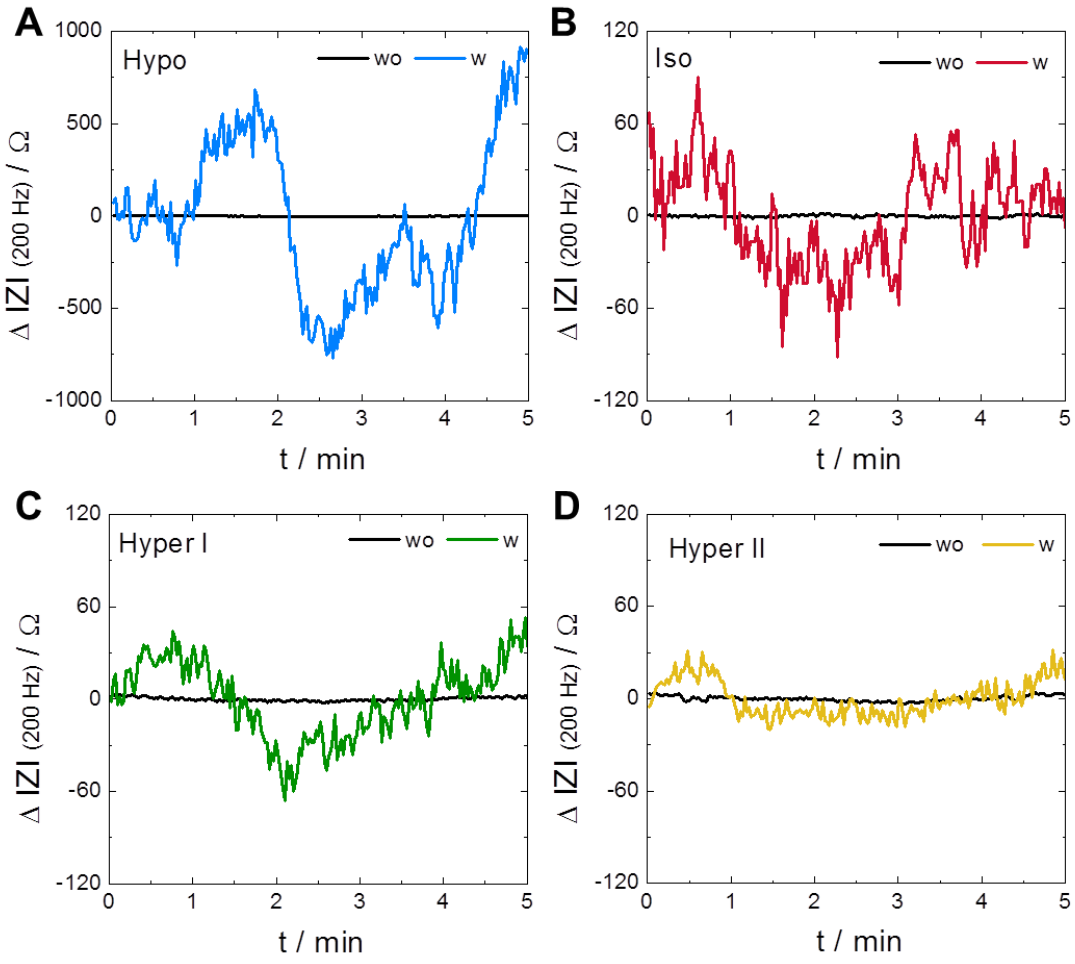

Fig. 49: Typical detrended RTC data at 200 Hz measured in FC-3 immediately before spheroid introduction (wo) and ~ 1 h after spheroid introduction (w) in hypoosmotic buffer (**A**), isoosmotic buffer (**B**), hyperosmotic buffer I (**C**) and hyperosmotic buffer II (**D**). T = 37 °C.

The typical detrended RTC data indicate reduced fluctuations of cells within spheroids in hypertonic buffers and increased fluctuations in the hypoosmotic buffer when compared to the spheroid fluctuations in the isotonic buffer. The analysis of variance after segmented detrending for all conditions was performed for RTC data measured in FC-3 and FC-1/-2 separately (Fig. 50). The variances for spheroids measured in FC-3 (A) are throughout higher than those for spheroids measured in FC-1 and -2 (B). Nevertheless, in both cases a trend is clearly visible indicating the decrease of micromotion for spheroids exposed to

increasing osmolarity. In A and B the differences of variance are significant between spheroids in the isotonic and hyperosmotic buffer II as well as between the spheroid-free channel and the spheroids in isoosmotic and hyperosmotic buffer II. Furthermore, in B there is an additional significance between the spheroid in hypoosmotic buffer and the spheroid-free FC-1/-2 channel as well as the spheroid in hyperosmotic buffer II.

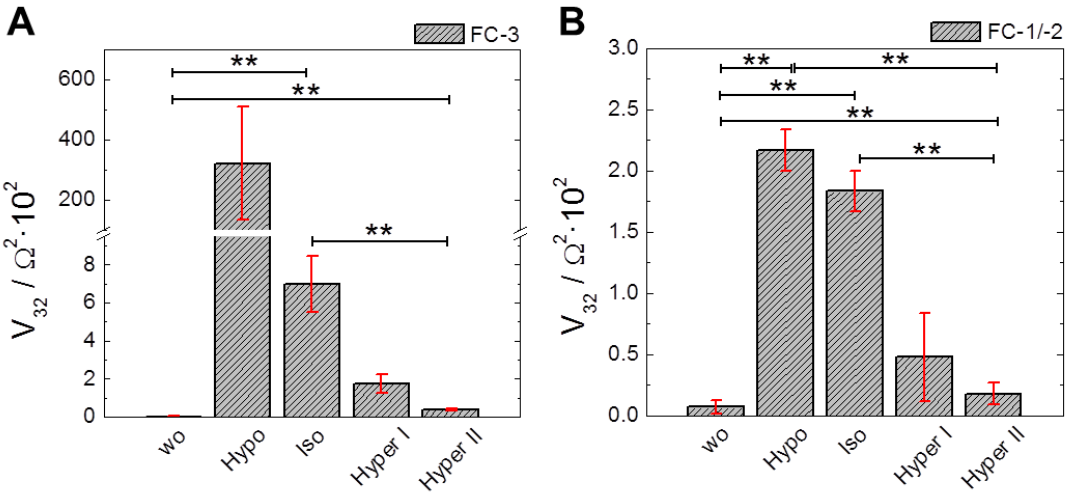

Fig. 50: Analysis of variance after segmented detrending of impedance time courses at 200 Hz for spheroids exposed to buffers with different osmolarities within FC-3 (**A**) and FC-1/-2 (**B**) (mean ± SE; FC-3: n = 3, FC-1/-2: n = 2). Significance was determined by a two-sample t-test using a significance level of 0.05 (**). T = 37 °C.

Using the new flow channel setup swollen, shrinked and control spheroids can be distinguished from each other in the total magnitude of impedance, the three spheroid parameters and in micromotion.

6.5 Investigation of the Spheroid Response to Cytochalasin D

The actin microfilaments as a component of the cytoskeleton are an important structural element of all eukaryotic cells. They are involved in the development of contractile forces and dominate cellular stiffness, controlling cell shape and mechanical properties (Elson, 1988). Furthermore, the microfilaments play an important role in biological processes like cell division and migration (Gunning et al., 2005; Yamaguchi and Condeelis, 2007). One way to study these properties is

by inhibition of the actin polymerization. This can be achieved for example with cytochalasin D, which is a member of the class of mycotoxins. It is a cell membrane permeable compound that binds to the end of actin microfilaments and thereby inhibits the association of actin subunits (Yahara et al., 1982). This way, the actin polymerization is inhibited, microfilament formation is disrupted and many important cellular processes are inhibited (Stevenson and Begg, 1994; Wakatsuki et al., 2001).

In this chapter it was investigated if the previously reported influence of cytochalasin D on cells can be proved also for spheroids measured with the novel setup. The effective concentration of cytochalasin D for cell monolayers was reported to be 1 – 2 µM (Wakatsuki et al., 2001; Oberleitner, 2015). Spheroids however, which are known to exhibit multicellular resistance to drugs (chapter 1.1.3), are expected to be more tolerant and to need a higher dosage.

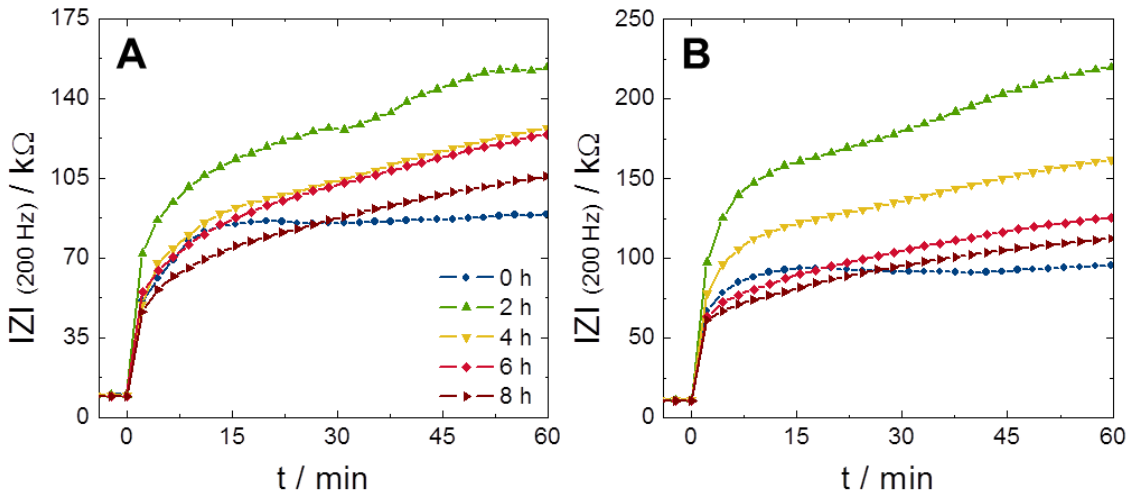

Fig. 51: Typical time courses of impedance magnitude IZI at 200 Hz for MCF-7 spheroids pre-incubated with 5 µM cytochalasin D for 0 / 2 /4 / 6 / 8 h and measured in medium in FC-3 (**A**) or FC-4 (**B**). T = 37 °C.

For this reason, the effect of 5 µM cytochalasin D on MCF-7 spheroids was investigated for different incubation times from 0 – 8 h in a two-hour interval (chapter 4.3.5.5) prior to insertion into the flow channel. Two typical measurement series are presented in Fig. 51, A and B (appendix A2, Fig. S5). After introduction of the control spheroids (0 h) the impedance increases immediately, followed by a continued slow increase over 15 min. Afterwards, the

impedance stays at a constant level for 45 min. All spheroids that were pre-incubated with cytochalasin D, however, show a steady increase in impedance during the entire 60 min of observation. The most pronounced impedance increase upon introducing the spheroid into the channel was obtained for the shortest pre-incubation time (2h) of spheroids with cytochalasin D. With increasing cytD incubation time the magnitude of impedance change decreases. This difference is already visible in the first minutes of the spheroid measurement. This trend is also reflected by respective differences in the parameter values for the extracellular resistance R_{ext} (Tab. 16).

Tab. 16: Overview of spheroid parameters R_{ext}, R_{int} and A_{sph} determined from spheroids pre-incubated with 5 µM cytochalasin D for 0 / 2 / 4 / 6 / 8 h. Spectra were recorded 1 h after spheroid introduction in FC-3/-4 and fitted as described in chapter 4.3.3 using the following parameter values: A_{el} = 2.3/2.0·10^{-6} Fs^{n-1}cm^{-2}, n_{el} = 0.95/0.96, R_{bulk} = 9.5/10.7 kΩ, A_{para} = 4.2/3.5·10^{-12} Fs^{n-1}cm^{-2}, n_{para} = 0.98, n_{sph} = 0.75 (mean ± SE, n = 2).

Incubation time / h	***0***	***2***	***4***	***6***	***8***
R_{ext} / kΩ	83 ± 3	181 ± 34	137 ± 18	117 ± 0	100 ± 3
R_{int} / kΩ	5.6 ± 0.6	7.8 ± 0.6	7.8 ± 0.3	7.5 ± 0.1	7.0 ± 0.1
A_{sph} / ·10^{-9} Fs^{n-1}cm^{-2}	2.10 ± 0.07	1.99 ± 0.05	2.16 ± 0.06	2.14 ± 0.08	2.25 ± 0.03

The control (0 h) shows the lowest R_{ext} value and among the spheroids pre-incubated with cytD the highest R_{ext} value is observed for spheroids that were pre-incubated for 2 h, and the lowest for spheroids pre-incubated for 8 h. The values for the intracellular resistance R_{int} show a similar trend but are less pronounced. The spheroid capacitance A_{sph} however, shows no remarkable trend.

The observation of the spheroids during the measurement using the digital microscope show no morphological abnormalities for control spheroids or for spheroids that were incubated with 5 µM cytD for different times (0 – 8 h) (Fig. 52 A). Images taken at the end of the measurement (B) show that the spheroids that were exposed to cytochalasin D migrate almost completely into the narrowed aperture (2 – 8 h), whereas the control spheroid (0 h) only penetrate about half the distance.

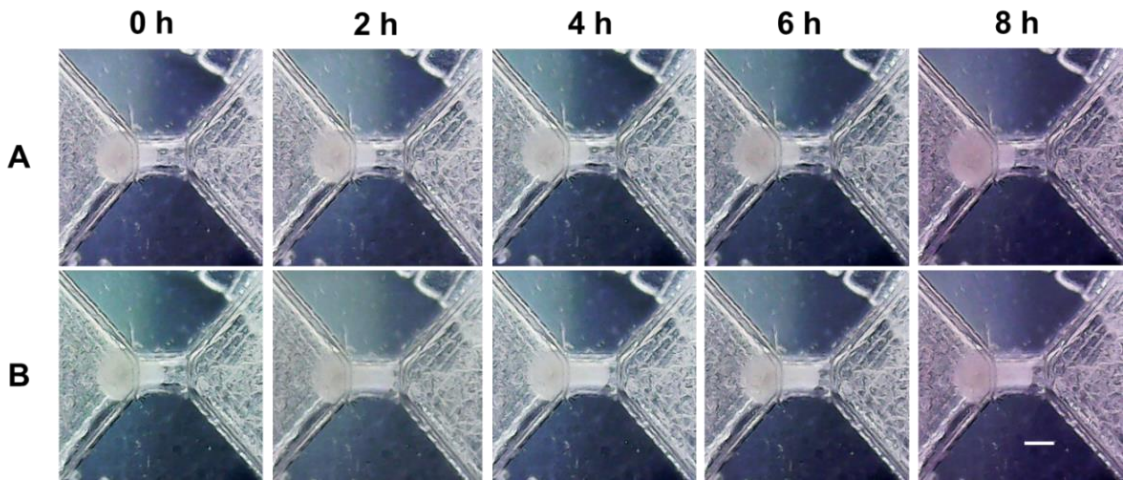

Fig. 52: Five typical spheroids after pre-incubation with 5 µM cytochalasin D for 0 / 2 / 4 / 6 / 8 h were photographed at the start (**A**) and end (**B**) of the measurement in FC-4 using the digital microscope (scale bar: 250 µm). T = 37 °C.

To get an impression of cytochalasin D impact on spheroid micromotion RTC data was collected and evaluated. In Fig. 53 A – F typical detrended impedance time courses for each condition are shown. The impedance time courses by themselves do not show any clear trend regarding their fluctuation characteristics. The amplitude of the fluctuations of spheroids pre-incubated for 2 h is seemingly increased in three out of four measurements when compared to the other conditions. This trend is confirmed by the analysis of variance (Fig. 54) for two single experiments conducted in FC-3 and FC-4. The variance of the other spheroids, which were exposed to cytochalasin D (4 – 8 h), is in most cases not significantly different to that of the control spheroids. This is especially the case for the spheroids measured in FC-3.

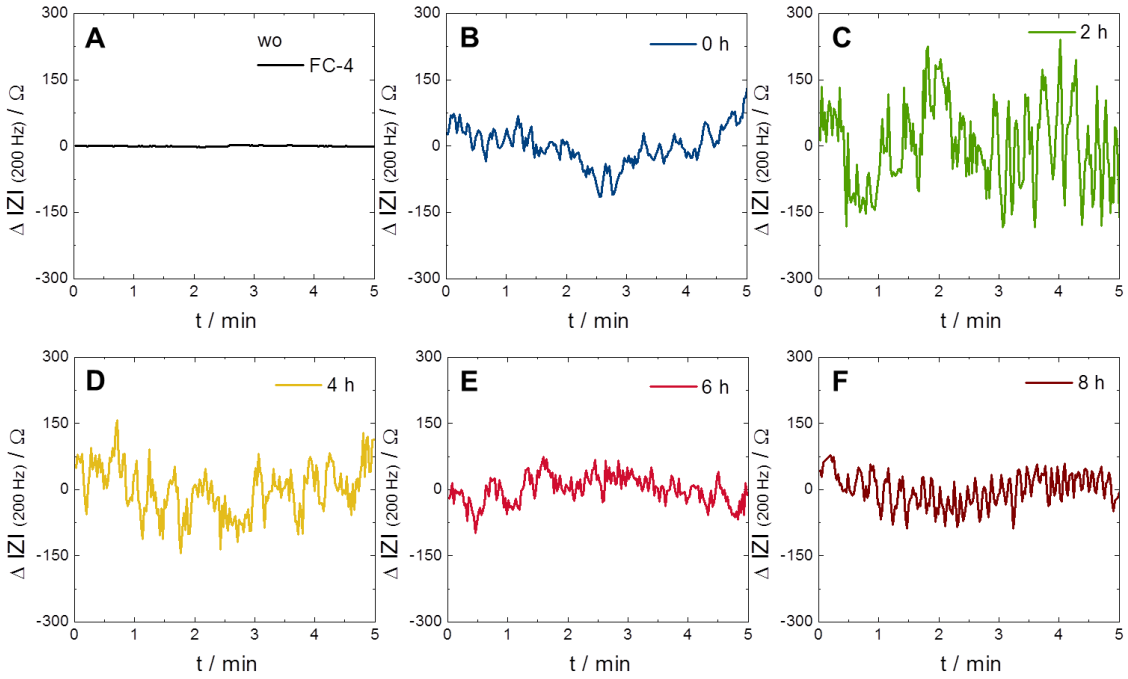

Fig. 53 Typical detrended RTC impedance time courses at 200 Hz for the medium-filled FC-4 without spheroid (**A**) and spheroids that were pre-incubated with 5 µM cytochalasin D for 0 h (**B**), 2 h (**C**), 4 h (**D**), 6 h (**E**) and 8 h (**F**). T = 37 °C.

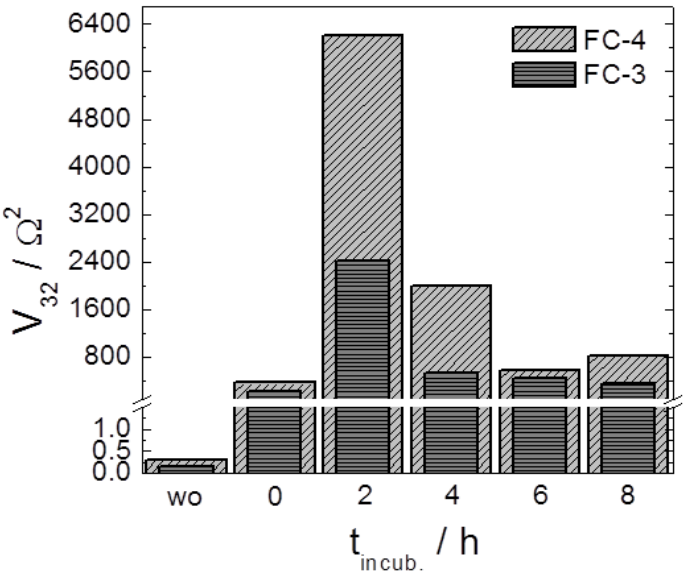

Fig. 54: Analysis of variance after segmented detrending of the typical impedance time courses shown in Fig. 51 for spheroids exposed to 5 µM cytochalasin D pre-incubated for 2 – 8 h, a control spheroid (0 h) and the flow channel without spheroid (wo). Data measured in FC-3 and -4 were evaluated separately. T = 37 °C.

6.6 Evaluation of the Spheroid Response to Hyperthermia

A special type of cancer treatment, which is still investigated, is thermal therapy, also called hyperthermia (HT). Research has shown so far that temperatures between 40 °C and 44 °C can be applied to the cancerous body tissue resulting in injury and death of the treated cells with minimal invasiveness for surrounding healthy cells (Hildebrandt et al., 2002; Ahmed et al., 2015). Generally, hyperthermia showed good results in combination with other cancer treatments like chemotherapy or radiation therapy (van der Zee, 2002; Wust et al., 2002). It has been reported that thermal therapy enhanced the effect of some anticancer drugs (Takahashi et al., 2002). In the studies mentioned above the tissue was first exposed to hyperthermia in order to make the cells more sensitive to the subsequent cancer treatment. The effectiveness of HT depends on the cell/tissue characteristics, the duration of exposure and the temperature that is achieved in the tissue. Depending on the tumor position in the body the heat delivery, control and regulation can be difficult and can lead to side effects e.g. burns (van der Zee, 2002).

Impedimetric Analysis

In this study, the effect of hyperthermia on breast cancer spheroids was investigated without subsequent treatments. The fact that spheroids are freely accessible (in comparison to tumors within the body) should enable a homogeneous heat application and eventually lead to a stronger impact. Spheroids were exposed to 41 / 43 / 45 °C for 1 h or for 3 h in order to investigate the effect of hyperthermia dependent on the temperature and the duration of exposure. The experimental protocol is described in detail in chapter 4.3.5.6 and the results can be seen in Fig. 55. The spheroid exposure for 1 h at all three temperatures shows no significant difference in the impedance signal when compared to the control spheroid (37 °C). Only in two out of six measurements the spheroid exposed to 45 °C shows a remarkably lower impedance than the others (Fig. 55, 1 h) (appendix A2, Fig. S6). However, when the spheroids were exposed to the three temperatures for 3 h a temperature dependent trend is observable. Control spheroids, which were held all times at 37 °C, show the highest impedance.

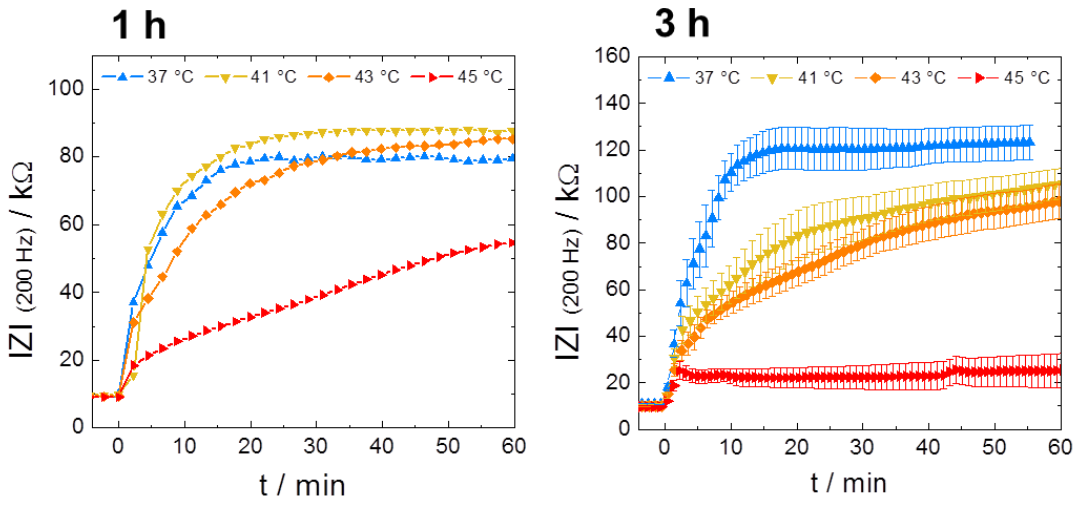

Fig. 55: Time courses of impedance magnitude at 200 Hz for spheroids that were exposed to 37 / 41 / 43 / 45 °C for 1 h in FC-3 (typical time course) or 3 h in FC-3/-4 (mean ± SE, n = 6). T = 37 °C.

Spheroids, which were exposed to 41 and 43 °C show an intermediate impedance with rather similar values approaching the impedance values of the control spheroids. Spheroids that were exposed to 45 °C always show a very low impedance.

Summed up, 1 h hyperthermia and subsequent impedimetric analysis at 37 °C does not show any distinct effects on the spheroid viability. Hyperthermia for 3 h however, leads to a temperature dependent decrease in spheroid impedance indicating a clear effect on the dielectric structure of spheroids. Therefore, the results for the 3 h exposure were further analyzed by determination of the spheroid parameters (Tab. 17).

Tab. 17: Overview of the spheroid parameters R_{ext}, R_{int} and A_{sph} for spheroids pre-incubated at 37 / 41 / 43 / 45 °C for 3 h. Spectra, recorded 30 min after spheroid introduction in FC-3/-4 were fitted as described in chapter 4.3.3 using the following parameter values: A_{el} = 2.1·10^{-6} Fs^{n-1}cm^{-2}, n_{el} = 0.96, R_{bulk} = 10.1/10.5/10.3 kΩ, A_{para} = 4.2/4.5·10^{-12} Fs^{n-1}cm^{-2}, n_{para} = 0.98, n_{sph} = 0.75 (mean ± SE, n ≥ 5).

***T* / °C**	***37***	***41***	***43***	***45***
R_{ext} / kΩ	112 ± 9	82 ± 10	71 ± 6	15 ± 5
R_{int} / kΩ	5.0 ± 0.5	4.0 ± 0.5	2.6 ± 0.4	2.1 ± 0.8
A_{sph} / ·10^{-9} Fsn^{-1}cm^{-2}	2.06 ± 0.06	2.2 ± 0.1	2.13 ± 0.06	7 ± 5

R_{ext} and R_{int} clearly decrease with increasing temperature. A_{sph} is similar for 37 – 43 °C and clearly increases for 45 °C.

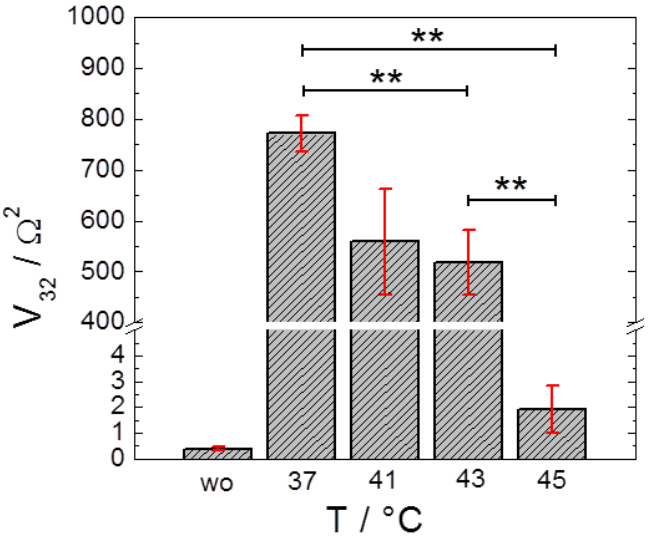

Fig. 56: Variance analysis of RTC impedance time courses after segmented detrending for spheroids exposed to hyperthermia for 3 h (mean ± SE, n ≥ 4). Significance was determined by a two-sample t-test using a significance level of 0.05 (**). T = 37 °C.

Furthermore, the effect of hyperthermia (3 h) on the micromotion of spheroids was investigated measuring RTC data and performing a qualitative analysis. Variance analysis for all experimental conditions was performed and resulted in strongly variable variances within the respective conditions (appendix A2, Tab. S3). If the values in grey in this table are neglected it is possible to recognize a trend showing the highest value of variance for spheroids at 37 °C, followed by decreasing variances of spheroids at 41 °C and 43 °C (Fig. 56). The variance of spheroids exposed to 45 °C is similar to that of a spheroid-free channel and significantly different to variances at other temperatures.

PrestoBlue® Assay Results

In order to verify the results of the impedimetric analysis, a PrestoBlue® assay was performed as described in chapter 4.1.8. Again, the effect of hyperthermia exposure for 1 h and 3 h was investigated for the same three temperatures of 41 / 43 / 45 °C.

Triton® X-100 treated spheroids served as positive control and spheroids held at 37 °C as negative control. As expressed by the cytotoxicity index values (Fig. 57), all conditions of hyperthermia do not induce cytotoxicity as compared to the positive control.

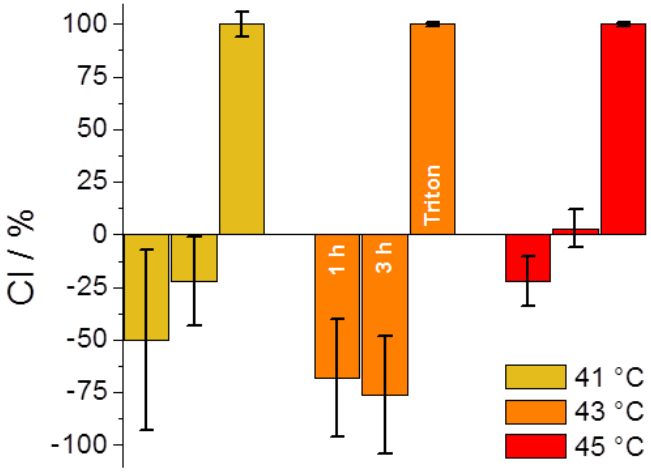

Fig. 57: Cytotoxicity index determined via PrestoBlue® assay conducted at 37 °C for spheroids pre-incubated at 41 °C (yellow), 43 °C (orange) and 45 °C (red) for 1 h (first column of each color) or 3 h (second column of each color) as well as spheroids that were treated with Triton® X-100 as positive control (third column of each color) (n ≥ 4). A *CI* value of 0 % corresponds to the negative control, which are spheroids held at 37 °C.

6.7 Investigating the Phototoxic Response of Spheroids

Another widely accepted treatment strategy for tumors is the photodynamic therapy (PDT). For this kind of treatment the target tissue is loaded with a photosensitizer. These are generally chemical agents with low dark toxicity that can be activated by the exposure to light. Typical classes of photosensitizers (PS) are chlorins, phthalocyanines, porphycenes and porphyrin derivatives (Robertson et al., 2009). Most of these molecules are fluorescent, which enables the combination of PDT and optical imaging. By choosing the appropriate wavelength the photosensitizer is excited and produces radicals and reactive oxygen species that can interact with cellular components and lead to cell death. This technique is meanwhile recognized as minimally invasive for the tumor surrounding healthy tissue and is a good alternative to extensive surgery (Lamberti et al., 2014).

In this study, two fluorescent substances were investigated for their potential phototoxic effect on spheroids. These are carbon nanodots and the live cell stain calceinAM. The C-dots were prepared and characterized by Michael Lemberger and Pierre Pütz and should be tested as photosensitizers for PDT. The well-established and often used live cell stain calceinAM was tested on spheroids in collaboration with Romy Freund.

6.7.1 Influence of CalceinAM

Investigation of the Phototoxicity on MCF-7 Cells in 2D Culture

The live cell stain calceinAM is one of the fluorochromes that are known to induce phototoxicity on animal cells when irradiated at its excitation wavelength. In this thesis the phototoxicity of this stain was tested also on 3D multicellular spheroids from MCF-7 cells. As a pre-experiment the phototoxicity of calceinAM should be proven first in the MCF-7 cell monolayers. The experiment was performed as explained in chapter 4.3.5.7 and the results of three measurements are shown in Fig. 58. For irradiation three different excitation wavelengths 330 – 380 nm, 420 – 490 nm and 510 – 560 nm of the fluorescence filter cubes from Nikon (appendix A2, Tab. S1) were used.

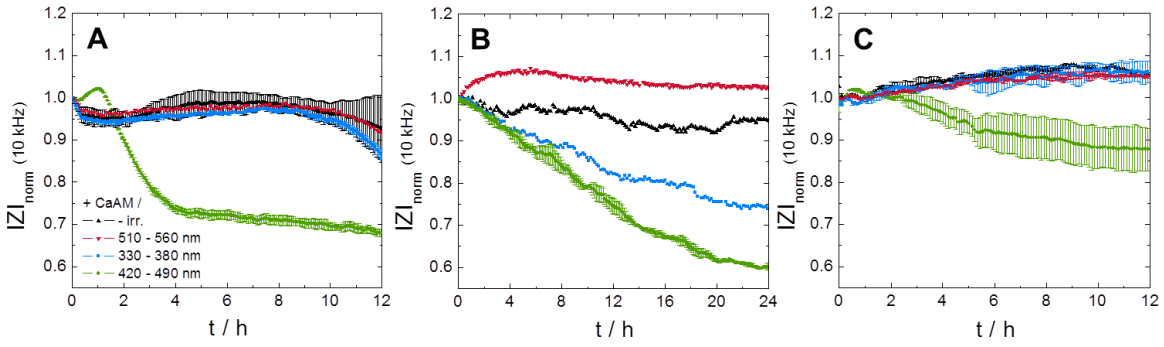

Fig. 58: Time courses of the corrected and normalized impedance magnitude at 10 kHz for calceinAM stained and irradiated (3 min) MCF-7 monolayer cells for three independent experiments (**A**, **B**, **C**). Control cells were not irradiated (- irr.), irradiated with light of 330 – 380 nm or 510 – 560 nm. The others were irradiated with 420 – 490 nm (each curve with error bars: mean ± SE, n = 2). T = 37 °C.

In three control conditions calceinAM stained cells were not irradiated (- irr.), irradiated with UV (330 – 380 nm) or with green (510 – 560 nm) excitation light. These control cells were not expected to show significant impedance changes. In fact, in two of three measurements (A, C) all control cells stay at a constant impedance level over 12 h after irradiation. In measurement B the cells that were not irradiated show stable impedance over 24 h, whereas cells that were irradiated with green excitation light increase slightly in impedance immediately after the exposure and then remain at a constant level. The cells that were irradiated with UV, show an unexpected steady decrease by 25 % within 24 h (B). As this unusual response is a single event it might be neglected. When the calceinAM loaded cells were irradiated with blue light (420 – 490 nm) the stain was excited and showed green fluorescence. In all three measurements after irradiation the cells show different extents of impedance decreases by ~ 30 % (A), ~ 40 % (B) and ~ 12 % (C). However, the time course of impedance decrease differs in the three measurements. A slight impedance increase immediately upon irradiation followed by a steep decrease over 3 h with a final approach to stable values is observed in measurement A. In measurement B there is an immediate and steady impedance decrease over 20 h and a subsequent almost stable plateau phase (B). In the third case the impedance stays constant in the 2 h after irradiation followed by a slight and short decrease over 3 h and finally approaching a stable impedance level (C). Although, the extent and time dependent decrease in impedance is variable, which may be related to cell specific differences (e.g. passage number), only the exposure to the excitation wavelenghth of calceinAM leads to a reduced cell viability.

This conclusion was confirmed with a Live/Dead staining at the end of the impedimetric measurements. The exemplary micrographs (Fig. 59) show that confluent cell layers with viable cells are present in all control conditions. However, there are also a lot of dead cells (-irr, 510 – 560 nm, 330 – 380 nm). After irradiation with the excitation wavelength of calceinAM the cells in the exposure area detached completely, since the Live/Dead staining in this area shows almost no remaining viable or dead cells. In the periphery of the exposed area there are still viable and dead cells, similar to the control conditions.

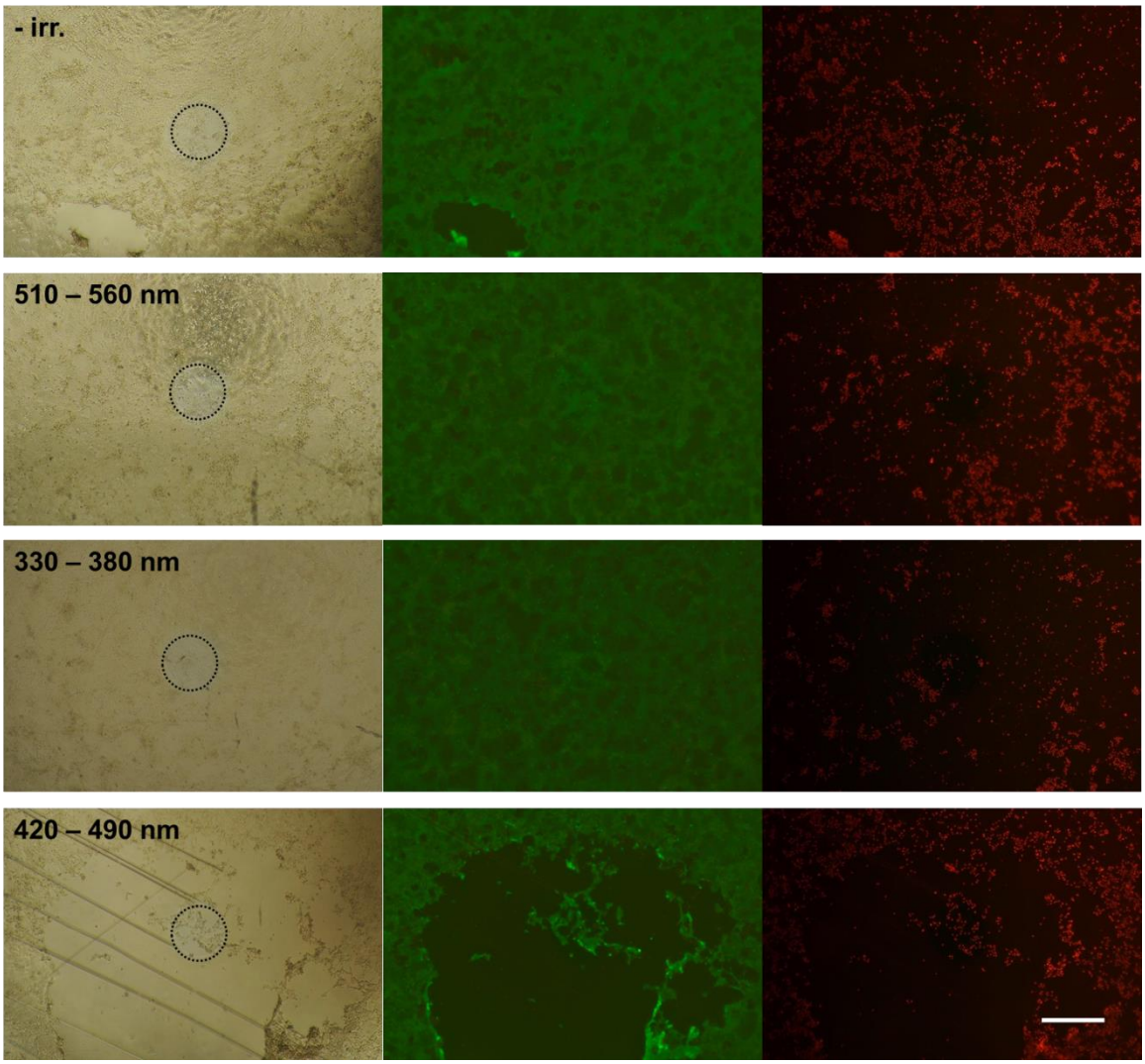

Fig. 59: Microscopic documentation of the cellular viability of all experimental conditions (-irr., 510 – 560 nm, 330 – 380 nm, 420 – 490 nm) ~ 24 h after irradiation. For each condition phase contrast images and images with Live/Dead stained cells have been taken using the 4x objective (scale bar: 400 µm). The dashed black ring marks the position of the working electrode in the phase contrast images as the focus point during excitation.

Romy Freund obtained similar micrographs when she investigated the phototoxicity of calceinAM on NRK cells, observing less dead cells in the control conditions (- irr., 510 – 560 nm, 330 – 380 nm) and less CaAM-loaded detached cells after irradiation with the excitation wavelength.

Investigation of Phototoxicity on MCF-7 Cells in 3D Culture

As a consequence of the observed phototoxicity of calceinAM on MCF-7 monolayer cells, the phototoxicity on MCF-7 spheroids was also tested. For this purpose the protocol in chapter 4.3.5.7 for spheroids was followed. The impedance measurements were supported by phase contrast and fluorescence micrographs of the spheroids before and during irradiation as well as after the measurement (Fig. 60). In these experiments unstained but irradiated spheroids served as controls. Any potential influence of non-excitation wavelengths or dark toxicity has already been excluded by the monolayer experiments. In all three measurements the control and CaAM spheroids were measured for ~ 30 min before they were irradiated for 10 min at the excitation wavelength inside the flow channel fixed by the aperture. In comparison to the 2D experiments the irradiation time was increased, as spheroids are reported to be more resistant to any kind of stimulation compared to monolayer cells. Right before exposure control (Fig. 60, control-1/-2/-3, 1) and CaAM (CaAM-1/-2/-3, 1) spheroids show a regular morphology. During irradiation the CaAM spheroids show a distinct green fluorescence located predominantly at the surface of the spheroids. The unstained control spheroids show no fluorescence as expected. In all cases, right after irradiation the time course of impedance shows a peak that is related to the temperature equilibration of the spheroids after cooling down to room temperature during the irradiation phase. Afterwards, a slight increase in impedance is observed for 3 – 5 h followed by a slight decrease until the end of the measurement. An exception is the control spheroid 3 in measurement C, which passes the channel. This leads to an abrupt and steep decrease of impedance to baseline values. The phase contrast micrograph at the end of the measurement (Control-3) shows the spheroid on the reservoir bottom of the flow channel with a few dead cells lying aside.

A transition of spheroids through the central channel was generally observed for injured and dying spheroids. It might be possible that a spheroid injury, which was, however, not visible on the microscopic images, occurred during pipetting.

For all other spheroids under test the impedance decrease is very weak, indicating no acute phototoxicity. For the control spheroids 1 and 2 the phase contrast images confirm this conclusion (control-1/-2, 3).

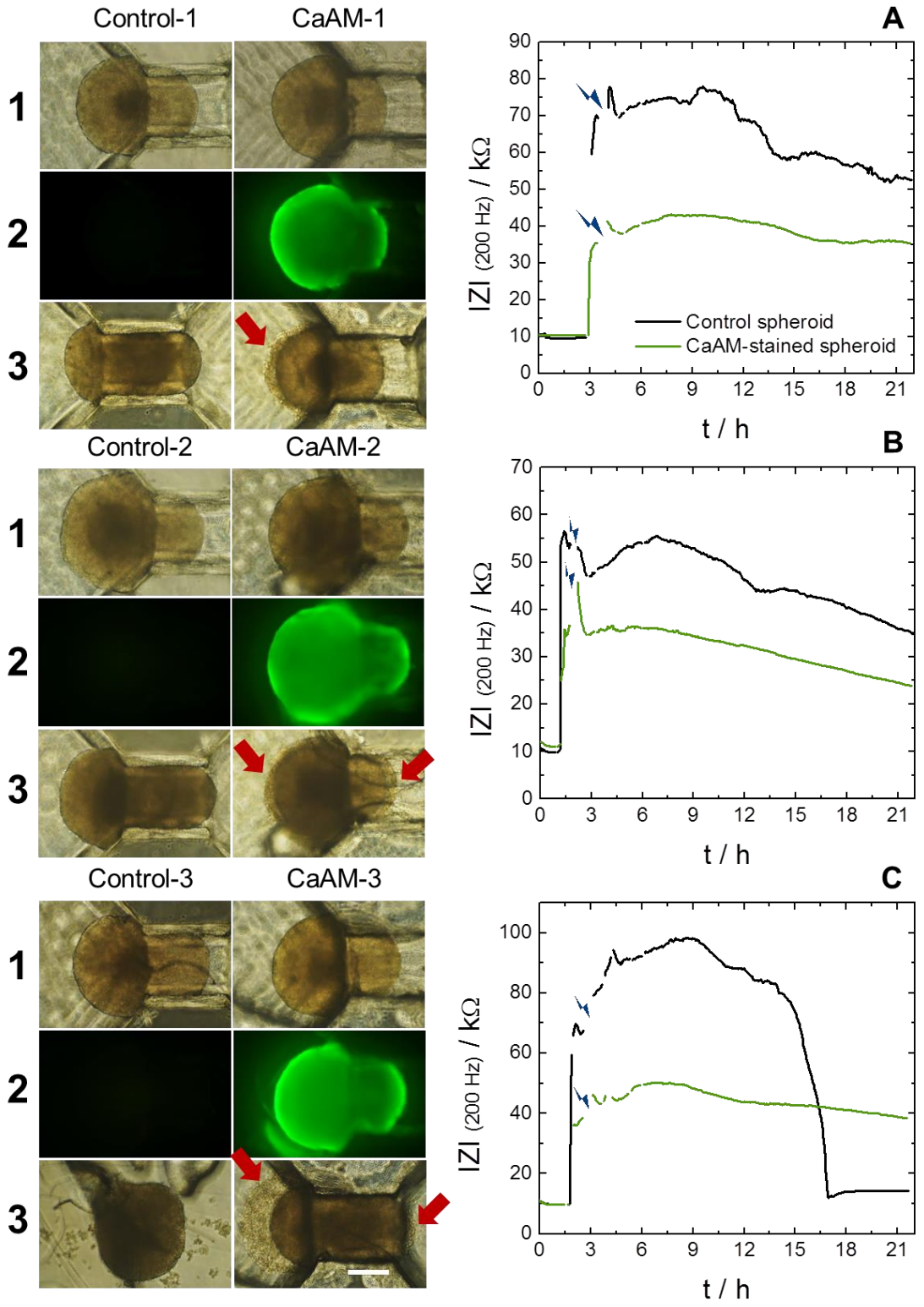

Fig. 60: Results of three measurements of the phototoxic effect of calcein AM on MCF-7 spheroids. On the left side the microscopic documentation of the spheroids in the channel before (**1**) and during (**2**) irradiation as well as at the end of the measurement (**3**) for unstained control spheroids and calceinAM spheroids is shown (scale bar: 200 µm). On the right side there are the corresponding time courses of impedance magnitude at 200 Hz for control spheroids and calceinAM stained spheroids (**A**-**C**). The blue flash marks the time point when both spheroids were irradiated sequentially for 10 min. T = 37 °C.

The spheroids still show an intact shape/morphology and they completely penetrate the central channel. Only one of the CaAM spheroids moves completely into the aperture (CaAM-3, 3), whereas the other two do not show any further penetration tendency (CaAM-1/-2, 3). Furthermore, the CaAM treated spheroids exhibit dead cells at the spheroid's surface (marked by red arrows), indicating that a local phototoxic effect occurred where also most of the fluorophore is observed and irradiation has highest intensity.

In the impedance time courses the control spheroids show a higher impedance than compared to the CaAM spheroids (A – C). This is due to the fact that the experiments were conducted in different flow channels, which can lead to a variation in the impedance values as discussed before (chapter 5.5.2).

By fitting of measurement A in Fig. 60 typical time courses for the spheroid parameters R_{ext}, R_{int} and A_{sph} of the control spheroid and the calceinAM stained spheroid were obtained (Fig. 61). The time course of R_{ext} for the control and the CaAM spheroid (Fig. 61 A) is very similar to the corresponding impedance magnitude. The time course of R_{int} for both conditions (B) is stable with values between 3 and 4 kΩ for the first ~ 10 h after irradiation followed by a slight increase for the CaAM spheroid and a slightly stronger increase for the control spheroid. Furthermore, throughout the measurement the R_{int} values of the CaAM spheroid are higher than those of the control spheroid. The same was observed for A_{sph}, which shows a slight increase for the CaAM spheroid and a slight decrease for the control over ~ 10 h after irradiation (C). Afterwards, both curves decrease slightly and then approach a constant capacitance.

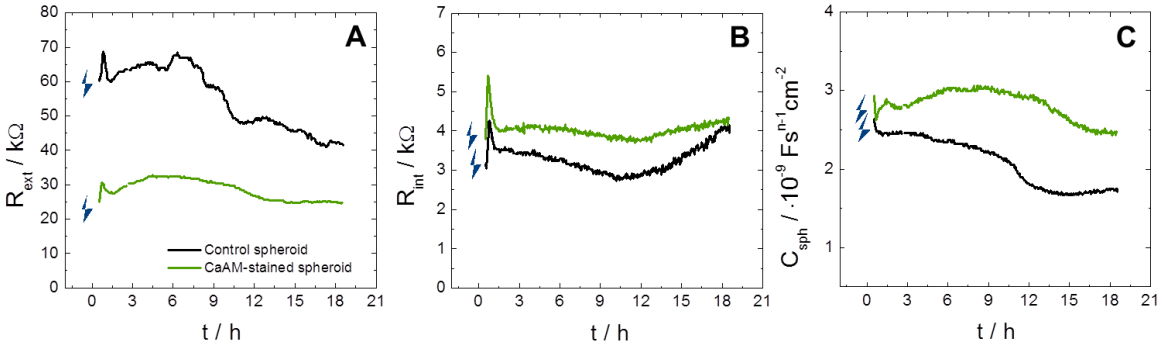

Fig. 61: Typical time course for the spheroid specific parameters R_{ext} (**A**), R_{int} (**B**) and A_{sph} (**C**) for the control spheroid and the calceinAM stained spheroid determined by fitting of measurement A in Fig. 60. The time courses start immediately after spheroid irradiation marked by the blue

flashes. Spectra were fitted as described in chapter 4.3.3 using the following parameter values: A_{el} = 2.1·10^{-6} Fs^{n-1}cm^{-2}, n_{el} = 0.95, R_{bulk} = 10.3 kΩ, A_{para} = 4.0·10^{-12} Fs^{n-1}cm^{-2}, n_{para} = 0.98, n_{sph} = 0.75.

6.7.2 Carbon Dots as Photosensitizers

Carbon nanodots have unique properties that make them applicable in various fields of science. Due to their good water dispersibility, good photoluminescence with broad excitation band and high photostability C-dots are potential tools in luminescence-based bioanalysis (Lemberger et al., 2014). Important requirements for labels that are used for cell-based applications are that they are inert and biocompatible with no significant cytotoxicity. If they should be used as photosensitizer however, there are even more requirements to be fulfilled. In addition to the characteristics listed above, photosensitizers should have a low mutagenic potential, the ability to accumulate in the specific tissue target and also to be eliminated rapidly after administration. Furthermore, for the excitation of PS wavelengths between 600 and 800 nm are preferred to avoid skin phototoxicity triggered by daylight (Baltazar et al., 2015). The most basic requirement is of course that ROS are produced by excitation of a potential photosensitizer that leads to phototoxicity. In this chapter the C-dots produced by Michael Lemberger were tested for this characteristic.

6.7.2.1 Cytotoxicity of C-Dots in Spheroids

First, the cytotoxicity of C-dots in contact to MCF-7 spheroids was evaluated. Cytotoxicity experiments with NRK monolayer cells perfomed by Michael Lemberger (2015) showed that particle suspensions up to 1 mg/mL showed no dark toxicity. Three-dimensional tissue models were incubated for 2 h with 1.5 mg/mL C-dots in EBSS^{++}. The measurement was performed three times as explained in chapter 4.3.5.9 and the resulting time courses of impedance are shown in Fig. 62. The three measurements show very similar results. After the introduction of the control spheroids into the channel the impedance first increases by ~ 10 – 20 kΩ within a few hours.

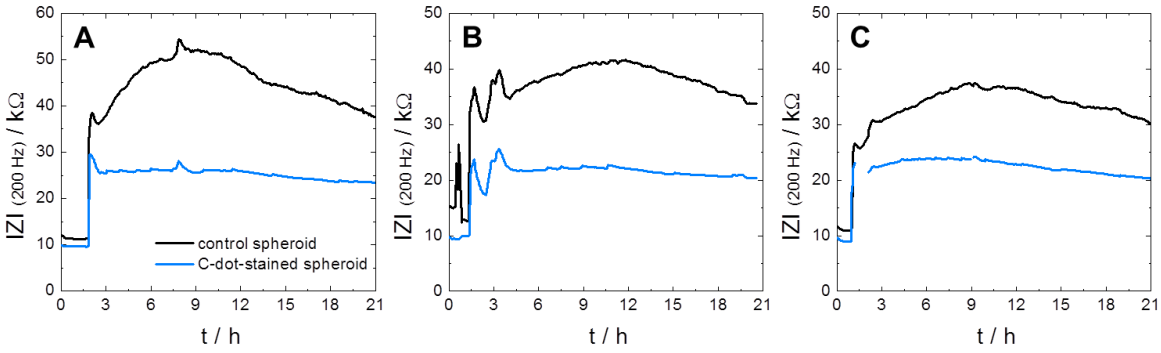

Fig. 62: Time courses of impedance magnitude at 200 Hz for a control spheroid and a spheroid pre-incubated with 1.5 mg/mL C-dots for 2 h shown for three individual measurements (A – C). T = 37 °C.

Then, the impedance decreases to a value similar to the impedance right after spheroid introduction. The C-dot spheroids remain at the impedance level that was reached right after introduction into the flow channel. The impedance of the control spheroids is higher than that of the C-dot spheroids, which is related to flow channel artifacts explained before.

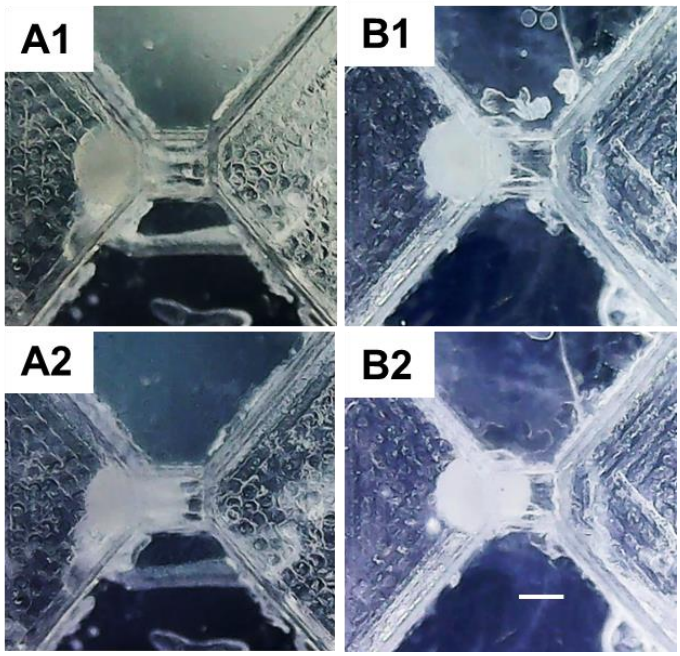

Fig. 63: Typical microscopic images of a control spheroid (**A**) and a spheroid that was exposed to 1.5 mg/mL C-dots for 2 h (**B**) right after the introduction into the flow channel (**1**) and at the end of the measurement (**2**) using the digital microscope (scale bar: 250 µm). T = 37 °C.

As can be seen in the micrographs (Fig. 63) the spheroids with (B) and without (A) C-dots both have a smooth shape in the beginning of the experiment (1) as well as in the end (2) of it. The images show neither dead cells nor a reduced size of the C-dot spheroid. From the microscopic and impedimetric results it is concluded that the applied C-dot concentration of 1.5 mg/mL shows no dark toxicity and was therefore used for the investigation of C-dot phototoxicity on spheroids.

6.7.2.2 Phototoxicity of C-dots in MCF-7 Cells in 2D Culture

Phototoxicity of C-dots was investigated by Michael Lemberger (2015) on NRK monolayer cells. Before C-dot phototoxicity was also investigated on MCF-7 multicellular spheroids their effect on MCF-7 monolayer cells was addressed. Three individual measurements were performed as described in detail in chapter 4.3.5.8. and are shown in Fig. 64.

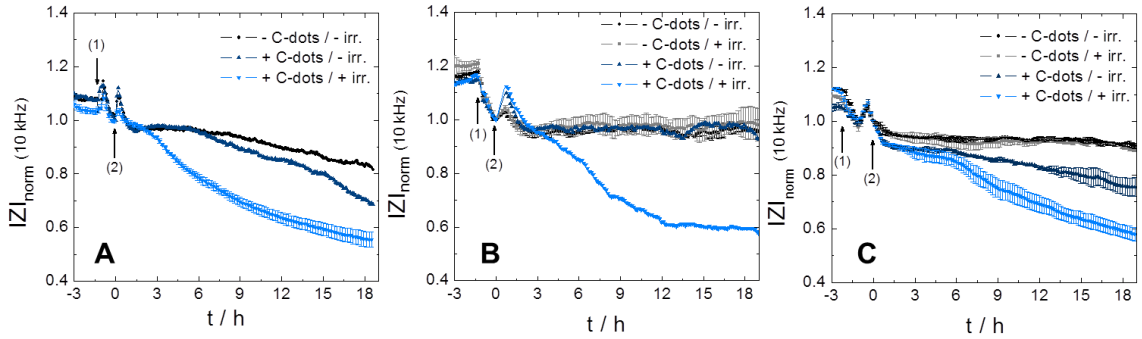

Fig. 64: Three measurements (**A**, **B**, **C**) showing the time courses of the corrected and normalized impedance magnitude at 10 kHz for MCF-7 monolayer cells incubated with 1 mg/mL C-dots for 1 h and irradiated for 3 min. Control cells were not stained/irradiated (-C-dots/- irr.), not stained but irradiated (-C-dots/+ irr.) or stained with C-dots but not irradiated (+C-dots/-irr.). The others were stained with C-dots and irradiated (+C-dots/+irr.) (each curve with error bars: mean ± SE, n ≥ 2). The black arrows mark the time points when 1 mg/mL C-dots were added to the cells (1) and when the cells were washed and irradiated for 3 min at 330 – 380 nm (2). T = 37 °C.

Up to three control conditions were used, which contain C-dot-free cells (- C-dots) with or without irradiation (± irr.) and C-dot loaded cells without irradiation. While in measurement B and C cells without C-dots stay at constant impedance values, independent of irradiation, in measurement A the impedance is slightly decreasing over time. This steady impedance decrease even under control

conditions is likely related to regular cell death and variations of cell viability.

Cells which were incubated with C-dots but were not irradiated show once a constant time course of impedance (B) and twice a biphasic behavior (A, C). The impedance is constant for the first ~ 6 h and then starts to decrease (A, C). At the end of these measurements the impedance decreases by 20 – 30 % of the initial value. This indicates that 1 mg/mL is a critical concentration that can be cytotoxic to MCF-7 monolayer cells. C-dot stained and irradiated cells show in all cases a decrease in impedance by 40 – 45 % within ~ 18 h after excitation light exposure. Thus, the impedance decrease is linked to a phototoxic effect.

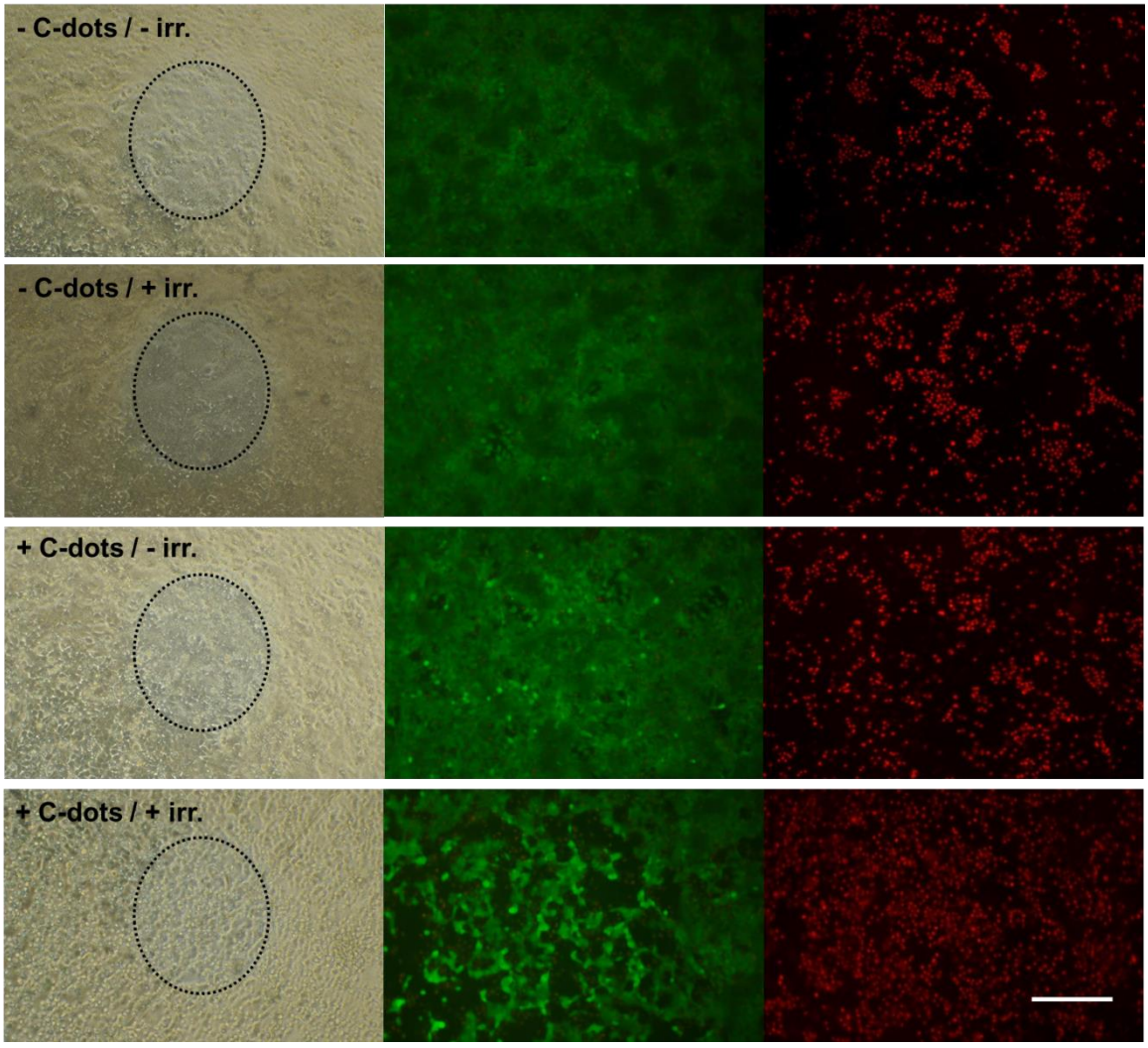

Fig. 65: Microscopic evaluation of cellular viability for all conditions under test (± C-dots / ± irr.) at the end of measurement C (Fig. 64). For each condition phase contrast images and images with Live/Dead stained cells were taken using the 10x objective (scale bar: 200 µm). The dashed ring marks the position of the working electrode.

The phototoxic effect is also confirmed by microscopic evaluation of the cells after the measurement using Live/Dead staining (Fig. 65). The images show a viable cell layer with some dead cells for unstained cells with and without irradiation (- C-dots / ± irr.), reflecting the normal condition of MCF-7 cells, which were cultured on the ITO array for a certain time. C-dot loaded cells that were not irradiated look similar to the controls. The C-dot loaded and irradiated cells (+ C-dots / + irr.), however, clearly show the loss of cells in the exposed area. The images show rounded cells (phase contrast), with only sporadic viable cells still adhering to the substrate and a lot of dead detached cells.

6.7.2.3 Phototoxicity of C-dots in MCF-7 Cells in 3D Culture

In order to prove the applicability of C-dots as PS three independent impedimetric experiments using MCF-7 spheroids and the novel setup were performed following the protocol in chapter 4.3.5.8. Phase contrast and fluorescence micrographs of the spheroids under study which were taken before and during irradiation as well as after the measurement, should provide additional information on the spheroid shape (Fig. 66).

For this study, two spheroids were pre-incubated with 1.5 mg/mL C-dots and measured ~ 30 min before one of them was irradiated directly at the aperture of the channel for 15 min with the C-dot excitation wavelength (330 – 380 nm) using the Nikon Diaphot. The other spheroid was not irradiated and served as control. Again, the increased C-dot concentration and light exposure in comparison to the 2D experiments were chosen on purpose to enhance a potential effect on the more resistent spheroids. The phase contrast images that were taken before irradiation show viable spheroids with regular smooth shape, partly penetrating the flow channel aperture (Control-1/-2/-3, C-dot-1/-2/-3, 1). During the irradiation of one of the C-dot spheroids a blue fluorescence is observed which seems to be distributed homogeneously over the whole spheroid. After irradiation at room temperature the spheroids within the flow channels were placed back in the incubator and the impedance measurement was continued. The equilibration of the spheroids to temperature change is reflected in the data as a brief decrease in impedance within the first half hour after exposure and is most pronounced in measurement C.

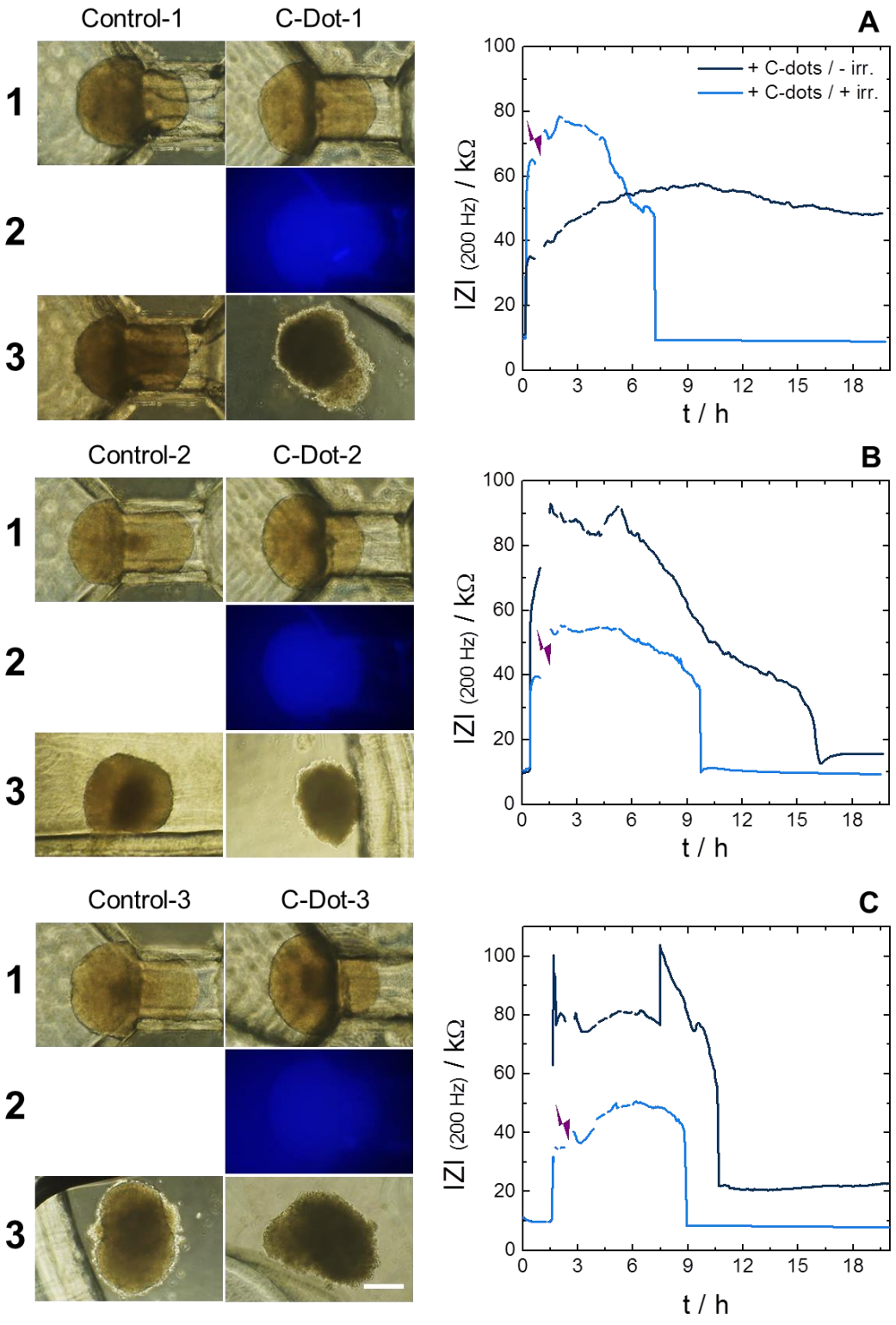

Fig. 66: Results of three measurements of the phototoxic effect of C-dots on MCF-7 spheroids. The left side provides the microscopic documentation of the C-dot spheroids in the channel before (**1**) and during (**2**) irradiation as well as at the end of the measurement (**3**). As control C-dot spheroids without irradiation were used (scale bar: 200 µm). On the right side there are the corresponding time courses of impedance magnitude at 200 Hz for C-dot spheroids with and without irradiation (**A**-**C**). The purple flash marks the time point when one C-dot spheroid was irradiated for 15 min. T = 37 °C.

Afterwards, the exposed C-dot spheroids show a slight increase in impedance (A, C) or remain constant (B), followed by a steep (A) or slight (B, C) decrease and a subsequent abrupt decline to baseline impedance 6 – 8 h after exposure. The time point of abrupt impedance decrease marks the transition of the exposed C-dot spheroid through the central opening of the channel. The phase contrast micrographs taken at the end of the measurement show all C-dot spheroids exposed to the excitation wavelength floating in the medium reservoir (C-dot-1/-2/-3, 3). They appear darker and smaller with single dead cells on the surface. The three control spheroids show significant differences in their time course of impedance. In measurement A the control spheroid behaves as expected from the cytotoxicity experiments. The impedance is slowly increasing over time and approaches a stable value reflecting no dark toxicity of C-dots. This is also confirmed by the phase contrast image that shows Control-1 at the end of the measurement partly penetrating the narrowed channel with a smooth and intact shape. In measurement B the impedance increases for ~ 4 h and then decreases continuously before declining to impedance values close to baseline. At the end of the measurement the spheroid was found in the opposing flow channel reservoir (Control-2, 3), showing a slightly irregular shape. For the Control-3 a decline in impedance close to a baseline level occurs slightly delayed compared to the impedance drop seen for the irradiated C-dot spheroid. The shape of Control-3 is deformed and damaged with dead cells on the surface especially at the spheroid center, which was formerly located at the aperture.

A time dependent equivalent circuit analysis of the control and C-dot spheroid parameters was performed for measurement A for the data prior to the decline seen for the irradiated C-dot spheroid (Fig. 67). The time course of R_{ext} for the spheroids incubated with C-dots with and without irradiation correlate with that of the impedance course (Fig. 66 A). The decrease in R_{ext} for the irradiated C-dot-loaded spheroid indicates an impairment of the viability. This effect is accompanied with the transition of the spheroid through the central opening of the channel.

The time course of R_{int} for the control spheroid is rather stable with values around 6 – 7 kΩ. The spheroid exposed to excitation light however, shows an initial increase from 6 to 8.5 kΩ during 3 h and an abrupt subsequent decrease back to

initial values.

A_{sph} of the control spheroid is stable during the evaluated time range. The irradiated spheroid shows a decrease in the time course of A_{sph} in the first hour after exposure and then settles off to stable values that are by ~ 0.5 · 10^{-9} $Fs^{n-1}cm^{-2}$ lower than those of the control. At t = 6.5 h a further steep decrease is observed.

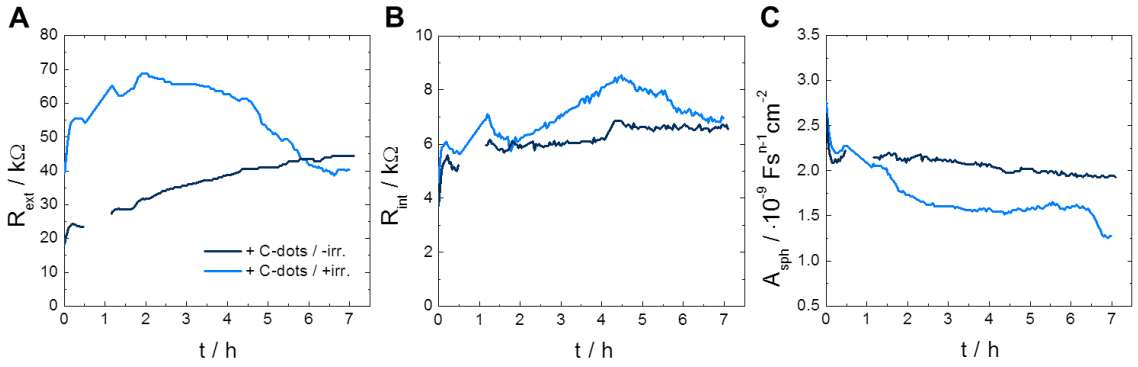

Fig. 67: Typical time courses for R_{ext} (**A**), R_{int} (**B**) and A_{sph} (**C**) as determined for the control spheroid and the C-dot spheroid by equivalent circuit modeling of measurement A in Fig. 66. Spectra were fitted as described in chapter 4.3.3 using the following parameter values: A_{el} = 2.3/2.2·10^{-6} $Fs^{n-1}cm^{-2}$, n_{el} = 0.95, R_{bulk} = 9.7/11 kΩ, A_{para} = 4.0/3.8·10^{-12} $Fs^{n-1}cm^{-2}$, n_{para} = 0.98, n_{sph} = 0.75.

6.8 Discussion

6.8.1 Characterization of MCF-7 Spheroids

Spheroids from MCF-7 cells were successfully prepared by aggregation in a non-adhesive culture vessel supported by orbital shaking. Using phase contrast microscopy the morphology and the growth of the prepared spheroids was investigated.

- MCF-7 spheroids are spherical, compact and show a smooth shape from day one after seeding.
- Reproducible generation of spheroids with defined sizes is possible. Spheroids produced by 1000 – 6000 cells/well show diameters in the range of ~ 200 – 550 µm between 1 and 7 d after seeding.

- The spheroid diameter increases linearly over seven days after seeding.
- Spheroids from smaller seeding densities grow faster than from higher seeding densities.

The MCF-7 spheroid morphology and growth behavior was also observed in various other studies that used the aggregation on a non-adhesive surface for spheroid generation. Ivascu and Kubbies (2006) for example prepared MCF-7 spheroids (5000 / 10.000 cells/well) in poly-HEMA-coated round bottom 96-well plates and observed a reproducible spheroid size (0.22 ± 0.03 mm^3, ~ 0.7 mm in diameter) and highly compact spheroids within the first 24 h after seeding. The latter was also observed by Nagelkerke et al. (2013).
Ho et al. (2012) generated MCF-7 spheroids with a seeding density of 50.000 cells/well in agar-coated (1 %) 96-well plates. They enhanced the cell aggregation by centrifugation and observed compact densely packed spheroids with a reproducible size (Ø = 1.1 ± 0.1 mm).
Lee et al. (2010) prepared MCF-7 spheroids with a seeding density of 400 cells/well in 96-well plates coated with 1.2 % agarose. They monitored spheroid growth over 13 d using light microscopy and observed tightly packed, round spheroids with a homogeneous size. They linked the strong cell-cell adhesion to the expression of E-cadherin on the surface of the MCF-7 cells. A growth curve of these spheroids showed a constant almost linear growth behavior with diameters of ~ 200 µm at day two and ~ 1000 µm at day ten after seeding. This would result in an average growth of 100 µm/d that is ~ 3 – 4-fold higher than the average growth of the spheroids prepared for the growth study in this thesis. This fast growth may be related to the smaller seeding density and the fact that the spheroids were fed every other day, whereas the spheroids in the study of this thesis were not fed at all.

Based on the results of the spheroid growth study shown here, seeding density and culture time were adapted according to the experimental requirements. Due to the dimensions of the PT-2 flow channel with a maximal height of 500 µm and a minimal height of 250 µm at the aperture, spheroids with diameters between 250 and 500 µm were used for the impedance measurements. Thus, the

intermediate seeding density of 3000 cells/well and a culture time of 7 days was chosen for regular MCF-7 spheroids.

6.8.2 Impact of Spheroid Fixation

The evaluation of the MFT measurements returned spheroid parameters indicating that it is possible to discriminate between spheroids in different stages of fixation.

- With increasing PFA concentration the spheroid impedance as well as the spheroid parameters R_{ext} and R_{int} decrease, while A_{sph} increases.
- Spheroid micromotion is gradually reduced in spheroids with higher levels of fixation.
- Spheroids pre-treated with increasing PFA concentrations show decreased tendency for deformation and penetration into the central opening of the channel.

The CPE parameter A_{sph} of the spheroid increased with increasing PFA concentration used for fixation towards values of the spheroid-free channel. This indicated a perforation of the membranes in the spheroid and would also explain the decreased intra- and extracellular resistance. Similar observations are reported in the doctoral thesis of Maximilian Oberleitner (2015). He investigated the cross-linking of MDCK-II cell monolayers using the ECIS technology. Upon addition of 1 % PFA the normalized resistance (at 316 Hz) was significantly reduced to 0.29 ± 0.01, whereas the change of the normalized capacitance (at 40 kHz) to 1.02 ± 0.06 within 3 h was almost negligible. In ECIS, the capacitance at high frequencies reflects the coverage of the working electrode with cells. After the fixation, cells were still adhered on the electrodes explaining the constant capacitance. The strong decline in resistance was supported by the results of a dye uptake study. The corresponding fluorescence micrographs can be seen in Fig. 68. The study was performed by Barbara Goricnik. Confluent NRK cell monolayers were cross-linked with 4 % PFA, 2 % PFA or not cross-linked. Then, a membrane impermeable FITC-labeled dextran (4 kDa) solution was provided extracellularly. The microscopic images show that cells which were not cross-

linked show no intracellular FITC fluorescence (A). However, a distinct intracellular green fluorescence was observed in approximately 50 % of the cells that were cross-linked with 2 % PFA (B). And for cells fixated with 4 % PFA intracellular FITC was detected in the whole cell layer (C).

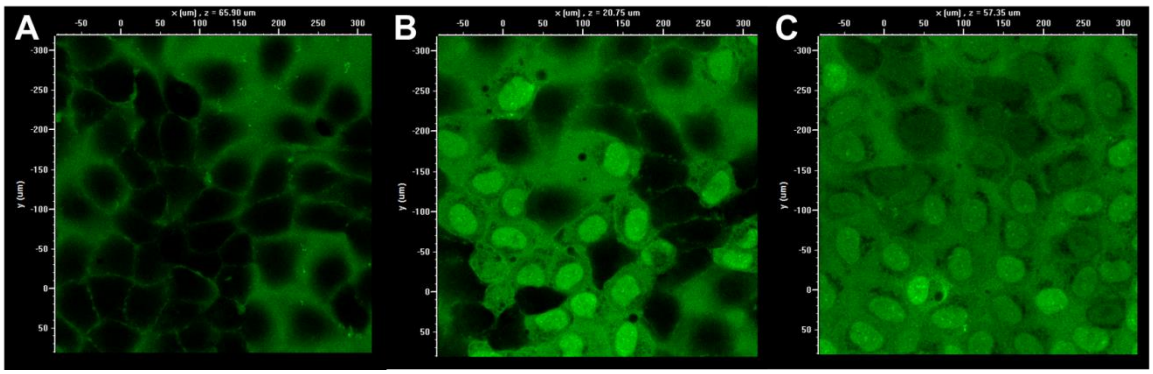

Fig. 68: Typical fluorescence micrographs of a dye uptake study. The study was performed on confluent NRK monolayer cells that were not fixated (**A**), cross-linked using 2 % PFA (**B**) or 4 % PFA (**C**). For microscopy a solution of membrane impermeable FITC-labeled dextran (4 kD) in PBS^{++} (1 mg/mL) was provided extracellularly.

The fact that a membrane impermeable dye was taken up by the cells after fixation with PFA clearly proved that the cross-linking process led to a membrane permeabilization. And this effect is also a feasible explanation of the results for cross-linked spheroids discussed above.

Results of RTC measurements proved that small fluctuations of cells in the spheroid, the so-called micromotions can be detected with the new setup. Moreover, spheroids with different levels of cross-linking could be distinguished showing a reduced micromotion for increasing PFA concentration (chapter 6.2). Micromotions are linked to shape fluctuations driven by metabolic activity. Lo et al. (1993) studied the micromotion of fibroblast cells using ECIS technology. They observed reduced cellular fluctuations when the cells were held at 27 °C instead of 37 °C or when they were deprived of extracellular glucose. This strongly indicated a link between micromotion and the activity of the cell metabolism. Tarantola et al. (2009) fixated monolayer MDCK-II cells with 4 % PFA and obtained very weak fluctuations that were similar to the ones seen for a cell-free electrode, whereas the viable unfixated cells showed strong fluctuations. All the results reported in the literature and in this study prove that micromotion is only

observed in living cells. The impedance of a viable cell monolayer is not a constant value as the current pathways around the cell bodies are constantly altered due to changes in cell shape and cell-cell junctions. The same applies for a spheroid. However, in a spheroid the current passes not just one layer of cells but several cell layers performing micromotion in three dimensions. Upon fixation the cells within the spheroid are mortified and freezed in their structure leading to an unchanged current pathway and consequently to a constant impedance value. These correlations make the RTC readings of spheroid micromotion a valueable parameter reflecting the viability or death of a spheroid.

The microscopic images taken during the impedimetric measurements showed a reduced tendency of spheroids to penetrate into the narrowed central part of the channel with higher levels of fixation. This penetration behavior indicated that with increasing level of fixation the stiffness was increased and the deformability and migration ability of spheroids was significantly decreased. This effect of fixation on tissues in general was also reported in literature (Kiernan, 2000). The cross-linking of proteins within the tissue enhances the mechanical stability and rigidity of the sample (Ganjali and Ganjali, 2013). This increased cellular stiffness after cross-linking was also demonstrated by AFM studies (Wu et al., 1998).

6.8.3 Impact of Spheroid Permeabilization

Saponin was used as detergent that should lead to the permeabilization of the cell membranes within the spheroid. The permeabilized spheroids were analyzed by a PrestoBlue® assay and by EIS measurements using the novel channel setup. For spheroids that were pre-incubated with an increasing concentration of saponin the following results were obtained:

- The spheroid impedance decreases for increasing saponin concentrations (Fig. 41).
- R_{ext} and R_{int} decrease for increasing saponin concentrations, while A_{sph} slightly increases for lower saponin concentrations and decreases for the highest saponin concentration (Tab. 14).

- The highest concentration of saponin (0.25 ‰) leads to the loss of cells on the spheroid surface and consequently to a reduced spheroid diameter (Fig. 42; B1, B2.1).
- The EC_{50} value of (0.10 ± 0.02) ‰ is in good agreement to the EC_{50} value determined with the PrestoBlue® assay (0.17 ± 0.01 ‰).
- Micromotion is significantly reduced in spheroids that were exposed to 0.1 ‰ and 0.25 ‰ saponin (Fig. 45).

The results clearly indicate that changes in spheroid morphology due to saponin exposure are detected by EIS measurements with the channel setup. With the gradual disintegration of the membranes within the spheroid the current can flow with less resistance through the spheroid. Consequently, the spheroid parameters R_{ext} and R_{int} were both expected to be reduced after permeabilization with saponin, whereas A_{sph} was expected to increase with inceasing levels of membrane permeabilization. The expected trend was in fact observed only for R_{ext} and R_{int}.

Thielecke et al. (2001) analyzed the permeabilization of T47D clone 11 human breast carcinoma spheroids using an impedance-based technique. They used planar circular gold electrodes (Ø = 100 µm) and placed spheroids that were exposed to the detergent Triton X-100 (10 %) or control spheroids on top of them. The measured data was fitted and the parameter R_{ser} was determined, which is a combination of the circuit elements for the resistance of the medium R_{med}, the total resistance of the extracellular space R_{ext} and the shunt resistance R_{shunt}, which depends on the sealing of the electrode against the culture medium by the spheroid. The intracellular resistance R_{int} and the total capacitance of the cell membranes were neglected. They observed alterations in the frequency range between 50 kHz and 500 kHz with a R_{ser} value of (10 ± 1) kΩ for a spheroid measured immediately after Triton exposure and a value of (16 ± 1) kΩ for the control spheroid. The reduced value for the Triton spheroid was explained by the disintegration of the lipid membranes and the resulting increase of the extracellular volume fraction within the tissue model. On the other hand a change of only 6 kΩ in R_{ser} shows that the experimental setup is not very sensitive.

Furthermore, R_{ser} is mainly affected by R_{ext} since R_{med} should stay constant, but R_{shunt}, which is dependent on the position of the spheroid on the electrode, can vary and influence R_{ser} as well. Overall, the obtained results are plausibly explained but the low sensitivity and reproducibility of the method should be kept in mind.

For A_{sph} no distinct trend was observed for concentrations between 0.01 ‰ and 0.1 ‰. For the highest concentration (0.25 ‰) however, A_{sph} was reduced in comparison to the control value. R_{int} for the highest concentration showed also an unexpected high value. The answer to these irregularities may be found in the microscopic images that revealed a reduced spheroid size after exposure to 0.25 ‰ saponin. The strong permeabilization of cell membranes especially at the outer spheroid surface may have led to the detachment of the outermost cell layers during the transfer of the spheroid from the plate where it was incubated with saponin into the channel. The extent of detached cells is variable and leads to differences in the spheroid diameter. For this purpose, three different cases were observed during the measurement: (i) the spheroid was too small to be held back at the aperture and passed it immediately (baseline impedance), (ii) an intermediate spheroid size led to a slow but complete migration into the aperture (increased impedance) or (iii) the spheroid size was still big enough resulting in a slow and partial penetration into the central aperture (reduced impedance). Spheroid dielectric parameters were only determined for two out of four measurements because the spherois passed the channel aperture immediately and only the pure channel impedance could be measured. However, the values of the remaining measurements are still problematic reflecting especially channel-related impedance variations of spheroids.

Nevertheless, it also shows that saponin concentrations above 0.1 ‰ clearly affect the spheroid viability. The two EC_{50} values determined by PrestoBlue® viability assay (0.17 ± 0.01 ‰) and evaluated from the impedance data (0.10 ± 0.02 ‰) confirm this observation. The fact that both values are in good accordance clearly shows: (i) that a standard cell viability assay can be used also for spheroids and (ii) that the assessment of cytotoxicity by impedance analysis provides similarly reliable results compared to standard cell viability assays but without the use of labels.

There is a high diversity of saponins with cytotoxic potential tested on different cell lines in monolayer culture (Sparg et al., 2004; Podolak et al., 2010). Therefore, there is a huge variance in the cytotoxicity reported in literature making a comparison with the results from this thesis difficult. Awasare et al. (2012) determined the cytotoxicity of the saponin Manilkoraside on MCF-7 monolayer cells using a MTT assay. They found an EC_{50} value greater than 0.08 ‰, which is also in good accordance to the results of this thesis.

As described before (chapter 6.8.2), micromotion of cells within a spheroid is linked to cell viability. When the cells are alive impedance fluctuations can be observed, whereas no fluctuations are observed when the cells are dead. For increased membrane permeabilization an increasing number of cells within the spheroid is dead. This was confirmed by the decreased variance V_{32}, a parameter reflecting the extent of micromotion in the spheroid. The differences in variance for different conditions were however, only in two cases significant, which is related to the high standard error.

6.8.4 Effect of Osmotic Pressure on Spheroids

Swelling and shrinking of spheroids was induced by exposure to buffers with different non-isotonic osmolarities. Via microscopy and EIS the morphological alterations were followed, yielding the following results:

- Exposure to hypo-, iso and two hyperosmotic buffers leads to reproducible changes in spheroid diameter.
- Using the channel setup distinct changes in impedance are recorded for spheroids in presence of different osmotic buffers.
- R_{ext} decreases for inceasing osmolarity. R_{int} shows the highest value for spheroids in isotonic buffer, a medium value for spheroids in hypotonic buffer and the two lowest values for the hypertonic buffers I and II. A_{sph} is slightly increased for increasing osmolarity.
- The micromotion is enhanced in swollen spheroids (hypotonic) and reduced in shrinked spheroids (hypertonic I, II).

The microscopic analysis clearly proves that the tissue models react to the different osmolarities (Fig. 47). An increase in diameter is caused by swelling of the cells in the spheroid due to water influx. Shrinking of spheroids is caused by water efflux from cells into the extracellular buffer. When the buffer was changed from isotonic to hypotonic or hypertonic osmolarity the main change in spheroid diameter was observed within 5 min followed by a further slow equilibration to the new buffer within 25 min. Following spheroid swelling or shrinking with the impedance setup, such changes manifested themselves in an impedance increase or decrease, respectively.

O'Connor et al. (1993) measured the cell volume changes in monolayer cultures of primary astrocyte cultures via electrical resistance measurements of the extracellular space. The setup comprises a flow channel with a central restriction parallel to the bottom of the flow chamber and large gold electrodes on either side of the channel. In the central restriction they placed a cover glass with an adherent cell monolayer (Fig. 69).

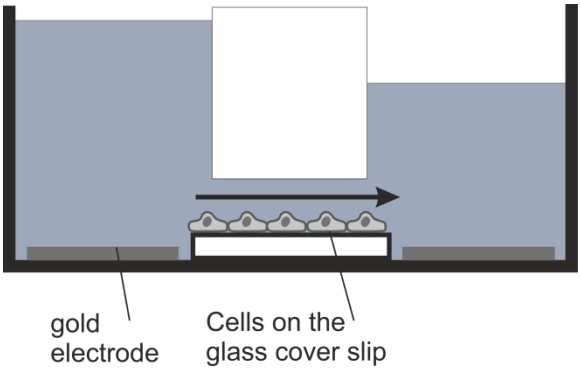

Fig. 69: Illustration of the chamber used for resistance measurements showing planar gold electrodes on either side of the channel and cells grown on a glass cover slip. The height of the fluid-filled chamber above the cells is ~ 100 µm.

When the cells were exposed to the hypoosmotic solutions (93 – 193 mOsmol/kgH_2O) via constant perfusion they showed a rapid swelling due to water influx. Consequently, the height of the electrolyte above the cell layer decreased resulting in an osmolarity dependent increase in the measured resistance through the channel. When the cells were exposed to hyperosmotic solutions (343 – 493 mosmol/kgH_2O) the cells shrinked, the channel height increased and the measured resistance of the channel decreased. This indirect

measurement of osmolarity-dependent cell volume changes nicely confirms the swelling and shrinking of cells, which was also observed in this thesis.

A more complex way to study osmotically induced cellular volume changes was performed by Sasser et al. (1993). They studied the changes caused by perfusing a rat's hind leg with an isotonic (318 mosmol/kg), hypotonic (150 mosmol/kg) or hypertonic (600 mosmol/kg) solution. Using EIS with a four electrode configuration with stainless steel hypodermic needles they measured changes in impedance developed across the tissue segment under study. They fitted the results to determine the average resistance of the extracellular R_e and intracellular R_i compartment as well as the total membrane capacitance C_m. They observed constant values for R_e, R_i and C_m when the tissue was perfused with isotonic solution. Upon application of hypotonic solution R_e and C_m increased whereas R_i was decreasing. During perfusion with hypertonic solution R_e and C_m decreased and R_i increased. They reasoned the experimental results with the increase or decrease of the cell volume fraction *p,* which was defined as follows:

$$p = \frac{V_i}{V_i + V_e} \qquad \textbf{Eq. 6.1}$$

with the intracellular volume V_i and the extracellular volume V_e.

Based on the assumptions that (i) tissues consist of homogeneous suspensions of spherical cells with membranes of negligible thickness and (ii) extra- and intracellular spaces are entirely resistive and the cell membranes are capacitive, they evaluated the theoretical dependence of the equivalent circuit parameters on the cell volume fraction. They found that for increasing cell volume fraction R_i decreased whereas R_e and C_m increased. This theoretical dependence fitted very well to the experimentally observed parameter values of Sasser et al (1993).

Comparing the theoretical dependence with the results from the work presented in this thesis (Tab. 15) only the parameter R_{ext} is in good accordance. A_{sph} shows a completely contradictory trend and R_{int} shows accordance only for the spheroid in hypo buffer indicating that there are other factors beside the volume fraction that influence the parameters. As pointed out by Sasser et al. (1993) the cells contain a certain intracellular ion concentration. When the cell is shrinking the water efflux leads to an increased concentration of ions and consequently to the

decrease in R_{int} for spheroids in hypertonic solutions. The observed behavior of A_{sph} is unclear at the moment.

The process of swelling and shrinking was also affecting the micromotion of the spheroids. For swollen spheroids an increased variance was observed, whereas for shrinked spheroids the variance was reduced. In shrinked spheroids the water deprivation might cause a less active metabolism and consequently a reduction of metabolically driven processes as for example reorganization of the cytoskeleton and cell-cell contacts or transport processes inside the cell. Dehydration of cells is reported to cause protein unfolding and membrane disturbances and can also lead to increased formation of reactive oxygen species with consequences on overall metabolism (Potts, 1994; França et al., 2007).
In swollen cells the increased micromotion might be related to cellular processes dealing with the adaption to the strained cell morphology. The fundamental mechanisms are, however, unclear.

6.8.5 Influence of Cytochalasin D on Spheroids

Exposure of MCF-7 spheroids to cytochalasin D for different times caused measurable but subtle alterations. The results observed in impedimetric measurements and microscopic studies are summarized below:

- The time course of impedance magnitude is constantly increasing for all conditions of cytD treated spheroids, whereas control spheroids show a stable impedance over time. With increasing exposure time of spheroids to cytD the change in impedance magnitude decreases.
- R_{ext} and R_{int} values are decreased for increasing exposure times in relation to spheroids exposed to cytD for 2 h, but do not fall below the values of control spheroids. A_{sph} shows no obvious trend.
- CytD treated spheroids migrate further into the aperture than control spheroids.

- The micromotion of spheroids that were incubated with cytD for 2 h is increased, whereas longer durations evoke micromotion similar to control spheroids.

Oberleitner (2015) investigated the effect of cytD on MDCK-II monolayer cells using a combined setup for QCM and ECIS. He observed a concentration dependent (0.1 / 1.0 / 5.0 µM) decrease of the normalized raw resistance and an increase in raw capacitance. Especially for the 1 and 5 µM cytD treated cells the resistances reached almost levels of a cell-free electrode within 1 – 2 h assuming a strong reduction of the cytomechanical stiffness and a degradation of barrier-forming tight junctions. Stevenson and Begg (1994) also investigated MDCK-II cell response to cytochalasin D (~ 4 µM, 1 h, 37 °C). They observed a distinct decrease in the transepithelial resistance upon incubation with 4 µM cytD. This finding was underlined by immunostained actin structures, which showed distinct disruption of actin after treatment with 4 µM cytD. Wakatsuki et al. (2001) used for their investigations fibroblast monolayer cells and a fibroblast populated matrix, a thin ring-shaped 3D tissue model prepared by seeding fibroblasts in collagen and culturing them in the gel for two days. For cells exposed to 2 µM cytD for 30 min almost all long actin filaments were disrupted and showed large focal aggregates of F-actin. Uniaxial stress-strain measurements showed that the stiffness was significantly reduced in comparison to the control.

The typical alterations after cytD treatment like a reduced cell or tissue stiffness as well as a decreased resistance in comparison to a control as observed by Oberleitner (2015) and Stevenson and Begg (1994) could not be observed directly through the measurements in this thesis. However, the strong penetration into the aperture compared to the control spheroid indicated a reduced spheroid stiffness. The time courses of impedance were at first sight completely contradictory to the results provided by other studies, showing higher impedances or R_{ext} and R_{int} values, respectively, for cytD treated spheroids than compared to control spheroids. Spheroids incubated for 2 h showed the highest R_{int} and R_{ext} values and with increasing incubation time the spheroid impedances decreased but were never significantly lower than the values for the control indicating that actin filament degradation might have occurred only in the outer cell layers of the spheroid. The resulting reduction in stiffness caused the

penetration of the spheroid into the aperture that might have led to the slow but constant increase in impedance over time for spheroids exposed to cytD for different times. Consequently, this effect might have interfered with a possible decrease in impedance due to cytD related actin disruption.
In contrast to monolayer cells, which were reported to show alterations already 0.5 – 1 h after addition of cytD, the spheroid response appeared delayed, most likely due to the limited diffusion into the spheroid. Analysis of the RTC data indicated strong micromotions in spheroids exposed to cytD for 2 h, whereas longer incubation times unexpectedly showed similar values like the control. Micromotion is also driven by actin association and dissociation and should therefore be reduced when cytD is applied. This was observed by Lo et al. (1993) and Opp et al. (2009) who reported less fluctuations for increasing concentrations of cytD and cytB in monolayer experiments.
The overall contradictory behavior of cytD treated spheroids in this study can not be explained properly and needs more investigation. Concentration dependent measurements and immunostaining of cytD treated spheroids might help to gain a better understanding of the processes.

6.8.6 Spheroid Response to Hyperthermia

Hyperthermia was applied for 1 h and 3 h on MCF-7 spheroids and the following results were obtained by impedance analysis and PrestoBlue® assay:

- Spheroid exposure to 41 – 45 °C for 1 h results in similar time courses of impedance like for the control spheroid and indicates no cytotoxicity.
- Exposure for 3 h at 41 – 45 °C results in a temperature dependent decrease of the spheroid impedance.
- The spheroid parameters R_{ext} and R_{int} decrease with increasing temperature applied for 3 h. A_{sph} values are low and stable for spheroids exposed to 37 – 43 °C and clearly increase for spheroids at 45 °C.
- Micromotion analysis for spheroids exposed to high temperatures for 3 h show decreasing values of variance for increasing temperature.

- A PrestoBlue® assay shows no cytotoxicity for 1 h and 3 h of exposure at 41 – 45 °C.

Environmental factors like hypoxia and low-pH regions within tumors make cancer cells more sensitive to hyperthermia than normal cells (Song et al., 1993). HT can induce several alterations in cells like protein unfolding and aggregation, disruption of the cytoskeleton, breakdown of intracellular transport processes, alterations in the cell membrane and a cell cycle arrest in the G2/M phase (Richter et al., 2010; Furusawa et al., 2012). Depending on the applied temperature and exposure time HT can induce intrinsinc or extrinsic apoptotic pathways (Ahmed et al., 2015). HT was also reported to induce the production of ROS (Hirano et al., 2005; Zhao et al., 2006).

Wartenberg et al. (2005) studied the effect of HT on DU-145 prostate cancer spheroids. Spheroids with diameters in the range of 300 – 400 µm were exposed to 42 °C for 0 – 120 min, which resulted in increasing lethality with duration of exposure and they observed a maximal lethality value of 49 ± 7 % after 120 min using the lethal cell stain Sytox green. Furthermore, a 30 min exposure of spheroids at 42 °C induced a clear increase in ROS levels.

Durand (1978) compared the effect of hyperthermia (39 – 45°C, 0 – 6 h) on Chinese hamster V79-171 spheroids that were 1 d and 20 d old. For spheroids exposed to 39, 41 and 42 °C no influence of HT was observed independent of spheroid age. Exposure at 43 °C for 6 h caused a decrease of viability to 10 % for 1 d spheroids and 30 % for 20 d spheroids. The exposure to 44 °C reduced the viability to 6 % for 20 d spheroids (after 6 h) and to 0.2 % for 1 d spheroids (after 3 h). Exposure to 45 °C for 1 h caused a decrease of cell viability to under 1 %.

In this thesis it was possible to measure the effect of hyperthermia on MCF-7 spheroids. This effect was dependent on the exposure time. Spheroids exposed to different temperatures for 1 h showed no thermal impact, whereas spheroids exposed for 3 h showed a temperature dependent decrease in impedance as well as in R_{ext} and R_{int} values, respectively. Exposure to 45 °C for 3 h reproducibly caused the highest impact on spheroids, which is in good accordance to the results of Durand (1978) illustrated above. Very low R_{ext} and R_{int} values, a high spheroid capacitance of $7 \cdot 10^{-9}$ $Fsn^{-1}cm^{-2}$ and strongly reduced micromotion in comparison to control spheroids indicated that the heat shock induced

irreversible injuries and membrane damage to the spheroids. Exposure to 41 °C and 43 °C are considered to be mild HT temperatures. They clearly show an effect on spheroids with slightly reduced values of R_{ext} and R_{int}. The spheroid capacitance is, however, similar to that of control spheroids, indicating that the membranes are intact.

Micromotion is reduced in both cases and for 43 °C significantly different to the control value. Mild hyperthermia at these temperatures was also observed by Durand (1978) and Wartenberg (2005) discussed above. These results show that temperature influences the cells. In this PhD thesis, the comparatively high temperatures led to a decrease in micromotion and consequently the treated spheroids were assumed to show less metabolically driven dynamic alterations of the cytoskeleton, membranes and cell-cell contacts.

The performed PrestoBlue® assay, which was conducted at 37 °C, showed contradictory results. Even for exposure to 45 °C for 1 h and 3 h no cytotoxicity was observed. Instead, the heat treated spheroids appeared more viable than the control spheroids as they converted more dye and produced higher fluorescence intensities. The PrestoBlue® assay principle is based on the reduction of blue resazurin to the pink resorufin and the oxidation of intracellular NADH to NAD^+. The cells generate NADH for example via glycolysis. Muckle and Dickson (1971) investigated the effect of hyperthermia (42 °C) on rabbit VX2 carcinoma cells *in vitro*. They observed the decrease in viability of these cells. However, glycolysis of the tumor cells was not affected by hyperthermia.
This observation might explain the reduced viability detected by impedance analysis, whereas the PrestoBlue® assay showed no reduction in cell viability. There might be, however, further factors influencing PrestoBlue® assay results. Pagliacci et al. (1993) studied the antiproliferative effect of genistein on MCF-7 and other cell lines. By counting of the cell numbers they proved that cell proliferation was significantly reduced in the treated cell lines and revealed that the cells showed a G2/M cell cycle arrest. However, when they used the tetrazolium-based colorimetric MTT assay, which is similar in principle to the PrestoBlue® assay, they failed to confirm the growth inhibition of genistein. They found out that the drug increased the mitochondrial number and activity that influenced the MTT reduction to formazan and led to the underestimation of the

antiproliferative effect of the drug.

The reasons for the PrestoBlue® assay results might be complex and include different reasons leading to the enhanced metabolic activity after hyperthermia treatment. Overall, the PrestoBlue® assay was not the adequate method to determine the effects of hyperthermia on spheroid viability and a direct comparison with the results of the impedimetric analysis is not reasonable.

6.8.7 Potential Phototoxicity of CaAM in Spheroids

The phototoxic potential of calceinAM was investigated on MCF-7 monolayer cells and spheroids leading to different results:

- Cells in 2D culture stained with calceinAM show a decrease in impedance magnitude after irradiation at the dye's excitation wavelength for 3 min, while exposure to other wavelengths has no effect.
- CalceinAM stained cells exposed to the excitation wavelength detach from the substrate in the exposed area.
- Unstained and calceinAM stained spheroids irradiated for 10 min at the excitation wavelength show stable time courses of impedance magnitude.
- The time course of R_{ext}, R_{int} and A_{sph} for stained and irradiated spheroids shows no remarkable alterations to that of the control spheroid.
- Phase contrast images document dead cells on the spheroid surface at the end of the measurement for stained and irradiated spheroids.

The impedimetric and microscopic results for cells in 2D monolayers showed that, in contrast to the general assumption that the imaging process has no influence on cell physiology, exposure of cells containing certain fluorochromes, in this case the live stain calceinAM, can very well lead to phototoxicity and consequently to decreased viability. This was also reported by Knight et al. (2003) who seeded bovine articular chondrocytes in a three-dimensional agarose gel, stained the cells with 5 µM calceinAM and exposed them for ~ 1 h to laser excitation light (λ_{exc} = 488 nm) at RT. Afterwards, the cell viability was evaluated using a Live/Dead assay. The result showed a viability of less than 10 % for

these cells, whereas stained cells without irradiation showed a viability of over 90 %. The increased cell death was linked to the light-induced generation of reactive oxygen species by calceinAM. Depending on the level of produced ROS apoptosis or necrosis can occur (Simon et al., 2000; Robertson et al., 2009). ROS includes species like superoxide anions, hydrogen peroxide, hydroxyl radicals or peroxyradicals. When these molecules appear in the cell they can be neutralized by endogenous enzymes like superoxide dismutase, glutathione peroxidase and others, or they can react with radical scavengers like exogenous antioxidants (e.g. vitamin C). In the case of very high ROS levels however, these mechanisms are overloaded and the ROS cause oxidative stress. This can result in cleavage of DNA strands, DNA-protein cross-linking or ROS-mediated protein modifications. ROS can also induce modification of lipids at double bonds of unsaturated fatty acids, which can lead to a loss of membrane integrity and consequently leakage of proteases or influx of Ca^{2+} and finally to the induction of necrosis (Zong and Thompson, 2006).

The results for 3D cultured cells are at first sight inconsistent with the 2D results, since no phototoxic effect could be observed for calceinAM stained and irradiated spheroids by impedance analysis. However, the microscopic images revealed dead cells at the spheroid surface. It is assumed that due to the limited penetration of calceinAM into deeper cell layers of the spheroid the fluorophore is predominantly located in cells at the surface of the spheroid (can be seen also in chapter 5.4 Fig. 30, 31). Consequently, the irradiation caused cell death of the outermost cell layers of the spheroid, whereas the majority of cells within the spheroid was unaffected. This was also reflected by the control-like impedance values at the end of the measurement and the stable values for R_{ext}, R_{int} and A_{sph} during the measurement. In summary, it can be stated that only a superficial phototoxic effect was observed due to incomplete staining of the spheroid. Furthermore, it is assumed that the sensitivity of the impedimetric analysis via the novel setup is not high enough to detect the cell death of a minority of cells in the outer shell, but rather reflects the physiological state of the majority of cells within a spheroid. Slight decreases in impedance magnitude in longtime measurements (e.g. Fig. 60 B) might indicate a reduced viability but these are also seen for control spheroids indicating an undersupply with nutrients.

6.8.8 Potential Phototoxicity of C-dots in Spheroids

The applicability of C-dots as photosensitizer was analyzed for MCF-7 monolayer cells and spheroids using the novel impedimetric setup in combination with microscopy. An analysis of cytotoxicity and phototoxicity led to the following results:

- C-dots at a concentration of 1.5 mg/mL are not cytotoxic for MCF-7 spheroids in the dark (Fig. 62).
- C-dots at a concentration of 1.0 mg/mL are phototoxic after 3 min irradiation of MCF-7 monolayer cells at the C-dot excitation wavelength (Fig. 64).
- A 15 min irradiation (C-dot excitation wavelength) of spheroids pre-incubated with 1.5 mg/mL C-dots causes a phototoxic effect marked by the channel transition of the spheroid 6 – 8 h after irradiation. Control spheroids show a stable impedance or delayed channel transition (Fig. 66 right).
- Phase contrast images prove that C-dot spheroids exposed to excitation light are strongly damaged, exhibiting a reduced diameter and dead cells on the surface (Fig. 66 left).
- Spheroid parameters R_{ext}, R_{int} and A_{sph} are stable for the control spheroid. For irradiated spheroids R_{ext} and R_{int} are decreasing from t = 4.5 h and A_{sph} is decreasing slightly from the start (Fig. 67).

Michael Lemberger (2015) prepared N-doped C-dots from starch and L-tryptophan by hydrothermal preparation and determined their cytotoxicity with a Presto assay and ECIS on monolayer cells. For this purpose, NRK monolayer cells were incubated with concentrations between 0.1 and 4.0 mg/mL for 24 h. He found an EC_{50} value of 1.1 mg/mL by classical Presto-based analysis, which was in good accordance to the ECIS results that showed a cytotoxic effect only for concentrations above 1 mg/mL.

In literature there are a lot of reports on the cytotoxicity of C-dots that were however, prepared by different techniques, with different functionalizations and

tested on different cell lines. Due to different functional groups on the surface and other characteristics there are differences in the observed cytotoxicity in literature. In order to do a meaningful comparison, references who also worked with N-doped C-dots were evaluated. Liu et al. (2011) for example worked with such C-dots, which were prepared from glycerol, and observed cytotoxicity on human hepatocellular carcinoma cells (Hep-G2) for concentrations from 0.4 mg/mL. Other N-doped C-dots prepared from ginger and tested on human breast cancer cells (MDA-MB-231) induced cytotoxicity only for concentrations higher than 1.4 mg/mL (Li et al., 2014).

These few results already show that the use of different cell lines as well as different reactants, dopants and methods of synthesis cause variations in the extent of cytotoxicity. Therefore, the most important point of reference was Lemberger's doctoral thesis with the characterization of the exact same C-dots as used in this thesis. The critical concentration of 1 mg/mL for monolayer cells was increased for spheroids, which showed no decrease in viability after treatment with 1.5 mg/mL. This was expected as spheroids are known to exhibit multicellular resistance dicussed in detail in chapter 1.1.3. Lemberger (2015) also studied the phototoxicity of his particles, showing that they produced ROS upon irradiation with the excitation wavelength. In a cellular study, confluent NRK cells were incubated for 1 h with 1.0 mg/mL C-dots and irradiated for 3 min. The immediate decrease in impedance magnitude clearly indicated a phototoxic effect of the C-dots. The induced cell death via apoptosis was proven by staining with Annexin V FITC/PI. The analog experiment performed in this thesis used MCF-7 monolayer cells instead of NRK cells and resulted in a less pronounced phototoxic effect. Furthermore, the control cells which contained C-dots but were not irradiated showed in some cases a reduced viability, too. Therefore, the optimal concentration of C-dots used for MCF-7 monolayer cells should be lower than 1.0 mg/mL in order to eliminate a combined effect of phototoxicity and dark toxicity.

Spheroids that were pre-incubated with 1.5 mg/mL C-dots and irradiated for 15 min showed a reproducible passage through the central opening of the EIS flow channel 6 – 8 h after irradiation and a completely damaged spheroid at the end of the measurement. The transition might be linked to the phototoxic damage

of cells and the weakened spheroidal integrity leading to the enhanced deformability and migration through the aperture. This effect was also reflected by the decrease in R_{ext} and R_{int} values after an initial increase. The non-ideal spheroid capacitance was decreasing after irradiation, eventually indicating the spheroid passing through the channel. The C-dot-loaded control spheroids, which were not exposed to excitation light, showed no or a delayed passage of the central channel opening indicating a cytotoxic effect of the C-dots. This was surprising since the EIS cytotoxicity measurements under the same conditions showed no effects. Parameters, which were different here, were the use of another flow channel and the control spheroid was at room temperature while the C-dot spheroid was exposed. Both are unlikely to affect the spheroid integrity that much to cause a transition so it has to be concluded that a dark toxicity is seen in some cases for C-dot concentration of 1.5 mg/mL.

In summary, the C-dots used in this thesis induced phototoxicity on MCF-7 monolayer cells and spheroids. However, due to the casual occurrence of dark toxicity the experiments should be repeated with lower C-dot concentrations before a final judgement can be given.

6.8.9 Results Overview

MCF-7 tumor spheroids served as 3D tissue model to measure their response to different stimuli. This way, the applicability of the novel EIS-based channel setup was tested. Tab. 18 provides an overview of the results for the different experimental treatments mimicking different scenarios of cell death in a spheroid. Generally, it was found that spheroid death is linked to a decrease in overall impedance and the spheroid parameters R_{ext} and R_{int}, whereas A_{sph} was generally increased. A decrease of A_{sph} was seen only for permeabilized spheroids (0.25 ‰ saponin) and C-dot pre-incubated and irradiated spheroids. These spheroids showed a disintegrated structure and tended to penetrate and sometimes pass the central channel. CaAM stained and irradiated spheroids showed overall stable values indicating that these spheroids were mainly intact and viable.

Tab. 18: Overview of the trends for R_{ext}, R_{int} and A_{sph} indicated by the direction of the arrows and determined for the different treatments applied to MCF-7 spheroids in this chapter. The red stars mark the treatments that led to a passage of the spheroid through the channel narrowing.

Treatment	Notes	IZI	R_{ext}	R_{int}	A_{sph}	Micro-motion
Cross-linking	Increasing PFA concentration	↓	↓	↓	↑	↓
Osmotic pressure	Increasing osmolarity (Hypo>Iso>Hyper)	↓	↓	↓	↑	↓
Hyperthermia 3 h	Increasing temperature	↓	↓	↓	↑	↓
Cytochalasin D	Increasing incubation time	↗↘	↗↘	↗↘	→	↗↘→
Phototoxicity CaAM	Increasing time after irradiation	→	→	→	→	
Permeabili-zation	Increasing saponin concentration	↓★	↓	↓	↗→↘	↓
Phototoxicity C-dots	Increasing time after irradiation	↓★	↓	↗↘	↓	

The micromotion is also a good indicator for spheroid viability. In most cases of spheroid death micromotion was reduced, reflecting a decreased metabolic activity. Tarantola et al. (2009) showed that micromotion was reduced for increasing concentrations of nanoparticles and thereby proved that micromotion is a good indicator for cytotoxicity. In comparison to the results of a standard MTS cytotoxicity assay the micromotion results were similar but moreover they could be performed without labels and in real-time.

Spheroid treatments like permeabilization and exposure to a hypoosmotic buffer are reflecting necrotic cell morphology changes. Thereby, cell swelling is an early hallmark in necrosis and breakdown of the plasma membrane occurs in the end. Swollen spheroids show increased values in impedance and micromotion, which is not seen for spheroids with any other treatments. Once the membrane is

disrupted the values for impedance and micromotion are decreased similar to the remaining treatments. Therefore, it is difficult to distinguish between different cell death types. This would require other experimental designs and the verification with other techniques, for example different stainings like Annexin V for apoptosis detection. Microscopic analysis of a stained spheroid could be performed simultaneous with the impedance measurement, provided that the microscope and impedimetric instrumentation can be combined in one setup.

Overall, it can be stated that the novel setup is applicable to measure and analyze the dielectric properties of spheroids in steady state and the variance of spheroid related internal shape fluctuations, which reflects a new measurement mode for spheroids. The new EIS setup has, however, also a few constraints like the limited suitability for long-term studies. Due to the channel design the spheroid stopps the fluid flow through the channel when it is trapped at the aperture leading to a local decrease of nutrients around the spheroid. This can cause a reduced viability of the spheroid when measured for a long time without repositioning and medium exchange. The block of fluid flow is also the reason why spheroids were in most experiments pre-incubated with the different stimuli instead of adding them during the impedance measurement, as performed e.g. in ECIS measurements. This makes it almost impossible to measure immediate spheroid responses to stimuli.

7 Impedimetric Model Studies on Cardiospheres

Cardiac tissue engineering is a field of research that is constantly advancing to gain improved model systems for cardiac development studies and as therapy for cardiac repair (Eschenhagen and Zimmermann, 2005). Especially the progress in stem cell research promotes the development of appropriate models like 3D *in vitro* cardiomyocyte spheres (Nguyen et al., 2014; Beauchamp et al., 2015). But before new model systems can be used, for example for the development of new therapies or the detection of cardiotoxicity, they need to be characterized properly. The contractile phenotype is an important indicator, which can be studied by modulating cardiac beat rate with substances of known effect using different techniques like analysis of video recordings and calcium imaging (Hossain et al., 2010; Hayakawa et al., 2012) or field potential measurements and patch clamp recordings (Caspi et al., 2009; Abassi et al., 2012). The development of new techniques for readout of cardiosphere viability and beating behavior should go side by side with the development of new 3D models. In this chapter the applicability of the developed EIS-based channel setup to study cardiospheres was investigated. For this purpose, cardiospheres were generated from Cor.At® cells by the hanging drop technique or by the formation on a non-adhesive surface. The beating behavior of the Cor.At® cardiospheres was modulated by removal of extracellular Ca^{2+} or by addition of 1-heptanol or isoprenaline. The analysis of the beating efficiency was performed by RTC measurements and subsequent data evaluation via a *LabView*-based software (written by J. Wegener), determining parameters like the beats per minute and the amplitude of the beating related fluctuations.

7.1 Characterization of Cor.At® Cardiospheres

For the generation of cardiospheres from Cor.At® cells the hanging drop technique and the formation on a non-adhesive surface were pursued as described in chapters 4.1.4 and 4.1.5. The formation and beating of cardiospheres was observed and documented using phase contrast microscopy or the digital microscope.

Microscopic Characterization of Cor.At® Cardiospheres

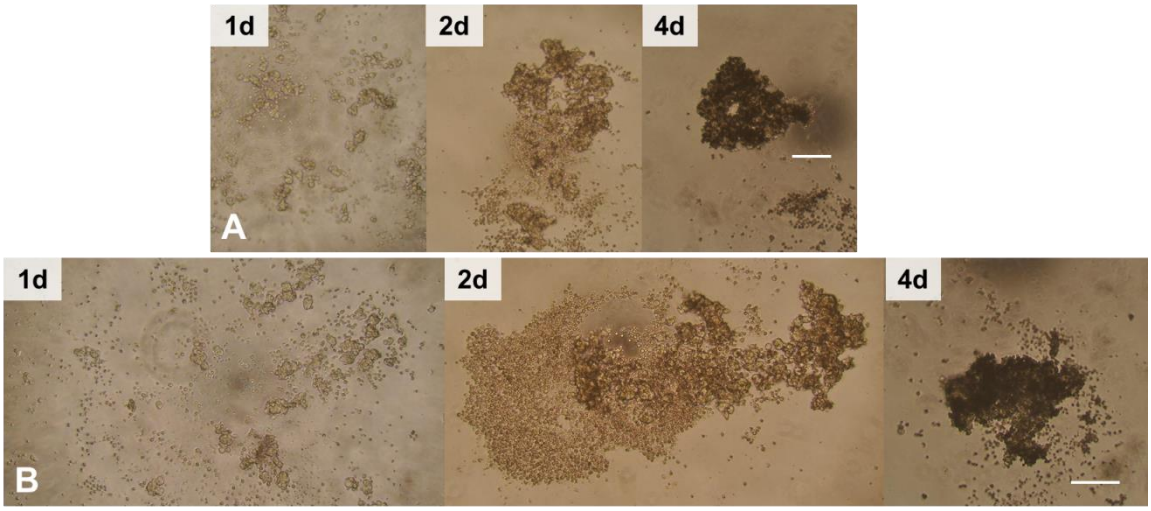

Fig. 70: Typical micrographs documenting the development of two cardiospheres (**A**, **B**) over 4 d that were generated by the hanging drop technique with a seeding density of 6000 cells/drop (scale bars: 200 µm).

The hanging drop technique was chosen in the first set of experiments. Typical micrographs (Fig. 70) show the development of two cardiospheres (A, B) over four days. At the first day after seeding there are mainly small cell aggregates and single cells in a random distribution. The small aggregates are already contracting regularly, while the single cells show no beating. On the second day after seeding single cells and small cell aggregates accumulate. Until day four after seeding the aggregates adhere to each other and compact. They appear darker than the days before and beat very slowly. All cardiopheres that are generated by hanging drop culture have a very irregular shape.

Also shapes that are not appropriate for impedance measurements in the flow channel are obtained, like the cardiosphere in image A 4 d, which has a cell-free gap in the center.

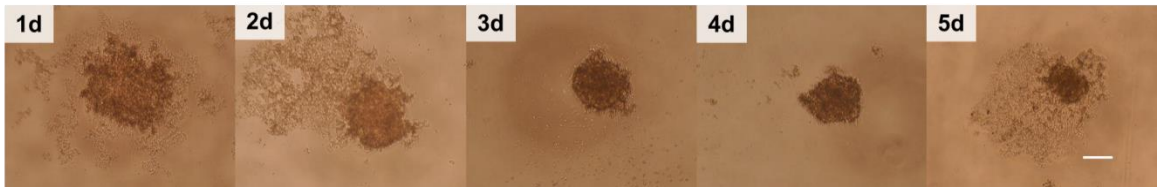

Fig. 71: Typical micrographs documenting the development of a cardiosphere over 5 days generated by the non-adhesive surface technique with a seeding density of 6000 cells/well (scale bar: 200 µm).

In the second set of experiments higher numbers of Cor.At® cells were available and in addition to the hanging drop culture the formation of cardiospheres on a non-adhesive surface was tested. In Fig. 71 one typical cardiosphere prepared in the 96-well plate is followed for 5 d. The cells aggregated to each other much faster than compared to the hanging drop method. On the first day after seeding most cells are adhered to each other, forming a flat aggregate of regularly beating cells. Some single non-beating cells are observed in the periphery of the aggregate. On the second day the aggregate is smaller than on day one and more single cells are observed in close proximity of the aggregate. Three and four days after seeding the compaction of the aggregate to a cardiosphere can be observed. This is accompanied by a further size reduction and a darker appearance of the cardiosphere. The shape is reproducibly smoother and more spherical than for cardiospheres from hanging drop culture. On day five after seeding a decomposition of the spheroid is observed. The size is again reduced and several single cells that detached from the cardiosphere are lying around it. The aggregates on different days show all a regular beating behavior. Due to the more reproducible shape of cardiospheres prepared in the coated 96-well plate they were preferred over hanging drop spheroids and used for most impedance measurements.

Impedimetric Characterization of Cardiospheres in the PT-1 Flow Channel

All measurements with cardiospheres were performed with the PT-1 flow channel on ITO-glass. Due to the different channel dimensions and the new spheroid model frequency scans were performed to identify a suitable monitoring frequency.

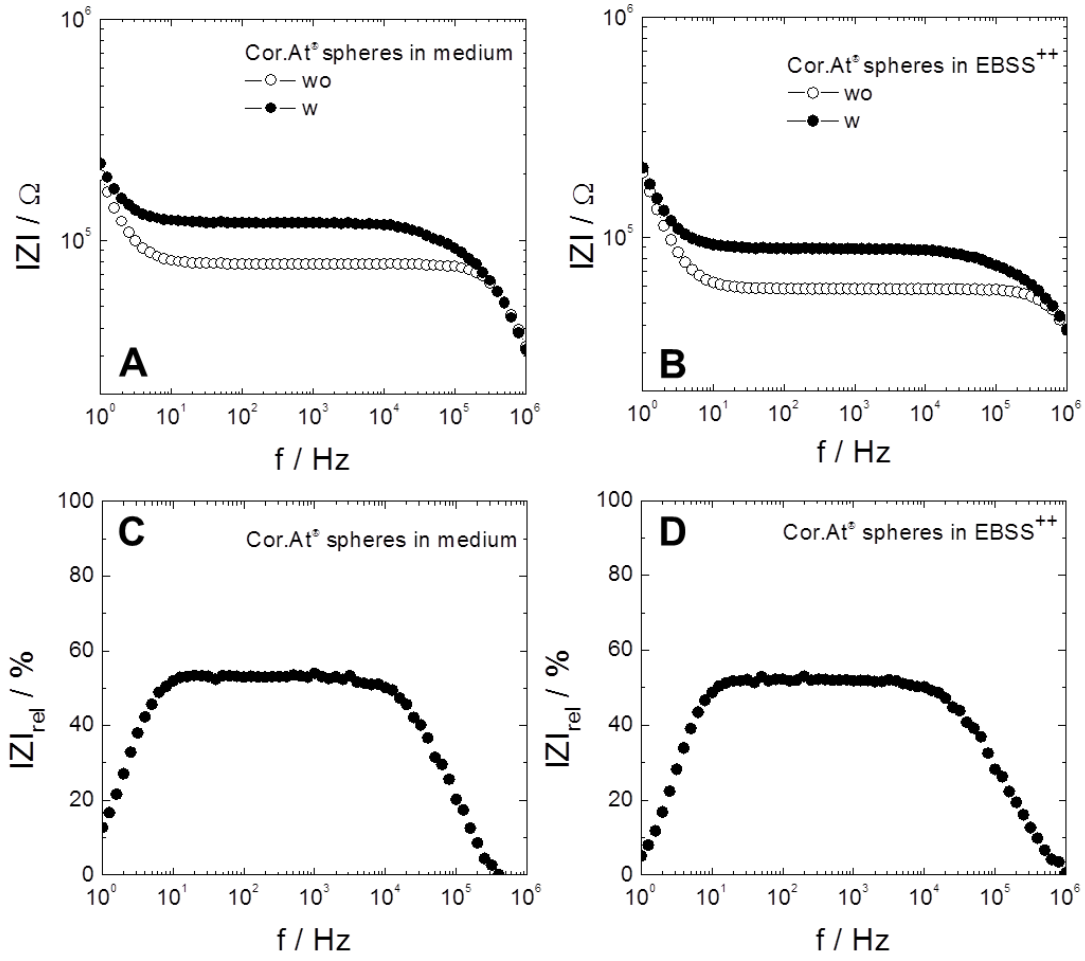

Fig. 72: Typical impedance spectra conducted with (**w**) and without (**wo**) cardiosphere in the PT-1 flow channel on ITO-glass measured in Cor.At® culture medium (**A**) or EBSS^{++}(**B**). From this data the respective relative impedance was calculated and plotted (**C**, **D**). T = 34 °C.

Fig. 72 shows the impedance spectra of a medium- (A) or buffer-filled (B) flow channel with or without a cardiosphere. Spectra from spheroid-free channels show a horizontal, frequency independent curve between ~ 10^1 and ~ 10^5 Hz at ~ 80 kΩ for the medium-filled channel and ~ 60 kΩ for the EBSS^{++}-filled channel. These impedance values are much higher than compared to the PT-2 flow channel values with ~ 10 kΩ due to the different dimensions. The decline in the

frequency range above 10^5 Hz reflecting the parasitic stray capacitance shows similar values (A_{para}: $2 – 3 \cdot 10^{-13}$ $Fs^{n-1}cm^{-2}$, $n_{para} = 0.99$) than for PT-2 flow channels. The increase in impedance after the introduction of a cardiosphere into the flow channel is in this example 30 – 40 kΩ (A, B). From the measured spectra the relative imedance $|Z|_{rel}$ was calculated and plotted against the frequency (Fig. 72, C and D). The plateau phase is observed for the medium- and buffer-filled channel at ~ 50 – 60 % in the frequency range between 10^1 and 10^4 Hz. For MCF-7 spheroids measured in the PT-2 flow channel a similar frequency range is observed including the monitoring frequency of 200 Hz. For this purpose, 200 Hz was used also as monitoring frequency for the presentation of impedance time courses of Cor.At® cardiospheres measured in the PT-1 ITO-glass flow channel.

Preliminary to the impedimetric results for cardiospheres measured in three different experimental scenarios a typical detrended RTC time course of impedance at 200 Hz for the medium-filled cardiosphere-free flow channel is shown in Fig. 73 A. The time course only exhibits small fluctuations that are related to electrical noise with a mean amplitude of 0.031 ± 0.009 kΩ. In contrast, an exemplary time course of a cardiosphere in medium (B) shows distinct spikes with a mean amplitude of 1.3 ± 0.2 kΩ.

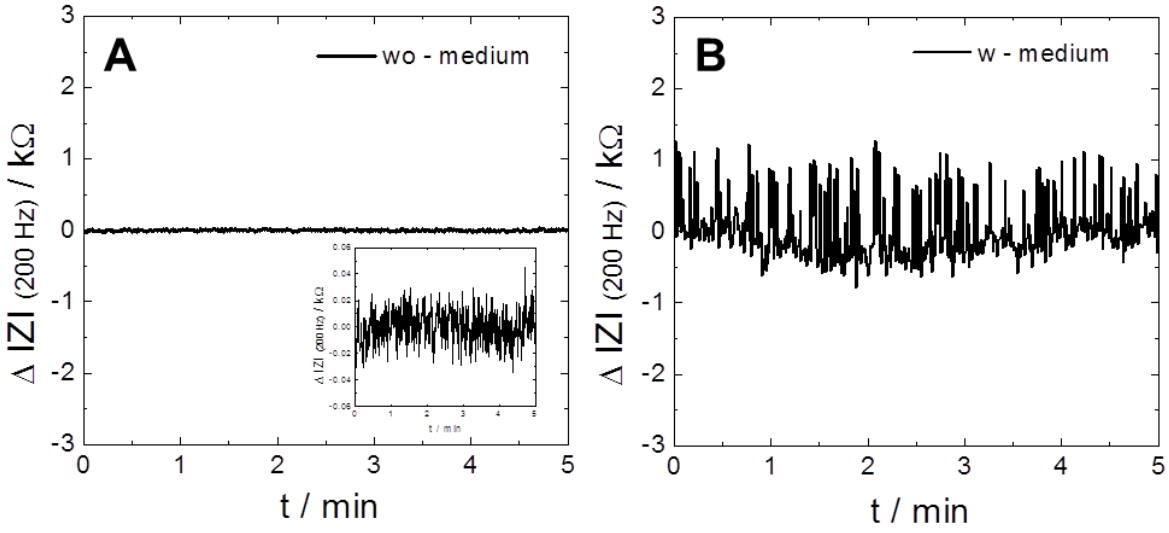

Fig. 73: Typical detrended RTC data of the medium-filled PT-1 on ITO-glass without cardiosphere (**A**) (also shown with a smaller y axis scale) and with cardiosphere (10000 cells/well, 4 d) (**B**). T = 34 °C.

A typical micrograph of a cardiosphere positioned in the central channel of the PT-1 flow channel is shown in Fig. 74. The beating of cardiospheres at the aperture was observed using the digital microscope.

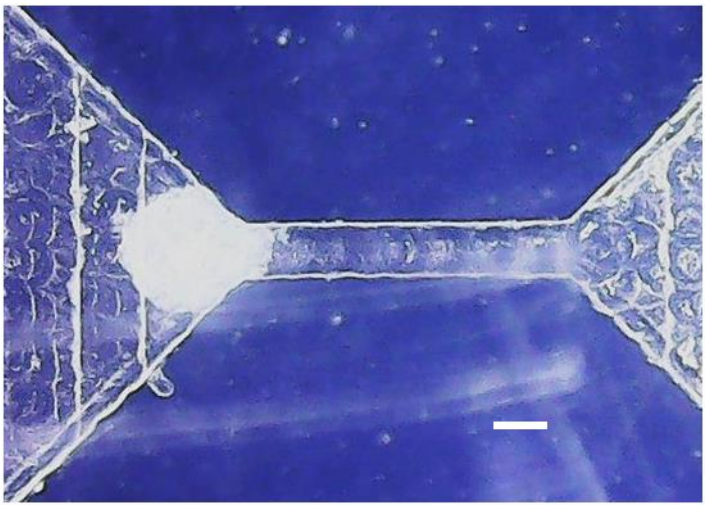

Fig. 74: Micrograph of a cardiosphere prepared by the formation on a non-adhesive surface (6000 cells/well, 5 d) at the aperture of the PT-1 channel (ITO-glass substrate) (scale bar: 150 µm).

7.2 Impedimetric Analysis of Cardiospheres in Absence of Extracellular Calcium

Intracellular and extracellular calcium plays an important role in the initiation of the contraction and relaxation of cardiomyocytes. Cell contraction is provoked by an increase in calcium concentration within the cytoplasm (MacLennan and Kranias, 2003). This calcium is released from Ca^{2+} stores in the sarcoplasmatic reticulum (SR) triggered by the prior calcium influx via plasma membrane channels from the extracellular solution upon membrane depolarization (Fabiato and Fabiato, 1975). This process is called the calcium-induced calcium release (CICR) (Endo, 1977; Roderick et al., 2003). Subsequent relaxation of the cell is achieved by a reduction of the Ca^{2+} concentration in the cytoplasm by pumping it back into the SR and exporting it to the extracellular space. In the absence of extracellular calcium however, the CICR mechanism is inhibited and no cardiomyocyte contractions are induced (Bers, 2002; Abassi et al., 2012).

In proof-of-concept experiments the correlation between the presence and absence of extracellular calcium and the beating behavior of cardiospheres was

veryfied using the EIS-based setup. Three individual measurements were performed (Fig. 75) using either a cardiosphere prepared by the hanging drop technique (A: 3000 cells/drop, 3 d) or cardiospheres prepared by the formation on a non-adhesive surface (B: 10.000 cells/well, 4 d and C: 6000 cells/well, 5 d). The experiments were conducted as described in chapter 4.3.7.1.

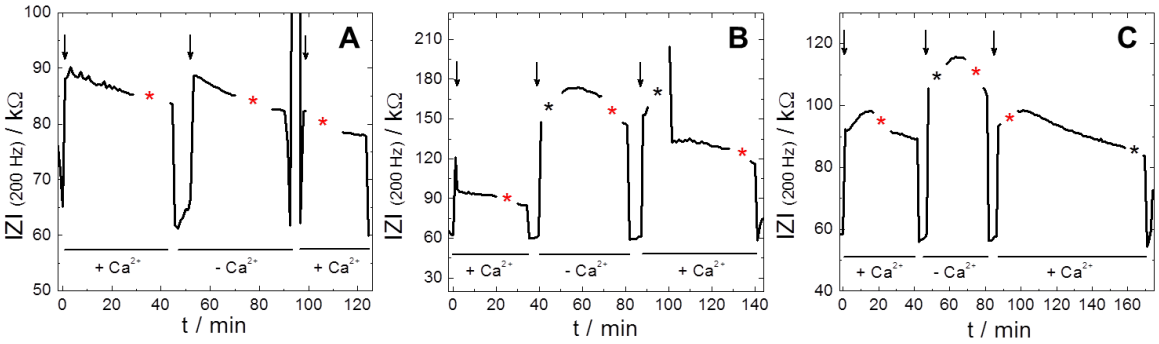

Fig. 75: Time courses of impedance magnitude at 200 Hz for three individual measurements **A** – **C** showing the response of a cardiosphere (3000 cells/drop, 3 d; 10000/6000 cells/well, 4/5 d) to EBSS with (**+ Ca^{2+}**) and without calcium (**- Ca^{2+}**). The stars in the time courses mark the time points when data was collected in RTC mode and the red ones stand for RTC data used for subsequent in-depth analysis. The black arrows mark the repositioning of the cardiosphere after buffer exchange. T = 34 °C.

In each experiment the cardiosphere was first measured in Ca^{2+}-containing EBSS reaching impedance values between 90 – 100 kΩ in all three cases. Then, the cardiosphere was removed from the central aperture of the channel and placed in the flow channel reservoir while the buffer was exchanged by EBSS without Ca^{2+}. The cardiosphere was positioned back at the channel aperture and measured again showing impedance values between 90 – 180 kΩ. In the last measurement period the cardiosphere was again measured in Ca^{2+}-containing EBSS yielding impedance values between 80 kΩ – 100 kΩ for measurement A and C, respectively. In measurement B the impedance first increases to 210 kΩ after repositioning of the cardiosphere, followed by a drop in impedance to ~ 130 kΩ.

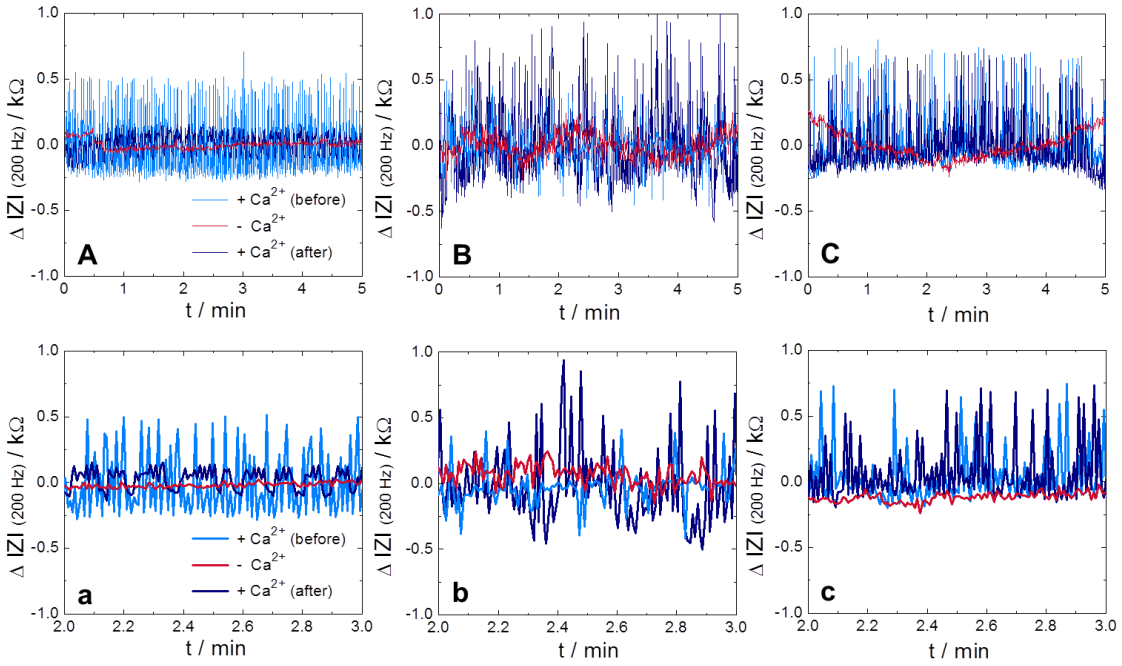

Fig. 76: Detrended RTC data from three individual experiments collected in the course of experiments **A** – **C** as shown in Fig. 75. The plots show the impedimetric beating pattern of the cardiospheres (3000 cells/drop, 3 d; 10000/6000 cells/well, 4/5 d) that were measured without extracellular calcium (red) or in presence of calcium before (light blue) and after (dark blue) calcium deprivation. A zoom-in is provided for each repeat measurement from t = 2 min to t = 3 min (**a** – **c**). T = 34 °C.

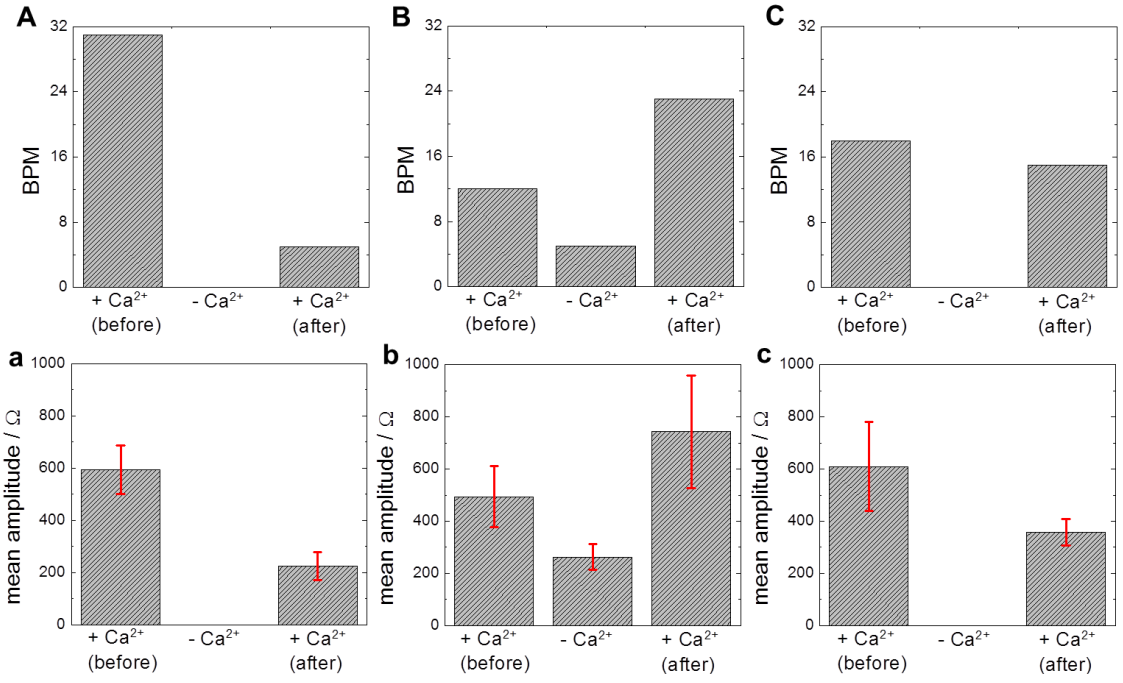

Fig. 77: RTC data analysis for three individual measurements (Fig. 76), showing the BPM values (**A** – **C**) and the mean amplitudes (mean ± SD) (**a** – **c**) for cardiospheres (3000 cells/drop, 3 d;

10000/6000 cells/well, 4/5 d) with (before and after Ca^{2+} depletion) and without extracellular calcium. The threshold values for measurement A – C were 125, 150 and 160 Ω, respectively. T = 34 °C.

At different time points the MFT measurement was stopped to collect data in RTC mode (marked with a star). The RTC data used for in-depth analysis was marked with a red star. In Fig. 76 one detrended RTC time course per condition (± Ca^{2+}) measured for 5 min is shown (A – C). A zoom-in of each time course (2. – 3. min) provides a better perspective on the fluctuation pattern (a – c). In all three cases the cardiospheres measured in $EBSS^{++}$ show distinct fluctuations (light blue). These appear regular in measurement A and C, whereas the observed spikes in B are irregular with a lower amplitude. When calcium was removed from the extracellular buffer the fluctuations are significantly reduced (red). In measurement A and C the signal is similar to that of a spheroid-free channel (Fig. 73 A), but in B the fluctuations are less reduced. When the cardiospheres were afterwards measured in Ca^{2+}-containing buffer again spiking reappears (dark blue). In measurement C the beating resembles that of before Ca^{2+} deprivation. In measurement B the amplitude is enhanced and still irregular. In measurement A a completely different signal pattern with a lower amplitude is observed. For each detrended RTC time course shown in Fig. 76 the BPM and the amplitude of the impedance fluctuation is determined (chapter 4.3.3) and the values are plotted in Fig. 77. In all three measurements cardiospheres show distinct beating in presence of Ca^{2+}, before and after Ca^{2+} deprivation (A: 31 bpm, 5 bpm; B: 12 bpm, 23 bpm; C: 18 bpm, 15 bpm). Without extracellular Ca^{2+} very weak or no beating is observed in the three measurements (A: 0 bpm; B: 5 bpm; C: 0 bpm). The values for the mean amplitude reflect the exact same trends for the beating behavior of cardiospheres in presence and absence of Ca^{2+}.

7.3 Impedimetric Investigation of the Spheroid Response to the Gap Junction Blocker 1-Heptanol

Cardiomyocytes in the heart undergo repeated cycles of synchronous contraction and relaxation. The high synchronicity of the cells is linked to the presence of gap junctions, intercellular channels that allow the transport of small (up to 1 kDa) metabolites and ions like Ca^{2+} between neighboring cells (Takens-Kwak et al., 1992; Kimura et al., 1995). In order to investigate the role of gap junctions in the contraction of cardiomyocytes the channels can be blocked with substances such as 1-heptanol, resulting in the reversible inhibition of synchronous beating (Takens-Kwak et al., 1992). In proof-of-concept experiments it was veryfied if the described effect of 1-heptanol (1 mM) on the beating of cardiospheres can be measured with the new EIS-based setup. The resulting time courses of impedance magnitude are shown in Fig. 78 (A, B). For these experiments cardiospheres were prepared by the formation on a non-adhesive surface (A: 10.000 cells/well, 4 d; B: 6000 cells/well, 5 d) as explained in chapter 4.3.7.2.

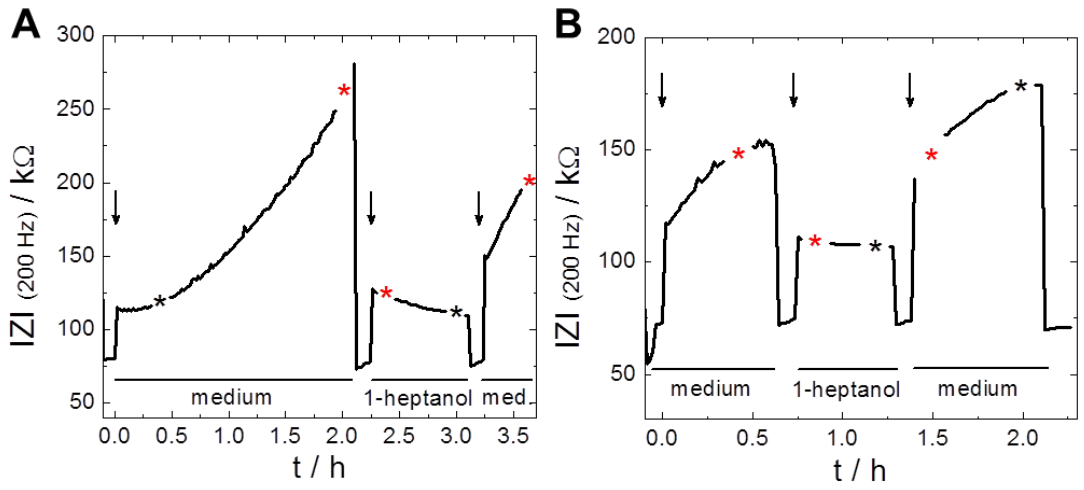

Fig. 78: Time courses of impedance magnitude at 200 Hz for two individual measurements **A**, **B** showing the response of a cardiosphere (10000/6000 cells/well, 4/5 d) to 1 mM 1-heptanol in Cor.At® culture medium and to pure culture medium (control). The stars in the time courses mark the time points when data was collected in RTC mode and the red ones stand for RTC data used for evaluation. The black arrows mark the repositioning of the cardiosphere after buffer exchange. T = 34 °C.

In the first measurement period the cardiospheres under study were measured in Cor.At® culture medium. In both cases the impedance is continuously increasing

from initially ~ 115 kΩ (A) and 118 kΩ (B) to ~ 130 kΩ (A) and 150 kΩ (B) 30 min later. In the subsequent measurement period the effect of 1 mM 1-heptanol on cardiosphere impedance signature was investigated, showing stable impedance values at ~ 110 kΩ. When the cardiosphere was measured again in medium the impedance increases over time, similar to the time courses during the first measurement period. In each measurement period RTC data of the cardiospheres were collected (marked by a red star in Fig 78). Impedance fluctuation patterns in medium before 1-heptanol treatment (light blue) show regular spiking with strong intensity (Fig. 79).

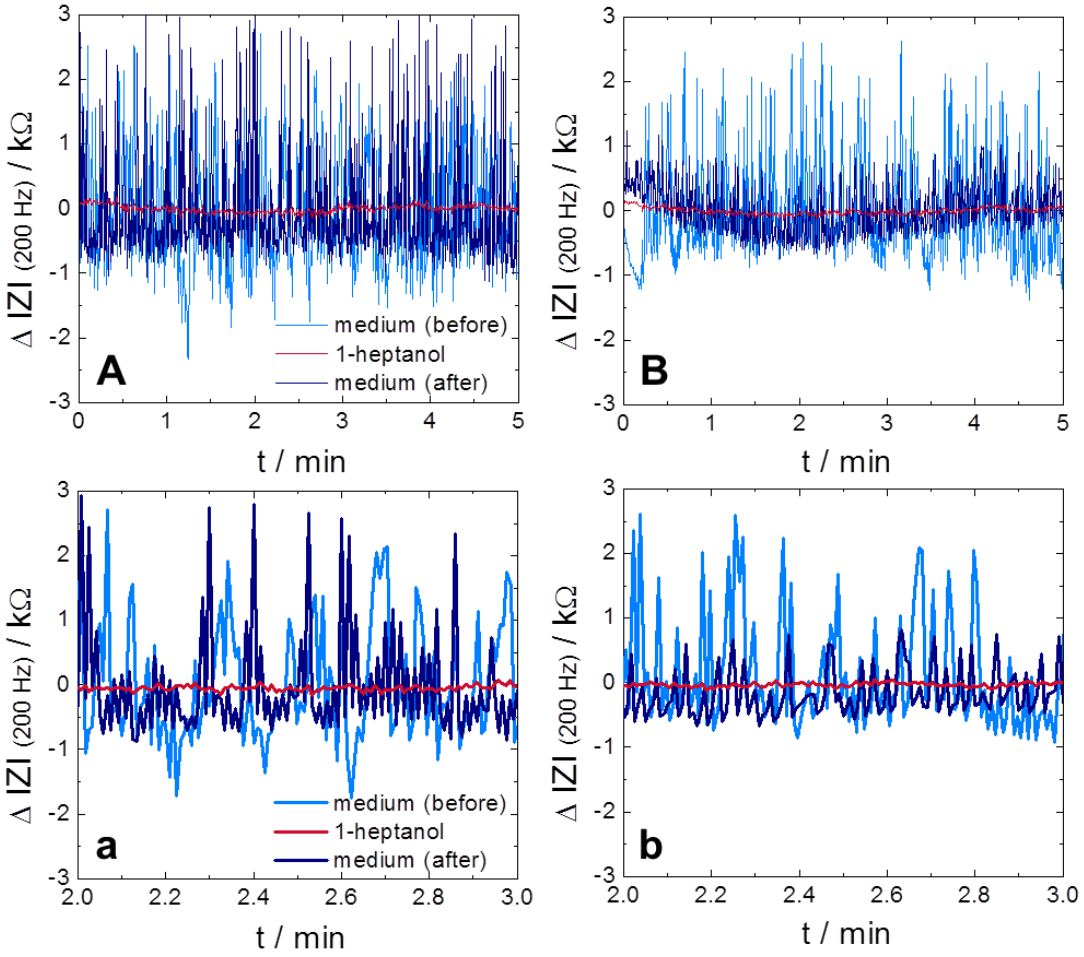

Fig. 79: Detrended RTC data collected in measurement A, B shown in Fig. 78. The plots show the impedimetric beating pattern of the cardiospheres that were measured in 1 mM 1-heptanol (red). As control the beating behavior in presence of Cor.At® culture medium was measured before (light blue) and after (dark blue) the response to 1-heptanol. A zoom-in is provided for each measurement from t = 2 min to t = 3 min (**a**, **b**). T = 34 °C.

Immediately after addition of 1-heptanol no distinct spiking is observed anymore (red). When the spheroid was brought back in medium, spiking recovers (dark blue) with a strong amplitude in measurement A and a less pronounced spiking profile in measurement B. The individual spiking was analyzed by evaluating the beats per minute and their mean amplitude (Fig. 80). Cardiospheres in medium before (A: 23 bpm, B: 22 bpm) and after (A: 28 bpm; B: 23 bpm) exposure to 1-heptanol show distinct beating. During incubation with 1-heptanol no beating is observed (A and B: 0 bpm). The mean amplitudes of cardiosphere fluctuations in medium before (A: 2.2 ± 0.7 kΩ; B: 2.0 ± 0.6 kΩ) and after (A: 2.3 ± 0.9 kΩ; B: 0.9 ± 0.3 kΩ) 1-heptanol treatment are approximately equal. During exposure to the drug no spiking as indicator for cardiosphere contractions are observed and consequently no mean amplitude values can be determined.

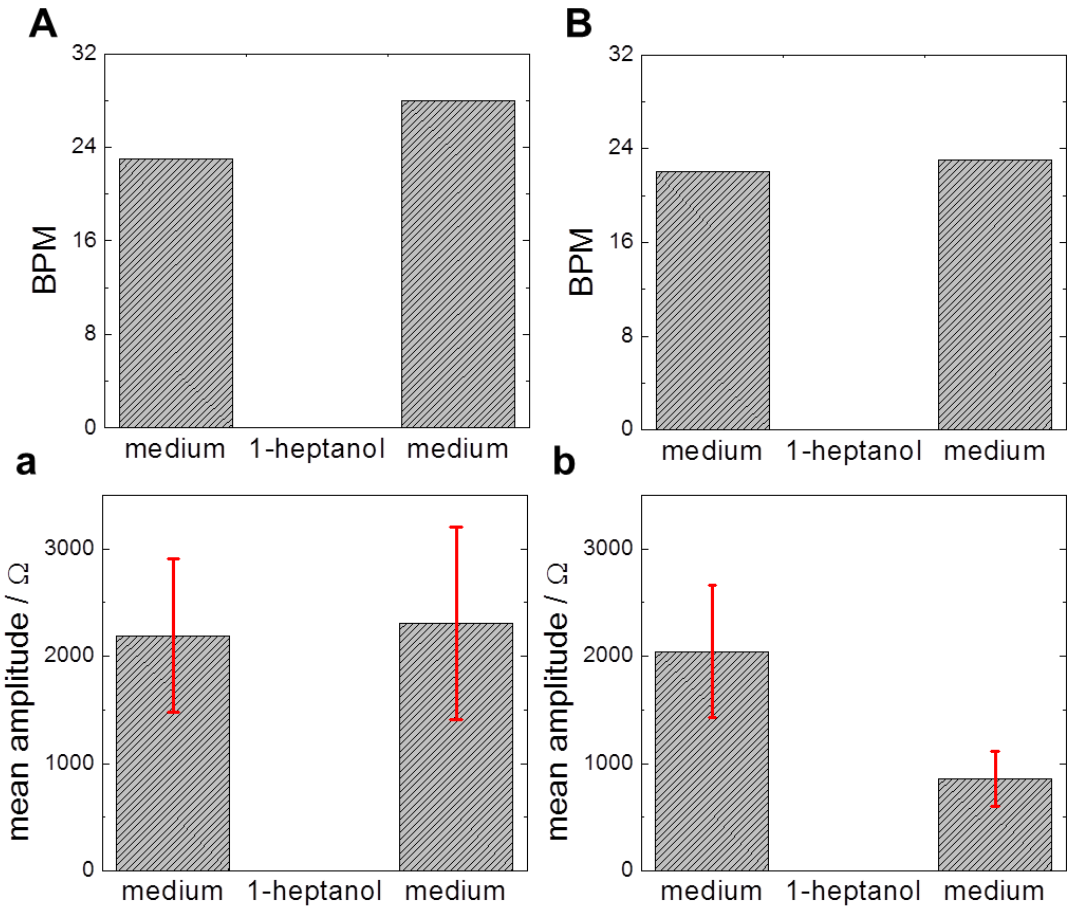

Fig. 80: RTC data analysis. For each measurement shown in Fig. 79 the beats per minute (**A**, **B**) and the mean amplitudes (mean ± SD) (**a**, **b**) for cardiospheres in medium and 1-heptanol were evaluated. The threshold value for measurement A and B was 200 Ω. T = 34 °C.

7.4 Measurement of the Spheroid Response to the Beta-Adrenergic Agonist Isoprenaline

Isoprenaline is a β-agonist that binds to the β-adrenergic receptors in the cell membrane and thereby initiates a signal transduction cascade (MacLennan and Kranias, 2003). In short, receptor activation leads to the stimulation of cAMP formation mediated by G proteins. The elevated cAMP concentration activates the cAMP-dependent protein kinase that phosphorylates certain cardiac proteins like phospholamban, a reversibly phosphorylated transmembrane protein in the sarcoplasmatic reticulum. Depending on its phosphorylation state it can bind to and regulate the Ca^{2+} pump sarcoplasmic reticulum Ca^{2+}-ATPase 2a (SERCA2a). This pump is, in turn, responsible for the removal of cytoplasmic calcium by transporting it into SR stores, thereby affecting muscle relaxation and cardiac contractility (Simmerman and Jones, 1998). Isoprenaline ultimately leads to an enhanced beating rate (Scott et al., 2014).

In this thesis the developed EIS-based device was used to measure the effect of 100 nM isoprenaline on the contractility of Cor.At® cardiospheres. Three individual measurements were performed as described in chapter 4.3.7.3 using one cardiosphere prepared by the hanging drop technique (A: 3000 cells/drop, 3 d) and two cardiospheres prepared by the formation on a non-adhesive surface (B: 10.000 cells/well, 4 d; C: 6000 cells/well, 5 d).

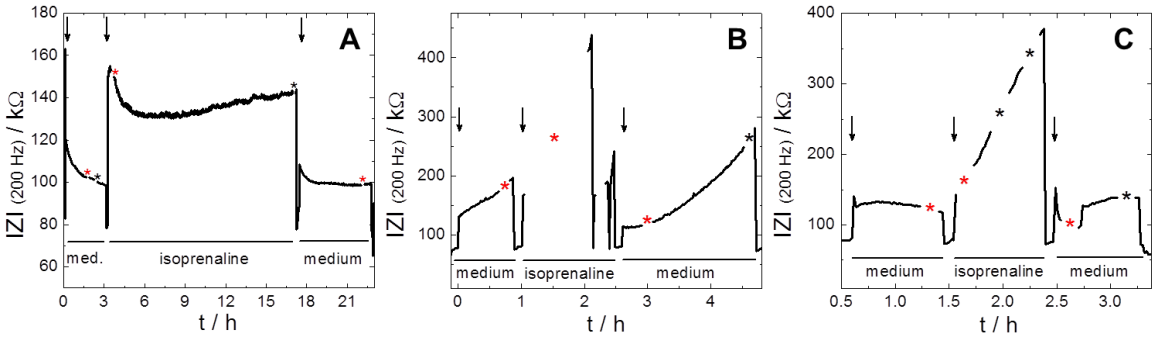

Fig. 81: Time courses of impedance magnitude at 200 Hz for three individual measurements **A** – **C** each showing the response of a cardiosphere (3000 cells/drop, 3 d; 10000/6000 cells/well, 4/5 d) to 100 nM isoprenaline in Cor.At® culture medium in comparison to the control beating in medium only. The stars in the time courses mark the time points when data was collected in RTC mode and the red ones stand for RTC data used for evaluation. The black arrows mark the repositioning of the cardiosphere after buffer exchange. T = 34 °C.

The time courses of impedance (Fig. 81 A – C) reflect the sequence of experiments. In the first phase the cardiospheres were measured in medium, in the second they were exposed to 100 nM isoprenaline and in the third phase the cardiospheres were again measured in medium. Overall, impedance values for cardiospheres in isoprenaline are higher than for those in medium. The RTC data in Fig. 82 (RTC data marked by a red star in Fig. 81) shows weak spiking for cardiospheres in medium before (light blue) isoprenaline exposure in measurement A and C, with mean amplitude values of 0.2 ± 0.04 kΩ (Fig. 83 A) and 0.7 ± 0.2 kΩ (C), but exhibit stronger spiking in measurement B with a mean amplitude of (1.2 ± 0.3) kΩ. In all three experiments the impedance spiking of cardiospheres in isoprenaline are increased with respect to the mean amplitude (A: (1.9 ± 0.3) kΩ; B: (2.3 ± 0.8) kΩ; C: (4.4 ± 1.9) kΩ) and after removal of isoprenaline mean amplitudes are decreased (A: (0.16 ± 0.04) kΩ; B: (1.7 ± 0.4) kΩ; C: (0.4 ± 0.06) kΩ). The BPM data obtained from the three measurements shows a slightly increased beating rate in isoprenaline (Fig. 83, A: 22 bpm, B: 25 bpm, C: 27 bpm) compared to the beating rate in medium before (A: 12 bpm, B: 18 bpm, C: 18 bpm). The beating rate of cardiospheres in medium after exposure to isoprenaline is decreased in measurement A and C and at a similar level than during isoprenaline incubation in measurement B (A: 19 bpm, B: 26 bpm, C: 13 bpm).

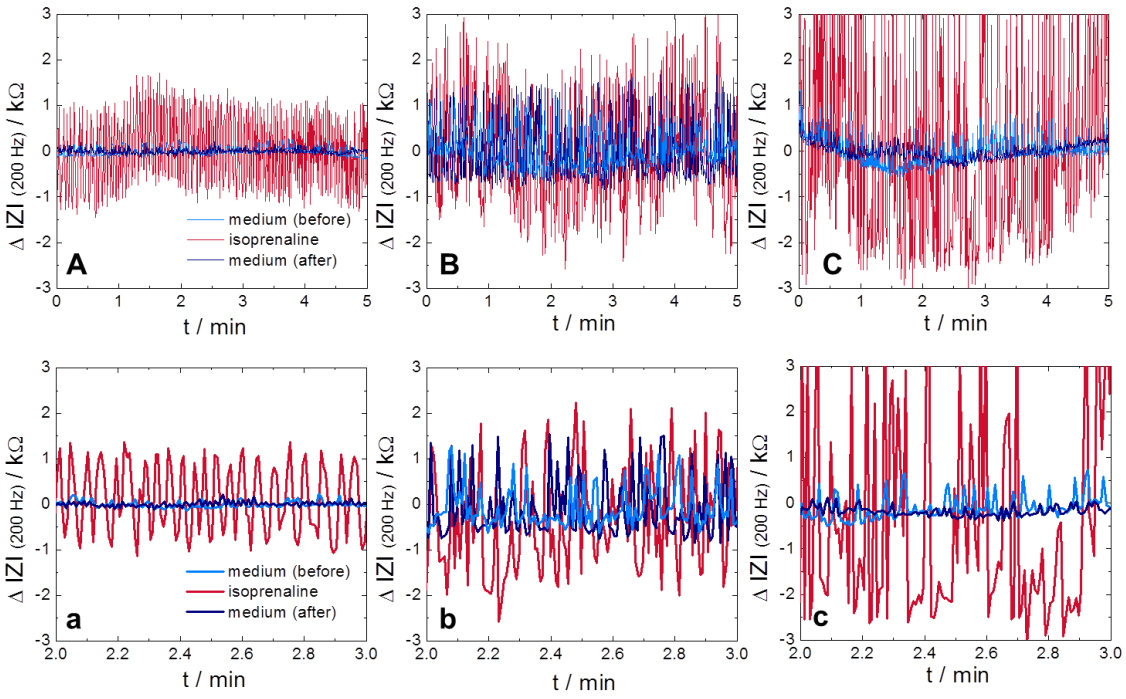

Fig. 82: Detrended RTC data collected in measurement A – C shown in Fig. 81. The plots show the impedimetric beating pattern of the cardiospheres that were measured in 100 nM isoprenaline (red). As control the beating behavior in presence of Cor.At® culture medium was measured before (light blue) and after (dark blue) the response to isoprenaline. A zoom-in is provided for each measurement from t = 2 min to t = 3 min (**a** – **c**). T = 34 °C.

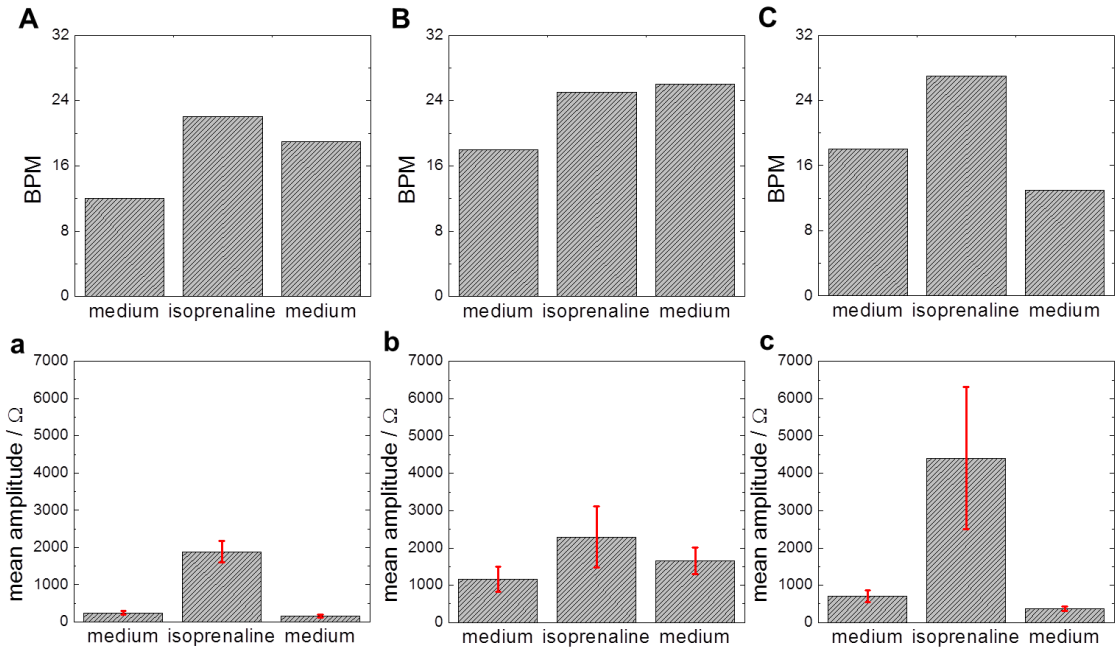

Fig. 83: RTC data analysis. For each measurement (Fig. 82) the BPM (**A** – **C**) and the mean amplitudes (mean ± SD) (**a** – **c**) for cardiospheres in medium or isoprenaline were evaluated. The threshold values for measurement A – C were 70, 200 and 160 Ω, respectively. T = 34 °C.

7.5 Discussion

7.5.1 Characterization of Cor.At® Cardiospheres

The formation of cardiospheres by the hanging drop technique and by formation on a non-adhesive surface was successful. Using microscopy the formation and morphology of these cardiospheres was characterized. Furthermore, the cardiospheres were impedimetrically characterized in the PT-1 flow channel.

- Cardiospheres from 96-well plates express a more regular spherical shape and a longer beating activity than spheres from hanging drop culture.
- The monitoring frequency was determined to be 200 Hz. The beating activity during the measurement was verified using the digital microscope.

Cardiosphere formation is possible with both techniques but the reproducibility of the spheroid size is limited. Although, identical seeding densities were used only a part of these cells participated in the cardiosphere formation (an unknown number of non-beating cells did not adhere to the aggregate) leading to a decreased effective seeding density and consequently to a variation in cardiosphere size. In addition, strongly irregular shaped cardiospheres from hanging drop culture might result in varying impedance contributions. Therefore, the application of cardiospheres from 96-well plates with more reproducible smooth round shape should be preferred for impedance analysis.

In comparison to PT-2 on ITO-PET the PT-1 flow channel on ITO-glass showed higher impedance values over the entire frequency range. These observations are related to the channel geometries, which cause a high channel resistance (see chapter 5.1.1 Tab. 8).

In order to analyze the beating of monolayer cardiomyocytes using impedance-based techniques there is the xCELLigence® RTCA Cardio system (ACEA Biosciences, Inc.). This system comprises an electronic 96-well microtiter plate with gold microelectrode arrays on the bottom of each well where the cells are allowed to attach. The system is characterized by a high rate of data acquisition

which enables the monitoring of cell contraction/relaxation in a non-invasive, label-free and time resolved manner (Jonsson et al., 2011).

7.5.2 Impact of Extracellular Ca^{2+} Deprivation on Cardiospheres

With a proof-of-concept experiment it was investigated if the novel EIS-based setup was capable of measuring the beating of cardiomyocytes as well as changes in the beating behavior upon the removal of extracellular calcium.

- The time courses of impedance at 200 Hz show no distinct difference for spheroids in calcium-containing or –free buffer.
- The analysis of RTC data shows a reduced or no contraction rate (BPM) and beating amplitude in absence of extracellular calcium.
- Beating activity recovers when cardiospheres are brought back in calcium-containing buffer. The spiking pattern is in some cases different to the initial pattern before deprivation.

Results prove that cardiosphere beating can be measured sensitively using the new setup. Impedance fluctuations in the RTC data are different compared to those of MCF-7 spheroids (chapter 6) and P19 embryonic bodies (chapter 8). The fluctuations for cardiospheres show repeated peaks with much higher intensity indicating a strong periodic motion of the cardiospheres which reflects the beating rhythm also observed via the digital microscope. The fluctuation patterns were however, different for the three cardiospheres under study which was caused presumably by a bad reproducibility of the cardiosphere size (chapter 7.5.1) and beating activity. Unfortunately, limited proliferative capacity of the embryonic stem cell-derived Cor.At® populations hampered repeated experiments. Nevertheless, the results prove that changes in the beating behavior can be detected. Upon calcium removal from the extracellular buffer the fluctuations were strongly reduced reflecting beating arrest, which was also observed with the digital microscope. After buffer exchange to $EBSS^{++}$ the beating resumed confirming the reversibility of the beating arrest induced by extracellular calcium deprivation.

In measurement A (Fig. 76 A, a; dark blue) an unusual beating pattern was

observed for the cardiosphere, which was prepared by hanging drop technique. A similar beating pattern was seen also in the report of Abassi et al. (2012) who studied beating anomalies in Cor.At® cells cultured as monolayers upon exposure to different drugs (E4031, Astemizole, Cisapride, Droperide, Sertindole) that are known to interact with and block the human ether-a-go-go (hERG) potassium channel activity. However, a similar beating pattern was observed only in one single RTC time course in this PhD thesis and a possible correlation with the prior calcium deprivation is uncertain and would require more experiments for clarification.

Parameters describing the contraction activity quantitatively are the mean amplitude and the beats per minute. The mean amplitude is a parameter that is able to reflect contracted versus relaxed state of the cardiospheres. The standard deviation reflects the uniformity of the fluctuation height. The beats per minute are generally a measure for the contraction rate.

Overall, a relationship between the contraction activity and the presence of extracellular calcium was confirmed. Abassi et al. (2012) showed that when isradipine, a well-known blocker of the voltage-activated L-type calcium channel, is applied to the cells the beating activity of Cor.At® monolayer cells was inhibited. Beauchamp et al. (2015) prepared cardiospheres from human cardiomyocytes derived from induced pluripotent stem cells using the hanging drop technique. In order to investigate cytosolic calcium signals and their response to external stimuli they used fluo-4 as calcium-sensitive fluorescent probe and high-resolution line-scan imaging using a confocal microscope. The label penetrated the outer cell layers of the cardiosphere so that line scans could be obtained in the tissue model periphery. When the bathing solution of cardiospheres containing 1.8 mM $CaCl_2$ was exchanged to one with 0.5 mM $CaCl_2$ spontaneous intracellular calcium release from the SR was interrupted and contractions, measured by video analysis of cardiosphere motion, inhibited.

The example with the fluo-4 staining shows the limited efficiency of label-based assays for investigation of spheroid responses. Due to limited penetration of labels into the spheroid the results reflect mainly the responses of cells on the spheroid surface. The EIS-based setup in contrast, measures the total spheroidal response to certain stimuli in a non-invasive and time-resolved manner.

7.5.3 Impact of 1-Heptanol on Cardiospheres

Using the EIS-based setup, the reversible inhibition of cardiosphere contraction by the gap junction blocker 1-heptanol (1 mM) was confirmed as reflected by the following results:

- The impedance for cardiospheres in 1-heptanol is lower than compared to control conditions.
- The detrended RTC data shows no beating activity for cardiospheres in 1-heptanol and high beating activity in medium before and after 1-heptanol exposure reflected by BPM values and mean amplitude values.
- Beating activity recovers when cardiospheres are brought in medium without 1-heptanol. The resulting fluctuation pattern is different from the initial pattern before 1-heptanol treatment.

Similar results on the effect of 1-heptanol were obtained in other studies using cardiomyocytes in 2D and 3D culture. Takens-Kwak et al. (1992) studied the effect of 1-heptanol on gap junctions of neonatal rat heart cells using the patch clamp method. They found that the inhibition of gap junctions decreased the junctional current in a dose-dependent and reversible manner. Kimura et al. (1995) confirmed these results investigating the concentration-dependent effect of 1-heptanol on the synchronous beating of primary neonatal rat cardiomyocytes using several optical techniques. In contrast to the results in this thesis, a concentration of 1.5 mM effected no alterations in beating behavior. Higher concentrations (2.0, 2.5 mM) however, caused the reversible inhibition of contractions and gap junctional communication and thereby prevented synchronization of intracellular Ca^{2+} fluctuations. The highest concentration (3.0 mM) had the same effects but showed a delayed recovery after heptanol was washed out. Caspi et al. (2009) prepared cardiospheres from human embryonic stem cell-derived cardiomyocytes and measured the influence of 1-heptanol on the 3D model using microelectrode array mapping. Simultaneous field potential recordings of contracting cardiospheres on 60 titanium-nitride electrodes were performed. Whereas a low 1-heptanol concentration (0.3 mM) caused a reduced conduction, higher concentrations (0.6 mM and 1.0 mM) led to

complete beating arrest and no or very weak conduction. Further heptanol studies on 3D tissue models were performed by Shapira-Schweitzer et al. (2009). They generated cardiospheres from human embryonic stem cell-derived cardiomyocytes and from rat neonatal cardiomyocytes using a polymerizable hydrogel for 3D culture. Upon administration of 0.5 mM 1-heptanol they observed the complete beating arrest for both cardiosphere species. They furthermore confirmed the reversibility of this inhibition.
These examples are in good accordance with the microscopic observations and changes in the mean amplitude and BPM values of RTC data with or without 1-heptanol as shown in Fig. 79/80 (A, a, B, b).

7.5.4 Impact of Isoprenaline on Cardiospheres

Reversible alterations in the fluctuation pattern of cardiospheres upon exposure to the beta-adrenergic agonist isoprenaline (100 nM) were measured using the EIS-based device:

- Increased impedance values (MFT) for cardiospheres in isoprenaline in comparison to medium.
- Cardiospheres in isoprenaline show an increased mean amplitude and beating rate in RTC impedance profiles.

While in literature no statements were found concerning the amplitude of the beating pattern, the BPM were regularly used as a parameter for beating pattern quantification. Abassi et al. (2012) measured a dose-dependent (0.41 – 300 nM) increase in contraction frequency of 2D cultured mouse embryonic stem cell cardiomyocytes (Cor.At®) using the impedance-based xCELLigence RTCA Cardio System. Jonsson et al. (2011) found an increased beating rate by 64 % (in human cardiomyocytes) and 85 % (in mouse cardiomyocytes) upon exposure to 80 nM isoprenaline. 3D cardiomyocyte cultures also showed an increased contraction frequency in studies of Bartholomä et al. (2005), Shapira-Schweitzer et al. (2009), Nguyen et al. (2014) and Beauchamp et al. (2015). However, they all used a 10 – 100-fold higher isoprenaline concentration, typically between 1 µM and 10 µM. Bartholomä (2005) further reported that they did not observe any

alterations in beating rate when cardiospheres were treated with 100 nM isoprenaline. This result is not in good accordance to the results of the isoprenaline study of this thesis (chapter 7.4). The rather low applied isoprenaline concentration of 100 nM, which was used in literature only for 2D cultured monolayer cardiomyocytes, led to an increase in the beating rate. It might be possible that the effect would have been more pronounced upon exposure to higher isoprenaline concentrations.

8 Impedimetric Model Studies of Embryonic Bodies

P19 embryonic carcinoma cells have the power to develop different phenotypes by differentiation into cells with characteristics of cardiomyocytes, neurons or skeletal muscle cells (van der Heyden and Defize, 2003). In order to perform cell differentiation *in vitro*, P19 cells need to form so-called embryonic bodies in presence of a chemical inducer, a reagent that stimulates differentiation (Bain et al., 1994). The most studied cell types derived from P19 cells are cardiac and neuronal cells. The typical inducer for cardiac differentiation is DMSO and for neuronal differentiation it is retinoic acid (McBurney, 1993; Bain et al., 1994). The process of cell differentiation into these two cells types as well as their physiology has been studied by several researchers. Conventional methods to monitor differentiation processes include e.g. microscopic observation, reverse transcription-polymerase chain reaction (RT-PCR), quantitative PCR (qPCR), Western Blot and fluorescence activated cell sorting (FACS) (Song et al., 2013). Some of these methods are invasive and alter or even damage the sample. Others are very time-consuming and lack quantitative analysis. A good alternative to these techniques provides the impedance-based analysis of cell differentiation. While the cells turn into neuronal or cardiac cells, their morphology and electrophysiological characteristics change, which is reflected by time-resolved changes in impedance (Song et al., 2013).

In proof-of-concept experiments the novel EIS-based device was used to measure the differentiation process of P19 embryonic bodies. These were generated in presence of the inducers DMSO and RA using either the hanging drop method or the formation on a non-adhesive surface. The morphology of embryonic bodies was observed using microscopy and different stages of differentiation should be revealed by impedance analysis using frequency scans (MFT) and high time resolution measurements. In the case of a successful differentiation, beating cardiomyocytes and neuronally active cells would be obtained. In chapter 7 it was already demonstrated that the beating of cardiomyocytes can be detected and analyzed with the new EIS device. Therefore, the impedimetric detection of cardiac differentiation, which is marked by beating cell aggregates, had the first priority compared to the analysis of

neuronal differentiation, whose impedimetric detection with the new device was not investigated before.

8.1 Characterization of Embryonic Bodies from P19 Cells With and Without Differentiation Factors

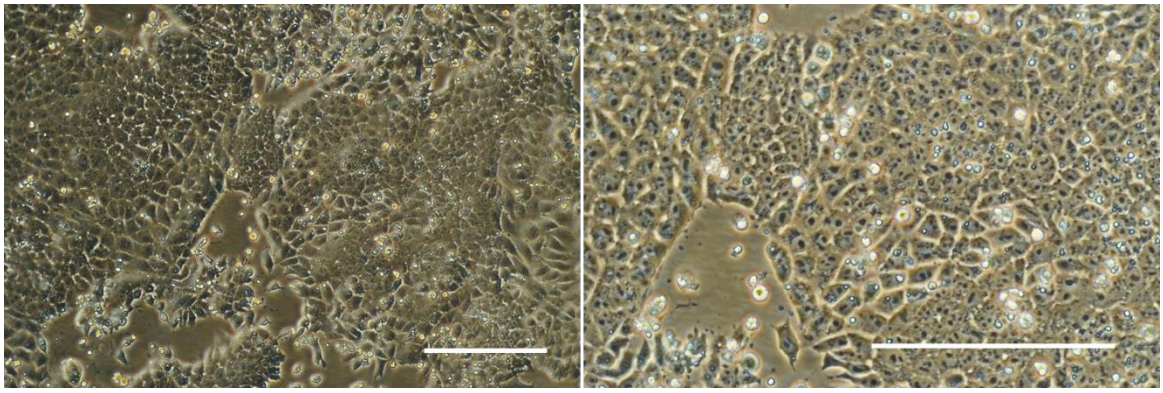

Fig. 84: Phase contrast micrographs of undifferentiated adherent P19 cells grown in 2D in a conventional cell culture flask recorded with two magnifications (scale bars: 200 µm).

The phase contrast micrographs in Fig. 84 show an almost confluent monolayer of P19 cells with epithelial-like morphology recorded with two magnifications. For the formation and differentiation of P19 embryonic bodies (EBs) two different methods were used. First, EBs were formed in a non-adhesive petri dish as it is often described in literature (Bain et al., 1993; Jasmin et al., 2010). The culture in agarose-coated 96-well plates was a modification of this method, which was tested to generate more reproducibly sized EBs. Another method applied by researchers was the hanging drop technique (Wobus et al., 1994; Marikawa et al., 2009). More information on the procedures is given in chapters 4.1.5 and 4.1.7.

EB Formation in a Non-Adhesive Petri Dish

Embryonic bodies were prepared in a non-adhesive petri dish (10^6 cells) in presence of DMSO for cardiac differentiation (Fig. 85). On day four after seeding multiple aggregates are present in the dish. Beside few single EBs with round shape mostly irregular formed interrelated aggregates are observed. Not all cells are included in the aggregate and remain singular. EB contractions as the most

obvious sign of differentiation into cardiac cells are not observed. In literature the EBs are generally transferred to an adhesive culture plate without inducer after ~ 4 d to enable attachment and cellular outgrowth of the EBs. This way, changes in the cell morphology upon differentiation can be studied.

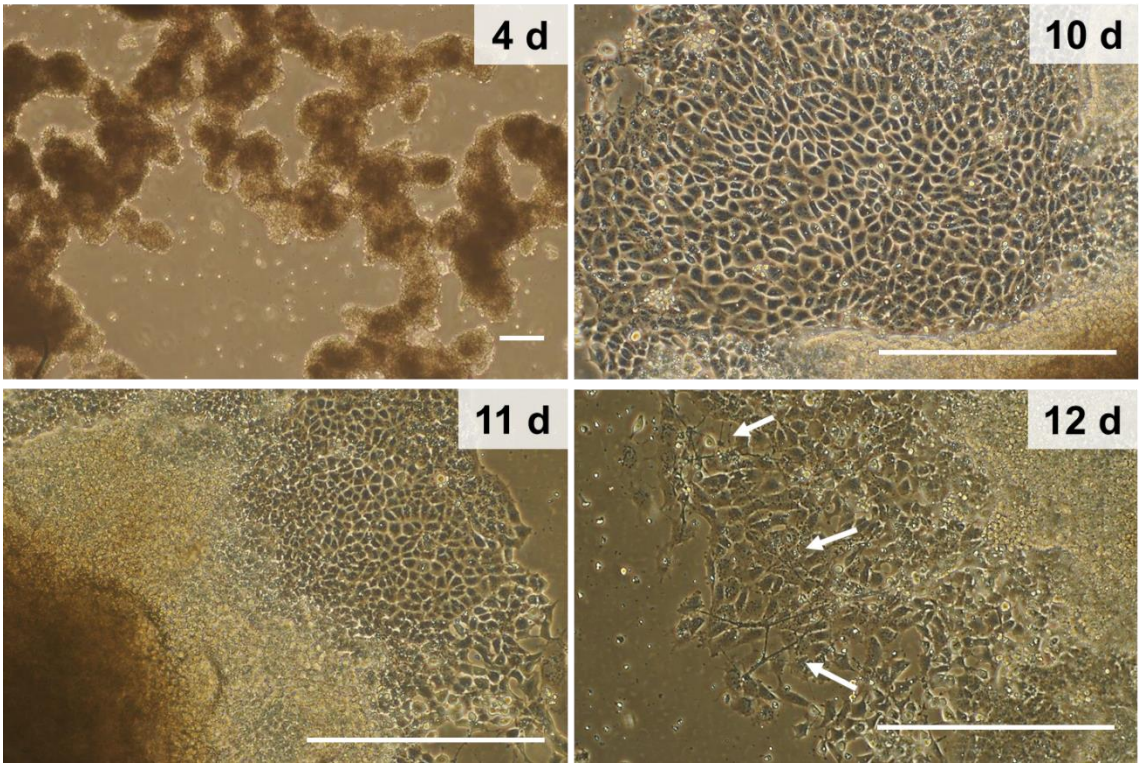

Fig. 85: Typical phase contrast micrographs of embryonic bodies 4 d after seeding in a non-adhesive petri dish in presence of DMSO (1 %). On day 5 EBs were transferred to an adhesive petri dish for adhesion and outgrowth of cells from EBs to monitor the cell morphology on day 10 – 12 after seeding and accordingly 5 – 7 d after transfer (scale bars: 200 µm). The white arrows point to axon-like extensions.

For this purpose, the DMSO-EBs were transferred to an adhesive petri dish without DMSO 5 d after seeding. Monolayer cells in the periphery of attached EBs 10 d and 11 d after seeding (i.e. 5 and 6 d after transfer) show a cobblestone or epithelial-like morphology similar to the monolayer cells in Fig. 84. However, there are also isolated spots in the far periphery of the cellular outgrowths where neuron-like structures with cellular extensions like axons are observed as indicated by the white arrows in the image taken 12 d after seeding. Beating of EBs or monolayer cells is still not observable.

The morphology of EBs generated in presence of the neuronal inducer RA and

their cellular outgrowths 10 – 12 d after seeding were also studied (Fig. 86). On day four after seeding several aggregates and a lot of singular cells are present in the dish. RA induced EBs are larger and more compact than the DMSO induced EBs. After the transfer to the adhesive substrate outgrowing cells exhibit different morphologies.

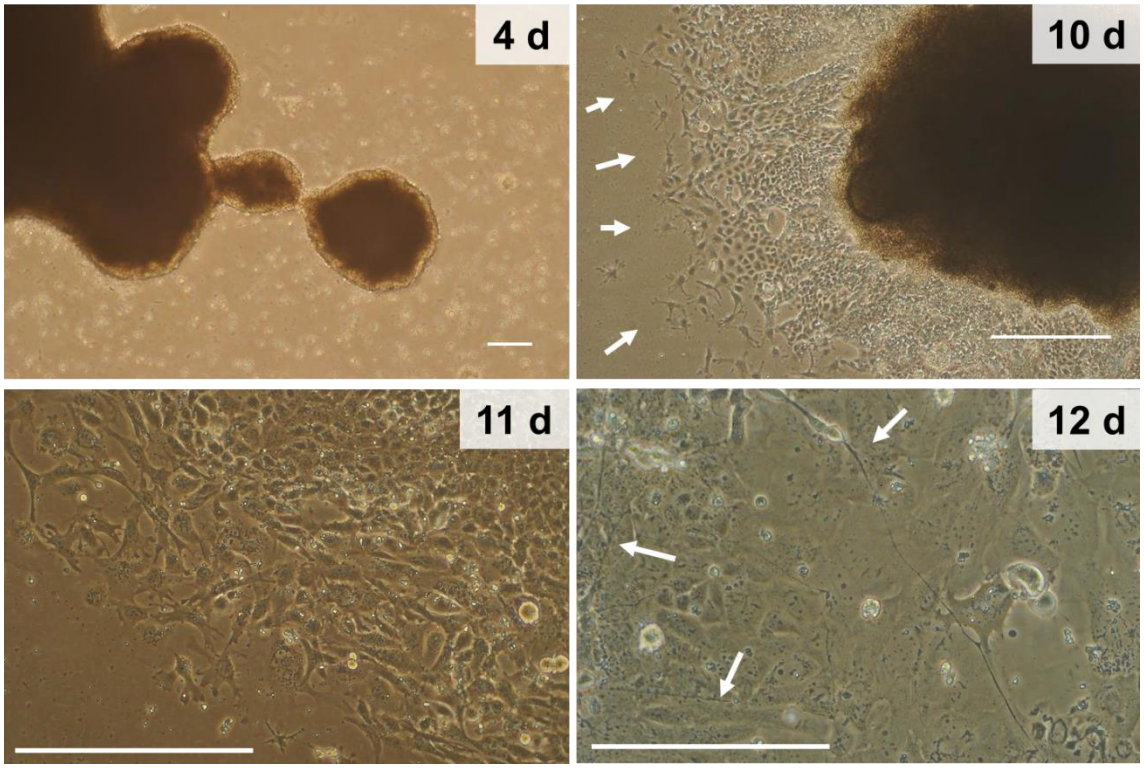

Fig. 86: Typical phase contrast micrographs of embryonic bodies 4 d after seeding in a non-adhesive petri dish in presence of RA (1 µM). On day 5 EBs were transferred to an adhesive petri dish for adhesion and outgrowth of cells from EBs to monitor the cell morphology on day 10 – 12 after seeding and accordingly 5 – 7 d after transfer (scale bars: 200 µm). The white arrows point to flat, elongated or dendritic-like cells and to axon-like structures.

In regions of the outgrowths that are in close proximity to the EB there are for example cells with epithelial-like structure obtained also in DMSO-EB outgrowths and undifferentiated P19 cells (10 d). Especially at the front of the outgrowths there are elongated flatter cells and cells with dendritic or stellate cell extensions (10 d, white arrows; 11 d). In some of these spots at the outgrowth front isolated neuron-like cells with long axons are observed in micrographs of day 10 – 12. A typical image of the observed axon-like structures spanning above a cell monolayer is shown in Fig. 86, 12 d.

EB Formation in Hanging Drops

The formation of EBs was also studied using the hanging drop technique. Herein, embryonic bodies from two seeding densities (300 and 600 cells/drop, 5 d) were prepared without inducer or with the cardiac inducer DMSO (1 %) (Fig. 87). EBs were not prepared in presence of RA and no outgrowth study was performed.

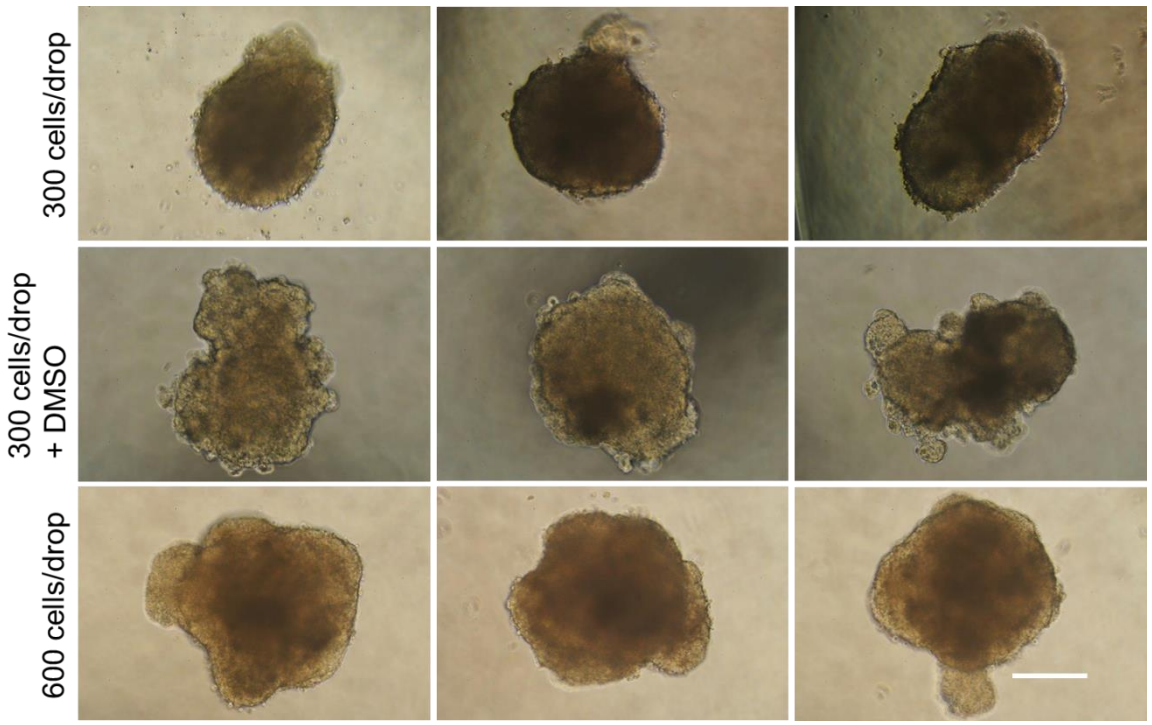

Fig. 87: Typical EBs (5 d) generated by the hanging drop technique from two seeding densities (300 / 600 cells/drop), and EBs were allowed to aggregate in presence of the cardio-differentiation inducer DMSO (1 %) (scale bar: 200 µm).

In hanging drops the cells aggregate to one EB per drop with only sporadic single cells in the periphery. EBs with a seeding density of 300 cells/drop are approximately round or oval. EBs from the same seeding density but generated in presence of DMSO form a more irregular shape with small bulges. They show no apparent contractility. EBs with a seeding density of 600 cells/drop without inducer are bigger in size than EBs produced from 300 cells/drop and have an irregular shape with big bulges.

EB Formation on Non-Adhesive 96-Well Plates

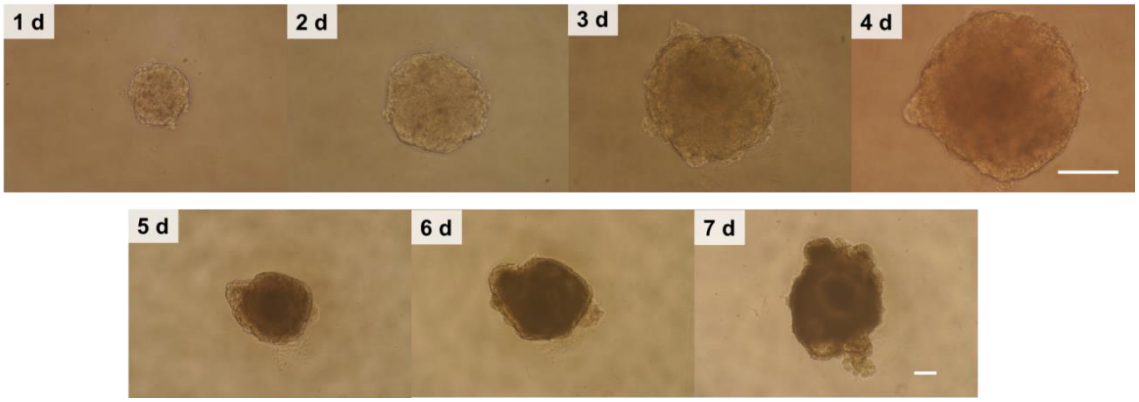

Fig. 88: Typical phase contrast micrographs of a P19 embryonic body (600 cells/well) shown at 1 – 4 d after seeding (10x objective) and at 5 – 7 d (4x objective) (scale bars: 200 µm).

EB formation in the non-adhesive 96-well plate produces also one EB per well. Their increase in diameter was monitored over 7 d (Fig. 88) showing approximately spherical aggregates already on the first day after seeding. With increasing size and cultivation time the outgrowths on the EB surface are increasing in size and number. On day seven after seeding the initially round shape is converted to an oval bulge-bearing shape.

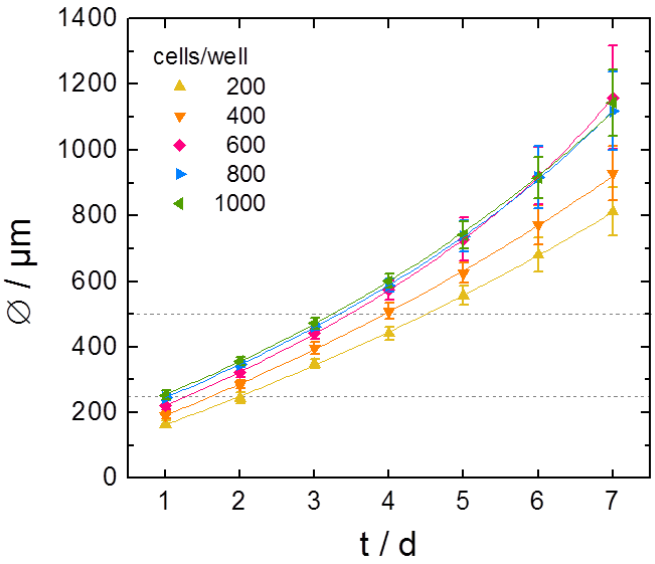

Fig. 89: Growth study of P19 EBs generated in a 96-well plate from different seeding densities (200 – 1000 cells/well) microscopically documented over seven days (mean ± SD, n ≥ 12). The grey dashed lines mark the minimal and maximal EB diameter that can be used in the PT-2 flow channel.

An evaluation of the diameters of EBs from different seeding sensities (200 – 1000 cells/well) over seven days was performed and plotted in Fig. 89. While MCF-7 spheroids in a seeding density of 1000 cells/well reach a diameter of ~ 400 µm on day seven after seeding (chapter 6.1), P19 EBs in the same seeding density are (1144 ± 101) µm in diameter. The growth of 200 and 400 cells/well EBs is distinguishable while the growth curves of EBs from the other three seeding are overlapping. The standard deviations of the diameters for all cell densities increase with time reflecting the variation of irregular EB shapes resulting from bulges. The two grey dashed lines in the plot at 250 µm and 500 µm mark the minimal and maximal EB diameters that fit into the PT-2 flow channel so that EBs are held back at the central aperture. EBs with seeding densities of 200 – 1000 cells/well grown for 2 – 3 d or 200 – 400 cells/well grown for 4 d after seeding have the optimal size for measurements in the flow channel.

Embryonic bodies (1000 cells/well, 3 d) were also prepared in presence of DMSO and RA in the 96-well plate. In Fig. 90 phase contrast micrographs of two undifferentiated EBs (A, B, -) are opposed to two DMSO-EBs (A, B, +DMSO) and two RA-EBs (A, B, +RA). The sizes of undifferentiated and DMSO-EBs are similar while RA-EBs are smaller with a rounder shape.

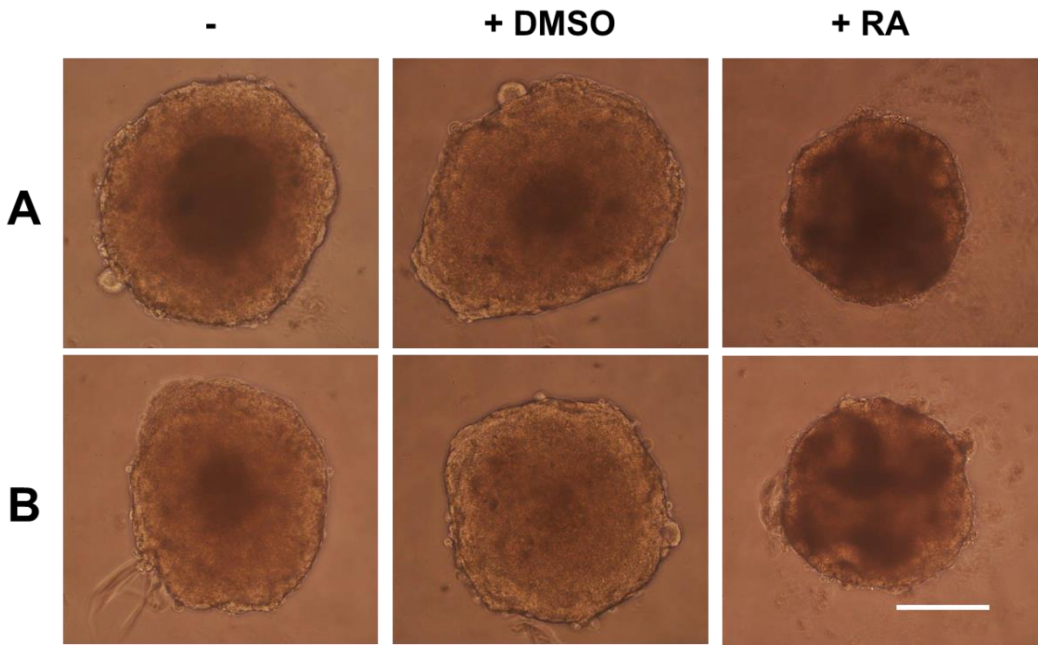

Fig. 90: Typical phase contrast micrographs of embryonic bodies (1000 cells/well, 3 d) (**A**, **B**) that were allowed to form without inducer (-), in presence of DMSO (1 %) for cardio-EB formation (+ DMSO) or in presence of RA (1 µM) for neuro-EB formation (+ RA) (scale bar: 200 µm).

8.2 Impedimetric Analysis of Undifferentiated and Differentiation-Induced Embryonic Bodies

The embryonic bodies prepared in a non-adhesive petri dish, in hanging drops and in a non-adhesive 96-well plate were all subjected to impedance analysis using the new device. While only preliminary experiments are presented for EBs from a petri dish and hanging drops, detailed results of four individual EIS measurements in duplicates are presented for EBs from the 96-well plate.

8.2.1 EIS Study with Embryonic Bodies Grown in Non-Adhesive Petri Dishes

Embryonic bodies prepared in petri dishes in presence of the inducers for cardiac and neural differentiation (10^6 and 10^5 cells) (chapter 4.1.7) were measured 4 d and 5 d after seeding in the setup with one flow channel.

In the petri dish hundreds of aggregates with different sizes, adhered to each other or as single EB, are present. For this purpose, single EBs with an appropriate size for the PT-2 flow channel were picked by eye. Fig. 91 presents the results for the measurement of 4 d old EBs prepared in DMSO and RA. The time course of impedance magnitude (A) shows that EBs prepared in DMSO, specified as cardio-EB, caused a slightly higher increase in impedance of 30 – 35 kΩ after introduction compared to the neuro-EB with ~ 20 kΩ. This is also reflected in the frequency spectra (B). Approximately 1.5 h after EB introduction and measurement in MFT mode there is a switch to RTC mode measuring the micromotion of both EBs at 200 Hz. The detrended RTC data (C) shows similar fluctuation patterns for both EBs with a slightly higher variance V_{32} for the cardio-EB (~ 13 Ω^2) than for the neuro-EB (~ 4 Ω^2). Microscopic images at the end of the experiment show both EBs (D) at the channel aperture and partly inside the narrowed channel. The part of the neuro-EB which was inside the narrow channel appears drawn-out, whereas no abnormalities are observed for the cardio-EB.

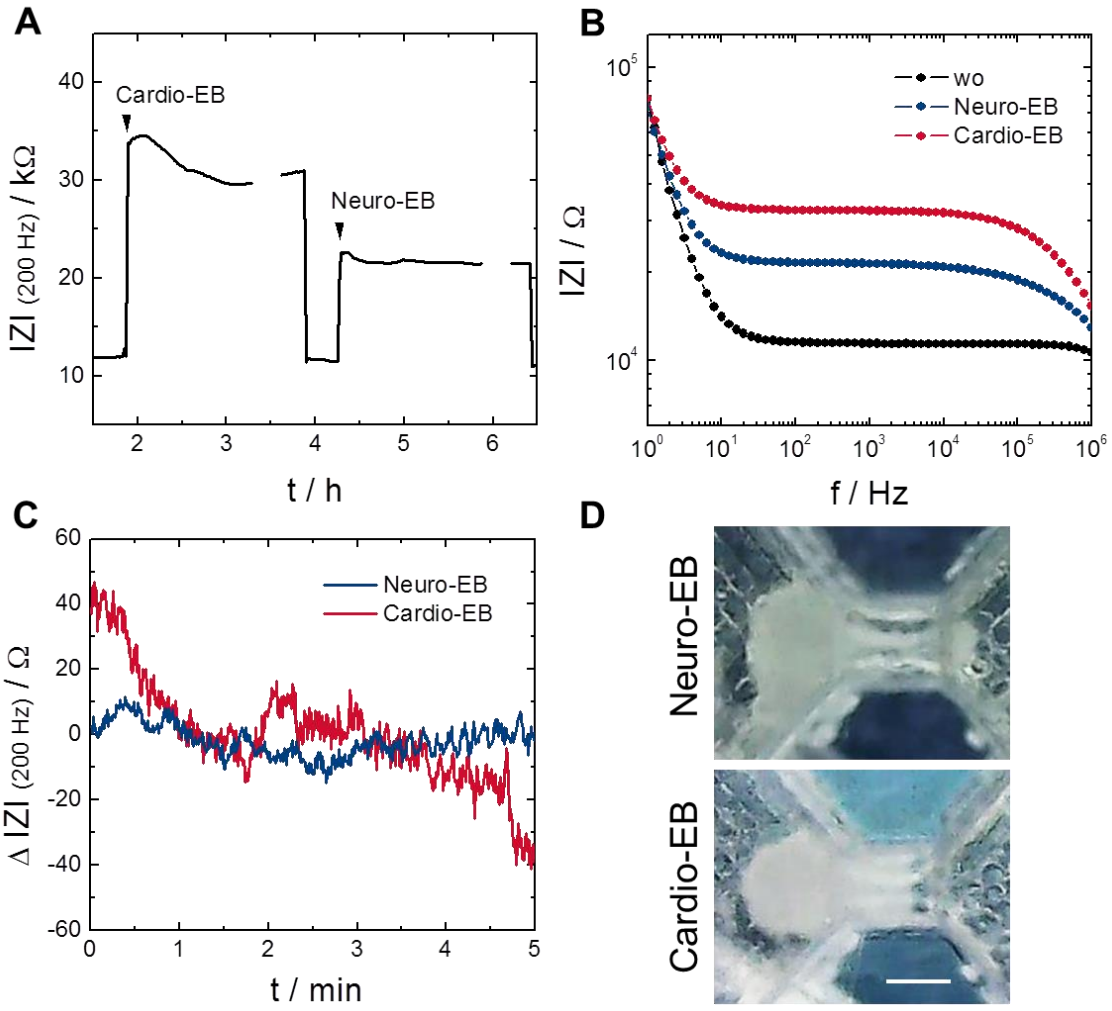

Fig. 91: Impedance analysis of differentiation-induced P19 embryonic bodies from petri dish (4 d) including the time course of impedance magnitude at 200 Hz (**A**), impedance spectra 30 min after EB introduction (**B**) and detrended RTC data (**C**) of a neuro- and cardio-EB. Both EBs are also documented microscopically at the end of the impedance measurement (**D**) (scale bar: 250 µm). T = 37 °C.

On the next day, the experiment was repeated obtaining the results shown in Fig. 92. This time, the cardio-EB leads to a minimal increase in impedance to ~ 12 kΩ, whereas the neuro-EB leads to a steady increase after introduction to ~ 45 kΩ and a sudden decrease to stable values around 35 kΩ (A). The distinct difference in impedance values of both EBs can be seen also in the frequency spectra (B). Detrended RTC data (C) reflect the low impedance value of the cardio-EB by very weak fluctuations with a variance V_{32} of ~ 0.8 Ω^2 (wo: ~ 0.09 Ω^2), whereas the neuro-EB shows stronger fluctuations with a variance of ~ 16 Ω^2.

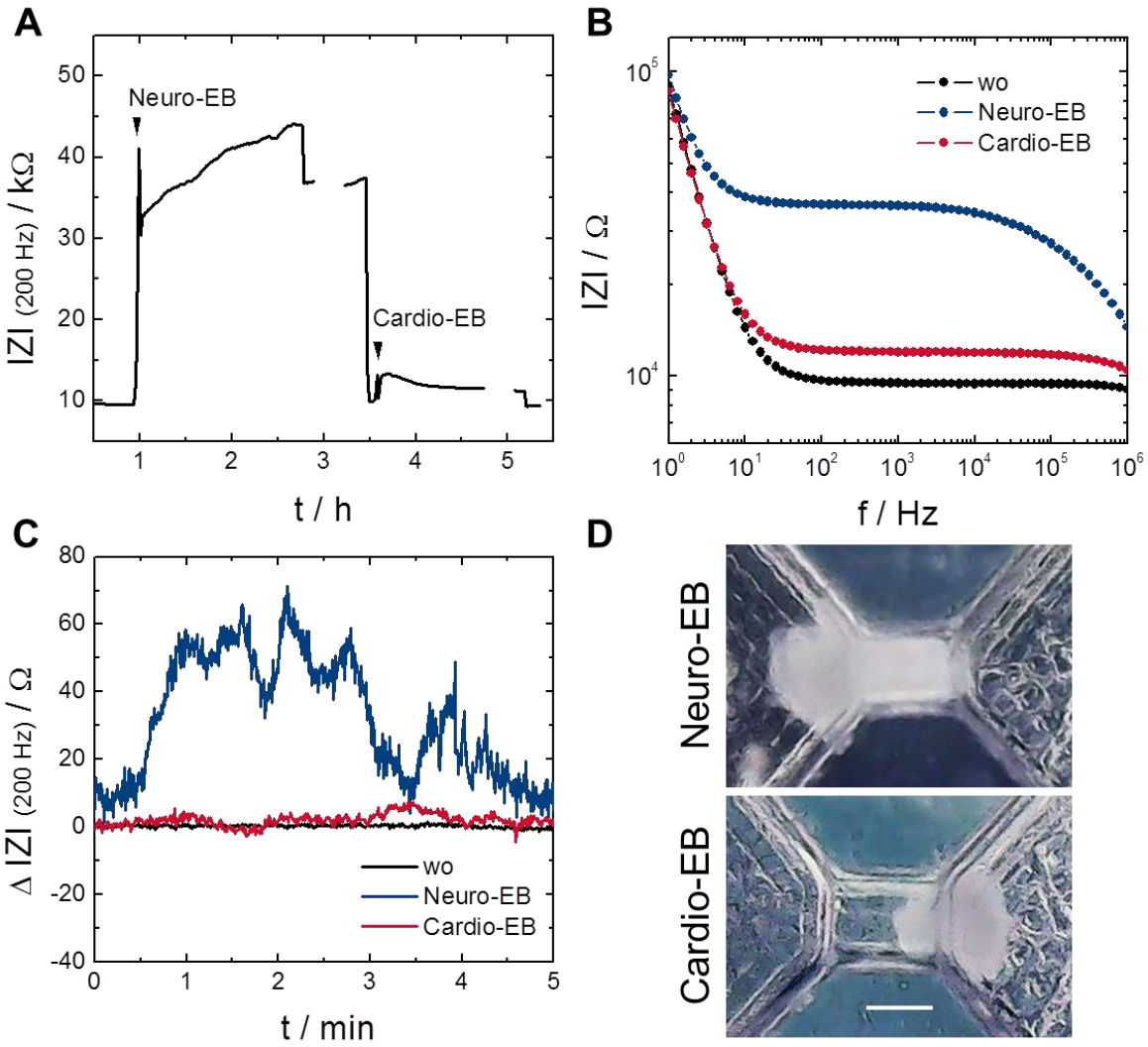

Fig. 92: Impedance analysis of differentiation-induced P19 embryonic bodies from petri dish (5 d). Including the time course of impedance magnitude at 200 Hz (**A**), impedance spectra 30 min after EB introduction (**B**) and detrended RTC data (**C**) of a Neuro- and Cardio-EB documented microscopically at the end of the impedance measurement (**D**) (scale bar: 250 µm). T = 37 °C.

The microscopic images (D) show that the cardio-EB is smaller than the neuro-EB and crosses the central channel instead of being positioned at the aperture in a stable way. The neuro-EB is rather big and fills the narrowed channel completely.

In both experiments beating of the cardio-EB is neither observed through the digital microscope nor in RTC impedance data.

In summary, these studies show that EBs grown in the non-adhesive petri dish are not applicable for an EIS analysis in the new flow channel due to the bad size reproducibility of the EBs.

8.2.2 EIS Study of Embryonic Bodies Grown in Hanging Drops

Impedance analysis was also performed on EBs prepared in hanging drops. First, EBs without inducers prepared with two different seeding densities (300 / 600 cells/drop) were investigated using the EIS channel setup with one flow channel. As can be seen in the time courses in Fig. 93 differently sized EBs cause similar impedance values (30 – 50 kΩ) which are stable over the entire observation period. The images on the right side show the EBs located partly inside the central channel. At the end of the MFT measurement these EBs are also recorded in RTC mode. The detrended RTC data in Fig. 94 show the fluctuations of the flow channel without embryonic body (A) with very weak fluctuations and a variance V_{32} of 0.2 Ω^2 in two individual measurements (1, 2). The fluctuations of two EBs that were prepared with a seeding density of 300 cells/well (B) show a variance of 79 Ω^2 (EB-1) and 76 Ω^2 (EB-2), respectively. Fluctuations of two EBs from 600 cells/well (C) are less pronounced with 16 Ω^2 (EB-1) and 12 Ω^2 (EB-2).

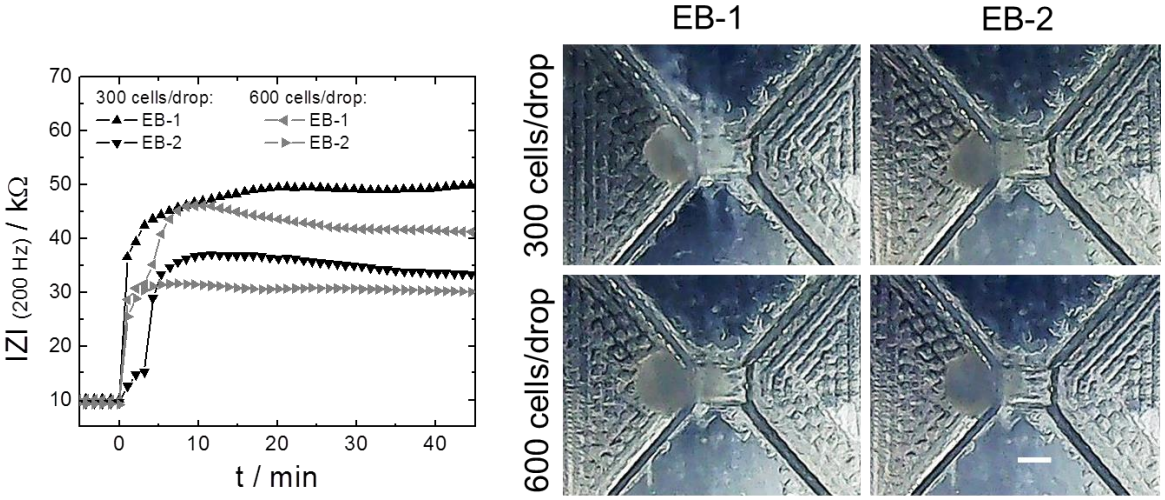

Fig. 93: Time course of impedance magnitude at 200 Hz for two EBs (EB-1, EB-2) from two seeding densities (300 / 600 cells/drop; 6 d). Micrographs of the respective EBs taken at the end of the measurement are shown on the right (scale bar: 250 µm). T = 37 °C.

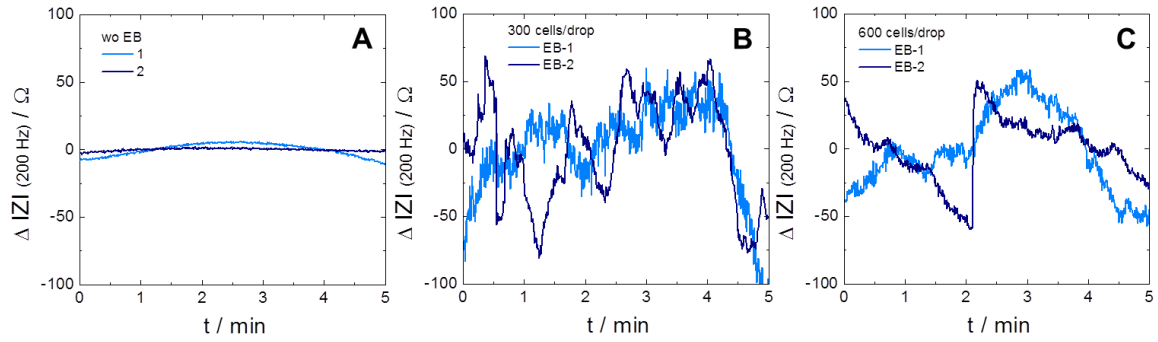

Fig. 94: Detrended RTC data at 200 Hz for the medium-filled channel without EB (A), with 300 cells/drop EBs (B) and with 600 cells/drop EBs. T = 37 °C.

The hanging drop EBs were also prepared in presence of DMSO to induce cardiac differentiation. Fig. 95 shows the time course of impedance for three EBs (A), whose introduction into the flow channel is marked by black arrows. First, an undifferentiated EB was measured leading to impedance values of 45 – 55 kΩ. Two subsequently measured EBs prepared in presence of DMSO show slightly lower impedance values between 35 and 45 kΩ. The corresponding detrended RTC data (B) shows strong superordinate fluctuations and moderate subordinate fluctuations with a variance V_{32} of ~ 99 Ω^2 for the undifferentiated EB and ~ 16 Ω^2 (EB-1) and ~ 38 Ω^2 (EB-2) for the two DMSO-induced EBs.

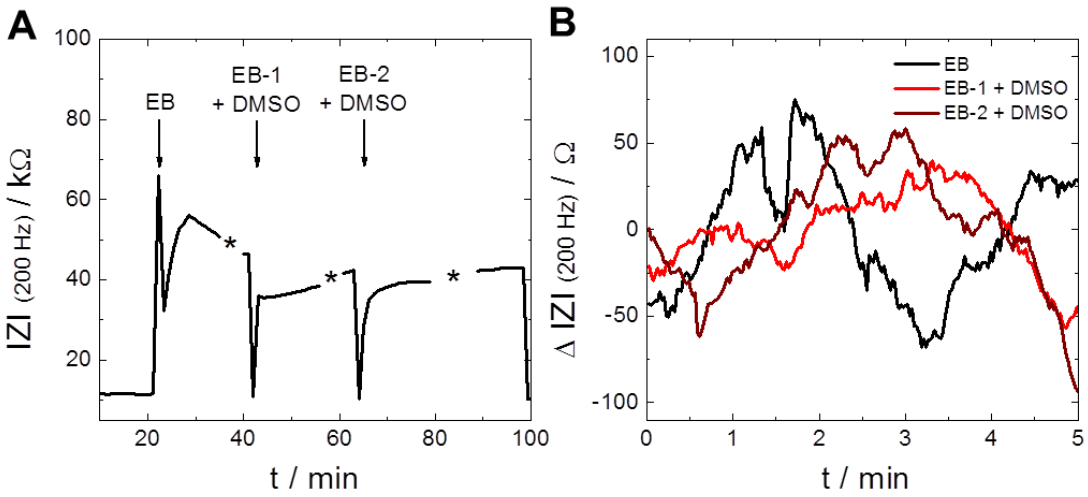

Fig. 95: Time course of impedance magnitude at 200 Hz for one EB (300 cells/drop, 5 d) without pre-treatment (EB) and two embryonic bodies pre-incubated in presence of 1 % DMSO (EB-1/-2 + DMSO) (**A**). The stars in the time course mark the time points when data was collected in RTC mode. The respective detrended RTC data is shown in **B**. T = 37 °C.

8.2.3 EIS Analysis of Embryonic Bodies Grown in the 96-Well Plate

Embryonic bodies with and without inducer for cardiac and neuronal differentiation were prepared in the non-adhesive 96-well plate (1000 cells/well; 3 / 4 d) and measured as described in chapter 4.3.6. Eight individual measurements were performed using FC-1, -2 and -3 and three typical time course measurements of impedance magnitude of the three EB types are shown in Fig. 96 (A – C).

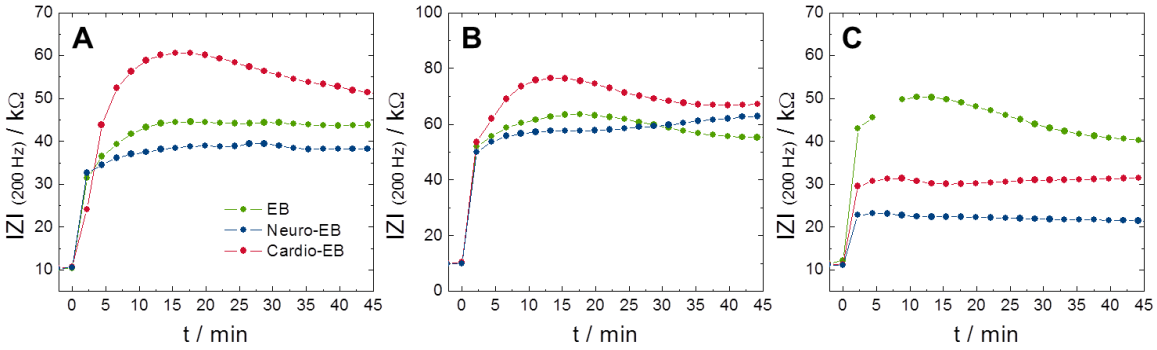

Fig. 96: Typical time courses of impedance magnitude at 200 Hz measured in FC-2/-3/-1 for undifferentiated EBs and EBs that were induced to differentiate into cardio- (1 % DMSO) and neuro-EBs (1 µM RA) (1000 cells/well; A,C: 3 d; B: 4 d). T = 37 °C.

In time course A cardio-EBs show the highest impedance, undifferentiated EBs a middle impedance and neuro-EBs the lowest impedance. This trend is observed in four out of eight measurements. Measurement B with its somewhat different ranking of impedance values for the different EB types is obtained twice as was for measurement C.

From the measured data the spheroid parameters R_{ext}, R_{int} and A_{sph} are determined by equivalent circuit modeling and summarized in Tab. 19. As seen in previous measurements the impedance values received from spheroids in FC-3 are higher than those received in FC-1/-2. For this purpose, data evaluation was performed separately for data measured in FC-3 and FC-1/-2 and only the observed trends (and not absolute values) in the spheroid parameters are compared. While R_{ext} values for undifferentiated EBs and cardio-EBs are similar, the values of neuro-EBs are reduced to about 50 %. R_{int} values for the three EB types are not significantly different.

A_{sph} values are similar for all conditions except for the neuro-EBs measured in FC-1/-2 whose A_{sph} value is about twice as high as the other values.

Tab. 19: Overview of the determined spheroid parameters R_{ext}, R_{int} and A_{sph} for embryonic bodies prepared with and without cardiac and neuronal inducers in 96-well plates. Spectra, 30 min after spheroid introduction in FC-3 or FC-1/-2 were fitted as described in chapter 4.3.3 using the following parameter values: A_{el} = 2 – 2.6 ·10^{-6} Fs^{n-1}cm^{-2}, n_{el} = 0.94, R_{bulk} = 9.4 – 13 kΩ, A_{para} = 3.5 – 5 ·10^{-12} Fs^{n-1}cm^{-2}, n_{para} = 0.99, n_{sph} = 0.75 (mean ± SE, n = 4).

FC-1/-2	*EB*	*Cardio-EB*	*Neuro-EB*
R_{ext} / kΩ	31 ± 2	37 ± 7	15 ± 4
R_{int} / kΩ	2.0 ± 0.3	4 ± 1	3 ± 1
A_{sph} / ·10^{-9} Fs^{n-1}cm^{-2}	1.7 ± 0.1	1.4 ± 0.2	3 ± 1

FC-3	*EB*	*Cardio-EB*	*Neuro-EB*
R_{ext} / kΩ	67 ± 8	62 ± 12	37 ± 10
R_{int} / kΩ	2.4 ± 0.2	2.7 ± 0.2	4 ± 2
A_{sph} / ·10^{-9} Fs^{n-1}cm^{-2}	1.69 ± 0.05	1.7 ± 0.1	1.8 ± 0.2

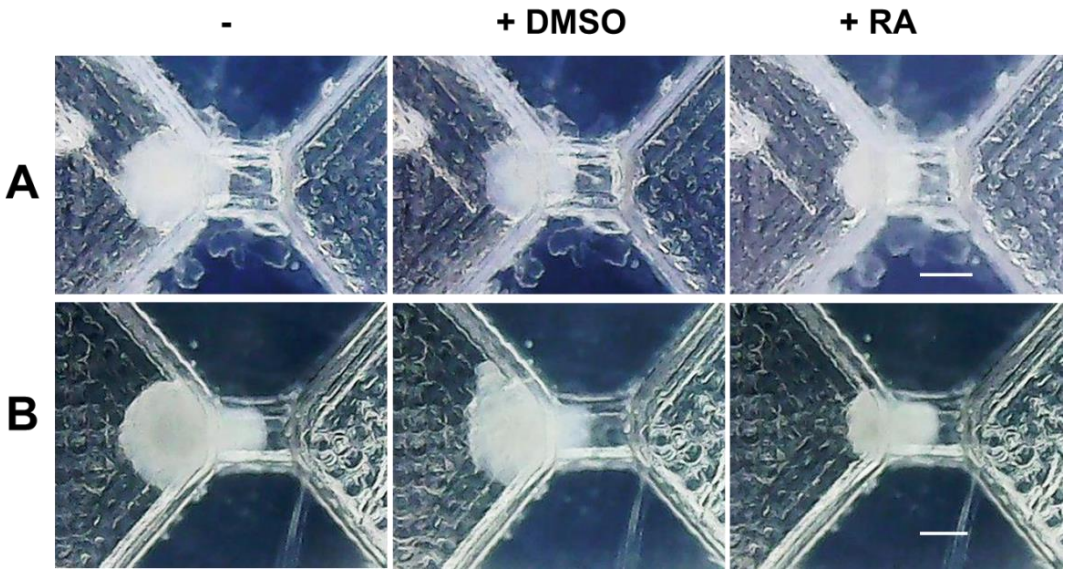

Fig. 97: Typical micrographs of two EBs (1000 cells/well; A: 3 d; B: 4 d) during the measurement in FC-2 (**A**) and FC-3 (**B**) without inducer (-) and with the inducer DMSO (1 %) or RA (1 µM) (scale bar: 250 µm). T = 37 °C.

Typical micrographs for each of the three EB types (A, B) are recorded during the measurement at/in the aperture and the central channel in Fig. 97. The EBs without inducer are similar in size (Ø = 515 ± 33 µm) compared to EBs generated in DMSO (Ø = 514 ± 26 µm). EBs with the inducer RA have smaller diameters (Ø = 412 ± 24µm) as was seen before in Fig. 90. They are barely held back by the aperture, although the same seeding density was used for the generation of all three types of EBs.

Each of the EBs was also measured in RTC mode subsequent to ~ 45 min MFT measurement in order to investigate the micromotion of the three EB types. Three detrended RTC time courses (A – C) are shown for each EB type in Fig. 98. The resulting fluctuation patterns are variable and show no obvious trend. The evaluation of the variance V_{32} of the fluctuations (Fig. 99 A, B) confirms that there is no significant difference in variance between EBs with and without inducers.

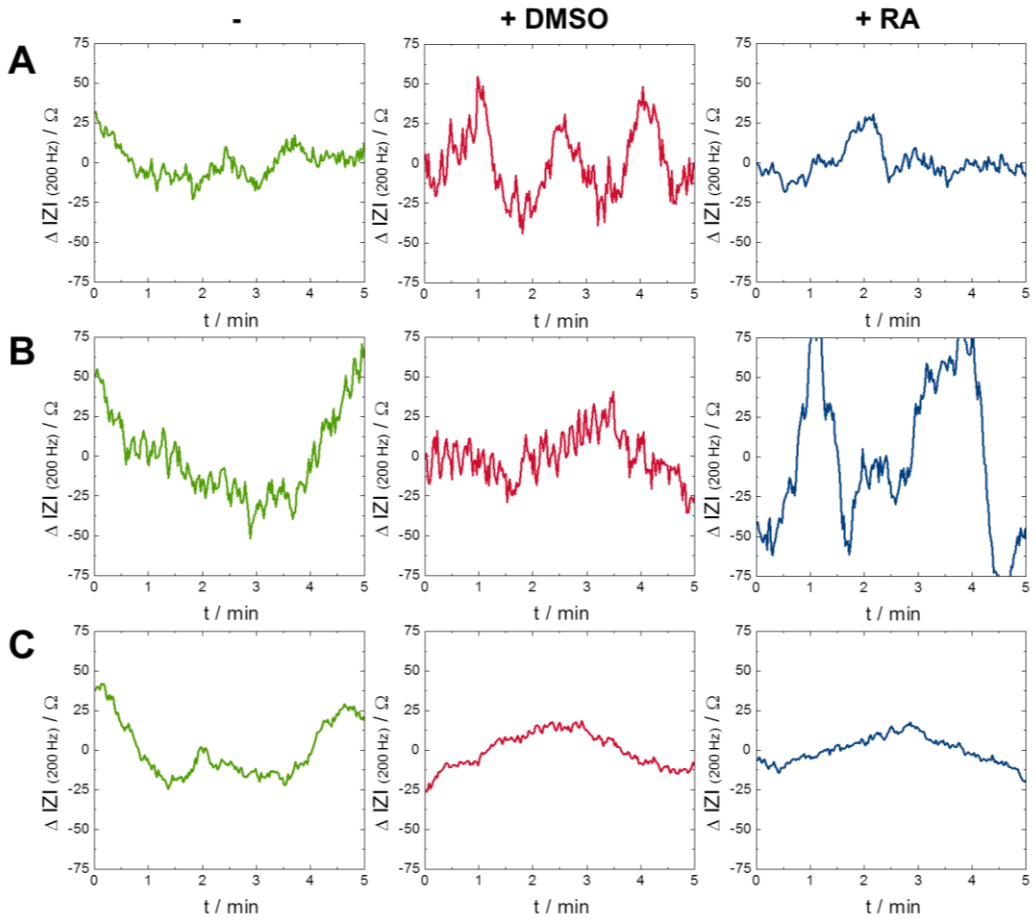

Fig. 98: Typical detrended RTC data from the three EB preparations shown in Fig. 96 (A: FC-2; B: FC-3; C: FC-1) for EBs without inducer (-) and with the inducer DMSO (1 %) or RA (1 µM). T = 37 °C.

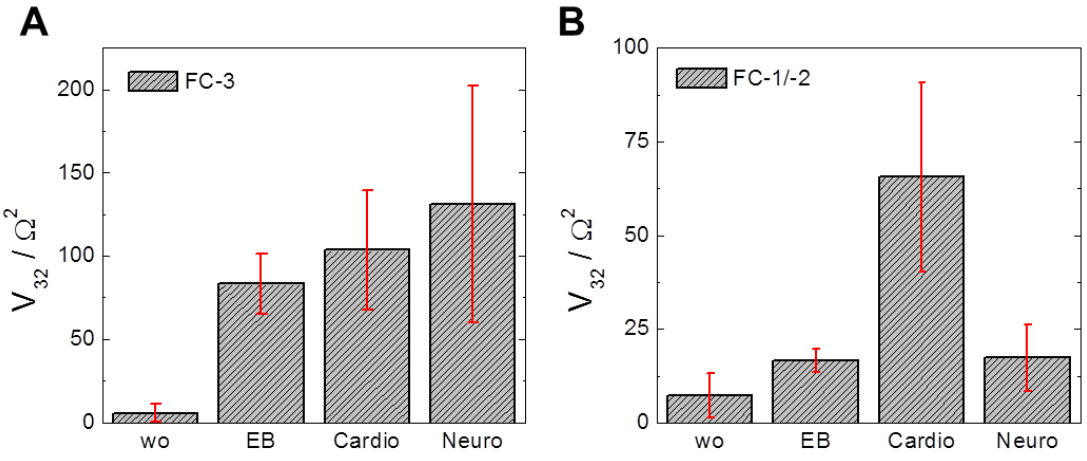

Fig. 99: Variance analysis of RTC data gained from differentiation-induced EBs (cardio, neuro), undifferentiated EBs and the flow channel without EBs (wo) measured in FC-3 (**A**) or FC-1/-2 (**B**) (mean ± SE, n = 4). The significance of V_{32} values was determined by a two-sample t-test using a significance level of 0.05. T = 37 °C.

8.3 Discussion

8.3.1 Characterization of Embryonic Bodies

P19 cells were seeded onto non-adhesive petri dishes, in hanging drops and in non-adhesive 96-well plates together with 1 % DMSO or 1 µM RA, the respective inducers for cardiac or neuronal differentiation. Each formation technique produced three-dimensional aggregates, the embryonic bodies. Using phase contrast microscopy the embryonic bodies and their possible differentiation was monitored.

- Cellular outgrowths of DMSO-EBs mainly resemble undifferentiated monolayer cells and show isolated axon-like structures. Cellular outgrowths of RA-EBs express different morphologies and also isolated axon-like structures.
- Hanging drop derived DMSO-EBs and 600 cells/drop undifferentiated EBs express bulges, whereas undifferentiated EBs from 300 cells/drop have a regular spherical or oval shape on day 5 after seeding.
- In the 96-well plate the bulge size of undifferentiated EBs increases with time in culture. In the growth curves from day 5 after seeding increased standard deviations are observable. Appropriate EB diameters for measurements in PT-2 flow channels are generated with seeding densities of 200 – 1000 cells/well grown for 2 – 3 d or 200 – 400 cells/well grown for 4 d. Undifferentiated and DMSO-EBs are similar in size and extent of bulges, whereas RA-EBs are smaller.
- EBs induced with DMSO are not beating during the observation period, independent of the EB formation technique.

Jasmin et al. (2010) used P19 cells as model system to study cardiac differentiation. They observed the spontaneous formation of embryonic bodies on bacteriological petri dishes (10^6 cells) in presence of 1 % DMSO. Four days after seeding they transferred the freshly formed EBs onto adhesive culture dishes containing medium without inducer. They observed that cells from

undifferentiated EBs were small with a high nucleus-to-cytoplasm ratio often observed for pluripotent cells. After differentiation into cardiac cells their most obvious characteristic was the rhythmical beating. On day seven after seeding in DMSO they observed beating areas in the EBs and the cellular outgrowths. The group confirmed the differentiation into cardiac cells by immunocytochemistry and calcium wave analysis. Shen et al. (2014) prepared their EBs also for 4 d in non-adhesive bacteriological petri dishes (10^6 cells) but used only 0.25 % DMSO. Afterwards, the EBs were transferred to adhesive gelatin-coated dishes and cultured for 8 more days in absence of DMSO. They obtained that ~ 30 % of the attached EBs beated on day eight after seeding. Wobus et al. (1994) prepared embryonic bodies in hanging drops (400 cells/drop) in presence of 1 % DMSO. After two days they were transferred to non-adhesive bacteriological petri dishes for five more days and subsequently they were adhered to 24-well culture plates. They observed the synchronous beating of up to 40 % of the EB outgrowths 12 d after seeding but the first spontaneous beating was detected 8 d after seeding among epithelial-like cells in outer regions of outgrowths.

In this thesis the differentiation to cardiac cells was performed using similar seeding densities, DMSO concentration and following the protocols for petri dish culture known from literature. Nevertheless, no beating of EBs could be observed during the observation period of 12 d at any time. Instead, the cellular morphology of the outer regions of outgrowths (Fig. 85) exhibit isolated axon-like structures although no neuronal inducer was present. These observations indicate that cardiac differentiation might not have occurred. Differences in the shape of DMSO-treated EBs in comparison to undifferentiated EBs (as seen in hanging drop EBs) might however, hint that some cellular alterations have occurred.

Jones-Villeneuve et al. (1982) performed the neuronal differentiation of P19 cells. They seeded 10^6 cells/mL in presence of 0.5 µM RA into a non-adhesive bacteriological petri dish where they formed aggregates. A transfer of the aggregates to adhesive culture dishes was performed 5 d after seeding. Within the following 24 h they observed the outgrowth of a flat layer of fibroblast-like cells from the aggregate (6 d). Again one day later neuron-like cells appeared with networks of processes (axon-related cellular extension) extending over the

monolayer of fibroblast-like cells (7 d). Micrographs proved these observations and showed also the morphology of undifferentiated P19 cells which are in good agreement to the P19 cells used in this thesis. In the review of Bain et al. (1994) the general process of neuronal differentiation is described starting with the formation of embryonic bodies in presence of RA for four days. Afterwards, the cell suspension from trypsinized EBs is seeded in adhesive culture plates in absence of the inducer. After cell plating they are capable of differentiating into neuron-, glia- and fibroblast-like cells. In the report the authors describe the neuronal differentiated cells to have small cell bodies and long processes similar to axons and dendrites. Yao et al. (1995) also performed a 4-day incubation period of P19 cells (10^5 cells/mL in culture dishes) with 0.35 – 0.7 µM RA followed by the adhesion of trypsinized EB cells on adhesive culture dishes. In the following 2 – 5 d the group also saw flat fibroblast-like cells and neuron-like cells with long processes.

Using similar culture conditions and a slightly higher RA concentration in this thesis the outgrowths of RA-induced EBs also show cells that appear flatter with fibroblast-like morphology and dendritic extensions (Fig. 86). However, neuron-like cells with extended processes were only sporadically observed (as was also seen in cardio-induced cultures). These observations indicate that a differentiation into neuronal cells was semi-successful. The fact that RA-EBs were smaller than undifferentiated EBs (from 96-well plate) and a lot of rounded singular cells were observed in the petri dish culture might be a hint that the used RA concentration has a slightly toxic effect reducing the proliferation or it might be related to the altered cellular morphology that produced smaller EBs.

In literature an altered cellular morphology upon differentiation was observed a few days after a 2 – 4 d incubation period with an inducer. These alterations were always identified by studying cells originated from EBs growing as a monolayer. It is not known if an altered cellular morphology is already present in the embryonic body in the first days together with the inducer. Due to the higher reproducibility of EB shape and size when produced in 96-well plates this formation technique was preferred over the others for the production of EBs for EIS measurements. However, the growth study of EBs prepared in the 96-well plate revealed that P19 EBs grow very fast so that only EBs that are 2 – 3 d old fit into the PT-2 flow

channels. Therefore, only morphological alterations in very early differentiation processes, of which it is unknown if they exist in EBs, can be studied using the new EIS device.

EBs produced in petri dishes and with the hanging drop method were only used for preliminary EIS measurements.

8.3.2 Impedimetric Analysis of Embryonic Bodies Grown in Non-Adhesive Petri Dishes and Hanging Drops

Embryonic bodies formed in a petri dish or in hanging drops were used only for preliminary impedimetric studies 4 – 6 d after seeding.

- DMSO- and RA-EBs from a petri dish lead to scattering values of impedance magnitudes in the range of 10 – 45 kΩ and variances in the range of 0.8 – 16 Ω^2.
- Hanging drop EBs from different seeding densities (300/600 cells/drop) lead to similar impedance magnitudes (30 – 50 kΩ). The variance of 300 cells/drop EBs (~ 80 Ω^2) is higher than that of 600 cells/drop EBs (10 – 20 Ω^2) and of 300 cells/drop EBs induced with DMSO (20 – 40 Ω^2).

The size distribution of EBs from the petri dish is very broad causing the contradictory results in EIS measurements. As long as EBs are not available with a reproducible size and shape they can be measured in the novel device but the results can not be compared with each other properly. EBs from hanging drops were generated in a more reproducible way. The results of the impedance-based analysis indicated that EBs from 300 cells/drop and 600 cells/drop can be distinguished from their micromotion which was higher for the smaller EBs. The fluctuations of small EBs prepared in presence of DMSO are lower than that of undifferentiated EBs of the same seeding density and showed no sign of beating indicating that cardiac differentiation did not take place or was still in progress. However, it should be kept in mind that this was just a single experiment that should not be overestimated.

8.3.3 Impedimetric Analysis of Embryonic Bodies Grown in the 96-Well Plate

Embryonic bodies produced in the non-adhesive 96-well plate in presence of the two inducers DMSO and RA were used to investigate if early cellular alterations and differentiation into cardiac or neuronal cells occured. In eight individual measurements using the novel EIS-based device the impedance and the variance of fluctuations of EBs (1000 cells/well, 3/4 d) were analyzed:

- The impedance of DMSO-induced EBs is in all cases higher than that of RA-induced EBs. The impedance of undifferentiated EBs is in four out of eight cases in between DMSO- and RA-induced EBs, in two cases higher than the DMSO-induced EBs and in two cases lower than the RA-induced EBs.

- R_{ext} values of neuro-EBs are lower than those of undifferentiated and cardio-EBs. R_{int} values are higher for cardio- and neuro EBs compared to undifferentiated EBs. A_{sph} values do not show any significant differences.

- Microscopic images from different EBs in the flow channel show that RA-EBs are smaller than undifferentiated and DMSO-EBs.

- The variances evaluated from RTC data of the three EB types measured in different flow channels are not significantly different.

From the growth study of EBs (chapter 8.1, Fig. 89) it was concluded that appropriate EB diameters for the measurement in PT-2 flow channels can be generated using seeding densities of 200 – 1000 cells/well grown for 2 – 3 d or 200 – 400 cells/well grown for 4 d. In order to let the EBs grow as long as possible and let them undergo cellular alterations, small seeding densities (200 cells/well) were used for the first impedance measurements conducted on day 4 – 5 after seeding (data not shown). Although, these EBs were theoretically big enough to be held back by the central aperture they crossed the channel, indicating that the deformability of P19 EBs was very high. For this purpose EBs with a higher seeding density of 1000 cells/well were prepared and measured on day 3 and 4 after seeding.

Only a few studies in literature investigate the differentiation process of cultured cells using impedance-based readout techniques. Bagnaninchi and Drummond (2011) as well as Hildebrandt et al. (2010) studied the osteogenic differentiation of stem cells using ECIS (2D) and EIS (3D), respectively. Due to different dielectric properties of stem cells and osteoblasts they were able to monitor the differentiation process in real-time without labels. Zhou et al. (2016) monitored mouse embryonic stem cells in different differentiation stages. The cells were prepared and fixed at different time points during the differentiation (0 / 24 / 48 h after differentiation) and single cells were trapped in a microfluidic device analyzing changes in the electrical parameters impedimetrically. The group was able to distinguish undifferentiated cells (0 h) from differentiating cells (24/48 h) by showing that the normalized impedance magnitude was increased for increasing differentiation time. Song et al. (2013) used a microfluidic impedance flow cytometer to distinguish undifferentiated P19 cells from RA-induced (1 µM) cells. Bieberich and Guiseppi-Elie (2004) used EIS-based interdigitated microelectrode arrays to measure *in vitro* neuronal differentiation of PC12 cells (2D) using the nerve growth factor (NGF) as inducer. They observed a lower impedance magnitude for differentiated cells compared to undifferentiated cells.

To my knowledge no reports were published dealing with EIS-based analysis of 3D embryonic bodies during early differentiation into cardiac and neuronal cells. The results on this topic in this thesis show that the new flow channel device can be used to measure embryonic bodies. However, different types of EBs (cardio, neuro, undifferentiated) showed no distinct and reproducible differences in impedance time courses and micromotion analysis. The reduced R_{ext} value for neuronal-induced EBs is assumed to be related to the distinctly smaller size of these EBs in comparison to the other EB types. It is therefore concluded that the measurement of 4 d-old EBs is probably too early to detect cellular alterations.

9 Summary

The use of 3D tissue models is an emerging branch of cell-based *in vitro* assays. However, the advancement of appropriate readout techniques capable of reaching into the center of those cell aggregates proceeds rather slowly.

This thesis addresses the characterization and testing of a new impedance-based device to analyze 3D multicellular spheroids non-invasively and label-free. The new device consists of a flow channel with a central aperture that is sealed by the spheroid. ITO electrodes positioned at the bottom of the two channel reservoires enable the EIS analysis of the trapped spheroid in the flow channel. The channel and the electrode layout are made of transparent material and therefore allow spheroid imaging within the channel.

The flow channel can be cleaned easily and re-used several times. Spheroid introduction into the channel and positioning in front of the central aperture by fluid flow is straightforward. Upon spheroid introduction and subsequent sealing of the aperture the impedance of the channel is significantly increased compared to the impedance of a spheroid-free channel. The overall impedance of the setup is dominated by the dielectric properties of the spheroid and allows for its detailed analysis. Spheroids with the same age and formed from the same seeding density as well as repositioned spheroids showed reproducible impedance characteristics. By implementation of a transfer function in a *LabView*-based software describing the equivalent circuit model of a spheroid in the EIS device it is possible to quantify the dielectric properties of spheroids. These are described by the three spheroid parameters: (i) R_{ext}, reflecting the extracellular resistance caused by the current flow around cellular bodies and through the extracellular matrix, (ii) the intracellular resistance R_{int} caused by the resistivity of the cytoplasm and (iii) the non-ideal total capacitance A_{sph} of the cell membranes.

For proof-of-concept studies MCF-7 tumor spheroids, P19 embryonic bodies and Cor.At® cardiospheres were prepared preferentially by cell aggregation on a non-adhesive surface in a 96-well plate, as it reproducibly generates spheroids of defined size. The tumor spheroids were used to study their morphological alterations upon exposure to invasive stimuli (PFA, saponin, osmotic pressure, cytochalasin D, hyperthermia, irradiation after CaAM or C-dot loading of

spheroids). Spheroid injury or death is reflected by a decrease in micromotion (V_{32}), overall impedance and the spheroid parameters R_{ext} and R_{int}, whereas A_{sph} shows individually different changes. Cardiospheres were investigated based on their beating behavior. Their response to well-known contraction enhancing or inhibiting substances was measured successfully and along physiological mechanisms. Embryonic bodies were used to study their differentiation into cardiomyocytes and neurons. However, due to inefficient differentiation, no distinct changes in impedance were observed.

In summary, the impedance-based flow channel is a label-free, non-invasive and time resolved new readout technique to monitor 3D tissue models and their changes within biomedical experiments.

10 Zusammenfassung

In Zell-basierten Analyseverfahren werden 2D planare Zellmodelle zunehmend durch 3D Gewebemodelle ersetzt. Die Weiterentwicklung und Anpassung der Auslesemethoden, um das neue Modellsystem bis zu seinem Kern zu analysieren ist jedoch ein langwieriger Prozess.

In dieser Arbeit wird ein neu entwickeltes Impedanz-basiertes Messsystem zur nichtinvasiven und markierungsfreien Analyse von 3D multizellularen Sphäroiden vorgestellt und dessen Anwendbarkeit geprüft. Bei dem neuen Messsystem handelt es sich um einen Fließkanal mit zentraler Engstelle, an der das Sphäroid zurückgehalten wird und zur Abdichtung des Kanals führt. Planare ITO Elektroden die sich jeweils am Boden der beiden Reservoire befinden ermöglichen die Impedanz-basierte Analyse des Sphäroids im Kanal. Die Verwendung von transparenten Materialien zur Herstellung des Kanals und des planaren Elektrodenlayouts ermöglicht die Beobachtung des Sphäroids im Kanal durch verschiedene mikroskopische Bildgebungsverfahren.

Weitere Vorteile des Systems sind die unkomplizierte Reinigung und die mehrfache Wiederverwendbarkeit des Fließkanals sowie die einfache Einführung und Positionierung des Sphäroids an der zentralen Engstelle im Kanal mithilfe des Flüssigkeitsstroms. Durch das Einbringen eines Sphäroids in den Kanal und die darauf folgende Abdichtung an der Engstelle wird ein signifikanter Anstieg der Impedanz gegenüber dem Sphäroid-freien Kanal ausgelöst. Die Gesamt-impedanz des Kanals wird von den dielektrischen Eigenschaften des Sphäroids dominiert und ermöglicht eine genaue Impedanz-basierte Analyse.

Sphäroide gleichen Alters und gleicher Aussaatdichte sowie repositionierte Sphäroide zeigten reproduzierbare Impedanzeigenschaften. Zur Untersuchung der dielektrischen Eigenschaften eines Sphäroids werden die erhaltenen Impedanzspektren mit Hilfe von Ersatzschaltbildern analysiert. Die dielektrischen Eigenschaften des Sphäroids werden von drei Parametern beschrieben. Dabei handelt es sich unter anderem um den extrazellulären Wiederstand R_{ext}, der durch den Stromfluß um die Zellen und durch die extrazelluläre Matrix verursacht wird. Weitere Parameter sind der intrazelluläre Wiederstand R_{int}, der vom Wiederstand des Zytoplasmas verursacht wird, sowie die nicht ideale gesamte

Kapazität A_{sph} aller Zellmembranen im Sphäroid.

Für die Durchführung von Modellstudien wurden MCF-7 Tumorsphäroide, P19 *embryonic bodies* und Cor.At® Cardiosphäroide verwendet. Diese wurden bevorzugt mit Hilfe der Methode der nicht-adhäsiven Oberflächenkultur in der 96-well Platte hergestellt, da die Sphäroide nach dieser Methode mit definierten Durchmessern reproduzierbar hergestellt werden konnten. Tumor Sphäroide, die durch verschiedene invasive Stimulantien (PFA, Saponin, osmotischer Stress, Cytochalasin D, Hyperthermie, Bestrahlung von Sphäroiden nach CaAM or C-dot Beladung) beschädigt oder abgetötet wurden, zeigten generell eine Abnahme der *micromotion* (V_{32}), der Impedanz und der Sphäroidparameter R_{ext} and R_{int}, während A_{sph} individuelle Änderungen verzeichnete. Der Einfluss von bekannten Reagenzien zur Steigerung oder zur Inhibierung der Kontraktionsfähigkeit von Cardiosphäroiden konnte anhand eines stark veränderten Kontraktionsmusters eindeutig nachgewiesen werden. *Embryonic bodies*, die eigentlich hinsichtlich ihrer Differenzierung in Cardiomyozyten und neuronale Zellen untersucht wurden, zeigten keine Impedanzänderungen aufgrund von unzureichender Differenzierung.

Auf Basis der erhaltenen Ergebnisse kann das neue Impedanz-basierte Messverfahren als markierungsfreie, nichtinvasive und zeitlich hochaufgelöste Anaylsemethode für 3D Gewebemodellen angesehen werden, mit der man die dielektrischen Eigenschaften von Sphäroiden und deren Änderung während biomedizinischen Experimenten erfassen kann.

11 Outlook

The new EIS-based flow channel is a promising setup for the time-resolved and non-invasive readout of spheroid responses that is applicable for basic research on different spheroid models and might be used also for cytotoxicity assessment such as screening of anticancer agents. However, impedance measurements with different types of 3D spheroid models showed that further improvements on the device will significantly increase its applicability and ease of handling.

The design of the flow channel should be optimized in order to enable the addition of reagents and the exchange of culture medium without the need of spheroid repositioning or pre-incubation of the spheroid with the respective test substance. Consequently, only then longtime measurements over several days and time resolved monitoring of fast kinetic processes occuring immediately after substance addition are possible in a standardized form. Such improvements on the device could for example comprise separate channels for spheroid loading and for perfusion with medium. For this purpose, the medium supply channel has to be in close proximity to the spheroid at the central aperture.

Another aspect for improvement is a better uniformity of the channel dimensions to prevent differences in the spheroidal impedance contributions from channel to channel and to enable a comparison of absolute values of different spheroids. Furthermore, for differently sized spheroids different channel and aperture heights are needed.

After optimization of the flow channel design, a chip including several flow channels might be developed to enable a higher throughput of measurements. For this purpose, standardized and well-established formats might be used (e.g. 8-well array, 96-well plate) to allow measurements in commercially available readout systems. Computer controlled pump systems for automated perfusion of the spheroid-loaded channel with fresh medium or medium supplemented with test substances might increase automation and improve reproducibility.

Such an optimized EIS device with increased channel height might be more suitable to measure longterm differentiation of big sized EBs including regular media changes and supply with differentiation inducers.

12 References

A

Abassi, Y. A., B. Xi, N. Li, W. Ouyang, A. Seiler, M. Watzele, R. Kettenhofen, H. Bohlen, A. Ehlich and E. Kolossov (2012). "Dynamic monitoring of beating periodicity of stem cell-derived cardiomyocytes as a predictive tool for preclinical safety assessment." British journal of pharmacology **165**(5): 1424-1441.

Achilli, T. M., S. McCalla, A. Tripathi and J. R. Morgan (2012). "Quantification of the kinetics and extent of self-sorting in three dimensional spheroids." Tissue Eng Part C Methods **18**(4): 302-309.

Ahmed, K., Y. Tabuchi and T. Kondo (2015). "Hyperthermia: an effective strategy to induce apoptosis in cancer cells." Apoptosis **20**(11): 1411-1419.

Amos, W. and J. White (2003). "How the confocal laser scanning microscope entered biological research." Biology of the Cell **95**(6): 335-342.

Anderson, J. M. (2001). "Biological responses to materials." Annual review of materials research **31**(1): 81-110.

Aoudjit, F. and K. Vuori (2001). "Integrin signaling inhibits paclitaxel-induced apoptosis in breast cancer cells." Oncogene **20**(36): 4995-5004.

Arndt, S., J. Seebach, K. Psathaki, H. J. Galla and J. Wegener (2004). "Bioelectrical impedance assay to monitor changes in cell shape during apoptosis." Biosens Bioelectron **19**(6): 583-594.

Asayesh, T., V. Changizi and N. Eyvazzadeh (2016). "Assessment of cytotoxic damage induced by irradiation combined with hyperthermia and Gemcitabine on cultured glioblastoma spheroid cells." Radiation Physics and Chemistry **120**: 44-48.

Athanasiou, K. A., R. Eswaramoorthy, P. Hadidi and J. C. Hu (2013). "Self-organization and the self-assembling process in tissue engineering." Annual review of biomedical engineering **15**: 115.

Awasare, S., S. Bhujbal and R. Nanda (2012). "In vitro cytotoxic activity of novel oleanane type of triterpenoid saponin from stem bark of Manilkara zapota Linn." Asian J Pharm Clin Res **5**(4): 183-188.

B

Bain, G., T. P. Ramkumar, J. M. Cheng and D. I. Gottlieb (1993). "Expression of the genes coding for glutamic acid decarboxylase in pluripotent cell lines." Molecular brain research **17**(1): 23-30.

Baltazar, L. M., A. Ray, D. A. Santos, P. S. Cisalpino, A. J. Friedman and J. D. Nosanchuk (2015). "Antimicrobial photodynamic therapy: an effective alternative approach to control fungal infections." Front Microbiol **6**: 202.

Bartholomä, P., E. Gorjup, D. Monz, A. Reininger-Mack, H. Thielecke and A. Robitzki (2005). "Three-dimensional in vitro reaggregates of embryonic cardiomyocytes: a potential model system for monitoring effects of bioactive agents." J Biomol Screen **10**(8): 814-822.

Bartholomä, P., Impidjati, A. Reininger-Mack, Z. Zhang, H. Thielecke and A. Robitzki (2005). "A more aggressive breast cancer spheroid model

coupled to an electronic capillary sensor system for a high-content screening of cytotoxic agents in cancer therapy: 3-dimensional in vitro tumor spheroids as a screening model." J Biomol Screen **10**(7): 705-714.

Beauchamp, P., W. Moritz, J. M. Kelm, N. D. Ullrich, I. Agarkova, B. D. Anson, T. M. Suter and C. Zuppinger (2015). "Development and Characterization of a Scaffold-Free 3D Spheroid Model of Induced Pluripotent Stem Cell-Derived Human Cardiomyocytes." Tissue Eng Part C Methods **21**(8): 852-861.

Berdichevsky, Y., H. Sabolek, J. B. Levine, K. J. Staley and M. L. Yarmush (2009). "Microfluidics and multielectrode array-compatible organotypic slice culture method." Journal of neuroscience methods **178**(1): 59-64.

Bers, D. M. (2002). "Cardiac excitation–contraction coupling." Nature **415**(6868): 198-205.

Bierwolf, J., M. Lutgehetmann, K. Feng, J. Erbes, S. Deichmann, E. Toronyi, C. Stieglitz, B. Nashan, P. X. Ma and J. M. Pollok (2011). "Primary rat hepatocyte culture on 3D nanofibrous polymer scaffolds for toxicology and pharmaceutical research." Biotechnol Bioeng **108**(1): 141-150.

Bilodeau, K. and D. Mantovani (2006). "Bioreactors for tissue engineering: focus on mechanical constraints. A comparative review." Tissue engineering **12**(8): 2367-2383.

Birchler, A., M. Berger, V. Jäggin, T. Lopes, M. Etzrodt, P. Misun, M. Pena-Francesch, T. Schroeder, A. Hierlemann and O. Frey (2016). "Seamless Combination of Fluorescence-Activated Cell Sorting and Hanging-Drop Networks for Individual Handling and Culturing of Stem Cells and Microtissue Spheroids." Analytical chemistry.

Brakenhoff, G., H. Van der Voort, E. Van Spronsen and N. Nanninga (1986). "Three-Dimensional Imaging by Confocal Scanning Fluorescence Microscopya." Annals of the New York Academy of Sciences **483**(1): 405-415.

Brohem, C. A., L. B. da Silva Cardeal, M. Tiago, M. S. Soengas, S. B. de Moraes Barros and S. S. Maria-Engler (2011). "Artificial skin in perspective: concepts and applications." Pigment cell & melanoma research **24**(1): 35-50.

Buchholz, B., G. Schley, D. Faria, S. Kroening, C. Willam, R. Schreiber, B. Klanke, N. Burzlaff, J. Jantsch and K. Kunzelmann (2013). "Hypoxia-inducible factor-1α causes renal cyst expansion through calcium-activated chloride secretion." Journal of the American Society of Nephrology: ASN. 2013030209.

Buchholz, B., B. Teschemacher, G. Schley, H. Schillers and K.-U. Eckardt (2011). "Formation of cysts by principal-like MDCK cells depends on the synergy of cAMP-and ATP-mediated fluid secretion." Journal of molecular medicine **89**(3): 251-261.

Bürgel, J. Y. K., A. Hierlemann, O. Frey (2013). "Electrical Impedance Spectroscopy for Label-Free, Continuous Monitoring of Drug Impact on 3D Tissue Spheroids." 17th International Conference on Miniaturized Systems for Chemistry and Life Sciences, Freiburg, Germany.

Bürgel, S. C., Y. Schmid, I. Agarkova, D. A. Fluri, J. M. Kelm, A. Hierlemann and O. Frey (2015). Simultaneous impedance spectroscopy and stimulation of human iPS-derived cardiac 3D spheroids in hanging-drop networks. 2015

28th IEEE International Conference on Micro Electro Mechanical Systems (MEMS), IEEE.

C

Candi, E., R. Schmidt and G. Melino (2005). "The cornified envelope: a model of cell death in the skin." Nature reviews Molecular cell biology **6**(4): 328-340.

Carterson, A., K. H. zu Bentrup, C. Ott, M. Clarke, D. Pierson, C. Vanderburg, K. Buchanan, C. Nickerson and M. Schurr (2005). "A549 lung epithelial cells grown as three-dimensional aggregates: alternative tissue culture model for Pseudomonas aeruginosa pathogenesis." Infect Immun **73**(2): 1129-1140.

Casey, R. C., K. M. Burleson, K. M. Skubitz, S. E. Pambuccian, T. R. Oegema, L. E. Ruff and A. P. Skubitz (2001). "β1-integrins regulate the formation and adhesion of ovarian carcinoma multicellular spheroids." Am J Pathol **159**(6): 2071-2080.

Caspi, O., I. Itzhaki, I. Kehat, A. Gepstein, G. Arbel, I. Huber, J. Satin and L. Gepstein (2009). "In vitro electrophysiological drug testing using human embryonic stem cell derived cardiomyocytes." Stem Cells Dev **18**(1): 161-172.

Chen, X., B. Zheng and H. Liu (2011). "Optical and digital microscopic imaging techniques and applications in pathology." Analytical Cellular Pathology **34**(1, 2): 5-18.

Chua, A. W. C., Y. C. Khoo, B. K. Tan, K. C. Tan, C. L. Foo and S. J. Chong (2016). "Skin tissue engineering advances in severe burns: review and therapeutic applications." Burns & Trauma **4**(1): 1.

Cowan, D. S. and I. F. Tannock (2001). "Factors that influence the penetration of methotrexate through solid tissue." International journal of cancer **91**(1): 120-125.

Croix, B. S., V. A. FLøRENES, J. W. Rak, M. Flanagan, N. Bhattacharya, J. M. Slingerland and R. S. Kerbel (1996). "Impact of the cyclin-dependent kinase inhibitor p27." Nature medicine **2**(11).

Curcio, E., S. Salerno, G. Barbieri, L. De Bartolo, E. Drioli and A. Bader (2007). "Mass transfer and metabolic reactions in hepatocyte spheroids cultured in rotating wall gas-permeable membrane system." Biomaterials **28**(36): 5487-5497.

D

de Vos tot Nederveen Cappel, W., H. J. Meulenbeld, J. H. Kleibeuker, F. M. Nagengast, F. H. Menko, G. Griffioen, A. Cats, H. Morreau, H. Gelderblom and H. F. Vasen (2004). "Survival after adjuvant 5-FU treatment for stage III colon cancer in hereditary nonpolyposis colorectal cancer." International journal of cancer **109**(3): 468-471.

Desoize, B. and J. Jardillier (2000). "Multicellular resistance: a paradigm for clinical resistance?" Crit Rev Oncol Hematol **36**(2-3): 193-207.

Duguay, D., R. A. Foty and M. S. Steinberg (2003). "Cadherin-mediated cell adhesion and tissue segregation: qualitative and quantitative determinants." Developmental biology **253**(2): 309-323.

Durand, R. and R. Sutherland (1972). "Effects of intercellular contact on repair of radiation damage." Exp Cell Res **71**(1): 75-80.

Durand, R. E. (1978). "Effects of hyperthermia on the cycling, noncycling, and hypoxic cells of irradiated and unirradiated multicell spheroids." Radiation research **75**(2): 373-384.

E

Edinger, A. L. and C. B. Thompson (2004). "Death by design: apoptosis, necrosis and autophagy." Current opinion in cell biology **16**(6): 663-669.

Eichler, M., H.-G. Jahnke, D. Krinke, A. Müller, S. Schmidt, R. Azendorf and A. A. Robitzki (2015). "A novel 96-well multielectrode array based impedimetric monitoring platform for comparative drug efficacy analysis on 2D and 3D brain tumor cultures." Biosensors and Bioelectronics **67**: 582-589.

Elson, E. L. (1988). "Cellular mechanics as an indicator of cytoskeletal structure and function." Annual review of biophysics and biophysical chemistry **17**(1): 397-430.

Endo, M. (1977). "Calcium release from the sarcoplasmic reticulum." Physiological Reviews **57**(1): 71-108.

Eschenhagen, T. and W. H. Zimmermann (2005). "Engineering myocardial tissue." Circ Res **97**(12): 1220-1231.

F

Fabiato, A. and F. Fabiato (1975). "Contractions induced by a calcium-triggered release of calcium from the sarcoplasmic reticulum of single skinned cardiac cells." J Physiol **249**(3): 469.

Fennema, E., N. Rivron, J. Rouwkema, C. van Blitterswijk and J. de Boer (2013). "Spheroid culture as a tool for creating 3D complex tissues." Trends Biotechnol **31**(2): 108-115.

Figaro, S., U. Pereira, H. Rada, N. Semenzato, D. Pouchoulin and C. Legallais (2015). Development and validation of a bioartificial liver device with fluidized bed bioreactors hosting alginate-encapsulated hepatocyte spheroids. 2015 37th Annual International Conference of the IEEE Engineering in Medicine and Biology Society (EMBC), IEEE.

Foty, R. A. and M. S. Steinberg (2005). "The differential adhesion hypothesis: a direct evaluation." Developmental biology **278**(1): 255-263.

França, M., A. Panek and E. Eleutherio (2007). "Oxidative stress and its effects during dehydration." Comparative Biochemistry and Physiology Part A: Molecular & Integrative Physiology **146**(4): 621-631.

Frankel, A., S. Man, P. Elliott, J. Adams and R. S. Kerbel (2000). "Lack of multicellular drug resistance observed in human ovarian and prostate carcinoma treated with the proteasome inhibitor PS-341." Clinical cancer research **6**(9): 3719-3728.

Frey, O., P. M. Misun, D. A. Fluri, J. G. Hengstler and A. Hierlemann (2014). "Reconfigurable microfluidic hanging drop network for multi-tissue interaction and analysis." Nature communications **5**.

Fricke, H. and S. Morse (1925). "The electric resistance and capacity of blood for frequencies between 800 and 4½ million cycles." The Journal of general physiology **9**(2): 153.

Fukuda, J. and K. Nakazawa (2011). "Hepatocyte spheroid arrays inside microwells connected with microchannels." Biomicrofluidics **5**(2): 22205.

Furusawa, Y., T. Iizumi, Y. Fujiwara, Q.-L. Zhao, Y. Tabuchi, T. Nomura and T. Kondo (2012). "Inhibition of checkpoint kinase 1 abrogates G2/M checkpoint activation and promotes apoptosis under heat stress." Apoptosis **17**(1): 102-112.

G

Ganjali, H. and M. Ganjali (2013). "Fixation in tissue processing." IJFAS **68**: 686-689.

Gao, X., W. Bian, J. Yang, K. Tang, H. Kitani, T. Atsumi and N. Jing (2001). "A role of N-cadherin in neuronal differentiation of embryonic carcinoma P19 cells." Biochem Biophys Res Commun **284**(5): 1098-1103.

Gerth, W. A. and C. M. Watke (1993). "Electrical Impedance Spectroscopic Monitoring of Body Compartmental Volume Changes." Journal of Clinical Engineering **18**(3): 253-260.

Giaever, I. and C. R. Keese (1984). "Monitoring fibroblast behavior in tissue culture with an applied electric field." Proc Natl Acad Sci U S A **81**(12): 3761-3764.

Giaever, I. and C. R. Keese (1991). "Micromotion of mammalian cells measured electrically." Proc Natl Acad Sci U S A **88**(17): 7896-7900.

Grinnell, F. (2003). "Fibroblast biology in three-dimensional collagen matrices." Trends in cell biology **13**(5): 264-269.

Gunning, P. W., G. Schevzov, A. J. Kee and E. C. Hardeman (2005). "Tropomyosin isoforms: divining rods for actin cytoskeleton function." Trends in cell biology **15**(6): 333-341.

H

Helmchen, F. and W. Denk (2005). "Deep tissue two-photon microscopy." Nat Methods **2**(12): 932-940.

Hildebrandt, B., P. Wust, O. Ahlers, A. Dieing, G. Sreenivasa, T. Kerner, R. Felix and H. Riess (2002). "The cellular and molecular basis of hyperthermia." Crit Rev Oncol Hematol **43**(1): 33-56.

Hildebrandt, C., H. Buth, S. Cho, Impidjati and H. Thielecke (2010). "Detection of the osteogenic differentiation of mesenchymal stem cells in 2D and 3D cultures by electrochemical impedance spectroscopy." J Biotechnol **148**(1): 83-90.

Hirano, H., Y. Tabuchi, T. Kondo, Q.-L. Zhao, R. Ogawa, Z.-G. Cui, L. Feril Jr and S. Kanayama (2005). "Analysis of gene expression in apoptosis of human lymphoma U937 cells induced by heat shock and the effects of α-phenyl N-tert-butylnitrone (PBN) and its derivatives." Apoptosis **10**(2): 331-340.

Hirschhaeuser, F., H. Menne, C. Dittfeld, J. West, W. Mueller-Klieser and L. A. Kunz-Schughart (2010). "Multicellular tumor spheroids: an underestimated tool is catching up again." J Biotechnol **148**(1): 3-15.

Ho, W. Y., S. K. Yeap, C. L. Ho, R. A. Rahim and N. B. Alitheen (2012). "Development of multicellular tumor spheroid (MCTS) culture from breast cancer cell and a high throughput screening method using the MTT assay." PLoS One **7**(9): e44640.

Holopainen, I. E. (2005). "Organotypic hippocampal slice cultures: a model system to study basic cellular and molecular mechanisms of neuronal cell death, neuroprotection, and synaptic plasticity." Neurochemical research **30**(12): 1521-1528.

Holtfreter, J. (1944). "A study of the mechanics of gastrulation." Journal of experimental zoology **95**(2): 171-212.

Horch, R. E., J. Kopp, U. Kneser, J. Beier and A. D. Bach (2005). "Tissue engineering of cultured skin substitutes." J Cell Mol Med **9**(3): 592-608.

Horning, J. L., S. K. Sahoo, S. Vijayaraghavalu, S. Dimitrijevic, J. K. Vasir, T. K. Jain, A. K. Panda and V. Labhasetwar (2008). "3-D tumor model for in vitro evaluation of anticancer drugs." Mol Pharm **5**(5): 849-862.

Hsu, P.-C. and H.-T. Chang (2012). "Synthesis of high-quality carbon nanodots from hydrophilic compounds: role of functional groups." Chemical Communications **48**(33): 3984-3986.

Huisken, J. and D. Y. Stainier (2009). "Selective plane illumination microscopy techniques in developmental biology." Development **136**(12): 1963-1975.

Huisken, J., J. Swoger, F. Del Bene, J. Wittbrodt and E. H. Stelzer (2004). "Optical sectioning deep inside live embryos by selective plane illumination microscopy." Science **305**(5686): 1007-1009.

I

Ivascu, A. and M. Kubbies (2006). "Rapid generation of single-tumor spheroids for high-throughput cell function and toxicity analysis." J Biomol Screen **11**(8): 922-932.

Ivascu, A. and M. Kubbies (2007). "Diversity of cell-mediated adhesions in breast cancer spheroids." Int J Oncol **31**(6): 1403-1413.

J

Jahnke, H. G., D. Steel, S. Fleischer, D. Seidel, R. Kurz, S. Vinz, K. Dahlenborg, P. Sartipy and A. A. Robitzki (2013). "A novel 3D label-free monitoring system of hES-derived cardiomyocyte clusters: a step forward to in vitro cardiotoxicity testing." PLoS One **8**(7): e68971.

Jakob, P. H., J. Kehrer, P. Flood, C. Wiegel, U. Haselmann, M. Meissner, E. H. Stelzer and E. G. Reynaud (2016). "A 3-D cell culture system to study epithelia functions using microcarriers." Cytotechnology: 1-13.

Jasmin, D. C. Spray, A. C. Campos de Carvalho and R. Mendez-Otero (2010). "Chemical induction of cardiac differentiation in p19 embryonal carcinoma stem cells." Stem Cells Dev **19**(3): 403-412.

Jonsson, M. K., Q. D. Wang and B. Becker (2011). "Impedance-based detection of beating rhythm and proarrhythmic effects of compounds on stem cell-derived cardiomyocytes." Assay Drug Dev Technol **9**(6): 589-599.

K

Kadouri, A. (1994). "Cultivation of anchorage-dependent mammalian cells and production of various metabolites." Colloids and Surfaces B: Biointerfaces **2**(1-3): 265-272.

Karp, J. M., J. Yeh, G. Eng, J. Fukuda, J. Blumling, K.-Y. Suh, J. Cheng, A. Mahdavi, J. Borenstein and R. Langer (2007). "Controlling size, shape and homogeneity of embryoid bodies using poly (ethylene glycol) microwells." Lab Chip **7**(6): 786-794.

Keese, C. R., J. Wegener, S. R. Walker and I. Giaever (2004). "Electrical wound-healing assay for cells in vitro." Proc Natl Acad Sci U S A **101**(6): 1554-1559.

Kelm, J. M. and M. Fussenegger (2004). "Microscale tissue engineering using gravity-enforced cell assembly." Trends Biotechnol **22**(4): 195-202.

Khaitan, D., S. Chandna, M. B. Arya and B. S. Dwarakanath (2006). "Establishment and characterization of multicellular spheroids from a human glioma cell line; Implications for tumor therapy." J Transl Med **4**: 12.

Kiernan, J. A. (2000). "Formaldehyde, formalin, paraformaldehyde and glutaraldehyde: what they are and what they do." Microscopy today **1**(5).

Kimura, H., Y. Oyamada, H. Ohshika, M. Mori and M. Oyamada (1995). "Reversible inhibition of gap junctional intercellular communication, synchronous contraction, and synchronism of intracellular Ca 2+ fluctuation in cultured neonatal rat cardiac myocytes by heptanol." Exp Cell Res **220**(2): 348-356.

Kloss, D., M. Fischer, A. Rothermel, J. C. Simon and A. A. Robitzki (2008). "Drug testing on 3D in vitro tissues trapped on a microcavity chip." Lab Chip **8**(6): 879-884.

Kloss, D., R. Kurz, H. G. Jahnke, M. Fischer, A. Rothermel, U. Anderegg, J. C. Simon and A. A. Robitzki (2008). "Microcavity array (MCA)-based biosensor chip for functional drug screening of 3D tissue models." Biosens Bioelectron **23**(10): 1473-1480.

Knight, M. M., S. R. Roberts, D. A. Lee and D. L. Bader (2003). "Live cell imaging using confocal microscopy induces intracellular calcium transients and cell death." American Journal of Physiology-Cell Physiology **284**(4): C1083-C1089.

Korniski, B., T. B. Darr and A. Hubel (1999). "Subzero osmotic characteristics of intact and disaggregated hepatocyte spheroids." Cryobiology **38**(4): 339-352.

Kotov, N. A., Y. Liu, S. Wang, C. Cumming, M. Eghtedari, G. Vargas, M. Motamedi, J. Nichols and J. Cortiella (2004). "Inverted colloidal crystals as three-dimensional cell scaffolds." Langmuir **20**(19): 7887-7892.

Krinke, D., H. G. Jahnke, T. G. Mack, A. Hirche, F. Striggow and A. A. Robitzki (2010). "A novel organotypic tauopathy model on a new microcavity chip for bioelectronic label-free and real time monitoring." Biosens Bioelectron **26**(1): 162-168.

Kyle, A. H., C. T. O. Chan and A. I. Minchinton (1999). "Characterization of three-dimensional tissue cultures using electrical impedance spectroscopy." Biophys J **76**(5): 2640-2648.

Kyle, U. G., I. Bosaeus, A. D. De Lorenzo, P. Deurenberg, M. Elia, J. M. Gómez, B. L. Heitmann, L. Kent-Smith, J.-C. Melchior and M. Pirlich (2004). "Bioelectrical impedance analysis—part I: review of principles and methods." Clinical nutrition **23**(5): 1226-1243.

L

Lamberti, M. J., N. B. Vittar and V. A. Rivarola (2014). "Breast cancer as photodynamic therapy target: Enhanced therapeutic efficiency by overview of tumor complexity." World J Clin Oncol **5**(5): 901-907.

Lankelma, J., H. Dekker, R. F. Luque, S. Luykx, K. Hoekman, P. van der Valk, P. J. van Diest and H. M. Pinedo (1999). "Doxorubicin gradients in human breast cancer." Clinical cancer research **5**(7): 1703-1707.

Laschke, M. W. and M. D. Menger (2016). "Prevascularization in tissue engineering: Current concepts and future directions." Biotechnology advances **34**(2): 112-121.

Lasia, A. (2002). Electrochemical impedance spectroscopy and its applications. Modern aspects of electrochemistry, Springer**:** 143-248.

Laurent, J., C. Frongia, M. Cazales, O. Mondesert, B. Ducommun and V. Lobjois (2013). "Multicellular tumor spheroid models to explore cell cycle checkpoints in 3D." BMC Cancer **13**: 73.

Lee, Jeong, Jeon, Kim and Kang (2010). "Implication of necrosis-linked p53 aggregation in acquired apoptotic resistance to 5-FU in MCF-7 multicellular tumour spheroids." Oncology Reports **24**(1).

Lee, J.-H., H.-H. Lee, K.-N. Kim and K.-M. Kim (2016). "Cytotoxicity and anti-inflammatory effects of zinc ions and eugenol during setting of ZOE in immortalized human oral keratinocytes grown as three-dimensional spheroids." Dental Materials **32**(5): e93-e104.

Lee, J., G. D. Lilly, R. C. Doty, P. Podsiadlo and N. A. Kotov (2009). "In vitro toxicity testing of nanoparticles in 3D cell culture." Small **5**(10): 1213-1221.

Lee, J. M., P. Mhawech-Fauceglia, N. Lee, L. C. Parsanian, Y. G. Lin, S. A. Gayther and K. Lawrenson (2013). "A three-dimensional microenvironment alters protein expression and chemosensitivity of epithelial ovarian cancer cells in vitro." Lab Invest **93**(5): 528-542.

Lee, K.-W., S. K. Lee, J.-W. Joh, S.-J. Kim, B.-B. Lee, K.-W. Kim and K. U. Lee (2004). "Influence of pancreatic islets on spheroid formation and functions of hepatocytes in hepatocyte-pancreatic islet spheroid culture." Tissue engineering **10**(7-8): 965-977.

Lemberger, M.-M., T. Hirsch and J. Wegener (2014). Carbon Nanodots: Synthesis, Characterization, and Bioanalytical Applications. Measuring Biological Impacts of Nanomaterials, Springer**:** 135-175.

Lemberger, M. M. (2015). Carbon Nanomaterials for Bioanalytical Sensing and Multicolor Cell Imaging Dissertation, University of Regensburg.

Levenson, A. S. and V. C. Jordan (1997). "MCF-7: The first hormone-responsive breast cancer cell line." Cancer Research **57**(15): 3071-3078.

Levy-Mishali, M., J. Zoldan and S. Levenberg (2009). "Effect of scaffold stiffness on myoblast differentiation." Tissue Engineering Part A **15**(4): 935-944.

Li, C.-L., C.-M. Ou, C.-C. Huang, W.-C. Wu, Y.-P. Chen, T.-E. Lin, L.-C. Ho, C.-W. Wang, C.-C. Shih and H.-C. Zhou (2014). "Carbon dots prepared from ginger exhibiting efficient inhibition of human hepatocellular carcinoma cells." Journal of Materials Chemistry B **2**(28): 4564-4571.

Li, C. L., T. Tian, K. J. Nan, N. Zhao, Y. H. Guo, J. Cui, J. Wang and W. G. Zhang (2008). "Survival advantages of multicellular spheroids vs. monolayers of HepG2 cells in vitro." Oncol Rep **20**(6): 1465-1471.

Li, J., R. Tao, W. Wu, H. Cao, J. Xin, J. Guo, L. Jiang, C. Gao and A. A. Demetriou (2010). "3D PLGA Scaffolds Improve Differentiation and Function of Bone Marrow Mesenchymal Stem Cell–Derived Hepatocytes." Stem Cells Dev **19**(9): 1427-1436.

Liang, X., X. Xu, F. Wang, N. Li and J. He (2016). "E-cadherin increasing multidrug resistance protein 1 via hypoxia-inducible factor-1α contributes to multicellular resistance in colorectal cancer." Tumor Biology **37**(1): 425-435.

Lieb, S., T. Littmann, N. Plank, J. Felixberger, M. Tanaka, T. Schäfer, S. Krief, S. Elz, K. Friedland and G. Bernhardt (2016). "Label-free versus conventional cellular assays: Functional investigations on the human histamine H 1 receptor." Pharmacological Research **114**: 13-26.

Lin, R. Z. and H. Y. Chang (2008). "Recent advances in three-dimensional multicellular spheroid culture for biomedical research." Biotechnol J **3**(9-10): 1172-1184.

Lin, R. Z., L. F. Chou, C. C. Chien and H. Y. Chang (2006). "Dynamic analysis of hepatoma spheroid formation: roles of E-cadherin and beta1-integrin." Cell Tissue Res **324**(3): 411-422.

Liu, C., P. Zhang, F. Tian, W. Li, F. Li and W. Liu (2011). "One-step synthesis of surface passivated carbon nanodots by microwave assisted pyrolysis for enhanced multicolor photoluminescence and bioimaging." Journal of materials chemistry **21**(35): 13163-13167.

Livera, G., G. Delbes, C. Pairault, V. Rouiller-Fabre and R. Habert (2006). "Organotypic culture, a powerful model for studying rat and mouse fetal testis development." Cell Tissue Res **324**(3): 507-521.

Lo, C. M., C. R. Keese and I. Giaever (1993). "Monitoring Motion of Confluent Cells in Tissue-Culture." Exp Cell Res **204**(1): 102-109.

Lorenzo, C., C. Frongia, R. Jorand, J. Fehrenbach, P. Weiss, A. Maandhui, G. Gay, B. Ducommun and V. Lobjois (2011). "Live cell division dynamics monitoring in 3D large spheroid tumor models using light sheet microscopy." Cell Div **6**: 22.

Lu, H.-F., K.-N. Chua, P.-C. Zhang, W.-S. Lim, S. Ramakrishna, K. W. Leong and H.-Q. Mao (2005). "Three-dimensional co-culture of rat hepatocyte spheroids and NIH/3T3 fibroblasts enhances hepatocyte functional maintenance." Acta Biomaterialia **1**(4): 399-410.

Lukic, S. and J. Wegener (2015). "Impedimetric Monitoring of Cell-Based Assays." eLS.

Lvovich, V. F. (2012). Impedance spectroscopy: applications to electrochemical and dielectric phenomena, John Wiley & Sons.

M

MacLennan, D. H. and E. G. Kranias (2003). "Phospholamban: a crucial regulator of cardiac contractility." Nature reviews Molecular cell biology **4**(7): 566-577.

Mahdavi, S. R., R. Yahyapour and A. Nikoofar (2016). "Cytotoxic effects of hyperthermia, chemotherapy (Navelbine) and radiation on glioma spheroids." Radiation Physics and Chemistry **123**: 20-24.

Martinsen, O. G. and S. Grimnes (2011). Bioimpedance and bioelectricity basics, Academic press.

McAdams, E. and J. Jossinet (1995). "Tissue impedance: a historical overview." Physiological measurement **16**(3A): A1.

McBurney, M. W. (1993). "P19 embryonal carcinoma cells." Int J Dev Biol **37**(1): 135-140.

McBurney, M. W. and B. J. Rogers (1982). "Isolation of male embryonal carcinoma cells and their chromosome replication patterns." Developmental biology **89**(2): 503-508.

Minchinton, A. I. and I. F. Tannock (2006). "Drug penetration in solid tumours." Nat Rev Cancer **6**(8): 583-592.

Minsky, M. (1988). "Memoir on inventing the confocal scanning microscope." Scanning **10**(4): 128-138.

Moscona, A. and H. Moscona (1952). "The dissociation and aggregation of cells from organ rudiments of the early chick embryo." Journal of Anatomy **86**(3): 287-301.

Muckle, D. and J. Dickson (1971). "The selective inhibitory effect of hyperthermia on the metabolism and growth of malignant cells." British journal of cancer **25**(4): 771.

Mueller-Klieser, W. (1984). "Method for the determination of oxygen consumption rates and diffusion coefficients in multicellular spheroids." Biophys J **46**(3): 343-348.

Mueller-Klieser, W. (1997). "Three-dimensional cell cultures: from molecular mechanisms to clinical applications." Am J Physiol **273**(4 Pt 1): C1109-1123.

Mueller-Klieser, W., J. Freyer and R. Sutherland (1986). "Influence of glucose and oxygen supply conditions on the oxygenation of multicellular spheroids." British journal of cancer **53**(3): 345.

Murakami, S., H. Ijima, T. Ono and K. Kawakami (2004). "Development of co-culture system of hepatocytes with bone marrow cells for expression and maintenance of hepatic functions." The International journal of artificial organs **27**(2): 118-126.

N

Nagelkerke, A., J. Bussink, F. C. Sweep and P. N. Span (2013). "Generation of multicellular tumor spheroids of breast cancer cells: How to go three-dimensional." Analytical biochemistry **437**(1): 17-19.

Nguyen, D. C., T. A. Hookway, Q. Wu, R. Jha, M. K. Preininger, X. Chen, C. A. Easley, P. Spearman, S. R. Deshpande, K. Maher, M. B. Wagner, T. C. McDevitt and C. Xu (2014). "Microscale generation of cardiospheres promotes robust enrichment of cardiomyocytes derived from human pluripotent stem cells." Stem Cell Reports **3**(2): 260-268.

Nguyen, H. T.-L., S. T. Nguyen and P. Van Pham (2016). "Concise Review: 3D cell culture systems for anticancer drug screening." Biomedical Research and Therapy **3**(5): 625-632.

Nista, A., C. Leonetti, G. Bernardini, M. Mattioni and A. Santoni (1997). "Functional role of a4b1 and a5b1 integrin fibronectin receptors expressed on adriamycin-resistant MCF-7 human mammary carcinoma cells." International journal of cancer **72**(1): 133-141.

No, D. Y., S.-A. Lee, Y. Y. Choi, D. Park, J. Y. Jang, D.-S. Kim and S.-H. Lee (2012). "Functional 3D human primary hepatocyte spheroids made by co-

culturing hepatocytes from partial hepatectomy specimens and human adipose-derived stem cells." PLoS One **7**(12): e50723.

O

O'Brien, L. E., M. M. Zegers and K. E. Mostov (2002). "Building epithelial architecture: insights from three-dimensional culture models." Nature reviews Molecular cell biology **3**(7): 531-537.

O'Connor, E. R., H. K. Kimelberg, C. R. Keese and I. Giaever (1993). "Electrical resistance method for measuring volume changes in monolayer cultures applied to primary astrocyte cultures." American Journal of Physiology **264**(2 Pt 1): C471-478.

Oberleitner, M. (2015). Label-free and multi-parametric monitoring of cell-based assays with substrate-embedded sensors Doctoral Thesis, University of Regensburg.

Olive, P., R. Durand, J. Banath and H. Evans (1991). "Etoposide sensitivity and topoisomerase II activity in Chinese hamster V79 monolayers and small spheroids." International journal of radiation biology **60**(3): 453-466.

Olive, P. L. and R. E. Durand (1994). "Drug and radiation resistance in spheroids: cell contact and kinetics." Cancer and metastasis reviews **13**(2): 121-138.

Ong, S.-M., Z. Zhao, T. Arooz, D. Zhao, S. Zhang, T. Du, M. Wasser, D. van Noort and H. Yu (2010). "Engineering a scaffold-free 3D tumor model for in vitro drug penetration studies." Biomaterials **31**(6): 1180-1190.

Opp, D., B. Wafula, J. Lim, E. Huang, J. C. Lo and C. M. Lo (2009). "Use of electric cell-substrate impedance sensing to assess in vitro cytotoxicity." Biosens Bioelectron **24**(8): 2625-2629.

Ouyang, L., Z. Shi, S. Zhao, F. T. Wang, T. T. Zhou, B. Liu and J. K. Bao (2012). "Programmed cell death pathways in cancer: a review of apoptosis, autophagy and programmed necrosis." Cell proliferation **45**(6): 487-498.

P

Pagliacci, M., F. Spinozzi, G. Migliorati, G. Fumi, M. Smacchia, F. Grignani, C. Riccardi and I. Nicoletti (1993). "Genistein inhibits tumour cell growth in vitro but enhances mitochondrial reduction of tetrazolium salts: a further pitfall in the use of the MTT assay for evaluating cell growth and survival." Eur J Cancer **29**(11): 1573-1577.

Pampaloni, F., E. G. Reynaud and E. H. Stelzer (2007). "The third dimension bridges the gap between cell culture and live tissue." Nat Rev Mol Cell Biol **8**(10): 839-845.

Patel, D. V. and C. N. McGhee (2007). "Contemporary in vivo confocal microscopy of the living human cornea using white light and laser scanning techniques: a major review." Clinical & experimental ophthalmology **35**(1): 71-88.

Petry, F., J. R. Smith, J. Leber, D. Salzig, P. Czermak and M. L. Weiss (2016). "Manufacturing of human umbilical cord mesenchymal stromal cells on microcarriers in a dynamic system for clinical use." Stem cells international **2016**.

Podolak, I., A. Galanty and D. Sobolewska (2010). "Saponins as cytotoxic agents: a review." Phytochemistry Reviews **9**(3): 425-474.

Potts, M. (1994). "Desiccation tolerance of prokaryotes." Microbiological reviews **58**(4): 755-805.

R

Ramu, V., F. Ali, N. Taye, B. Garai, A. Alam, S. Chattopadhyay and A. Das (2015). "New imaging reagents for lipid dense regions in live cells and the nucleus in fixed MCF-7 cells." Journal of Materials Chemistry B **3**(36): 7177-7185.

Rehder, D., S. Iden, I. Nasdala, J. Wegener, M.-K. M. Zu Brickwedde, D. Vestweber and K. Ebnet (2006). "Junctional adhesion molecule-a participates in the formation of apico-basal polarity through different domains." Exp Cell Res **312**(17): 3389-3403.

Richter, K., M. Haslbeck and J. Buchner (2010). "The heat shock response: life on the verge of death." Molecular cell **40**(2): 253-266.

Rijal, G. and W. Li (2016). "3D scaffolds in breast cancer research." Biomaterials **81**: 135-156.

Robertson, C., D. H. Evans and H. Abrahamse (2009). "Photodynamic therapy (PDT): a short review on cellular mechanisms and cancer research applications for PDT." Journal of Photochemistry and Photobiology B: Biology **96**(1): 1-8.

Robinson, E. E., R. A. Foty and S. A. Corbett (2004). "Fibronectin matrix assembly regulates alpha5beta1-mediated cell cohesion." Mol Biol Cell **15**(3): 973-981.

Roderick, H. L., M. J. Berridge and M. D. Bootman (2003). "Calcium-induced calcium release." Current Biology **13**(11): R425.

Rouwkema, J., J. D. Boer and C. A. V. Blitterswijk (2006). "Endothelial cells assemble into a 3-dimensional prevascular network in a bone tissue engineering construct." Tissue engineering **12**(9): 2685-2693.

S

Sasser, D. C., W. A. Gerth and Y. Wu (1993). "Monitoring of segmental intra-and extracellular volume changes using electrical impedance spectroscopy." Journal of Applied Physiology **74**(5): 2180-2187.

Schumacher, Z., O. Frey and A. Hierlemann (2011). "Microfluidic Impedance Spectroscopy Scanner for Spherical Microtissues." 15th International Conference on Miniaturized Systems for Chemistry and Life Sciences, Seattle, Washington, USA.

Scott, C. W., X. Zhang, N. Abi-Gerges, S. D. Lamore, Y. A. Abassi and M. F. Peters (2014). "An impedance-based cellular assay using human iPSC-derived cardiomyocytes to quantify modulators of cardiac contractility." Toxicol Sci **142**(2): 331-338.

Senyavina, N., T. Gerasimenko, N. Pulkova and D. Maltseva (2016). "Transport and Toxicity of Silver Nanoparticles in HepaRG Cell Spheroids." Bulletin of experimental biology and medicine **160**(6): 831-834.

Sham, E. and R. E. Durand (1998). "Cell kinetics and repopulation mechanisms during multifraction irradiation of spheroids." Radiotherapy and oncology **46**(2): 201-207.

Shapira-Schweitzer, K., M. Habib, L. Gepstein and D. Seliktar (2009). "A photopolymerizable hydrogel for 3-D culture of human embryonic stem cell-derived cardiomyocytes and rat neonatal cardiac cells." Journal of molecular and cellular cardiology **46**(2): 213-224.

Simmerman, H. K. and L. R. Jones (1998). "Phospholamban: protein structure, mechanism of action, and role in cardiac function." Physiological Reviews **78**(4): 921-947.

Simon, H.-U., A. Haj-Yehia and F. Levi-Schaffer (2000). "Role of reactive oxygen species (ROS) in apoptosis induction." Apoptosis **5**(5): 415-418.

Song, C. W., J. C. Lyons, R. J. Griffin, C. M. Makepeace and E. J. Cragoe (1993). "Increase in thermosensitivity of tumor cells by lowering intracellular pH." Cancer research **53**(7): 1599-1601.

Song, H., O. David, S. Clejan, C. L. Giordano, H. Pappas-Lebeau, L. Xu and K. C. O'connor (2004). "Spatial composition of prostate cancer spheroids in mixed and static cultures." Tissue engineering **10**(7-8): 1266-1276.

Soule, H. D. (1973). "A Human Cell Line From a Pleural Effusion Derived From a Breast Carcinoma." J. Natl. Cancer Inst. **51**.

Sparg, S., M. Light and J. Van Staden (2004). "Biological activities and distribution of plant saponins." Journal of ethnopharmacology **94**(2): 219-243.

Stevenson, B. R. and D. A. Begg (1994). "Concentration-dependent effects of cytochalasin D on tight junctions and actin filaments in MDCK epithelial cells." Journal of cell science **107**(3): 367-375.

Stolwijk, J. A., C. Hartmann, P. Balani, S. Albermann, C. R. Keese, I. Giaever and J. Wegener (2011). "Impedance analysis of adherent cells after in situ electroporation: non-invasive monitoring during intracellular manipulations." Biosens Bioelectron **26**(12): 4720-4727.

Stolwijk, J. A., S. Michaelis and J. Wegener (2012). Cell growth and cell death studied by electric cell-substrate impedance sensing. Electric cell-substrate impedance sensing and cancer metastasis, Springer**:** 85-117.

Stoppini, L., P.-A. Buchs and D. Muller (1991). "A simple method for organotypic cultures of nervous tissue." Journal of neuroscience methods **37**(2): 173-182.

Sutherland, R., J. Freyer, W. Mueller-Klieser, R. Wilson, C. Heacock, J. Sciandra and B. Sordat (1986). "Cellular growth and metabolic adaptations to nutrient stress environments in tumor microregions." International Journal of Radiation Oncology* Biology* Physics **12**(4): 611-615.

Sutherland, R. M. (1988). "Cell and environment interactions in tumor microregions: the multicell spheroid model." Science **240**(4849): 177-184.

T

Tadrous, P. J. (2000). "Methods for imaging the structure and function of living tissues and cells: 3. Confocal microscopy and micro-radiology." The Journal of pathology **191**(4): 345-354.

Takahashi, I., Y. Emi, S. Hasuda, Y. Kakeji, Y. Maehara and K. Sugimachi (2002). "Clinical application of hyperthermia combined with anticancer drugs for the treatment of solid tumors." Surgery **131**(1): S78-S84.

Takens-Kwak, B., H. Jongsma, M. Rook and A. Van Ginneken (1992). "Mechanism of heptanol-induced uncoupling of cardiac gap junctions: a

perforated patch-clamp study." American Journal of Physiology-Cell Physiology **262**(6): C1531-C1538.

Takens-Kwak, B. R., H. J. Jongsma, M. B. Rook and A. C. Van Ginneken (1992). "Mechanism of heptanol-induced uncoupling of cardiac gap junctions: a perforated patch-clamp study." American Journal of Physiology **262**(6 Pt 1): C1531-1538.

Tan, Q., J. K. Saggar, M. Yu, M. Wang and I. F. Tannock (2015). "Mechanisms of Drug Resistance Related to the Microenvironment of Solid Tumors and Possible Strategies to Inhibit Them." The Cancer Journal **21**(4): 254-262.

Tannock, I. F., C. M. Lee, J. K. Tunggal, D. S. Cowan and M. J. Egorin (2002). "Limited penetration of anticancer drugs through tumor tissue a potential cause of resistance of solid tumors to chemotherapy." Clinical cancer research **8**(3): 878-884.

Tarantola, M., D. Schneider, E. Sunnick, H. Adam, S. Pierrat, C. Rosman, V. Breus, C. Sonnichsen, T. Basche, J. Wegener and A. Janshoff (2009). "Cytotoxicity of metal and semiconductor nanoparticles indicated by cellular micromotility." ACS Nano **3**(1): 213-222.

Theer, P., M. T. Hasan and W. Denk (2003). "Two-photon imaging to a depth of 1000 µm in living brains by use of a Ti: Al 2 O 3 regenerative amplifier." Optics letters **28**(12): 1022-1024.

Thielecke, H., A. Mack and A. Robitzki (2001). "Biohybrid microarrays--impedimetric biosensors with 3D in vitro tissues for toxicological and biomedical screening." Fresenius J Anal Chem **369**(1): 23-29.

Thielecke, H., A. Mack and A. Robitzki (2001). "A multicellular spheroid-based sensor for anti-cancer therapeutics." Biosens Bioelectron **16**(4-5): 261-269.

Thurber, G. M. and K. D. Wittrup (2008). "Quantitative spatiotemporal analysis of antibody fragment diffusion and endocytic consumption in tumor spheroids." Cancer research **68**(9): 3334-3341.

Toda, S., K. Watanabe, F. Yokoi, S. Matsumura, K. Suzuki, A. Ootani, S. Aoki, N. Koike and H. Sugihara (2002). "A new organotypic culture of thyroid tissue maintains three-dimensional follicles with C cells for a long term." Biochem Biophys Res Commun **294**(4): 906-911.

Tung, Y. C., A. Y. Hsiao, S. G. Allen, Y. S. Torisawa, M. Ho and S. Takayama (2011). "High-throughput 3D spheroid culture and drug testing using a 384 hanging drop array." Analyst **136**(3): 473-478.

V

Vaira, V., G. Fedele, S. Pyne, E. Fasoli, G. Zadra, D. Bailey, E. Snyder, A. Faversani, G. Coggi and R. Flavin (2010). "Preclinical model of organotypic culture for pharmacodynamic profiling of human tumors." Proceedings of the National Academy of Sciences **107**(18): 8352-8356.

van der Heyden, M. A. and L. H. Defize (2003). "Twenty one years of P19 cells: what an embryonal carcinoma cell line taught us about cardiomyocyte differentiation." Cardiovascular Research **58**(2): 292-302.

van der Zee, J. (2002). "Heating the patient: a promising approach?" Annals of oncology **13**(8): 1173-1184.

Van Wezel, A. (1967). "Growth of cell-strains and primary cells on micro-carriers in homogeneous culture."

Verveer, P. J., J. Swoger, F. Pampaloni, K. Greger, M. Marcello and E. H. Stelzer (2007). "High-resolution three-dimensional imaging of large specimens with light sheet-based microscopy." Nat Methods **4**(4): 311-313.

von der Mark, K., V. Gauss, H. von der Mark and P. Müller (1977). "Relationship between cell shape and type of collagen synthesised as chondrocytes lose their cartilage phenotype in culture."

W

Wakatsuki, T., B. Schwab, N. C. Thompson and E. L. Elson (2001). "Effects of cytochalasin D and latrunculin B on mechanical properties of cells." Journal of cell science **114**(5): 1025-1036.

Walpita, D. and E. Hay (2002). "Studying actin-dependent processes in tissue culture." Nature reviews Molecular cell biology **3**(2): 137-141.

Wartenberg, M. and H. Acker (1995). "Quantitative recording of vitality patterns in living multicellular spheroids by confocal microscopy." Micron **26**(5): 395-404.

Wartenberg, M., F. Donmez, F. C. Ling, H. Acker, J. Hescheler and H. Sauer (2001). "Tumor-induced angiogenesis studied in confrontation cultures of multicellular tumor spheroids and embryoid bodies grown from pluripotent embryonic stem cells." FASEB J **15**(6): 995-1005.

Wartenberg, M., S. Gronczynska, M. M. Bekhite, T. Saric, W. Niedermeier, J. Hescheler and H. Sauer (2005). "Regulation of the multidrug resistance transporter P-glycoprotein in multicellular prostate tumor spheroids by hyperthermia and reactive oxygen species." International journal of cancer **113**(2): 229-240.

Wartenberg, M., J. Hescheler, H. Acker, H. Diedershagen and H. Sauer (1998). "Doxorubicin distribution in multicellular prostate cancer spheroids evaluated by confocal laser scanning microscopy and the“optical probe technique”." Cytometry **31**(2): 137-145.

Weaver, V. M., S. Lelièvre, J. N. Lakins, M. A. Chrenek, J. C. Jones, F. Giancotti, Z. Werb and M. J. Bissell (2002). "β4 integrin-dependent formation of polarized three-dimensional architecture confers resistance to apoptosis in normal and malignant mammary epithelium." Cancer cell **2**(3): 205-216.

Wegener, J., C. R. Keese and I. Giaever (2000). "Electric cell-substrate impedance sensing (ECIS) as a noninvasive means to monitor the kinetics of cell spreading to artificial surfaces." Exp Cell Res **259**(1): 158-166.

Weiswald, L. B., J. M. Guinebretiere, S. Richon, D. Bellet, B. Saubamea and V. Dangles-Marie (2010). "In situ protein expression in tumour spheres: development of an immunostaining protocol for confocal microscopy." BMC Cancer **10**: 106.

Wu, H., T. Kuhn and V. Moy (1998). "Mechanical properties of L929 cells measured by atomic force microscopy: effects of anticytoskeletal drugs and membrane crosslinking." Scanning **20**(5): 389-397.

Wust, P., B. Hildebrandt, G. Sreenivasa, B. Rau, J. Gellermann, H. Riess, R. Felix and P. Schlag (2002). "Hyperthermia in combined treatment of cancer." The lancet oncology **3**(8): 487-497.

X

Xing, H., S. Wang, K. Hu, W. Tao, J. Li, Q. Gao, X. Yang, D. Weng, Y. Lu and D. Ma (2005). "Effect of the cyclin-dependent kinases inhibitor p27 on resistance of ovarian cancer multicellular spheroids to anticancer chemotherapy." J Cancer Res Clin Oncol **131**(8): 511-519.

Y

Yahara, I., F. Harada, S. Sekita, K. Yoshihira and S. Natori (1982). "Correlation between effects of 24 different cytochalasins on cellular structures and cellular events and those on actin in vitro." The Journal of Cell Biology **92**(1): 69-78.

Yamada, K. M. and E. Cukierman (2007). "Modeling tissue morphogenesis and cancer in 3D." Cell **130**(4): 601-610.

Yamaguchi, H. and J. Condeelis (2007). "Regulation of the actin cytoskeleton in cancer cell migration and invasion." Biochimica et Biophysica Acta (BBA)-Molecular Cell Research **1773**(5): 642-652.

Yang, J., S. J. Ko, B. S. Kim, H. S. Kim, S. Park, D. Hong, S. W. Hong, J. H. Choi, C. Y. Park, S. C. Choi, S. J. Hong and D. S. Lim (2009). "Enhanced cardiomyogenic differentiation of P19 embryonal carcinoma stem cells." Sunhwangi **39**(5): 198-204.

Yang, S.-T., X. Wang, H. Wang, F. Lu, P. G. Luo, L. Cao, M. J. Meziani, J.-H. Liu, Y. Liu and M. Chen (2009). "Carbon dots as nontoxic and high-performance fluorescence imaging agents." The Journal of Physical Chemistry C **113**(42): 18110-18114.

Yoshii, Y., T. Furukawa, H. Aoyama, N. Adachi, M.-R. Zhang, H. Wakizaka, Y. Fujibayashi and T. Saga (2016). "Regorafenib as a potential adjuvant chemotherapy agent in disseminated small colon cancer: Drug selection outcome of a novel screening system using nanoimprinting 3-dimensional culture with HCT116-RFP cells." Int J Oncol **48**(4): 1477-1484.

Yuajit, C., S. Homvisasevongsa, L. Chatsudthipong, S. Soodvilai, C. Muanprasat and V. Chatsudthipong (2013). "Steviol reduces MDCK Cyst formation and growth by inhibiting CFTR channel activity and promoting proteasome-mediated CFTR degradation." PLoS One **8**(3): e58871.

Z

Zhang, X., W. Wang, W. Yu, Y. Xie, Y. Zhang and X. Ma (2005). "Development of an in vitro multicellular tumor spheroid model using microencapsulation and its application in anticancer drug screening and testing." Biotechnol Prog **21**(4): 1289-1296.

Zhang, Z., K. Vuori, J. C. Reed and E. Ruoslahti (1995). "The alpha 5 beta 1 integrin supports survival of cells on fibronectin and up-regulates Bcl-2 expression." Proceedings of the National Academy of Sciences **92**(13): 6161-6165.

Zhao, Q.-L., Y. Fujiwara and T. Kondo (2006). "Mechanism of cell death induction by nitroxide and hyperthermia." Free Radical Biology and Medicine **40**(7): 1131-1143.

Zong, W.-X. and C. B. Thompson (2006). "Necrotic death as a cell fate." Genes & development **20**(1): 1-15.

13 Appendix

A1 Abbreviations and Symbols

A

A	cross sectional area
A_i	CPE parameter, i: el, para, sph
AC	alternating current
ADM	adriamycin
ANOVA	analysis of variance
ATP	adenosine triphosphate

B

β	mass concentration
BPM	beats per minute
BrdU	bromodeoxyuridine

C

C	capacitance
°C	degree Celsius
CaAM	calcein acetoxymethylester
cAMP	cyclic adenosine monophosphat
CCD	charge coupled device
Cdks	cyclin dependent kinases
C-dot	carbon dot
CI	cytotoxicity index
CICR	calcium-induced calcium release
CLSM	confocal laser scanning microscope
CPE	constant phase element
CTT	camptothecin
cytD	cytochalasin D

D

DAPI	4', 6-diamidino-2-phenylindole
DMEM	Dulbecco's Modified Eagle's Medium
DMSO	dimethylsulfoxide
DNA	deoxyribonucleic acid
DSMZ	*Deutsche Sammlung von Mikroorganismen und Zellkulturen*
Δ	difference
Ø	diameter

E

EBs	embryonic bodies
$EBSS^{++}$	Earle's balanced salt solution
$EBSS^{-+}$	Earle's balanced salt solution (without Ca^{2+}, with Mg^{2+})
$EBSS^{--}$	Earle's balanced salt solution (without Ca^{2+}, without Mg^{2+})
EC_{50}	half maximal effective concentration
ECIS	electric cell-substrate impedance sensing
ECM	extracellular matrix
EDTA	ethylenediaminetetraacetic acid
EdU	5-ethynyl-2'-deoxyuridine
e.g.	(Lat.: *exempli gratia*) for example
et al	(Lat.: *et alii*) and others
EthD-1	ethidium homodimer

F

f	frequency
FACS	fluorescence activated cell sorting
FC- (1 – 4)	flow channel
FCS	fetal calf serum
Fig.	figure
FITC	fluorescein isothiocyanate

G

glc	glucose

H

H (1 – 3)	channel height
H&E	hematoxylin and eosin
HEPES	4-(2-hydroxyethyl)-1-piperazineethane-sulfonic acid) buffer
Ho/Pi	hoechst/propidium iodide
HT	hyperthermia

I

I	current
I_0	amplitude of current
$I_{sample/control}$	fluorescence intensity of the sample/control
i	imaginary factor
IC_{50}	half maximal inhibitory concentration
Im, *X*	imaginary fraction of a complex quantity
IS	impedance spectroscopy
ITO	indium tin oxide

J

φ	phase shift

L

l	length
L	inductance
L (1 – 3)	channel length
LED	Light-emitting diode
LDH	lactate dehydrogenase
λ	wavelength

M

MCA	microcavity array
MCF-7	Michigan cancer foundation
MCR	multicellular resistance
MDCK	Madin-Darby canine kidney
MFT	multiple frequency/time
Mio.	million
MTT	3-(4,5-dimethylthiazol-2-yl)-2,5-diphenyltetrazolium bromide

N

n	number of experiments
n_i	CPE parameter, i: el, para, sph
n.s.	not significant
NGF	nerve growth factor
NRK	normal rat kidney

P

PBS^{--}	phosphate buffered saline (without Ca^{2+} and Mg^{2+})
PC	personal computer
PCL	polycaprolactone
PDMS	poly (dimethylsiloxane)
PDT	photodynamic therapy
PEG	poly (ethylene glycol)
PET	polyethylene terephthalate
PFA	paraformaldehyde
PLGA	poly (lactic-co-glycolic acid)
PMMA	poly (methyl methacrylate)
poly-HEMA	poly (2-hydroxyethyl methacrylate)
PS	photosensitizer
PT (-1/-2)	prototype
2P Mic.	Two-photon excitation microscopy

Q

qPCR	quantitative polymerase chain reaction

R

R	resistance, real part
R_{bulk}	bulk resistance
R_{ch}	channel resistance
R_{ext}	total extracellular resistance
R_{int}	total intracellular resitance
RA	retinoic acid
Re	real fraction of a complex quantity
ROS	reactive oxygen species
RT	room temperature
RTC	rapid time collect
RT-PCR	reverse transcription-polymerase chain reaction
rpm	rounds per minute
ρ	specific resistivity

S

S	spheroid
SD	standard deviation
SE	standard error
SEM	scanning electron microscopy
SPIM	selective plane illumination microscopy
SR	sarcoplasmatic reticulum
σ	Warburg impedance

T

t	time
$t_{a.a.}$	time after spheroid addition into the channel
Tab.	table
TB	trypan blue

TEM	transmission electron microscopy
TUNEL	terminal deoxynucleotidyl transferase dUTP nick end labeling

U

U	voltage
USB	universal serial bus
UV	ultraviolet

V

V_i	variance, i: 16, 32, 64

W

w	with
W (1 – 3)	channel width
wo	without
ω	angular frequency

Z

Z	impedance
IZI	impedance magnitude
$\|Z\|_{rel}$	relative impedance
Z_{cell}	impedance of a cell
Z_{sph}	impedance of the spheroid
Z_{total}	total impedance of the system

A2 Supplementary Figures and Tables

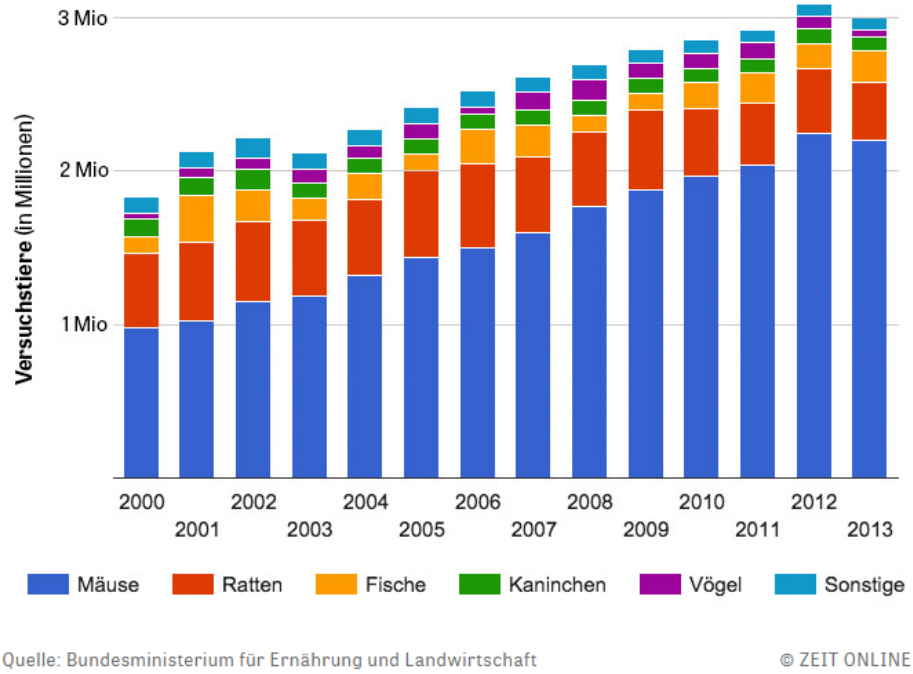

Fig. S1: Statistic of the German Federal Ministry of Food and Agriculture showing the total number of animals used for scientific purposes from the year 2000 to 2013. The total number of animals used in the year 2014 was ~ 2.8 million.

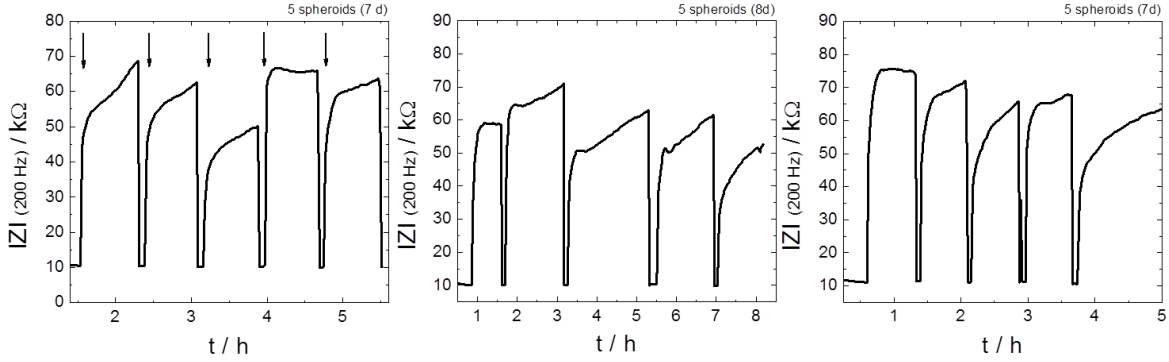

Fig. S2: Three individual measurements showing each the time course of the impedance magnitude at 200 Hz for five spheroids of the same batch (#1 – 3). The arrows mark the time points when the spheroids were introduced in the channel. T = 37 °C.

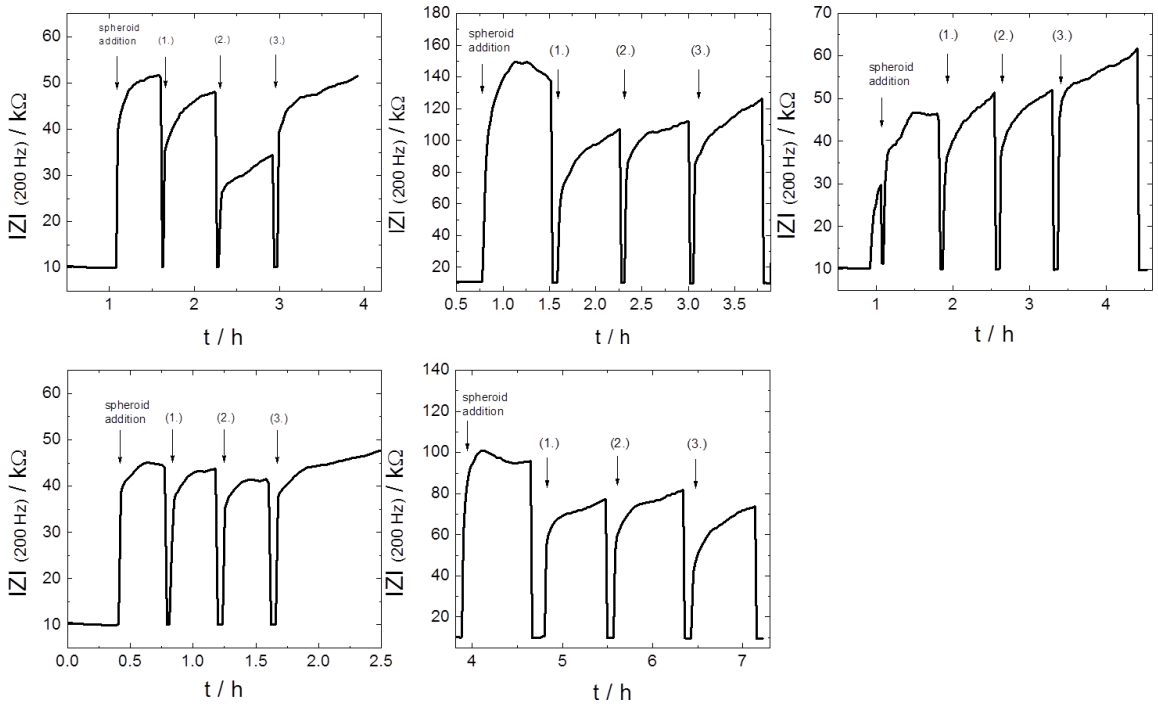

Fig. S3: Five individual measurements showing the influence of repositioning of spheroids (3000 cells/well) on the impedance. Shown are time courses of impedance magnitude at 200 Hz for a 9 d old spheroids which were repositioned three times (1. – 3.) after first addition (arrows).

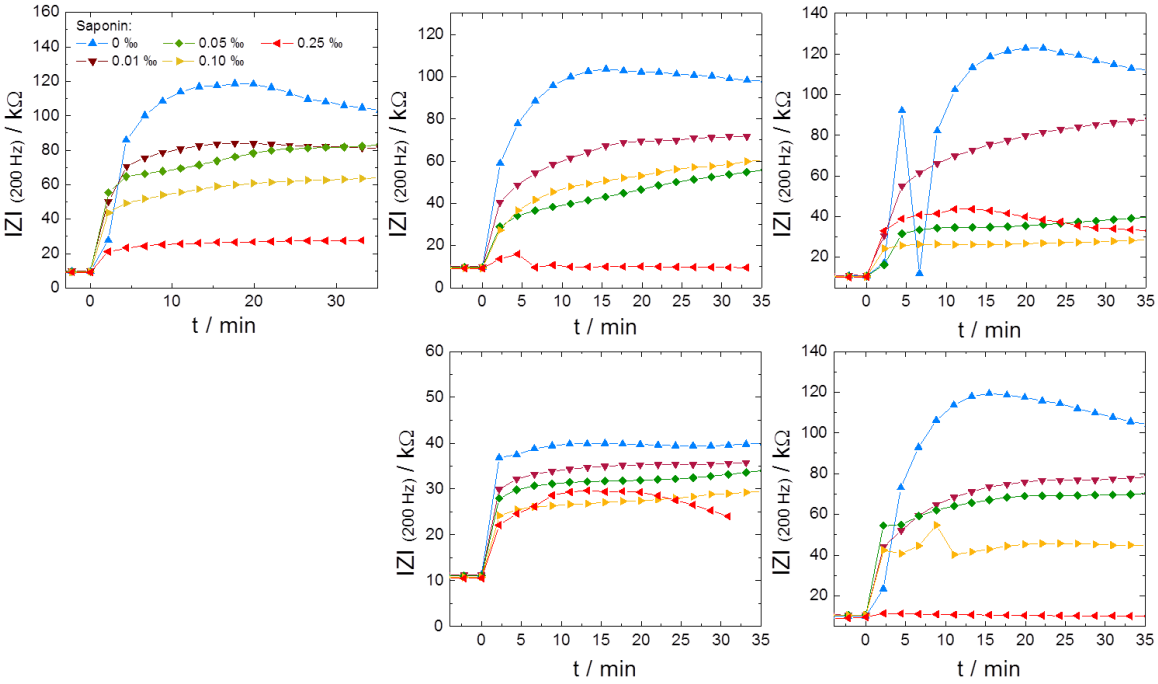

Fig. S4: Five individual permeabilization experiments showing each serial measurements of gradually permeabilized MCF-7 spheroids (3000 cells/well, 7/8 d) measured in FC-1/-3/-4. Shown are time courses of impedance magnitude at 200 Hz for spheroids after pre-incubation with different saponin concentrations (0 ‰ – 0.25 ‰) for 4 h. T = 37 °C.

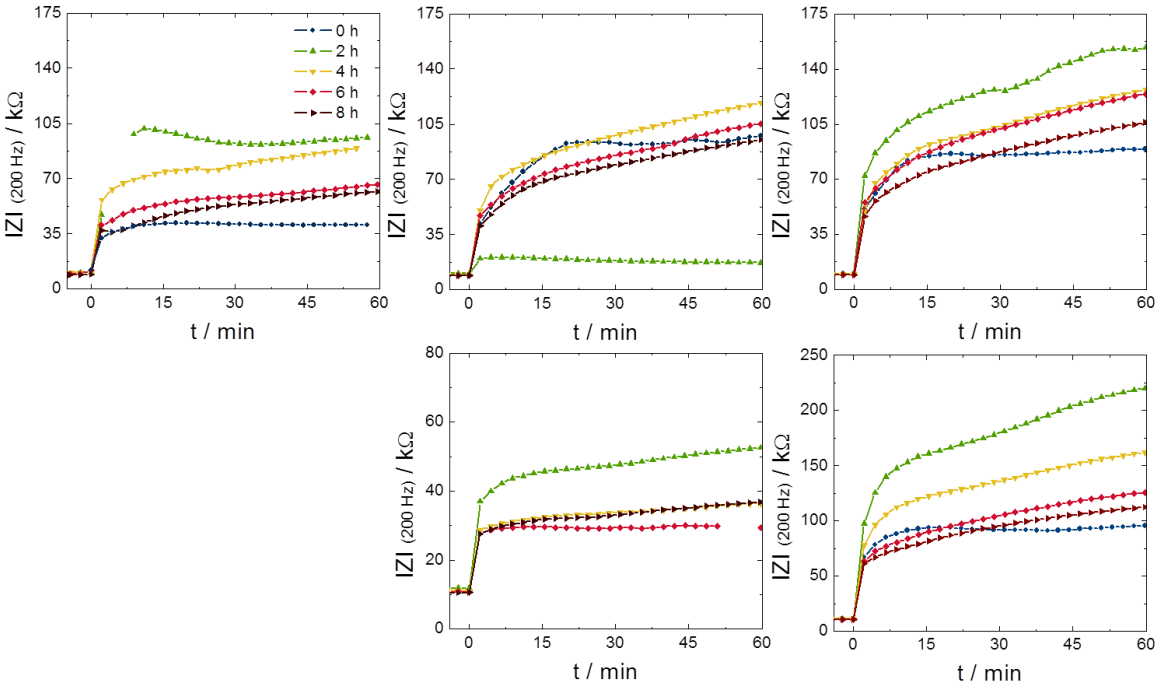

Fig. S5: Five individual experiments showing the serial measurements of MCF-7 spheroids (3000 cells/well, 7/8 d) pre-incubated with 5 µM cytochalasin D for 0 / 2 /4 / 6 / 8 h as time courses of impedance magnitude |Z| at 200 Hz and measured in medium in FC-1/-2/-3/-4. T = 37 °C.

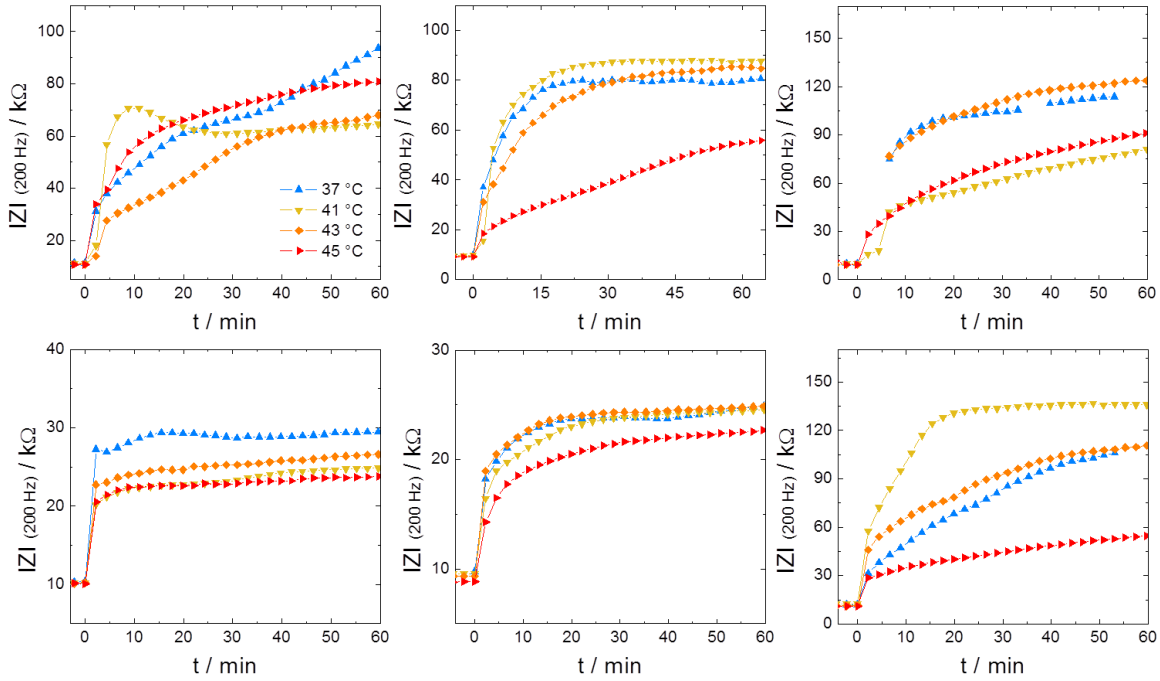

Fig. S6: Six individual hyperthermia experiments showing the serial measurements of MCF-7 spheroids (3000 cells/well, 7 d). Shown are the time courses of impedance magnitude at 200 Hz for spheroids that were exposed to 37 / 41 / 43 / 45 °C for 1 h in FC-2/-3/-4. T = 37 °C.

Tab. S1: Filter Specifications used in the Nikon Diaphot.

Fluorescence filter	*excitation / nm bandpass*	*Dichroidic mirror / nm*	*emission / nm longpass*
UV-2A	330-380	400	420
B	420-490	510	520
G	510-560	580	590

Tab. S2: Overview of the relative spheroid impedances IZI_{rel} of five MCF-7 spheroids 22 min after initial addition (**0**) and after three subsequent repositionings (**1.** – **3.**) with the mean ± SD given for each spheroid.

IZI_{rel}	***0***	***1.***	***2.***	***3.***	***Mean ± SD***
S-1	4.1	3.5	2.1	3.6	3.3 ± 0.9
S-2	3.4	3.3	3.0	3.4	3.3 ± 0.2
S-3	13.1	8.3	9.5	10.1	3.9 ± 0.4
S-4	8.8	5.6	6.6	5.8	10.3 ± 2.0
S-5	3.5	3.6	3.8	4.5	6.7 ± 1.4

Tab. S3: Variance analysis of RTC data comprising six individual hyperthermia measurements investigating the spheroidal response to temperatures between 37 and 45 °C and the data for the flow channel without MCF-7 spheroid. Values in grey fields correspond to data measured with FC-3, values in white field correspond to data measured in FC-4.

V_{32} / Ω^2	***T / °C***				
	37	***41***	***43***	***45***	***wo***
1	673.0	188.4	502.4	0.3	0.5
2	1251.6	491.4	676040.7	249.7	0.3
3	791.5	630.0	480.4	0.5	0.5
4	1189.5	723.7	695.4	5.5	22.2
5	775.0	1103.3	2960.2	1.2	41.5
6	846.9	761.5	392.7	2.1	0.2

Tab. S4: P19 EB parameters: petri dish; n_{para} = 0.99, n_{sph} = 0.75

	R_{ext} / kΩ	R_{int} / kΩ	A_{sph} / $\cdot 10^{-9}$ $Fs^{n-1}cm^{-2}$	A_{CPE} / $\cdot 10^{-6}$ $Fs^{n-1}cm^{-2}$	n_{CPE}	R_{bulk} / kΩ	A_{para} / $\cdot 10^{-12}$ $Fs^{n-1}cm^{-2}$
Cardio-EB 1	20.9	4.0	0.9	2.4	0.96	11.8	2.7
Cardio-EB 2	2.3	4.4	25	1.9	0.96	9.8	3.0
Neuro-EB 1	10.1	21	2.1	2.4	0.97	11.4	3.0
Neuro-EB 2	26.8	6.6	1.1	1.9	0.96	9.5	3.0

Tab. S5: P19 EB parameters: hanging drop; n_{para} = 0.99, n_{sph} = 0.75

	R_{ext} / kΩ	R_{int} / kΩ	A_{sph} / $\cdot 10^{-9}$ $Fs^{n-1}cm^{-2}$	A_{CPE} / $\cdot 10^{-6}$ $Fs^{n-1}cm^{-2}$	n_{CPE}	R_{bulk} / kΩ	A_{para} / $\cdot 10^{-12}$ $Fs^{n-1}cm^{-2}$
(1) 300 cells/well	39.3	2.9	1.5	2.4	0.93	9.9	2.0
(2) 300 cells/well	25.6	3.4	1.7	2.4	0.93	9.4	3.3
(3) 300 cells/well	36.9	4.1	1.2	1.8	0.94	10.1	2.5
(1) 300 cells/well +DMSO	32.8	2.6	2.2	1.8	0.94	10.1	2.5
(2) 300 cells/well +DMSO	33.5	2.9	1.6	1.8	0.94	10.1	2.5
(1) 600 cells/well	32.1	4.4	1.3	2.4	0.93	9.9	3.0
(2) 600 cells/well	21.6	3.6	1.6	2.4	0.93	9.1	2.5

A3 Materials and Instrumentation

A

Argon Plasma Cleaner (Harrick Plasma)
Ascent Reader (Labsystems)
Autoclave (DX-45, Systec, Wettenberg)

B

Bunsen burner for cell culture (Fireboy Tecnomare, Fernwald)
Bürker hemocytometer (Marienfeld)

C

Calcein AM (Molecular Probes)
Calcium chloride (Sigma-Aldrich)
Cell culture dishes: Greiner bio-one (9.2 cm^2), Sarstedt (60.1 cm^2)
Cell culture flasks (12.5 cm^2) (25 cm^2) (75 cm^2)
Cell culture incubator (Thermo Fisher Scientific Inc.)
Cell culture medium: DMEM, MEM Eagle (Sigma-Aldrich, Biochrom)
Cell culture 96-well plates (TPP, Greiner)
Centrifuge Heraeus Multifuge 1S-R for cell culture (Thermo Fisher Scientific)
Centrifuge tubes: 15 mL, 50 mL (Sarstedt, Greiner)
Cor.At® Cells (Axiogenesis)
Cor.At® Culture Medium (Axiogenesis)
Cryovials 1.8 mL (Nunc)
Cytochalasin D (Sigma-Aldrich)

D

DAPI: *4',6-diamidino-2-phenylindole* (Sigma-Aldrich)
Digital USB microscope (Supereyes, Shenzhen D&F Co)
Disposable pipettes: 1, 2, 5, 10, 25 ml (Sarstedt)
DMSO: *dimethyl sulfoxide* (Roth)

E

$EBSS^{++}$ (Sigma-Aldrich)
$EBSS^{--}$ (Life Technologies)
ECIS 1600R (Applied BioPhysics, Troy, NY, USA)

EDTA: *ethylenediaminetetraacetic acid* (Sigma-Aldrich)
Electrode arrays (commercially available): 8W1E, 8W10E (Applied BioPhysics Inc.)
EthD-1: Ethidium Homodimer (Molecular Probes)
Eppendorf Centrifuge 5415R

F

FCS: *fetal calf serum* (Biochrom)
FITC dextran: *Fluorescein isothiocyanate* dextran with average mol wt 4 kDa, (Sigma-Aldrich)
Frequency generator 33120 A (HP-Agilent)

G

D-Glucose (Merck)
L-Glutamine (Biochrome)

H

HEPES (Roth)
1-heptanol (Sigma-Aldrich)
Hydrogen Chloride (VWR International GmbH)

I

Impedance analyzer SI-1260 (Solartron Instruments)
Isoproterenol hydrochloride (Sigma-Aldrich)
ITO-PET foil (Sigma-Aldrich, USA)

L

Laminar flow hood (HERAsafe®, Thermo Scientific, München)
Latex gloves (Roth)

M

Magnesium chloride hexahydrate (Sigma-Aldrich)
Micro Centrifuge (Roth)
Microscopes: Nikon Diaphot, Nikon Eclipse 90i (Nikon), Zeiss Axiovert 200M

N

Nitric Acid (VWR International GmbH)

O

Orbital shaker KM-2 AKKU (Edmund Bühler GmbH)
Osmometer: Osmomat 030 (Gonotec)

P

PBS^{--}/ PBS^{++} (Sigma-Aldrich)
PDMS: *Polydimethylsiloxan* (Dow Corning)
Penicillin/Streptomycin (Sigma-Aldrich)
PFA: *paraformaldehyde* (Sigma-Aldrich)
Pipette Tips: 10 µL; 100 µL; 1000 µL (Sarstedt)
PrestoBlue® cell viability assay (Invitrogen)
Puromycin (Axiogenesis)

R

Reaction Tubes: 500 µL – 2 mL (Sarstedt, Greiner)

S

Saponin (Sigma-Aldrich)
Silicon Glue Aquadicht PROBAU (Bauhaus)
Sodium Hydroxide (VWR International GmbH)
Sterile Filter: pore diameter 0.2 µm (TPP)

T

Thermomixer compact (Eppendorf)
Triton-X-100 (Sigma-Aldrich)
0.05 %; 0.25 % (w/v) Trypsin (Sigma-Aldrich)

U

Ultrasonic Bath: Sonorex Digitech (Bandelin Electronics)

V

Vortex mixer (Heidolph)

W

Waterbath (TW12, Julabo, Seelbach)
Weighing Instrument (Mettler Toledo)

A4 Software

EZ-C1 3.90 FreeViewer (Nikon)

LSM Image Browser (Zeiss)

ImageJ

ECIS Software (Applied BioPhysics, Inc.)

ECIS Viewer

LabVIEW-based Software (J. Wegener) for:

- the manual/automated fitting of impedance spectra (Nr. 1)
- the variance analysis of RTC data (Nr. 2)
- the analysis of cardiosphere RTC data (Nr. 3)

Danksagung

An dieser Stelle möchte ich mich bei den Menschen bedanken, die mich während meiner Doktorarbeit unterstützt haben.

Mein größter Dank gilt Prof. Dr. Joachim Wegener, der mich in meiner Arbeit angeleitet hat und mir gleichzeitig die Freiheit gab eigenständig zu forschen.

Ich möchte mich ebenfalls bei Frau Prof. Dr. Antje J. Bäumner für die Übernahme des Zweitgutachtens, bei Frau PD Dr. Miriam Breunig für die Übernahme des Amtes der Drittprüferin und bei Prof. Dr. Müller für die Übernahme des Amts des Vorsitzenden bedanken. Vielen Dank, dass Sie sich für mich Zeit genommen haben.

Ganz besonderer Dank gilt Dr. Judith Stolwijk für die Korrekturlesung meiner Doktorarbeit und Dr. Stefanie Michaelis für ihre Unterstützung und Beratung.

Ich bedanke mich auch für die tolle Zusammenarbeit mit Barbara Goricnik, Nadja Hinterreiter und Angelika Stoiber. Sowie bei Romy Freund, Dr. Michael Lemberger und Pierre Pütz für ihre Unterstützung bei den Phototoxizitäts-messungen.

Von Herzen danke ich dem ganzen AK Wegener für die gemeinsame Zeit, die wir auf Gemeinschaftsausflügen, Tagungen und Feiern verbracht haben. Vom ersten Tag, an dem ich von meinen ehemaligen - und einmaligen - Laborkollegen Michaela Sperber und Maximilian Oberleitner aufgenommen wurde, bis heute bin ich froh und dankbar, dass ich ein Teil dieser Gruppe war.

Schließlich möchte ich mich auch noch bei Eva, Johanna, Uli und meiner Familie bedanken. Ihr habt mich stets unterstützt und ermutigt.